OPTIMAL PLANNING OF VIRTUAL INERTIA INSTALLATIONS TO IMPROVE THE POWER SYSTEM FREQUENCY RESPONSE

A Thesis Submitted to the
College of Graduate and Postdoctoral Studies
In Partial Fulfillment of the Requirements
For the Degree of Doctor of Philosophy
In the Department of Electrical and Computer Engineering
University of Saskatchewan
Saskatoon

By

Peiyan Li

PERMISSION TO USE

In presenting this thesis/dissertation in partial fulfillment of the requirements for a Postgraduate degree from the University of Saskatchewan, I agree that the Libraries of this University may make it freely available for inspection. I further agree that permission for copying of this thesis/dissertation in any manner, in whole or in part, for scholarly purposes may be granted by the professor or professors who supervised my thesis/dissertation work or, in their absence, by the Head of the Department or the Dean of the College in which my thesis work was done. It is understood that any copying or publication or use of this thesis/dissertation or parts thereof for financial gain shall not be allowed without my written permission. It is also understood that due recognition shall be given to me and to the University of Saskatchewan in any scholarly use which may be made of any material in my thesis/dissertation.

Requests for permission to copy or to make other uses of materials in this thesis/dissertation in whole or part should be addressed to:

Head of the Department of Electrical and Computer Engineering
University of Saskatchewan
57 Campus Drive
Saskatoon, Saskatchewan, S7N 5A9
Canada

OR

Dean
College of Graduate and Postdoctoral Studies
University of Saskatchewan
116 Thorvaldson Building, 110 Science Place
Saskatoon, Saskatchewan S7N 5C9 Canada

Abstract

In recent years, the power system has seen a fast transformation from one primarily based on fossil energy to one where renewable energy, especially wind and solar power, takes a more significant proportion in the energy profile. With the shift in energy profile come the changes in the electricity generation units. The solar panels and wind turbines replace the synchronous generators in electricity generation. Most solar and wind generation units is converter-interfaced. In contrast, the synchronous generator is connected to the power grid directly. For this reason, the future power system of a high level of renewable penetration will exhibit dynamic properties different from the traditional power system, which poses many challenges. One of the challenges is related to frequency stability.

The frequency stability of a traditional power system is secured with a three-level frequency control scheme. The scheme is composed of three frequency regulation mechanisms at different time scales. The fastest control mechanism, named *primary frequency control*, needs about 5 s to be fully deployed to arrest the frequency drops or overshoots. After that, the other two frequency controls, *secondary* and *tertiary* frequency control mechanisms, are then slowly deployed to bring the system frequency back to the nominal value. Under this control scheme, the overall active power generation and consumption in a power system get balanced, and the power frequency variation is limited within a narrow range around a nominal value. However, before the primary frequency control is sufficiently deployed, the system relies on the natural inertia response of the synchronous generators to maintain the active power balance at the sacrifice of changes in the generators' rotational speeds. As the power frequency is decided collectively by the rotational speeds of all synchronous generators in the system, larger system inertia means smaller power frequency variation when subject to the same disturbance.

Since there is no lack of system inertia in a synchronous generator-dominant power system, the power frequency variation with the help of the tertiary control scheme is usually

contained within a limited range. For a future power system with more and more synchronous generators being displaced by converter-interfaced generation (CIG) units, the system inertia decreases. The tertiary frequency control scheme alone can no longer limit the power frequency variation within an acceptable range. For this reason, techniques were proposed to emulate inertia response on a converter-interfaced generation unit.

Apart from the level of total system inertia, studies show that the spatial distribution of system inertia can also influence the frequency response. Under this context, a well-planned virtual inertia installation at selected locations can achieve a satisfactory level of improvement on frequency response at a low investment cost. This thesis work aims at developing a systematic method to search for the most economical plan of virtual inertia installations while ensuring a satisfactory level of frequency response.

In order to derive the most economical plan of virtual installation, a mathematical optimization problem is proposed with constraints formulated with the help of a newly proposed metric of inertia response that quantifies the influence of inertia on the system frequency response. The formulation of the optimization problem considers all possible combinations of loading and renewable generation profiles.

Two methods are proposed to solve the optimization problem of the mixed-integer type. The first one is based on the classic scheme of dynamic programming. The second method adopts a relaxation technique based on the sparsity promotion or Majorize-Minimization (MM) method. Furthermore, parallel and cloud programming techniques are used to facilitate computation speed.

Other minor contributions include a design of a supplementary controller on top of the inertia emulation control to improve the voltage stability of a converter-interfaced generation unit.

Finally, case studies were conducted on a modified Southeast Australian power system against different types of faults to validate the performance and investment cost of the virtual inertia installation plan given by the proposed method in comparison with two other methods. The result shows that the virtual inertia installation plan given by the proposed method produces better performance while at lower investment costs.

Acknowledgement

I would like to express my most profound appreciation for my supervisors: Prof. C. Y. Chung and Prof. S. O. Faried. Without their continuous supports, guidance, and encouragement, I could never complete my Ph.D. study. From them, I learned not only knowledge but also patience, persistence, and optimism. I do not think I could have any better supervisors.

I also thank every member of my advisory committee, Prof. Zhixin Miao, Prof. Rajesh Karki, Prof. Reza Fotouhi, Prof. Xiaodong Liang, and Prof. Ebrahim Bedeer Mohamed, for their invaluable advice and insightful comments.

I am indebted to Mahdi, Weijia, Junpeng, Jeo, Osama, Yuchuan, Mohamed, Bo, Bingzhi, Alex, Alireza, and every member in the SMARTGEN lab. They are always warm-hearted and compassionate. They gave me precious academic advice, and they shared happiness with me. They made me a better person. I am grateful to the University of Saskatchewan, where I got the best learning environment.

Finally, I would like to thank my parents, family, and friends. They were always by my side whenever I needed them. They made me feel confident in pursuing the Ph.D. degree.

Table of Contents

List of Tables

List of Figures

List of Algorithms

List of Symbols and Abbreviations

Abbreviations

AEMO	Australian Energy Market Operator
AoA	Angle of Attack
AVR	Automatic Voltage Regulator
BES	Battery Energy System
BESS	Battery Energy Storage System
CIG	Converter Interfaced Generation
COI	Center of Inertia
DFIG	Doubly-Fed Electric Generator
DP	Dynamic Programming
EMF	Electromotive Force
ENTSO-E	European Network of Transmission System Operator for Electricity
ERCOT	Electric Reliability Council of Texas
FR	Frequency Response
I.V.P.	Initial Value Problem
IEEE	Institute of Electrical and Electronics Engineers
LQ	Linear Quadratic
LQR	Linear Quadratic Regulator
LVRT	Low Voltage Ride Through
MM	Majorize-Minimization or Minorize-Maximization
MPPT	Maximum Power Point Tracking
NSW	New South Wales
O.D.E.	Ordinary Differential Equation
OS	Operating System

P.D.E.	Partial Differential Equation
PD	Proportional Differential
PEBS	Potential Energy Boundary Surface
PI	Proportional Integral
PLL	Phase-Locked Loop
PSS	Power System Stabilizer
PST	Power System Toolbox
PV	photovoltaic generation
PWM	Pulse-Width Modulation
QLD	Queensland
RoCoF	Rate of Change of Frequency
SA	South Australia
SG	Synchronous Generator
STATCOM	Static Synchronous Compensator
SVC	Static VAR Compensator
TSO	Transmission System Operator
UCTE	Union for the Coordination of Transmission of Electricity
VIC	Victoria
VSG	Virtual Synchronous Generator

Math Symbols

Physical Symbols

b, B	Susceptance (S or p.u., $b \in \mathbb{R}$)
c, C	Capacitance (F or p.u., $C \in \mathbb{R}_+$)
d	Generator's Drooping Coefficient (kW/Hz, s, or p.u.)
δ	Rotor's Electrical Angle in a Synchronous Angular Reference (rad, $\delta \in \mathbb{T}$)
E	Electromotive Force ($V, E \in \mathbb{R}$)
f	Frequency (unit: Hz, domain: $f \in \mathbb{R}_+$)
f_{COI}	Center-of-Inertia Frequency (Hz)
g, G	Conductance (S or p.u., $R \in \mathbb{R}_+$)

M, H	Time Constant of Inertia (seconds)
i, I	Current (A or p.u., $I \in \mathbb{R}$)
L	Inductance (H or p.u., $L \in \mathbb{R}_+$)
m	Generator's Moment-of-Inertia (Rotational Inertia) ($\text{kg} \cdot m^2$ or p.u., $mf \in \mathbb{R}_+$) or Modulation Signals for Power Switches (as in m_{dq} but $m \in \left[-1, 1\right]$)
ω	Rotational Speed (rad/s, $\omega \in \mathbb{R}$)
P	Active Power (kW or p.u., $P \in P \in \mathcal{R}$)
p	Number of Pole Pairs in a Generator/Motor or Active Power (kW or p.u., $p \in \mathbb{R}$)
$p_{\text{e}}, P_{\text{e}}$	Electrical Power (kW or p.u., $p_{\text{e}} \in \mathbb{R}$)
$p_{\text{gen.}}, P_{\text{gen.}}$	Active Power generation (kW or p.u., $p_{\text{gen.}} \in \mathcal{R}$)
$p_{\text{m}}, P_{\text{m}}$	Mechanical Power (kW or p.u., $p_{\text{m}} \in \mathbb{R}$)
ψ	Magnetic Flux Linkage in a Generator/Motor (Wb or p.u., $\psi \in \mathbb{R}_+$)
Q	Reactive Power (kVar or p.u., $P \in \mathbb{R}$)
r, R	Resistance (Ω or p.u., $R \in \mathbb{R}_+$)
S	Machine's kVA Rating
t	Time (seconds, $t \in \mathbb{R}$)
τ_{e}	Electrical Torque (p.u., $\tau_{\text{e}} \in \mathbb{R}$)
τ_{m}	Mechanical Torque (p.u., $\tau_{\text{m}} \in \mathbb{R}$)
θ	Rotor's Electrical Angle in Stationary Angular Reference (rad, $\theta \in \mathbb{T}$)
v, V	Voltage (V or p.u., $V \in \mathbb{R}_+$)
X	Reactance (Ω or p.u., $X \in \mathbb{R}_+$)
Y	Admittance Matrix

Variables and Functions

e_i	Unit Vector along the i-th Direction
$\mathcal{J}$, `BIN` (Calligraphic Uppercase Letters or a word in monospaced typeface)	Countable Set (possibly infinite or countably infinite)

$\mathbb{R}$ (Double-struck Uppercase Letters)	Mathematical Field
v (Italic Lowercase Letters)	Column Vector (including one dimensional vector, a.k.a., a scalar)
Y (Italic Uppercase Letters)	Matrix (including 1×1 matrix, a.k.a., a scalar)

Group 1

$\mathcal{H}_2$	Hardy 2-norm
$\mathcal{H}_\infty$	Hardy ∞-norm
$\mathbb{1}$	Column Vector Consisting of All Ones

Group 2

A	Adjacency Matrix of a Graph
$\mathcal{E}$	Set of a Graph's Edges, i.e., a Set of Transmission Links
G	Graph $G = (\mathcal{V}, \mathcal{E}, A)$ consisting of a Set of Vertices $\mathcal{V}$, Edges $\mathcal{E}$, and Adjacency Matrix A
L	Laplacian Matrix of a Graph
0_-	Time Indicating Steady Conditions prior to System Contingency, $0_- := \lim_{t \uparrow 0} t$
0_+	Time Indicating Initial Conditions, $0_+ := \lim_{t \downarrow 0} t$

Group 3

$U_k(x_k)$	Set of Control Inputs for State x_k at the k-th Stage
f_c	Cost Objective
f_m	Surrogate Metrics of Frequency Stability
h_j	Virtual Inertia Installation at Bus Indexed by j
J	Cost Function in Discrete Dynamic Programming Problem
J^*	Optimal Cost Function in Discrete Dynamic Programming Problem

$\mathcal{J}$	Index Set of Buses Selected for Virtual Inertia Installations
μ	Decision Policy
π	Sequence of Control Policies at Each Stage
x_k	Iterates at the i-th Step or System States at the i-th Stage in Dynamic Programming
$\mathcal{J}$	Set of Generation Buses in a Power Grid
$\mathcal{R}$	Region of Attraction
$\mathcal{V}$	Set of Buses in a Power Grid
`BIN`	Set of Candidate Nodes in Dynamic Programming
`CHILDREN`	Set of Candidate Nodes in Dynamic Programming Algorithm
`UPPER`	Register of Known Optimal Value in Dynamic Programming Algorithm

Scripts

$\cdot_{\alpha\beta}$	Quantity in $\alpha\beta$-axis
$\cdot_{\text{avg.}}$	Time-Average of a Quantity, $f_{\text{avg.}} = \int_t \frac{1}{t} f(t)$
$\mathsf{Card}(\cdot)$	Cardinality of a Set
$\cdot_d$	d-axis Component of a Quantity
$\cdot_{\text{dc}}$	Quantity in DC Circuit
$\cdot_{\text{emergency}}$	Emergency Value of a Quantity
$\cdot_f$	Quantity in Field Circuit
$\mathfrak{Im}\{\cdot\}$	Imaginary Component of a Quantity
$\cdot_{(i)}$	the i-th element of a Vector
$\cdot^{(k)}$	Iteration Counter
$\underline{\cdot}$	the Lower Limit of a Quantity
$\cdot_{\text{nadir}}$	Nadir Value of a Quantity, $f_{\text{nair}} := \inf_{t\geq 0} f(t)$
$\cdot_{\text{nominal}}$	Nominal Value of a Quantity
$\cdot_q$	q-axis Component of a Quantity

$\__r$	Rotor's Quantity
$\mathfrak{Re}\{\_\}$	Real Component of a Quantity
$\overline{\_}$	the Upper Limit of a Quantity
$\__0$	Quantity's Initial Value
$\hat{\_}$	Estimated Quantity or a Feasible Solution to an Approximation Problem
$\_^*$	Quantity's Reference Value or Optimal Value, or complex conjugate
$\|\_\|$	Quantity's Absolute Value
$\|\|\_\|\|$	Quantity's 2-Norm

Chapter 1

Introduction

This chapter discusses the background and motivation for the research. The discussion starts with an introduction to the shift in the energy profile in the power system, with renewables taking an increasing proportion in electricity generation. Meanwhile, the traditional synchronous generators for fossil-fuel-based generation are being replaced by converter-interfaced generation units, like in the wind the solar power generation.

Unlike the synchronous generators, those converter-interfaced generation units as pieces of stationary devices cannot contribute rotational inertia to the power system. Therefore, overall system rotational inertia decreases. The lack of rotational inertia poses significant challenges to the stability of the modern power system. This chapter draws attention to the impact of low system inertia on frequency stability.

In order to mitigate the diminishing level of system inertia, several forms of virtual inertia emulation control have been proposed on the converter-interfaced generation units. In the second half of this chapter, existing forms of virtual inertia control are introduced. Among them, the grid-forming and grid-following types of virtual inertia emulation are compared. Finally, this chapter is concluded with a presentation of the primary objectives of the research and the main contribution. The methodology of achieving the main research goal is also summarized.

1.1. The Motivation

1.1.1. Shifts in Energy Landscape

Under the auspices of the Pairs Agreement [1], the goal has been set in many countries to substitute renewable energy resources for fossil fuel and nuclear energy. Because of their relative maturation and cost-effectiveness, wind power and photo-voltaic generations are the preferred means of renewable generation on a large scale. The following is a short survey of renewable installation plans of some big power system operators.

1. In Ireland (EirGrid) [2], the installation of all-island wind capacity reached 3320 MW in 2019, accounting for more than 22% of the yearly electricity generation. The instantaneous penetration level reaches as high as 54% in operation.

2. Australia [3] sees a similar shift in the energy landscape. The combined solar (excluding rooftop PV) and wind power generation accounted for 22% of the total 2020-2021 electricity production. According to the development plan of the Australian Energy Market Operator (AEMO), the sum of solar (excluding rooftop PV) and wind power generation will account for more than 34% of annual electricity generation in the near future.

3. In Canada [4], the installed wind turbine and solar generation capacity has reached 16300 MW, accounting for more than 7% of total annual generation in 2018. But solar and wind generations are the fastest-growing forms of electricity production.

Wind and solar generation are known to be unpredictable and volatile. As the power system's penetration level of renewable generation increases, it may face many challenges in system operation. On the one hand, the renewable power generation is volatile and hard to be planned. On the other hand, wind and solar generation require converter-interfaced generation (CIG) units as the means of electricity generation, which exhibits different dynamic characteristics than synchronous generators in traditional fossil-fuel-based electricity generation.

For example, in a system contingency that happened to the European interconnection network (UCTE), now known as ENTSO-E in November 2006, the system was split into three separate (West, Northeast, South East) subsystems. It caused a power outage that

affected more than 15 million households. Although the post-accident investigation identified a misplanned disconnection of a tie line (the Conneforde-Diele connection) as the root cause, the study also found that the exceeding amount of wind generation at the time of accident played a contributing role [5]. Due to the high penetration level of wind power generation, the line trip caused a low-frequency dip in the European interconnection. The under-frequency relays were triggered across the grid, eventually resulting in the grid being split into three sections and a large amount of system load being shed to help the power system regain active power balance.

Another example is the 2016 blackout event in South Australian power grid. The accident investigation incriminated the exceeding amount of wind power as the primary contributing factor [6]. Immediately before the blackout, the wind power generation reached as high as 880 MW, accounting for 46.4% of the total system demands.

Renewable generation challenges the power system in multiple aspects. This thesis work focuses on one of the aspects that is the decreased level of frequency stability, which is related to the creases in system inertia.

1.1.2. The Decreases in System Inertia

In a traditional power system, the electricity is mostly generated by synchronous generators. As rotational devices, synchronous generators can natural provide inertia response. Though lacking a proper definition, inertia response's basic principles are well understood: when a synchronous generator encounters an imbalance in the "*supply*" of mechanical power (decided by governors) and the "*consumption*" of active electricity power, the rotor's rotational speed vary in a rate decided by the *supply-consumption* imbalance. Like a cistern, the rotor's rotational mass can absorb the exceeding mechanical power input as kinetic energy storage or release its kinetic energy to meet the excessive electricity demand. Through this control mechanism, the active power balance is always balanced at the expense of variations in the rotor's rotational speed. For a large inertia generator, its kinetic energy-rotational speed sensitivity $\partial E_{\frac{\text{kinetic}}{\partial \omega}}$ is large. Therefore, a smaller rotational speed change can result in a large variation in kinetic energy.

Often the inertia response is compared with the primary frequency control. They are usually the first two frequency control mechanisms involved in a generator's frequency

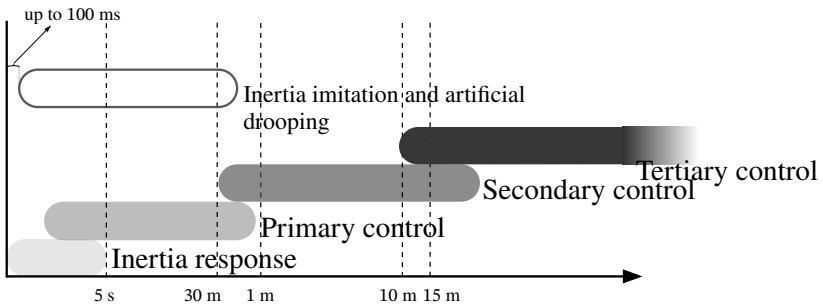

Figure. 1.1.: Typical time scale separation in frequency dynamics [7].

transient in terms of response time. Both are control mechanisms to increase/reduces the active power production at a rotational speed below/above the nominal value. However, these two control schemes differ in their response speed (or their dynamic's time constant). As the governor is involved, the primary frequency control takes a few seconds to fully deploy, whereas the inertia response is effective immediately after the fault occurrence. (Figure. 1.1). A complete frequency regulation also involves *secondary* and *tertiary control*, which come into play at a later time.

However, as a stationary device, the wind and solar generation unit cannot provide natural inertia response. In fact, CIG units are controlled to output an optimal value of active power with the Mpaaximum Power Point Tracking (MPPT) control to capture as much renewable power as possible. Therefore, CIG units are often modelled as constant reactive and active injections in the transient stability analysis. To make things worse, CIGs displace fossil-fuel-based synchronous generators in the generation dispatch. Under the combined effects of these two factors, the system inertia of a future power system with high penetration level of renewables will become much lower. Without enough inertia response, the power frequency is subject to more significant variation.

Figure 1.2 shows the system inertia variation in a month for the South-East Australia network with an average of 40% renewable generation penetration, as given by the market simulation. The purple line shows the system's total inertia variation without any renewable generation; the green line corresponds to a system with an average of 40% wind and solar penetration under the same loading profile. Data are given in 30-min intervals in a month. It shows that *1)* the variation of system inertia is much larger in the power system with high renewable penetration, and *2)* the inclusion of renewable generation greatly reduces the

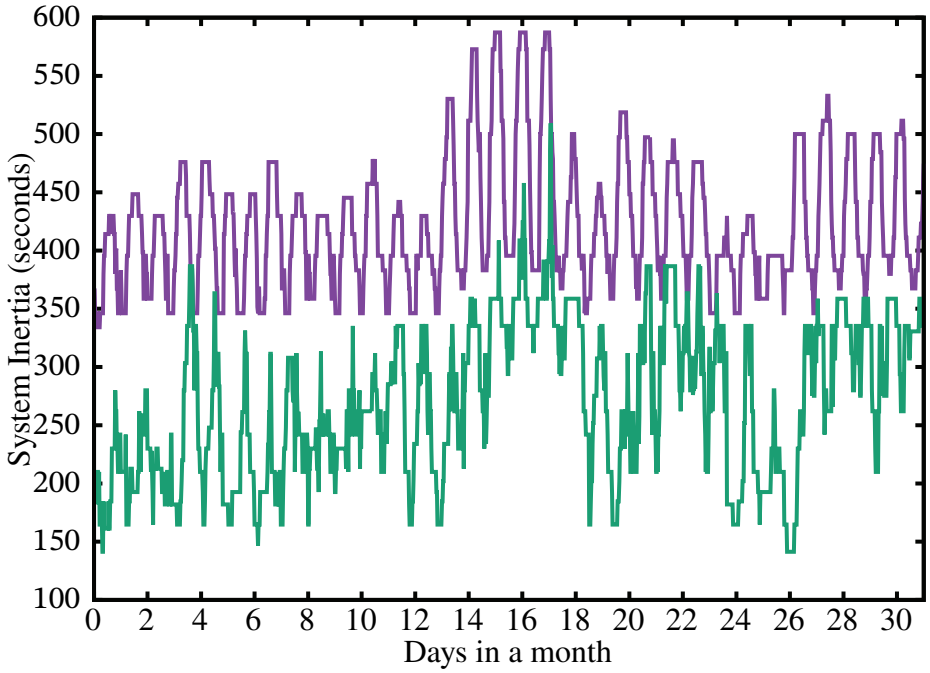

Figure. 1.2.: Variations of system inertia in per-unit.

system's overall inertia. Lower system inertia implies higher chances of frequency violation as shown in the plot of frequency deviation versus renewable penetration in Figure 1.3.

Many electricity utilities have identified the low system inertia as the main factor hindering further integration of renewable generations into power systems. In fear of poor frequency response, many power system operators limit the integration of non-synchronous generation. For example, western USA interconnection proposed to set an integration limit at 30% [9] until a better solution is possible.

Other than passively limiting the integration level of the non-synchronous generation, many control techniques have been proposed to emulate the inertia response on the converter-interfaced generation units. The earliest emulation method came into existence in 1990s [10] and have been under constant improvement since then [11].

The details of virtual inertia emulation control will be introduced in Chapter 2. The virtual inertia emulation control may alter dynamic characteristic properties of CIGs. Therefore, the classical generation control for the CIG deserves a thorough investigation.

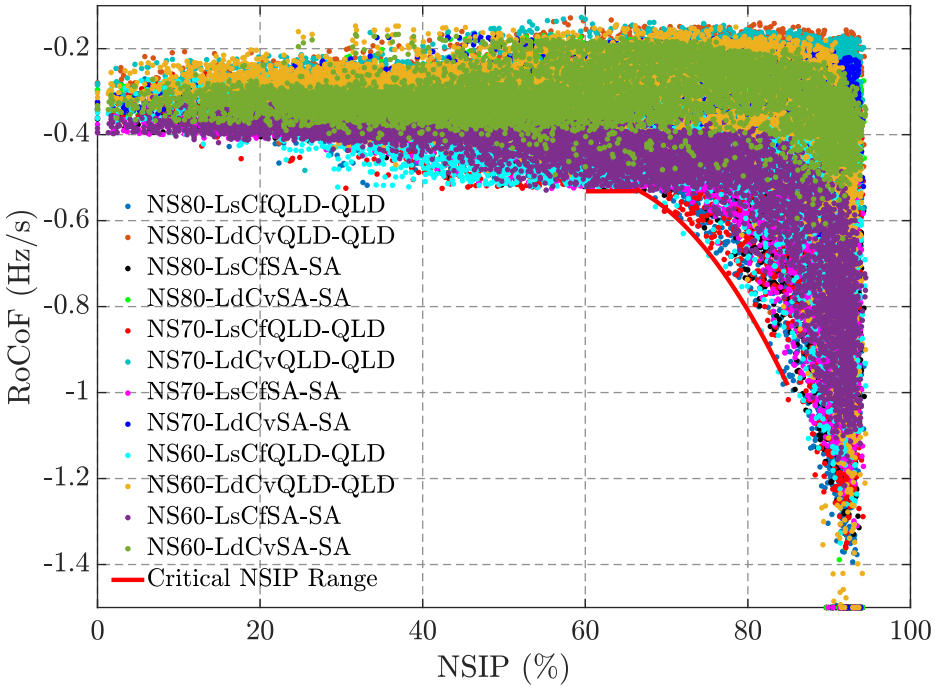

Figure. 1.3.: Frequency degradation versus *non-synchronous instantaneous penetration* (NSIP) [8].

1.2. Classical Control Methods for the Converter-Interfaced Generation Units in Wind and Solar Power Generation

Most modern solar and wind generation units except for the Doubly-Fed Electric Generator (DFIG) are interfaced with the power grid via a fully rated voltage source converter. The DFIG is a common type of wind turbine widely used in wind power generation. Its rotor is connected to the power grid through a partially rated power converter, whereas its stator directly connects the grid; therefore, DFIG is not a full converter-interfaced generation unit.

For both CIG units and DFIGs, the active and reactive power generations are controlled independently under classical control schemes. Figure. 1.4 is a schematic plot of a permanent magnet wind generator. The induction machine converts the raw wind energy into electricity via an induction generator. Its turbine is regulated at an optimal rotational speed for a given

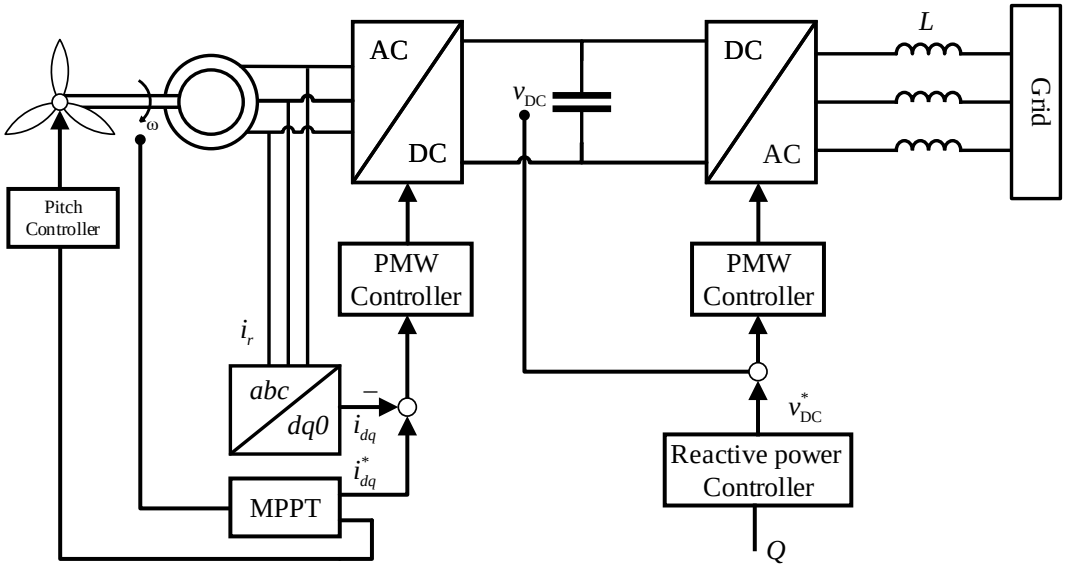

Figure. 1.4.: Fully rated converter system.

wind speed to maximize the wind power capturing along the red line in Figure. 1.5. The solid gray curves show the power output-rotation speed relation. As the rotational speed of wind turbines increases from stationary, the captured wind power increases at the beginning and then decreases. In practice, the wind turbines' rotational speed is set slightly larger than the optimal rotational speed ω_{opt} at the corresponding wind speed for a stable operation, and the wind turbines' mechanical power is limited by $P_{T_{\max}}$. This kind of active power generation regulation is called *Maximum power point tracking* (MPPT). By controlling the blades' pitch angle, the power output-rotation speed relation can be changed, and the wind turbine's rotational speed varies. The response of the pitch controller and the turbines' pitch servo motor is fast, with a time constant as low as 10 ms. The fast responsiveness makes the pitch control not only valuable in setting the blade's rotational speed in MPPT but also possible to recapture the kinetic energy of the rotating blades.

As shown in Figure. 1.4, the captured wind power is converted into electricity via an induction generator. Fully rated machine-side and grid-side converters are required to inject the generated electricity to the power grid at an appropriate power frequency. The machine-side converter is responsible for adjusting the active power output, whereas the

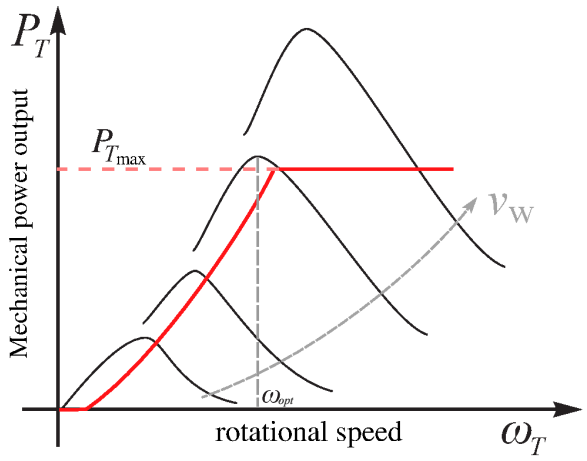

Figure. 1.5.: Maximum Power Point Tracking (MPPT) control for wind power generation.

grid-side converter adjusts the reactive power output and maintains a constant voltage across its DC link capacitor.

Usually, the machine-side converter operates in current control mode, and the direct and quadrature current components, I_{sd} and I_{sq}, of the stator's current are controllable. For a permanent induction machine, the mechanical torque τ_{m} applied on the shaft is expressed as

$$\tau_{\mathrm{m}} = p\psi_{\mathrm{pm}} I_q \tag{1.1}$$

in steady states. Therefore, by adjusting the stator's quadrature-current I_q, the shaft torque can be changed. For an induction machine magnetized with a winding circuit, the shaft torque is

$$\tau_{\mathrm{m}} = p\frac{L_{\mathrm{m}}}{L_r}\psi_{rd} i_{sq}, \tag{1.2}$$

in a dq-frame oriented along the rotor flux. The rotor's magnetic flux ψ_{rd} dynamic is given by

$$\frac{\mathrm{d}}{\mathrm{d}t}\psi_{rd} = -\frac{R_r}{L_r}\psi_{rd} + \frac{L_{\mathrm{m}}R_r}{L_r} i_{sd} \tag{1.3a}$$

$$0 = -\left(\omega_s - \omega_r\right)\psi_{rd} + \frac{L_{\mathrm{m}}R_r}{L_r} i_{sq}. \tag{1.3b}$$

Therefore, the torque loading can be effectively controlled via i_{sq} as long as i_{sd} (and ψ_{rd}) is kept constant under the machine-side converter.

The grid-side converter operates in voltage control mode. It plays dual roles. Firstly, it is responsible for maintaining a constant value across the DC link capacitor. Secondly, it controls the unit's reactive power output. Both power converter is controlled with Pulse-Width Modulation (PWM). From the grid side, the wind turbine can be seen as a voltage source E. Its active and reactive power output are

$$P = |V|\frac{|E|\sin(\theta)}{X} \tag{1.4a}$$

$$Q = |V|\frac{|E|\cos(\theta) - |V|}{X} \tag{1.4b}$$

where θ is the power angle, phasor angle difference between E and V.

By controlling the machine-side and grid-side converters, the wind turbine's torque loading τ_m (or active power P or, indirectly, the rotational speed ω) and reactive power Q (or terminal voltage magnitude $|V|$) can be controlled separately.

Solar panels have a similar structure, except that solar power is converted into DC electricity through solar cells other than an induction generator and is modelled as a current source as shown in Figure. 2.2. In practice, boost DC-DC converters are required between the solar panel and the DC capacitor, but it is omitted in the figure. The *maximum power point tracking* (MPPT) control is achieved by adjusting the solar cells' pointing direction if it is equipped with the mechanisms to do so. The reactive power is controlled via the grid-side inverters, which is also the only converter in Figure. 2.2.

In summary, under traditional control schemes, the active and reactive power can be controlled separately via two independent feedback loops in a normal operational mode. In both cases, the active power output is decided only by the *maximum power point tracking* control. In the transient stability study, the active power output is set as a constant value. Therefore, the inertia response characteristics do not naturally exist in a CIG unit under the traditional control scheme.

Table. 1.1.: Example of allowed fluctuation range of system frequency.

	Denmark	**Germany**
f_{nominal}	$[49.9,\ 50.1]$ Hz	$[49.5,\ 50.5]$ Hz
$f_{\text{emergency}}$	$[47.5,\ 51.0]$ Hz	$[47.0,\ 52.0]$ Hz

1.3. Frequency Performance Indices

Power frequency is one of the most important factors in power quality evaluation. Poor frequency quality not only poses a stability concern, increasing the chances of a large-scale cascading failure, but it may also negatively affect users' load and system operator's power equipment, shorting their lifespan. For example, the over-low power frequency may cause sub-synchronous resonance in turbine and power generators' shafts.

The frequency response performance is assessed based on whether or not, following contingent events, the frequency drop or surge can be arrested before under-frequency load shedding or over-frequency relays are initiated. Therefore, the operation code sets the requirements on power frequency in terms of the allowable range of frequency variation in normal and emergency operating conditions, as shown in the operation codes of many TSOs on the power frequency (Table 1.1). Usually, the power system operates in the normal operational mode. Whenever a system fault happens and leads to is-landing, it shall satisfy the emergency limits on the power frequency. The under-frequency over-frequency relays are set accordingly to accommodate the allowable range of frequency variation. These frequency indices' requirements are specified arbitrarily based on the experience of power system operation and the system conditions. They set a uniform standard so that the related system setting, like the primary frequency reserve, under-frequency relays, etc., can be coordinated. If frequency violation happens, the protective relays across the power system may react to cut system loads or electricity generation units.

1.3.1. Frequency Indices

Traditionally the maximum RoCoF, frequency nadir f_{nadir} or overshoot $f_{\text{overshoot}}$, and settling frequency f_{ss} have been used to plan fast-spinning reserve and tune settings for the primary frequency control. These classical indices of frequency quality have also been used to size the system's virtual inertia [12]–[14].

In reference to Figure. 1.6, which is a typical plot of frequency transient following a contingency event, the classical indices include the frequency nadir f_{nadir}, frequency overshoot $f_{\text{overshoot}}$, and settling frequency f_{ss}:

$$f_{\text{nadir}} := \min_{t\geq 0} \frac{1}{2\pi}\,\omega(t) = \qquad f_{\text{overshoot}} := \max_{t\geq 0} \frac{1}{2}\omega(t) \qquad f_{\text{ss}} := \lim_{t\to\infty} \frac{1}{2\pi}\,\omega(t),$$

the instances when either the frequency nadir or overshoot are observed:

$$t_{\text{nadir}} := \arg\min_{t\geq 0} 2\pi\,\omega(t) \qquad t_{\text{overshot}} := \arg\max_{t\geq \infty} 2\pi\,\omega(t),$$

and the frequency setting time:

$$t_{\text{ss}} := \inf\left\{ t \;\middle|\; |f(t) - f_{\text{ss}}| \leq \zeta \right\},$$

where $\zeta > 0$ is a small threshold value. Moreover, the *RoCoF* and (nadir-based) *Average Change of Frequency* are often used to assess the quality of system's frequency response:

$$\text{RoCoF} := \frac{1}{2\pi} \max_{t\geq 0} |\dot{\omega}(t)| \quad \text{RoCoF}_{\text{avg.}} := \frac{1}{2\pi} \frac{\left|\omega_{\text{nadir}} - \omega_{\text{pre-fault}}\right|}{t_{\text{nadir}}}.$$

Frequency Response (FR) and *frequency nadir-based Frequency Response* ($\text{FR}_{\text{nadir-based}}$) are a rough indicator of the amount of energy reserve for every Herz of frequency drop,

$$\text{FR} := 2\pi \frac{P_{\text{gen. loss}}}{\omega_{\text{pre-fault}} - \omega_{\text{ss}}}, \tag{1.5a}$$

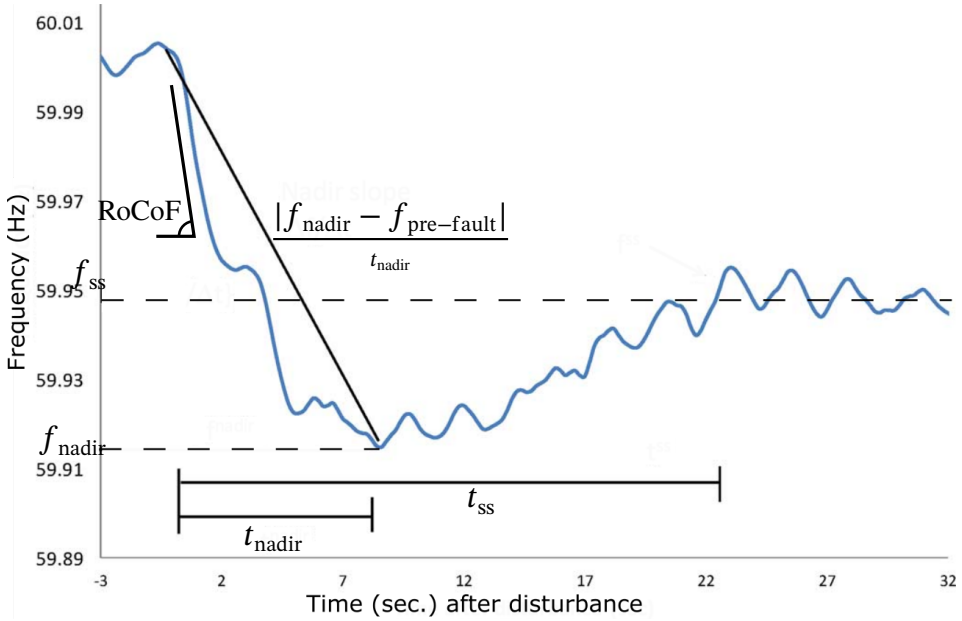

Figure. 1.6.: Frequency dynamics, frequency measured in CO, USA following a disturbance on December 6, 2011 at 11:27 [15].

and,

$$\text{FR}_{\text{nadir-based}} := 2\pi \frac{P_{\text{gen. loss}}}{\omega_{\text{pre-fault}} - \omega_{\text{nadir}}}. \tag{1.5b}$$

From their definition, it is obvious that FR and $\text{FR}_{\text{nadir-based}}$ are all based on steady-state quantities. For this reason, FR and $\text{FR}_{\text{nadir-based}}$ have little use in assessing system frequency during transient.

1.3.2. Quadratic Measurement of Frequency Response

Since either minimization or maximization is involved in computing the frequency nadir, overshoot, and RoCoF, it is difficult to express them in analytical mathematical expressions, and the time-domain simulation is usually required. Furthermore, a large number of wind turbines and solar cells that are small in rating and installed dispersedly across the future power system make the power system more likely to be subject to failure of small generation units, and more small frequency variations are likely to observe as shown in Figure. 1.7. The traditional frequency indices cannot capture these type of frequency disturbances.

Figure. 1.7.: Small frequency disturbances under a series of small disturbances on system's power balance.

Therefore, the authors in [14], [16], [17] proposed a weighted 2-norm function of rotor's rotational speed ω and angular acceleration $\dot{\omega}$ to measure the frequency response:

$$\int_0^\infty \left(\omega^\top Q_\omega \omega + \dot{\omega}^\top Q_{\dot{\omega}} \dot{\omega}\right) \mathrm{d}\, t, \tag{1.6}$$

where $\omega \in \mathbb{R}^n$ is a vector of generators' rotational speeds in the power system. This metric is similar to those used in studying average consensus problem of network-connected oscillators [18]. Furthermore, (1.6) is in form of $\mathcal{L}_2$ metric and can be easily used LQ optimal control.

1.4. Literature Review

To overcome the lack of inertia response capacity in CIG units, researchers proposed various kinds of inertia emulation technology at the device level. Based on their underlying principle, the virtual inertia emulation methods can be categorized differently.

One way of categorization differentiates between grid-following and grid-forming types of virtual inertia emulations depending on whether external frequency synchronization mechanisms, e.g., Phase-Locked Loops (PLLs), are being used. The grid-following type of virtual inertia emulation control is formulated on the external frequency synchronization mechanism and cannot influence the system's power frequency. The grid-forming virtual inertia emulation control can instead influence the power frequency as with synchronous generators as with synchronous generators.

Another categorical method differentiates the virtual inertia emulation techniques between "synchronous generator model-based," "swing equations based," "frequency-power response based," etc. based on the degree that the swing dynamic being emulated. The section gives

more details on the different ways of categorization as well as representative method of virtual inertia emulation in each category.

Finally, subsection 1.4.2 discusses ways of efficiently utilizing virtual inertia installation by *allocating* a given amounts of virtual inertia in the power system [17], [19]. This method reveals how the spatial distribution of system inertia can affect the system's overall frequency response. Therefore, these studies highlight the importance of an appropriate plan of virtual inertia installation in improving the system's frequency response.

1.4.1. Categories of Virtual Inertia Techniques

Grid-following and Grid-Forming Controls

Like classical control algorithms of CIGs, virtual inertia emulation is also formulated on a rotating $dq0$-frame. In steady-state, the rotational speed of $dq0$-frame is synchronized with the power frequency. The $dq0$-frame rotational speed is analog to a synchronous generator's rotor speed. However, frequency measured at one location of a power grid is different from the other location during a transient after a disturbance event.

Depending on how the $dq0$-frame's rotational speed is decided during the system transient, the virtual inertia emulation techniques can be categorized into either grid-forming or grid-following type.

Grid-following control If the rotational speed of $dq0$-frame is decided by the frequency measurement $\hat{\omega}$ at CIG's terminal, this virtual inertia emulation technique is of the *grid-following control* type. The frequency measurements are usually given by PLL (Figure. 1.8).

The basic operation principle of the grid-following type of virtual inertia emulation is to inject to the reference signal of active power generation an additional term ΔP_k^* proportional to the frequency deviation $\Delta\hat{\omega} = \omega_{\text{pre-fault}} - \hat{\omega}$ and RoCoF $\dot{\hat{\omega}}$ from the frequency measurement:

$$\Delta P_k^* = K_k \begin{bmatrix} \omega_{\text{pre-fault}} - \hat{\omega} \\ \dot{\hat{\omega}} \end{bmatrix}, \tag{1.7}$$

where

$$K_k := \begin{bmatrix} d_k & m_k \end{bmatrix}. \tag{1.8}$$

Therefore, the grid-following control can be represented as a proportional-differential controller loop as shown in Figure. 1.9. The proportional gain d_k and differential gain m_k decide the emulated drooping factor and virtual inertia, respectively.

With the additional term ΔP_k^* for the active power generation, the active power output of a CIG unit is expressed as

$$P_e = P^* + d_k \Delta\hat{\omega} + m_k \dot{\hat{\omega}}.$$

If active power output P^* equals the input of mechanical power P_m of the governor, i.e., $P^* = P_m$, rearranging the above equation gives

$$m_k \, \dot{\hat{\omega}}_k = d_k \, \Delta\hat{\omega} + P_m - P_e, \tag{1.9}$$

where the m_k and d_k are coefficients for $\dot{\omega}$ and ω, respectively. Because this type of virtual inertia emulation relies on frequency measurement as the feedback signal, it can only "follows" the system's frequency. Therefore, it is named *grid-following types*.

Although the grid-following type of virtual inertia emulations tend to have a simpler structure and can be easily implemented, they may suffer from many severe drawbacks.

First of all, because the grid-following type of virtual inertia emulation relies on the external frequency measurement as the feedback signal, they require a strong AC voltage source. The grid-following type of virtual inertia emulation methods cannot be used in a weak AC grid, e.g., micro-grids or a power system with a very high level of renewable penetration.

Secondly, due to the slow dynamic of *propotional-integrral* (PI) controller in the PLL as in Figure. 1.8, a PLL usually takes a long time, around $100 - 200$ ms, to obtain an accurate frequency measurement. It is even harder for a PLL to measure a varying frequency while in a system transient.

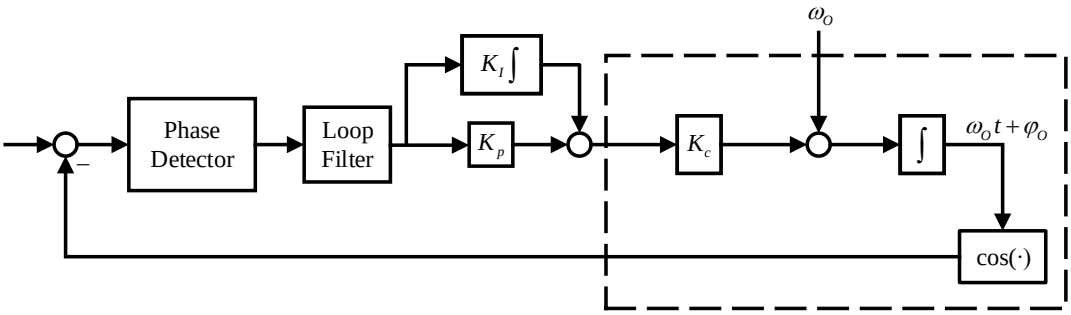

Figure. 1.8.: Schematic plot of Phase-Locked Loop [7].

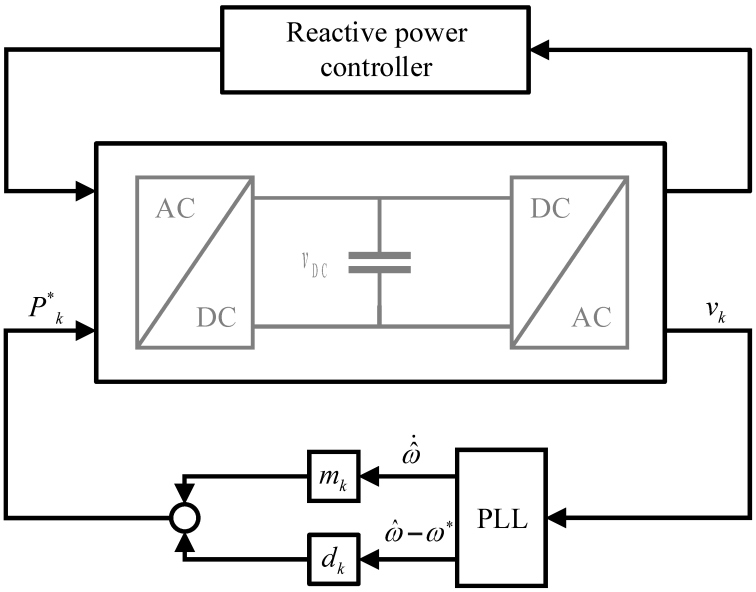

Figure. 1.9.: Independent active and reactive power control in grid-following type of virtual inertia emulation.

The grid-following type of virtual inertia emulation methods does not break the independence of active and reactive power control. The CIG's reactive power output can thus be separately regulated via a reactive power controller. The overall control scheme is plotted in Figure. 1.9.

Grid-forming control In comparison to the grid-following type of virtual inertia emulation, the *grid-forming* type of virtual inertia emulation regulates the virtual rotational speed, i.e., the rotational speed of a $dq0$-frame from the system's active power balance.

Under the *grid-forming* control, the CIG's virtual rotational speed becomes a system state whose dynamic depends on the active power balance. In steady-state, the virtual rotational speed is in sync with other grid-forming power sources, including synchronous generators. The synchronized physical and virtual rotational speeds decide the power frequency. While in system transient, the virtual rotational speed is decided directly by the balance of the mechanical power input and the electricity generation output, which is analog to the natural inertia response of a synchronous generator. The *matching control*—one of the implementing methods grid-forming control—utilizes the DC voltage dynamics of DC-link capacitor to emulate the natural inertia response of a synchronous generator [20]. [21] uses a specially designed output filter instead to emulate the natural inertia response.

Under the grid-forming control, the virtual rotational speed ω_k, i.e., the rotational speed of $dq0$-frame in CIG's internal control logic, is expressed in

$$\dot{\theta}_k = \omega_k \tag{1.10a}$$

$$m_k\dot{\omega}_k = -d_k\big(\omega_k - \omega_{\text{nominal}}\big) - \delta P_k, \tag{1.10b}$$

where m_k, d_k, and δP_k are the size of emulated inertia, damping ratio, and disturbance in the power balance, respectively. The dynamic of virtual rotational speed emulates the swing dynamics of a synchronous generator. The state responses $\omega_k(t)$ and $\dot{\omega}(t)$ in (1.10) are decided directly by the balance of mechanical power input and electrical power output at the CIG unit.

The system frequency at the new steady state is decided collectively by SGs and the CIGs under virtual inertia and drooping control.

Compared with grid-following control, the grid-forming control has unparalleled advantages. First of all, free from the dependence on the external frequency measurement, the gird-forming type of virtual inertia emulation control can instantaneously respond to changes in the power balance of a system fault. Therefore, a true inertia response can be formulated with the grid-forming control of virtual inertia emulation. Secondly, without the need for external mechanisms for frequency measurement and synchronization, the grid-forming

control can be deployed on a week power system, e.g., micro-grids or future power system with high level of renewable penetration.

Alternative Classification

Alternative categorization method classifies the methods of virtual inertia emulation based on how the swing dynamics of a synchronous generator being emulated.

The grid-following and grid-forming types of virtual inertia emulation all try to emulate the dynamics of a synchronous generator. Many studies have also provided more simplified versions of virtual inertia emulation that do not emulate the swing dynamics in full. Depending on the extent of swing dynamics being emulated in the controller design, these methods of virtual inertia emulation can be categorized into: *1) frequency/power response based*, *2) swing equation based*, *3) synchronous generator model-base*, etc., as shown in Figure. 1.10. The implementation details of each controlling type are introduced in the following paragraphs.

Synchronous generator model based The virtual inertia emulation methods of synchronous generator model-based type try to emulate the full dynamics of a synchronous generator. Under this type of virtual inertia emulation control, the CIG unit is seen as a synchronous generator from the grid side. The *synchronverter* [23] is a representative of this virtual inertia emulation method.

The basic principles of synchronverter are depicted in Figure. 1.11 and Figure. 1.12. The CIG is controlled as voltage source by regulating the magnitude e and phase angle θ of the voltage behind its terminal bus. The voltage magnitude e and phase angle θ are decided by the feedback controller "Controller of Synchronous Generator Emulation," as shown in Figure. 1.11. The controller takes active power P^* and reactive power Q^* as the reference inputs and produces a voltage phasor of magnitude e and phase angle θ to the PWM generator, which in turn dictates switches to generate a terminal voltage at the connection point. The amount of emulated virtual inertia and drooping character are decided by parameters J and D_p, respectively.

As shown in Figure. 1.12 for the controller design, J is the time coefficient of the integrator

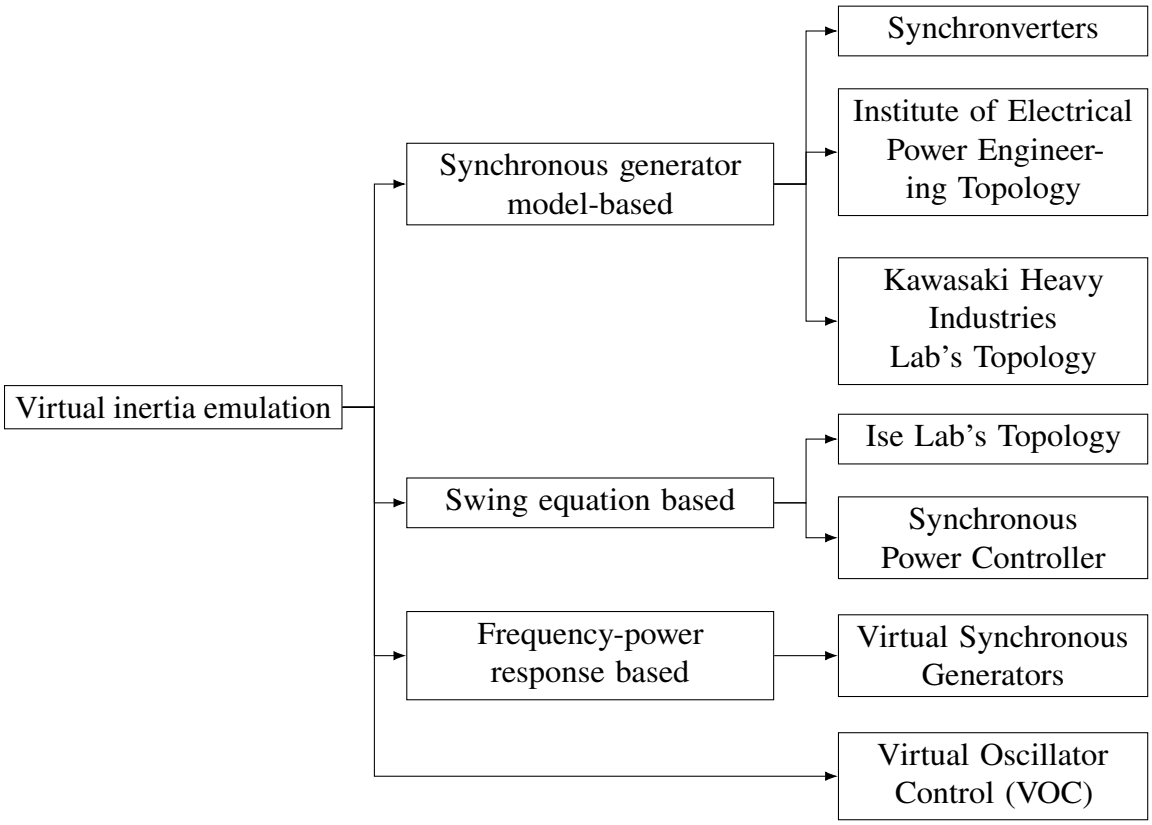

Figure. 1.10.: Classification of virtual inertia emulation technologies based on their underlying principle [22].

of the active power control loop, whereas D_p is the feedback gain of the same control loop. The feedback signals v and i are fed into the reactive control loop and "*SG model*." The "SG model" emulates electromechanical relation of a synchronous generator:

$$e = \dot{\theta}\, M_f\, i_f\, s(\theta) \tag{1.11a}$$

$$P = \dot{\theta}\, M_f\, i_f\, \langle\, i,\, s(\theta)\,\rangle \tag{1.11b}$$

$$Q = -\dot{\theta}\, M_f\, i_f\, \langle\, i,\, c(\theta)\,\rangle, \tag{1.11c}$$

where M_f is the virtual mutual inductance between the field circuit and stator circuit, and the i_f is the field current. In three-phase frame, the i, functions $s = s(\theta)$ and $c = c(\theta)$ are

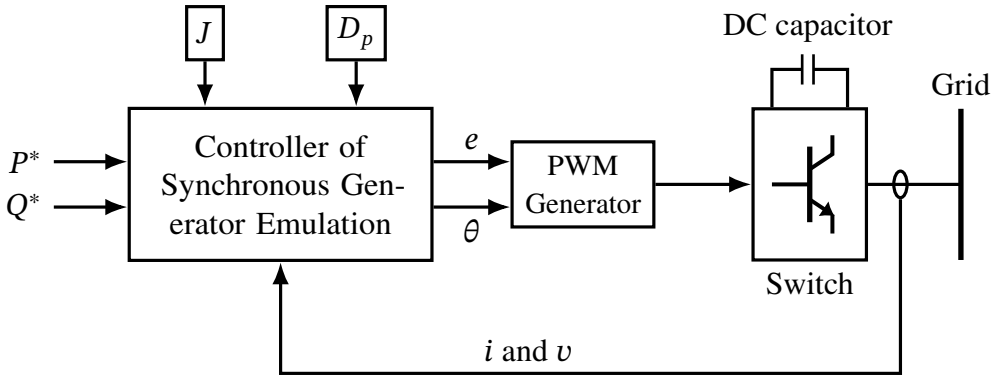

Figure. 1.11.: Synchronverter topology [22].

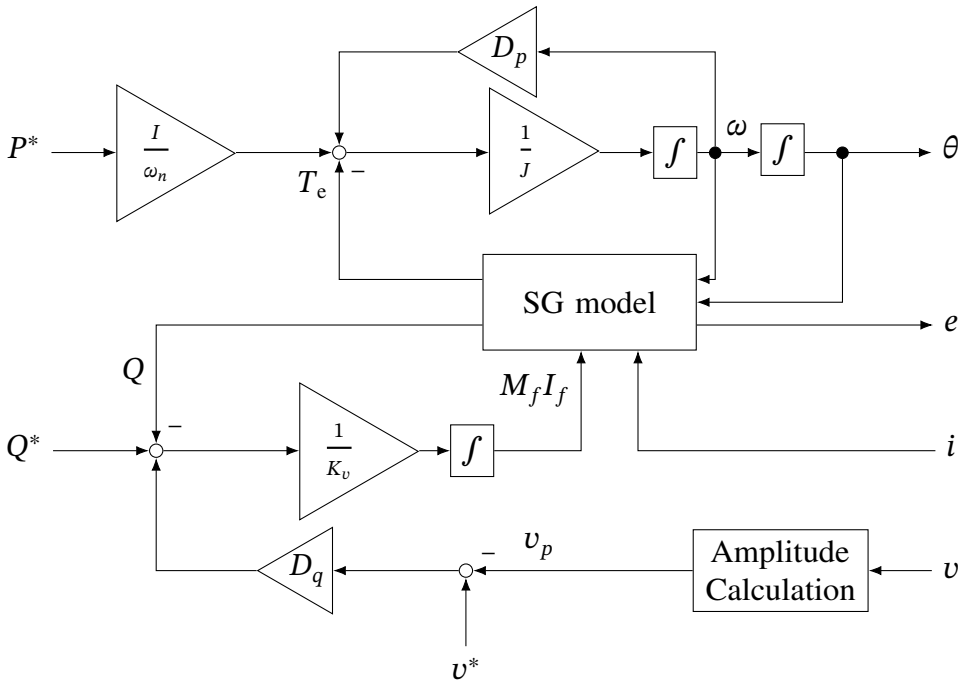

Figure. 1.12.: Schematic diagram of synchronous generator emulation controller [22].

formulated as

$$i = \begin{bmatrix} i_a & i_b & i_c \end{bmatrix} \tag{1.12a}$$

$$s(\theta) = \begin{bmatrix} \sin(\theta) & \sin\left(\theta - \frac{2}{3}\pi\right) & \sin\left(\theta - \frac{4}{3}\pi\right) \end{bmatrix} \tag{1.12b}$$

$$c(\theta) = \begin{bmatrix} \cos(\theta) & \cos\left(\theta - \frac{2}{3}\pi\right) & \cos\left(\theta - \frac{4}{3}\pi\right) \end{bmatrix}. \tag{1.12c}$$

In conclusion, synchronverter and other SG model-based inertia emulation techniques aim to recreate a complete representation of an SG dynamic. But the differential terms of the SG model and the double integrals may lead to numerical instability problem. Furthermore, as in the voltage-source converter setup, an external over-current protection mechanism is required.

A Swing Equation-Based Topology Instead of emulating a synchronous generator's full dynamic, the *Swing Equation-Based Topology* emulates the rotational inertia by solving the swing equation at constant time intervals and constantly adjusting active power generation according to the computation results [24]. The *Ise Lab's topology* as shown in Figure. 1.13 and Figure. 1.14 is an example of the Swing Equation-Based Topology.

As with SG model-based inertia emulation topology, CIG's interfacing converter is operated as a controlled voltage source, and an external over-current protection mechanism is also required. The active power reference P^* in Figure. 1.13 is provided by a governor Figure. 1.14, whose mathematical formulation is

$$\dot{\theta}_g = \omega_g \tag{1.13a}$$

$$T_d\,\dot{x} = K\,\left(\omega^* - \omega_g\right) - x \tag{1.13b}$$

$$P^* = x + P_0. \tag{1.13c}$$

With an appropriate choice for the propositional gain K and the time constant T_d, a satisfactory level of SG-like drooping characteristic and inertia response can be emulated at a CIG unit.

The "*control algorithm*" block determines the magnitude e and phase shift θ and has a similar design as Figure. 1.12. But the inertia and drooping emulation is delegated to its governor. The "PWM generator" then translates the e and θ into modulation signal for the voltage-source converters.

An external synchronization mechanism, shown as "Power and Frequency Measurement" in Figure. 1.13 is used in the Ise Lab's topology. Therefore, the Ise Lab's topology is of grid-following type of virtual inertia emulation and cannot be used in a weak power system. Moreover, the Ise Lab's topology lacks the reactive power control loop, and external reactive power compensation mechanisms, e.g., STATCOM, SVC, etc., should be used to regulate

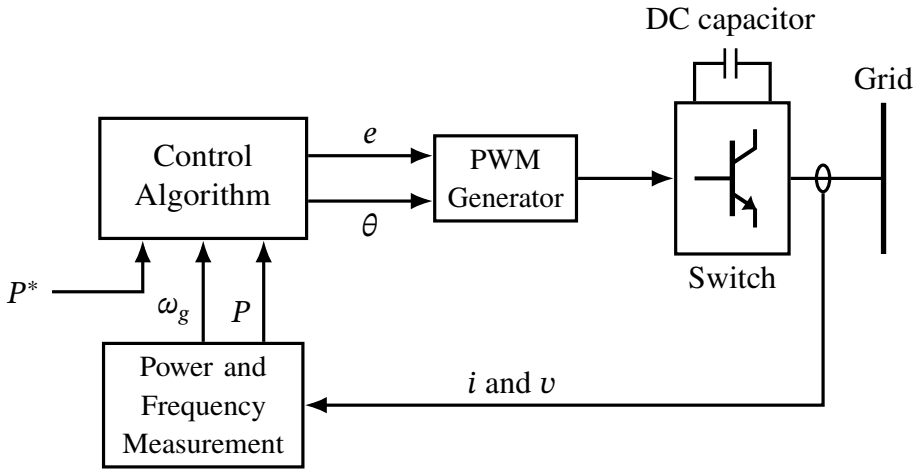

Figure. 1.13.: Ise Lab's topology [22].

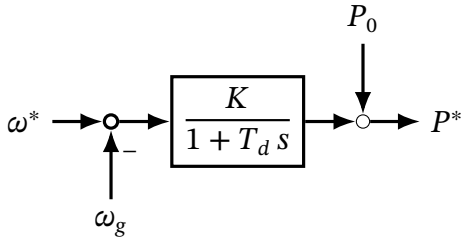

Figure. 1.14.: Governor's control design in Ise Lab's topology [22].

the terminal voltage.

The same drawbacks plaguing the SG model-based topology are also true for the swing equation-based topology. For example, Ise Lab's topology is also susceptible to numerical instability.

Frequency-power Response Based Topology In the SG model-based and Ise Lab's typologies introduced above, the voltage source converter interface is required in the voltage source mode. In *Frequency-power Response-Based* topology, the interfacing power converter is operated as a current source. The *Virtual Synchronous Generator* (VSG) is a classical example of Frequency-Power Response-Based Topology as shown in Figure. 1.10.

VSG implements its inertia emulation control and drooping characteristics at its governor. The variation of active power setting point ΔP_{VSG} is proportional to both the frequency

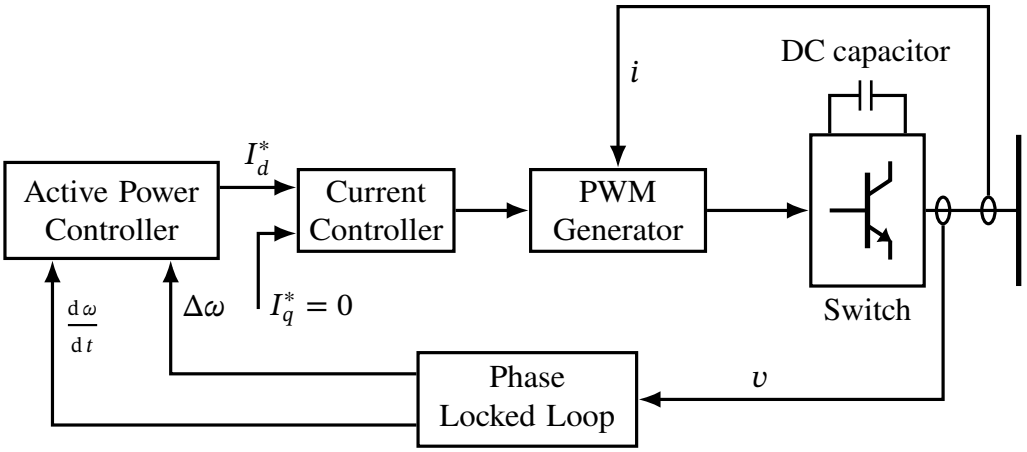

Figure. 1.15.: Virtual synchronous generator (VSG) topology [22].

variation $\Delta\omega$ and RoCoF $\frac{\mathrm{d}\,\omega}{\mathrm{d}\,t}$:

$$\Delta P_{\mathrm{VSG}} = K_D \Delta\omega + K_I \frac{\mathrm{d}\,\Delta\omega}{\mathrm{d}\,t}, \tag{1.14}$$

where K_D is the virtual damping coefficient and K_I is the amount virtual inertia emulated at the CIG unit. It is obvious from (1.14) that VSG is simply a PD controller.

The PLL is also required in VSG fo grid frequency and the RoCoF measurement. Thus, VSG suffers as well from inaccurate measurement and numerical instability. The "Active Control Algorithm" takes the frequency measurement $\Delta\omega$ and RoCoF measurement $\frac{\mathrm{d}\,\omega}{\mathrm{d}\,t}$ as the inputs and outputs to "*Current Controller*" a current reference of direct-quadrature axis I_d^*:

$$I_d^* = \frac{2}{3}\left(\frac{V_{\mathrm{d}}\,P_{\mathrm{VSG}} - V_q Q}{V_d^2 + V_q^2}\right), \tag{1.15}$$

where V_d and V_q are d-axis and q-axis components of the measured grid voltage. The q-axis current reference I_q^* is related to CIG's reactive power control.

Like Synchronverter and Ise lab's Topology, VSG depends on PLLs for synchronization and frequency measurement. Therefore, VSG can only be used in a strong power network.

Table. 1.2.: Types of hybrid BESS for virtual inertia emulation.

Type	Citations
Battery / Ultra capacitors	[27]
Battery / Capacitors	[25], [26]
Distributed Energy Storage	[28]

Survey of Energy Systems in Inertia Emulation Application

Just as SG's physical rotational inertia responds to frequency variations by automatically discharging and charging the kinetic energy of the rotor's rotational mass, there is a similar energy exchange in virtual inertia emulation. However, other forms of energy storage must be used in place of the kinetic energy for a stationary CIG unit. A properly designed battery energy storage system has high energy storage density and high charging and discharging capacity. Therefore, it may substitute the generator's rotor for the energy storage for the virtual inertia response.

The rotating wind turbine stores a considerable amount of kinetic energy. However, unlike SGs, the power grid has no direct connection with the rotating wind but via a power converter. Therefore, a dedicated control scheme is required for the induction generator to exploit the untapped kinetic energy.

Battery Energy Storage System (BESS) and Mechanical Power Control are introduced below as the energy reserve for the virtual inertia emulation.

Battery Energy Storage System (BESS) In [25], [26], the BESS, DC links, and ultra-capacitor are proposed as the energy reserve of fast energy response for virtual inertia emulation. The super-/ultra-capacitor has a very high energy charging/discharging rate (high charging/discharging power), whereas Lithium-Ion battery has very high energy storage density.

A Hybrid Energy Storage System (Hybrid BESS) is designed as a mix of different types of storage media in utilities and prosumers for different functionalities. Table 1.2 lists a few types of Hybrid BESS for virtual inertia emulation application.

Mechanical Power Control Instead of using energy storage to provide for the fast active power exchange in virtual inertia emulation, some generation control methods, like pitch control [29], [30] and slip control [31], were proposed to regulate induction generators' generation for virtual inertia emulation.

The physical principle underneath pitch control lies in the aerodynamic principle. As the pitch angles β increasing from zero, the captured aerodynamic power first increases till reaching a maximum and then decreases. The aerodynamic power is approximated by

$$P_{\text{aero}} = 0.5\rho A C_p(\beta) V^3,$$

where the ρ is air density, the A is the blade's sweeping area, V is wind velocity, and $C_p := C_p(\beta, \tau)$ is the power coefficient that depends on the pitching angle of turbine blades β and the tip-speed ratio τ,

$$\tau = \frac{r\omega}{\upsilon},$$

where r is the blade length, ω is the rotating speed, and υ is the wind speed. The coefficient function $C_p(\beta, \tau)$ is plotted in Figure. 1.16 and depends on the blade design [32].

The blades' pitch angle can be adjusted by a actuator motor, whose dynamic is

$$J_{\text{blade}}\,\ddot{\beta} = T_{\text{dive}} - (\mu + f)\,\dot{\beta},$$

where β is blade's pitching angle, and T_{drive} is the servomotor's driving torque exerted on the wind blades, and μ and f are the coefficients of blade root friction and wind drag, respectively. The driving torque is exerted by the servomotor of blade's actuation unit, which can be represented by a delay transfer function,

$$G(s) = \frac{1}{\tau_\beta s + 1}.$$

The actuator's time constant τ_β is around 0.01 s. A PD controller is often used to regulate blade angle, as shown in Figure. 1.17. Whenever there is a change in the aerodynamic power P_{aero}, the blade's rotating speed varies until a new steady state is reached as decided by the

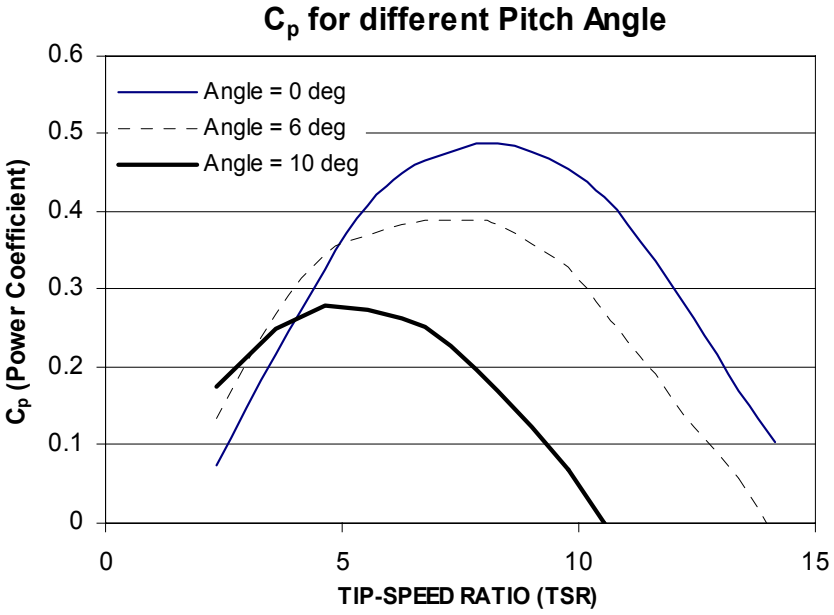

Figure. 1.16.: Power coefficient versus different pitch angle and tip-speed ratios of a blade design [33].

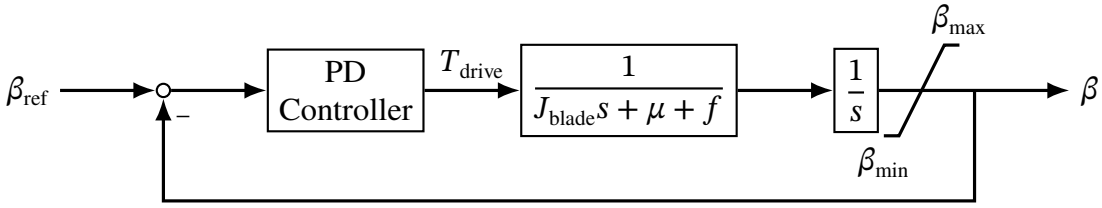

Figure. 1.17.: The control of wind turbine's pitch angle [34].

shaft mechanical dynamic:

$$2H_{\mathrm{t}}\dot{\omega}_{\mathrm{t}} = \tau_{\mathrm{t}} - K_s\delta_{\mathrm{tm}} \tag{1.16a}$$

$$2H_{\mathrm{tm}}\dot{\omega}_{\mathrm{tm}} = K_s\delta_{\mathrm{tm}} - \tau_{\mathrm{e}} \tag{1.16b}$$

$$\dot{\delta}_{\mathrm{tm}} = \Omega_b(\omega_{\mathrm{t}} - \omega_{\mathrm{m}}), \tag{1.16c}$$

where H_{t} is the inertia of wind turbine, H_{tm} is the rotor inertia, K_s is the shaft stiffness, τ_t is the mechanical torque exerted by the wind turbine, τ_e.

Figure 1.18 illustrates the setup of virtual inertia emulation with the pitch angle β control.

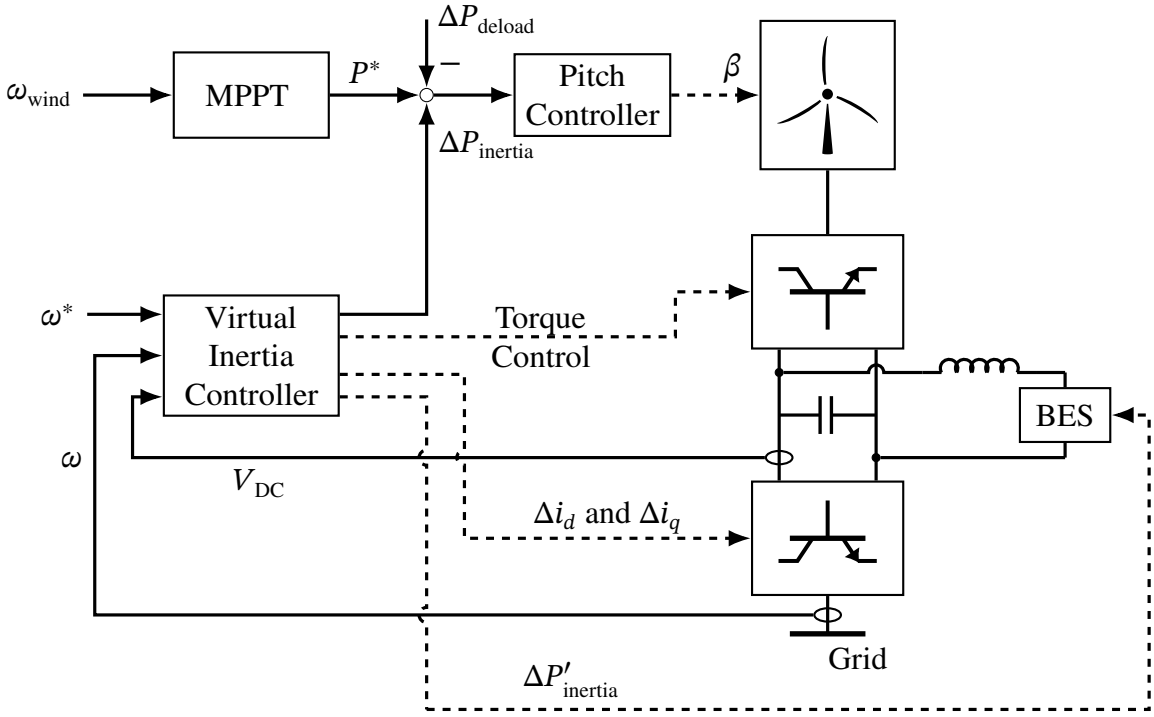

Figure. 1.18.: Pitch control and storage system in virtual inertia emulation.

The wind turbine may operate below the MPPT as the energy reserve. When system faults occur, and the frequency variation is detected, the "*Virtual Inertia Controller*" commands the "*Pitch Controller*" to adjust wind turbine blades' pitch angle to adjust the aerodynamic power capture and active power generation. The ΔP_{deload} is the commanding signal fed into the "Pitch Controller."

At the same time, the "Virtual Inertia Controller" is also responsible for coordinating the operation of the machine-side converter so that an appropriate loading torque can be produced at the other end of the turbine's diving train. By adjusting the magnitude and frequency of rotor current the electrical torque τ_{e} in (1.16) is changed [35]. By increasing the electrical torque τ_{e}, the kinetic energy of these rotating mass is recovered for the virtual inertia emulation [36].

Whenever a system disturbance or change of network topology causes an abrupt changes in power generation, the loading torque T_{e} can be momentarily increased. In this process, the kinetic energy is released and converted to active power generation for arresting the frequency drop in the power system at the sacrifice of a drop in the turbine's rotating speed

ω_g. However, the inertia recovery control may cause a second dip in the power frequency response due to the decreasing turbine speed, resulting in lower aerodynamic power P_{aero} [37].

1.4.2. Optimal Allocation of Virtual Inertia

Milano showed in his study [38] the spatial difference in the frequency measurement caused by the spatial distribution of grid-forming generation agents. Therefore, it can be deduced that allocation of system inertia can affect the system's overall frequency response.

The study [17] considers the problem of finding the optimal allocation of system inertia in the power network. Because of its similarity to the problem of optimally planning virtual inertia installation of this thesis work across the power network, Poolla's study [17] is introduced below in this sub-section.

Problem Statement Poolla [17] considers the following problem:

> *Finding an optimal way to allocate the virtual inertia installation in the power network to attaint the best overall system frequency response.*

The study adopts the optimal control technique by formulating the problem as a mathematical optimization problem of minimizing a $\mathcal{H}_2$ metric. The problem's decisions are the amount of virtual inertia installation at candidate buses in the power system, and they are all continuous.

System Modelling Linearization technique and Kron reduction (Schur complement) [39] has been used to model the power system as an interconnected synchronous generators, and it is assumed that all system loads are passive as constant impedance. Therefore, the resulting system can be described by a series of second-order ordinary differential equations,

$$m_i\ddot{\theta}_i + d_i\dot{\theta}_i = p_{in,i} - p_{e,i} \qquad \forall i \in \{1, \dots, n\},$$

where m_i is the generator's physical or virtual inertia, and d_i is the damping force accounting for the primary frequency control, power system stabilizer, automatic voltage regulator

(AVR), etc. The $p_{\mathrm{in},i}$ and $p_{\mathrm{e},i}$ are mechanical power input to the generator and electrical power output, respectively. The electricity power generation $p_{\mathrm{e},i}$ is given as

$$p_{\mathrm{e},i} = \sum_{j=1}^{n} b_{ij}(\theta_i - \theta_j), \qquad i \in \{1, \dots, n\},$$

where $b_{ij} \geq 0$ is approximately the susceptance of the transmission link between node i and j, in the linearized power system model. The power system dynamic is then given as

$$\begin{bmatrix} \dot{\theta} \\ \dot{\omega} \end{bmatrix} = \underbrace{\begin{bmatrix} 0 & I \\ -M^{-1}L & -M^{-1}D \end{bmatrix}}_{=:A} \begin{bmatrix} \theta \\ \omega \end{bmatrix} + \underbrace{\begin{bmatrix} 0 \\ M^{-1} \end{bmatrix}}_{=:B} p_{\mathrm{in}} \tag{1.17}$$

where the L is a Laplacian matrix for the power network represented as a mathematical graph with its edge weights being b_{ij}—the line impedance, and matrix $M := \mathrm{diag}\{m_i\}$ and $D := \mathrm{diag}\{d_i\}$, $d_i > 0$, are diagonal matrix.

Matrix A has an obvious zero eigenvalue corresponding to eigenvector $\begin{bmatrix} \mathbb{1}^\top & \mathbb{0}^\top \end{bmatrix}^\top$. Applying *centre manifold theory* [40], we can conclude that, if all other eigenvalues have only negative real parts, the nonlinear system (1.17) has the centre subspace as the ω-limit set; hence, the stability of the original system is established.

The Coherency Performance Metric The study [17] proposes a $\mathcal{L}_2$ function as the optimization objective:

$$\int_0^\infty \sum_{i \neq j} a_{ij} \left(\theta_i(t) - \theta_j(t)\right)^2 + \sum_{i=1}^{n} s_i \omega_i^2 \, \mathrm{d}\, t \tag{1.18}$$

where $a_{ij} = a_{ji} > 0$ if (i, j) is among the edges of the graph, $s_i > 0$ and $\omega_i := \dot{\theta}_i - \omega_n$. By defining another Laplacian matrices,

$$N := \mathrm{diag}\left(\sum_{i \neq j} a_{ij}\right) - \begin{bmatrix} a_{ij} \end{bmatrix} \qquad S := \mathrm{diag}(s_i),$$

where the $\left[a_{ij}\right]$ is a matrix whose element at the cross of i-row and j-column is a_{ij}, $a_{ij} \geq 0$. The matrix N and S are the designing parameters of the optimal control, which shall be tuned to produce an optimal result.

The equation (1.18) models a sum of potential and kinetic energy in the linearized system. It can be equivalently expressed as

$$\int_{t=0}^{\infty} y(t)^{\top} y(t)\,\mathrm{d}t \tag{1.19}$$

where the y is

$$y = \underbrace{\begin{bmatrix} N^{\frac{1}{2}} & 0 \\ 0 & S^{\frac{1}{2}} \end{bmatrix}}_{=:C} \begin{bmatrix} \theta \\ \omega \end{bmatrix}. \tag{1.20}$$

(1.17) and (1.20) constitute a linear system, identified by a tuple (A, B, C) of three matrices in (1.17) and (1.20). The vector space spanned by $\left[\mathbb{1}^{\top}\ \mathbb{0}^{\top}\right]^{\top}$ is the unobservable linear subspace of system (A, B, C).

For a stable linear system, it is well known that the $\mathcal{L}_2$ metric is equivalent to $\mathcal{H}_2$ metric. Therefore, the optimal virtual inertia allocation problem is a $\mathcal{H}_2$ control problem with the objective of minimizing the $\mathcal{H}_2$ metric (or $\mathcal{L}_2$ metric).

Fault Modelling In (1.17), the fault is modelled as an input of power disturbance p_{in}. The $\mathcal{H}_2$ metric is however a stable system's $\mathcal{L}_2$ measure of system's output response to an unit Dirac function input. To reconcile this difference, (1.17) is reformulated with the following addition matrices

$$p_{\text{in}} = \Pi^{\frac{1}{2}} \eta, \qquad \Pi = \operatorname{diag}(\pi_i), \quad \pi_i \geq 0, \tag{1.21}$$

and (1.17) can be equivalently expressed as

$$\begin{bmatrix} \dot{\theta} \\ \dot{\omega} \end{bmatrix} = \underbrace{\begin{bmatrix} 0 & I \\ -M^{-1}L & -M^{-1}D \end{bmatrix}}_{=:A} \begin{bmatrix} \theta \\ \omega \end{bmatrix} + \underbrace{\begin{bmatrix} 0 \\ M^{-1}\Pi^{\frac{1}{2}} \end{bmatrix}}_{=:B} \eta. \tag{1.22}$$

The $\left[\Pi^{\frac{1}{2}}\right]_{ii}$ is valued to reflect the combined effect of the likelihood of system faults and the size of disturbance to the active power balance at generators' terminal.

Efficient Algorithm to evaluate the $\mathcal{H}_2$ metric Furthermore, authors proposed an algorithm to efficiently compute the $\mathcal{H}_2$ metric in [17] based on a well known relationship between observability Grammian, Lyapunov equation, and the formulation of $\mathcal{H}_2$ metric. The algorithm is summarized as below.

In reference to definition for matrices A, B, and C of (1.22), the $\mathcal{H}_2$ metric (1.18) is equivalently formulated in terms of observability Grammian $O \in \mathbb{R}^{2n\times 2n}$,

$$\|G\|^2_{\mathcal{H}_2} = \operatorname{trace}\big(B^\top O B\big), \tag{1.23}$$

which can be efficiently computed by solving the following Lyapunov equation with some additional constraints

$$OA + A^\top O + C^\top C = 0 \tag{1.24}$$

$$O\begin{bmatrix} \mathbb{1}_n \\ \mathbb{0}_n \end{bmatrix} = \mathbb{0}_{2n}. \tag{1.25}$$

Therefore, [17] solves for the optimal inertia allocation as the optimal solution that minimizes the $\mathcal{H}_2$ metric (1.23).

Summary

The study [17] reveals how the spatial inertia distribution can affect the response of the system's frequency. An optimal spatial inertia allocation can significantly improve the

frequency response.

To the extent of my knowledge, [17] is the first study that considered the influence of inertia's spatial distribution on the system's frequency response. The coherency based frequency performance metric (1.18) was proved to be more practical than classic metrics (frequency nadir/overshoot and RoCoF) in study system's inertia response.

However, [17] made several unrealistic assumptions. Firstly, virtual inertia is more like a control parameter than resources. Secondly, the cost of installing the same amount of virtual inertia at different locations is also different. Thirdly, the fault model depends on the matrix Π. A different choice of Π can result in quite different results. An appropriate choice of Π should correctly reflect the likelihood and size of a particular fault. Finally, the $\mathcal{L}_2$ metric measures the degrees of synchronization of network-connected oscillators, including synchronous generators and CIG units of grid-forming control. It is well known that the generator's frequency response immediately after power disturbance is decided by both rotational inertia (including virtual inertia) and primary frequency response. This metric definition cannot isolate the impact of system inertia on the frequency response.

It is the objective of my work to resolve above-mentioned issues. Chapter 5 includes comparative studies in terms of investment cost and control performances of the newly proposed method versus [17].

1.5. The Objectives and Contribution

1.5.1. Assumptions

As the grid-forming type of virtual inertia emulation techniques mature, the power utility considers centralized virtual inertia installation to allow for more wind and solar power generation. Under this assumption, the *Transmission System Operator* (*TSO*) is responsible for the investment in the centralized virtual inertia installation. Such a centralized virtual inertia installation "station" is composed of large-scale electricity storage and power a conversion interface. Insofar as the inertia emulation is considered, the optimal amount of energy storage and other control resources shall be planned at prime locations.

In practice, many decentralized renewable generations are connected to the main power grid through the micro-grids. The micro-grids have dual operational modes. It can either operate independently or in connection with the main power grid. Therefore, the planning of virtual inertia installation should consider the dual operational mode so that a satisfactory power frequency response can be attained in both operation modes. However, in this research, the virtual inertia installation within a micro-grid is not considered.

This research aims to find the most economical plan for the virtual inertia installation at prime locations across the transmission network to ensure good frequency response for the future power system with large renewable penetration.

1.5.2. Methodology overview

In order to obtain an optimal plan of virtual inertia installation, a solution workflow is proposed, as depicted in Figure 1.19 above and Figure 4.2 of Chapter 4.

The framework starts with the step of "*stability scanning*" of [41]. This step is composed of unit commitment and market simulation against inputs of forecast of load demand and renewable generation available for power dispatch. The "stability scanning" produces a list of working conditions, upon which a mathematical optimization problem can be formulated at the second step.

In the second step, an optimization problem is formulated on a list of critical operating scenarios. The optimizer of the optimization problem is the required system inertia installation that should satisfy the frequency stability requirement formulated with a newly proposed metric that quantifies the impact of system inertia on the frequency stability.

Finally, two methods are proposed to solve the optimization problem of the mixed-integer type. The first method is a dynamic programming-based method. In contrast, the sparsity promotion-based relaxation technique is used in the second method, which converts the mixed-integer programming problem into a continuous optimization problem. A cloud computation framework is designed to support the large-scale computation involved in running time-domain simulation and solving the optimization problem.

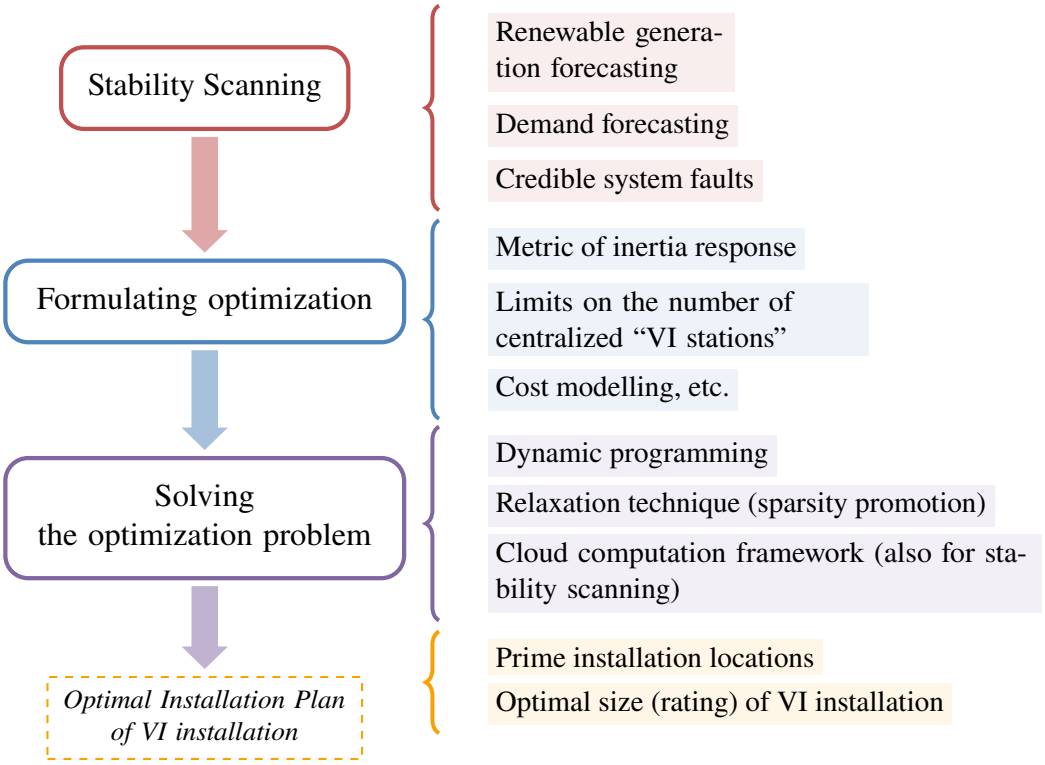

Figure. 1.19.: Overview of the methodology in the research

1.5.3. Contributions

Though there are many publications about the operation [17], [42] or implementations [36], [43] of virtual inertia, they do not consider the installation of virtual inertia as an economic planning problem to increase the system's frequency stability. The most similar study is the optimal virtual inertia installation study [19] discussed previously in Subsection 1.4.2.

In the thesis work, a mathematical optimization problem is proposed to minimize the cost of investment in virtual inertia installation while ensuring a good frequency response.

In order to facilitate the formulation of this mathematical problem, this thesis work proposes a new metric definition to quantify the influence of system inertia on the frequency response. The derivation of this metric definition utilizes *singular perturbation theory*. The *singular perturbation method* helps separate the system's frequency response into a fast and slow dynamic component. The fast dynamic component is sensitive to the system inertia and characterizes the fast dynamic response immediately after fault occurrence. The slow

dynamic characterizes the slow frequency response and is largely determined by the classic tertiary frequency control.

Compared with the classic frequency stability indices and the $\mathcal{H}_2$ metric of frequency response used in [17], [19], the newly proposed system metric can directly measure the influence of system inertia on the frequency response. Therefore, it is more suitable to be used in attaining the objective of finding the optimal virtual inertia installation.

Finally, the research proposed two solution methods. The first one is based on the classic dynamic programming. In contrast, the second one adopts a relaxation technique based on the sparsity promotion technique. Moreover, multi-processing and multi-threading computation techniques are used to facilitate the computational speed, and a cloud computing platform is developed to utilize the cloud computation power to support large-scale parallelization.

Apart from searching for an optimal plan of virtual inertia installation, this study also designed, as a minor contribution, a supplementary control scheme on top of the matching control.

The matching control [20] is a topology of virtual inertia emulation control of grid-forming type. However, the matching control also introduces undesired coupling between the active and reactive control, which are, otherwise, independent. While controlling the CIG 's active power generation, the matching control may also cause voltage instability. The supplementary control proposed in this thesis work helps stabilize the system voltage and improve the system's overall stability.

Finally, the proposed method is tested on a simplified version of the Southeast Australian power system retrofitted with considerable renewable generation against two fault types. The results show that the optimal plan of virtual inertia installation helps the power system attain better performance of frequency response performance and at lower investment cost than other comparative methods.

1.6. Overview of the Remaining Contents

The synopses of the remaining chapters are shown below.

1) In Chapter 2, the principle of matching control—a particular type of grid-forming virtual inertia installation control—is studied.

   This chapter shows that the matching control emulates the inertia response by matching the virtual rotation speed to the DC voltage of a DC coupling capacitor. The voltage dynamic of the DC capacitor decides the virtual inertia emulation.

   Then, the coupling of active and reactive power generation as introduced by the matching control is discussed. Finally, a supplementary controller is designed to stabilize the terminal voltage.

2) In Chapter 3, a new metric definition is derived as the $\mathcal{L}_2$ metric of the fast dynamic component of the frequency response. This fast dynamic component is obtained by applying the singular perturbation theory to the system's frequency dynamic. It is shown that the fast dynamic component is sensitive to the system inertia and, therefore, referred to as "*inertia dynamic*." The slow dynamic is not sensitive to the system inertia.

   This metric is used later to form the frequency stability constraints for searching the optimal plan of virtual inertia installation.

3) Chapter 4 translates the search for an optimal plan of virtual inertia installation into a mathematical optimization problem. It is shown that the mathematical optimization problem is of a mixed-integer type and is solved with two methods. The first method is based on dynamic programming, and the other method adopts a relaxation technique based on sparsity promotion.

   A cloud computation framework and multi-threading computation are also proposed to facilitate the computation speed. The technical details are introduced in this chapter.

4) In Chapter 5, two case studies are conducted on a simplified version of Southeast Australian Connection retrofitted with renewable generation according to the future development plan of the system operator. The newly proposed method is compared with other comparative methods in obtaining an optimal plan of virtual inertia installation. The newly proposed method demonstrates better improvement in the system's frequency response at a lower investment cost.

5) Finally, Chapter 6 wraps up the thesis by concluding the main finding and contribution.

A suggestion for future work is also given in this chapter.

Chapter 2

Matching Control and Its Improvement

This chapter discussed the basic principles of *matching control* [20] — a particular implementation of the grid-forming type of virtual inertia emulation. Without reliance on the PLLs or other external frequency measurement mechanisms, the virtual system frequency of the CIG unit is decided directly from the balance between the input of captured renewable power and active power generation. Moreover, without the time delay of the frequency measurement, the control of virtual inertia emulation is immediate after a fault occurrence.

However, the matching control introduces coupling between the active and reactive power generation in that the changes in the active power generation may also lead to changes in the reactive power output. This coupling effect is undesirable and can lead to instability. In order to mitigate the problem of this undesired coupling, a supplementary controller is designed.

There are many implementations of matching control, where the DC link capacitor is assumed to provide the energy reserve of virtual inertia emulation. However, the storage of capacitive energy in these DC link capacitors alone is not enough for emulating a large amount of system inertia for the power system, and energy storage system is additionally required for emulating a large amount of virtual inertia.

Finally, the investment cost of virtual inertia installation is estimated based on different designs of battery storage system.

2.1. Matching Control

2.1.1. Introduction of Matching Control

Park-Clarke Transformation

The matching control achieves virtual inertia emulation control by establishing an equivalence between parameters of synchronous generators and the CIG unit. The design of CIG controller is formulated in the $dq0$-frame, but the power system and synchronous generators are modelled in three phases, the abc-frame. Therefore, Park transformation is needed to reformulate the synchronous generator's dynamic model [44] in $dq0$-frame.

Park transformation first converts a quantity z_{abc} in abc-frame to an equivalent quantity in another stationary orthogonal frame—the $\alpha\beta\gamma$-frame:

$$\begin{bmatrix} z_{\alpha\beta} \\ z_{\gamma} \end{bmatrix} = \sqrt{2/3} \begin{bmatrix} 1 & -\frac{1}{2} & -\frac{1}{2} \\ 0 & \frac{\sqrt{3}}{2} & -\frac{\sqrt{3}}{2} \\ \frac{1}{\sqrt{2}} & \frac{1}{\sqrt{2}} & \frac{1}{\sqrt{2}} \end{bmatrix} z_{abc}. \tag{2.1}$$

If z_{abc} is balanced, it has, $z_{\gamma} = z_{abc}\mathbb{1} = 0$. The $z_{\alpha\beta}$ is a component rotating at a speed of $2\pi f$ with f being the power frequency in the stationary $\alpha\beta\gamma$-frame.

Then, the $z_{\alpha\beta}$ quantity can be represented equally in the rotating $dq0$-frame as z_{dq}:

$$z_{dq} := R_{\theta}^{\top} z_{\alpha\beta} \tag{2.2a}$$

where

$$R_{\theta} := \begin{bmatrix} \cos\theta & -\sin\theta \\ -\sin\theta & -\cos\theta \end{bmatrix} \tag{2.2b}$$

is the rotation transformation, and

$$z_0 := z_{\gamma} \tag{2.2c}$$

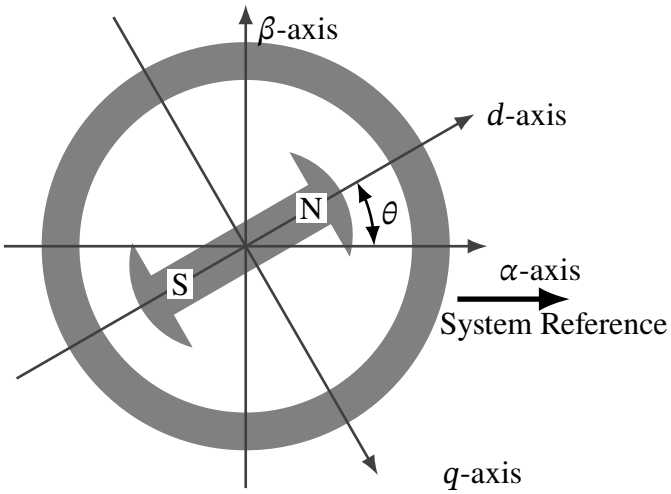

Figure. 2.1.: Assumed orientation of the dq-frame.

is the zero component. The rotation angle θ is selected so that the unit phasor $\angle\theta := e^{i\theta}$ is align with the rotor's orientation as shown in Figure. 2.1.

Synchronous Generators in dq-Frame

Consider a synchronous generator and a dq-frame rotating at synchronous speed $\dot{\theta} = \omega_s$ in (2.2b). Its mechanical dynamics can be expressed in *swing equations*:

$$\dot{\delta} = \omega - \omega_s \tag{2.3a}$$

$$m\dot{\delta} = \tau_{\mathrm{m}} - \tau_{\mathrm{e}} - d(\omega - \omega_s), \tag{2.3b}$$

where the d is generator's damping radio, m is the rotational inertia; τ_{e} and τ_{m} are generator's electrical and mechanical torque. In the dq-frame, the mechanical torque τ_{m} and the electricity torque τ_{e} are

$$\tau_e = \psi_d i_q - \psi_q i_d, \tag{2.4}$$

where ψ_d and ψ_q are d- and q-components of the stator's magnetic flux. The flux linkage dynamics are

$$0 = -\dot{\psi}_d + r_d i_d + \omega\psi_q + v_d \tag{2.5a}$$

$$0 = -\dot{\psi}_q + r_q i_q - \omega\psi_d + v_q, \tag{2.5b}$$

where the $\dot{\psi}_d$ and $\dot{\psi}_q$ are decided by the excitation dynamics and generators' damping windings, and ω is generator's rotation speed. According to the grid code requirement on the system frequency in Table 1.1 for the German power grid, the rotor speed's fluctuation $\Delta\omega := \omega - \omega_s \in [-0.06\ p.u., 0.04\ p.u.]$ and $\Delta\omega \in [-0.01\ p.u., 0.01\ p.u.]$ when in emergency.

Stator's magnetic fluxes ψ_d and ψ_q are decided by the rotor's excitation system, the currents of the rotor's damping winding, and the armature current of the stator. Sauer-Pai's Model [45], Marconato's Model, or Anderson-Fouad's Model [46] describe the magnetic flux of the d- and q-axes, ψ_d and ψ_q. The simplified systems of the flux dynamics are derived in [47]:

$$\psi_d = -L_d i_d + L_m i_f \tag{2.6a}$$

$$\psi_q = -L_q i_q \tag{2.6b}$$

$$\psi_f = -L_m i_d + L_f i_f. \tag{2.6c}$$

The generator's mechanical torque τ_m is determined by the generator's governor. The governor's dynamic is

$$T_g \dot{x} = \frac{1}{r}(\dot{\delta} - \omega_{\text{ref}}) - x \tag{2.7a}$$

$$\tau_m = x + \tau_m^* \tag{2.7b}$$

where r is the governor's drooping character, T_g is governor's time constant T_g whose typical value is around 0.05 s for a non-hydraulic generator, and τ_m^* is the reference input of mechanical torque.

The output active and reactive power generations are expressed as

$$p_{\text{out}} = v_d i_d + v_q i_q \tag{2.8}$$
$$q_{\text{out}} = v_q i_d - v_d i_q. \tag{2.9}$$

In summary, the following equations fully describe a synchronous generator:

$$\dot{\delta} = \omega - \omega_s \tag{2.10a}$$
$$M\dot{\delta} = \tau_{\text{m}} - \tau_{\text{e}} - d(\omega - \omega_s) \tag{2.10b}$$
$$\tau_e = \psi_d i_q - \psi_q i_d \tag{2.10c}$$

$$0 = -\dot{\psi}_d + r_d i_d + \omega\psi_q + v_d \tag{2.10d}$$
$$0 = -\dot{\psi}_q + r_q i_q - \omega\psi_d + v_q \tag{2.10e}$$
$$\psi_d = -L_d i_d + L_m i_f \tag{2.10f}$$
$$\psi_q = -L_q i_q \tag{2.10g}$$
$$\psi_f = -L_m i_d + L_f i_f \tag{2.10h}$$

$$T_g \dot{x} = \frac{1}{r}\left(\dot{\delta} - \omega_{\text{ref}}\right) - x \tag{2.10i}$$
$$p_{\text{m}} = x + \tau_{\text{m}} \tag{2.10j}$$

$$p_{\text{out}} = v_d i_d + v_q i_q \tag{2.10k}$$
$$q_{\text{out}} = v_q i_d - v_d i_q. \tag{2.10l}$$

CIG Units in dq-Frame

Figure. 2.2 is a schematic plot of a CIG-unit. The controlled-current source i_{dc} models the initial phase of electricity generation. For wind power generation, the current source models the wind turbine and the machine-side power converter. For the solar panel, it models the solar panel and multiple series of boost DC-DC converters to increase the power voltage of the photovoltaic electricity. The shunt conductance G_{dc} models the power losses at the phase of electricity generation.

The DC-link capacitor C_{DC} separates the electricity generation phase and power conversion

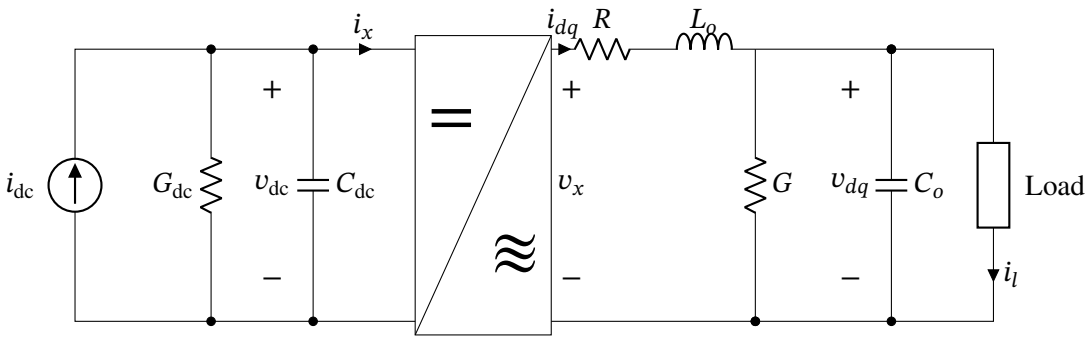

Figure. 2.2.: The simplified power electronic circuit for matching control [20].

phase. It also provides DC voltage for the power switch, which is shown in the Figure as a big rectangle labelled as "$=/\approx$." The voltage source converts DC electricity into a (balanced) three-phase AC. Due to the balanced three phases, the electrical quantities of the AC circuit can be reformulated in dq-frame. But, Figure. 2.2 plots only a single-phase circuit as a representation.

The R, L_o, and C_o model the output filter and the parasitic resistance, inductance, and capacitance. The shunt resistor G models the power losses in the power converter. The averaging switching modulation is used for the CIG unit. In other words, the switching dynamics are neglected. The dynamic models of a CIG unit are shown as follows in $dq0$-frame:

$$i_x = m_{\mathrm{dq}}^{\top} i_{\mathrm{dq}} \tag{2.11a}$$

$$v_x = m_{\mathrm{dq}} v_{\mathrm{dc}} \tag{2.11b}$$

$$C_{\mathrm{dc}} \dot{v}_{\mathrm{dc}} = -G_{\mathrm{dc}} v_{\mathrm{dc}} + i_{\mathrm{dc}} - m_{\mathrm{dq}}^{\top} i_{\mathrm{dq}} \tag{2.12a}$$

$$L_o \dot{i}_{dq} = -R i_{dq} - \eta v_{\mathrm{dc}} L_o \mathbf{J} i_{dq} - v_{dq} + m_{dq} v_{\mathrm{dc}} \tag{2.12b}$$

$$C_o \dot{v}_{dq} = -G v_{dq} - \eta v_{\mathrm{dc}} C_o \mathbf{J} v_{dq} + i_{dq} - i_l, \tag{2.12c}$$

where v_x and i_x are the output voltage and the current injection of the power converter, respectively. The m_{dq} are the duty ratio of the of the Pulse-Width Modulation signal.

Matching Control in CIG

By comparing the dynamics of CIG units in dq-frame (2.11) and (2.12) with the dynamics of synchronous generators (2.10) in dq-frame, the matching control is defined simply by building the following identities of equality, thereafter referred to as *matching relations*:

$$\eta v_{\mathrm{dc}} = \omega \tag{2.13a}$$

$$m_{\mathrm{dq}}^{\top} = \frac{1}{\mu}\begin{bmatrix}0 & \mathbf{e}\end{bmatrix}, \tag{2.13b}$$

where η and μ are the two control parameters for the matching control.

Under the matching control, the electrical torque τ_e is described as

$$\tau_e := v_{\mathrm{dc}} i_x = v_{\mathrm{dc}} m_{dq} \begin{bmatrix} i_d \\ i_q \end{bmatrix}. \tag{2.14}$$

With the help of matching relation (2.13), the following O.D.E. can be obtained,

$$\begin{aligned} \frac{1}{\eta} v_{\mathrm{dc}}\, C_{\mathrm{dc}} \dot{\omega} &= -\frac{1}{\eta} v_{\mathrm{dc}} G_{\mathrm{dc}} \omega + v_{\mathrm{dc}} i_{\mathrm{dc}} - v_{\mathrm{dc}} m_{dq}^{\top} i_{dq} \\ v_{\mathrm{dc}}\, C_{\mathrm{dc}} \dot{v}_{\mathrm{dc}} &= -G_{\mathrm{dc}} v_{\mathrm{dc}}^2 + \tau_{\mathrm{in}} - \tau_{\mathrm{e}}, \end{aligned} \tag{2.15}$$

where τ_{in} represents the "force" of the initial electricity generation process on the voltage dynamics of DC-link capacitor, and τ_{e} is the electrical torque define above. The O.D.E. (2.15) describes the emulated mechanical response of a CIG unit under the matching control and is called "*virtual swing equation*."

By comparing (2.15) with the swing dynamic (2.10b) for a synchronous generator, it is conclude that the DC-link capacitance C_{dc} is analog to the inertia M of a synchronous generator. If the per-unit system, $v_{\mathrm{dc}} \approx 1$ and $\omega \approx 1$ during normal system operation; therefore, it can be written as (2.12b):

$$C_{\mathrm{dc}} \dot{v}_{\mathrm{dc}} = -G_{\mathrm{dc}} v_{\mathrm{dc}} + i_{\mathrm{dc}} - m_{dq}^{\top} i_{dq}.$$

The DC-link capacitance C_{dc} then becomes the emulated virtual inertia. Larger DC-link capacitance is, larger virtual inertia is emulated.

The capacitive energy storage is analog to the kinetic energy of the generator's rotational mass. Whenever there is mismatch between τ_{m} and τ_{e}, or the input of captured renewable power $i_{\mathrm{dc}}v_{\mathrm{dc}}$ and the output of active power generation, the capacitive energy of the capacitor either increases or releases.

The inductive dynamic (2.12b) can be seen as an equivalent of flux equations (2.10d) and (2.10e) of a synchronous generator. By the substitution of $m_{dq}^{\top} = \frac{1}{\mu}\begin{bmatrix}-\psi_q & \psi_d\end{bmatrix}$ in (2.10d) and (2.10e):

$$L\begin{bmatrix}\dot{i}_{\mathrm{d}}\\ \dot{i}_{\mathrm{q}}\end{bmatrix} + \eta v_{\mathrm{dc}} L_{\mathrm{dq}}\mathbf{J}i_{\mathrm{dq}} = -R\begin{bmatrix}i_{\mathrm{d}}\\ i_{\mathrm{q}}\end{bmatrix} - \begin{bmatrix}v_{\mathrm{d}}\\ v_{\mathrm{q}}\end{bmatrix} + \frac{1}{\mu}\begin{bmatrix}0\\ \mathbf{e}\end{bmatrix} v_{\mathrm{dc}}.$$

With the additional assumption:

$$L_{\mathrm{dq}} i_{\mathrm{dq}} = \psi_{\mathrm{dq}}, \tag{2.16a}$$

$$\psi_f = \frac{1}{\mu\eta} \tag{2.16b}$$

and the matching relation, $\omega = \eta v_{\mathrm{dc}}$, the inductive dynamic (2.12b) can be rewritten as

$$\begin{bmatrix}\dot{\psi}_{\mathrm{d}}\\ \dot{\psi}_{\mathrm{q}}\end{bmatrix} + \omega\begin{bmatrix}-\psi_{\mathrm{q}}\\ \psi_{\mathrm{d}}\end{bmatrix} = R\begin{bmatrix}i_{\mathrm{d}}\\ i_{\mathrm{q}}\end{bmatrix} - \begin{bmatrix}0\\ \psi_f\end{bmatrix}\omega, \tag{2.17}$$

which is referred to as "*virtual flux dynamics*."

In summary, under the matching control, a CIG unit can fully emulate synchronous generation in almost all aspects.

Emulating Governor's Primary Frequency Control

It is well known that the power system will not be stable without generators' drooping characteristics. Though the G_{dc} in (2.15) is equivalent to the generator's synchronous damping, the G_{dc} is considerably small. Therefore, an additional mechanism is designed to help emulate the drooping characteristic. Assuming the emulated drooping factor is $\frac{1}{r}$, the

drooping control characteristic is emulated with the following O.D.E.:

$$\dot{x} = \frac{1}{r}(v_{DC} - v_{DC,0}) - x \tag{2.18a}$$

$$i_{DC} = x + i_{DC,0}. \tag{2.18b}$$

This desgin is equivalent to synchronous generator governor's dynamics (**??**). The effective drooping coefficient is [20]

$$d = -\frac{2(G_{\mathrm{dc}} + K_p)}{\eta^2}\omega^* + \frac{i_0}{\eta}. \tag{2.19}$$

2.1.2. Implementations of Matching Control and Cost Estimates

The matching control discussed in the previous section is more a theoretical topology design than real-world implementations. Different implementations of matching control involve different designs of electricity storage systems for the virtual inertia emulation, the investment costs are different for a different design of electricity storage.

This subsection discusses several practical ways of implementing matching control. To compare the investment costs of different electricity storage design, the discussion is based on an example of an aggregated 100 MW CIG generation of a wind park. The terminal AC voltage of CIG is assumed to be 10 kV, and the rated DC voltage v_{DC} is 5 kV.

Straightforward Implementation

A straightforward implementation of matching control is to implementing the matching relations (2.13) in a digital controller. As shown in Figure. 2.3, the controller takes as the input the voltage measurement v_{dc} across the DC-link capacitor and then compute for the orientation θ of its internal $dq0$-frame,

$$\theta = \int_{t_0}^{t} \eta v_{\mathrm{dc}}\, \mathrm{d}\tau. \tag{2.20}$$

Then the modulation signal m_{dq} are formulated upon this rotating $dq0$-frame according to the equality (2.13b).

Under this controller design, capacitive electricity energy is naturally released or charged for virtual inertia emulation. The amount of DC capacitance required to emulate a second * of virtual inertia can be found from

$$\begin{aligned} E_{\text{kinetic}} &= E_{\text{capacitive}} \\ \frac{1}{2} M \omega_{\text{nominal}}^2 &= \frac{1}{2} C_{\text{dc}} \, {v_{\text{dc}}}_{\text{nominal}}^2 \end{aligned} \tag{2.21}$$

where $\omega_{r_{\text{nominal}}} = 2\pi f_{\text{nomial}}$ is the rotor's electrical rotating speed, and M is the generatior's rotational mass. Therefore, for capacitance C_{dc}

$$M_{\text{VI}} = \frac{C_{\text{dc}} v_{\text{dc}_{\text{nominal}}}^2}{\omega_{r_{\text{nominal}}}^2}, \tag{2.22}$$

where every quantity is in SI units. Often, the per-unit system is used in the study of power system dynamics. The unit bases for the capacitor and inertia are

$$C_{\text{base}} = \frac{S_{\text{base}}}{\omega_{\text{nominal}} V_{\text{base}}^2} \qquad \text{Dimension:} \quad \frac{M L^2 T^{-1}}{T^{-3} \, (M L^2 T^{-3} I^{-1})^2} \tag{2.23a}$$

$$M_{\text{base}} = \frac{S_{\text{base}}}{\omega_{\text{nominal}}^2} \qquad \text{Dimension:} \quad \frac{M L^2 T^{-3}}{T^{-2}}, \tag{2.23b}$$

respectively. The rotational inertia and the emulated virtual rotation are derived as

$$\text{Dimension of } \textit{rotational mass} = M L^2 \tag{2.24a}$$

$$\text{Dimension of } \textit{virtual rotational mass} = \frac{\left(M^{-1} L^{-2} T^4 I^2\right) \, \left(M L^2 T^{-3} I^{-1}\right)^2}{T^{-2}} = M L^2. \tag{2.24b}$$

Therefore, the virtual rotational inertia M_{VI} is in seconds,

$$\text{Dimension of } M \text{ or } M_{\text{VI}} \text{ in per-unit} = \frac{M L^2}{\frac{M L^2 T^{-3}}{T^{-2}}} = T.$$

*in the power system's conventional per-unit system convention, inertia is in seconds.

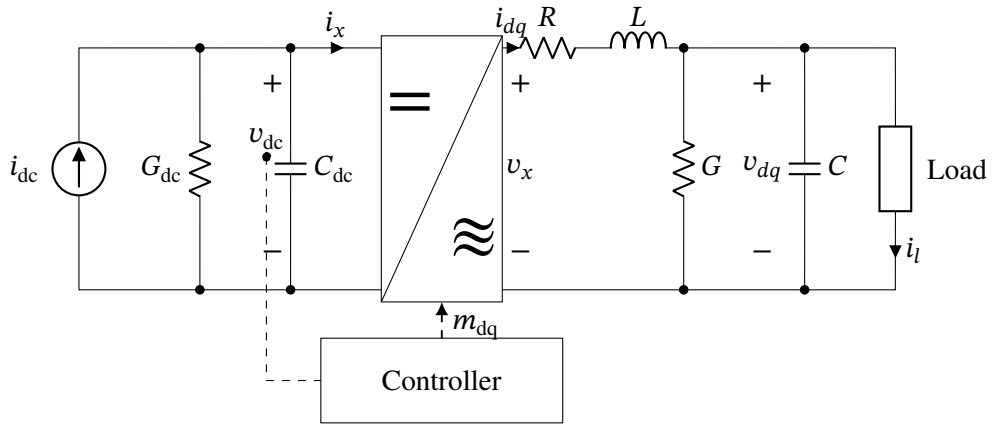

Figure. 2.3.: Straightforward implementation of matching control

In contract, the ω is still in rad $\cdot\, s^{-1}$.

For emulating a second of virtual inertia in per-unit, the required size of DC capacitor installation is

$$C_{\mathrm{dc}} = \frac{\frac{S_{\mathrm{base}}}{\omega^2_{\mathrm{nominal}}} \times \omega^2_{\mathrm{nominal}}}{v^2_{\mathrm{dc_{nominal}}}} = \frac{S_{\mathrm{base}}}{v^2_{\mathrm{dc_{nominal}}}} = \frac{100\ \mathrm{M}}{5\ \mathrm{K} \times 5\ \mathrm{K}} = 4\ \mathrm{F}.$$

Usually, high voltage DC capacitors are rated in watt-seconds. The required DC-link capacitor should be rated $E_{\mathrm{C}} = 50\ \mathrm{MW} \cdot \mathrm{s} = 13.89\ \mathrm{kW{\cdot}h}$. Only ultra-capacitors (also known as super-capacitor) is capable for such an application. It is a large investment and takes large space to accommodate it. A typical ultra-capacitor has energy density of 15000–30000 $\mathrm{W{\cdot}s}$ per liter. Although the energy density of the newest generation of ultra-capacitors was reported to be 10 times higher in energy density [48]. However, this type of ultra-capacitor is not yet widely available.

External energy storage

Under the matching control, the DC voltage v_{dc} is linked to the virtual rotational speed ω_{dq} of a CIG unit. The variation of virtual rotational speed ω_{dq} is limited to 4% even during a large system transient event. Therefore, the electricity stored in a DC-link capacitor cannot

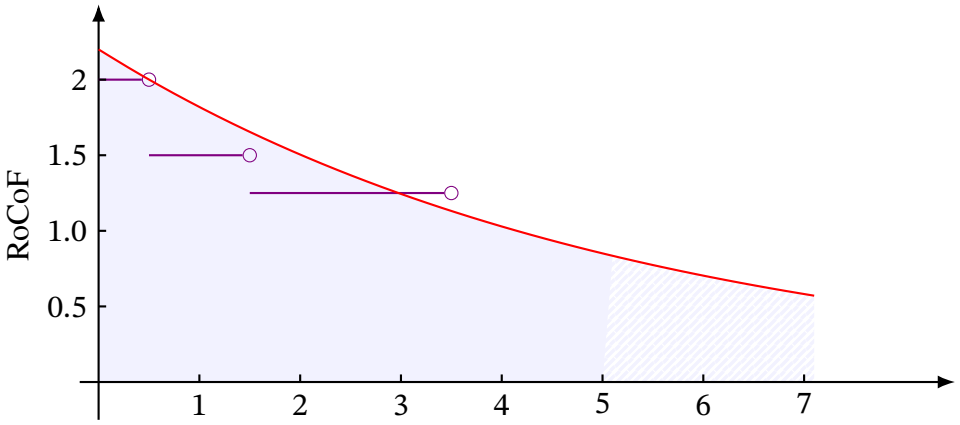

Figure. 2.4.: The estimated requirement on the system frequency

be fully utilized in the straightforward way of matching control implementation. Therefore, external energy storage is used to supplement the DC capacitor in virtual inertia emulation. During the emulated inertia response, the electricity storage of the external energy storage is fully depleted in emulated inertia response.

The *Battery Energy Storage System* (BESS) is deemed as the most effective way for electricity storage. Compared with a super- or ultra-capacitor, BESS has a larger energy capacity but less power rating [49]. In other words, BESS takes time for the discharging power of electricity storage to reach maximum.

Depending on the different functionalities the BESS may serve, a mix of different battery storage media may be used for the BESS. As illustrated in the shaded area of Figure. 2.4, the super-capacitor supports the large power demand immediately after the fault occurrence for the virtual inertia response. Then, as the variation system frequency becomes stable, the electric power output of BESS is supported by other forms of electricity storage media that has higher energy density but lower power density, e.g., Lithium-Ion or Lead-Acid, as shown in the stripped area of Figure. 2.4.

If BESS is used to supplement the DC-link capacitor for virtual inertia emulation, the implementation of matching control should be modified accordingly as shown in Figure. 2.5. The external supplementary power storage is modelled as C'_{dc}. The shunt resistance G'_{dc} and series inductance L' model the power losses and parasitic inductance, respectively. The external power source is interfaced to the DC circuit component of CIG via a DC-DC power

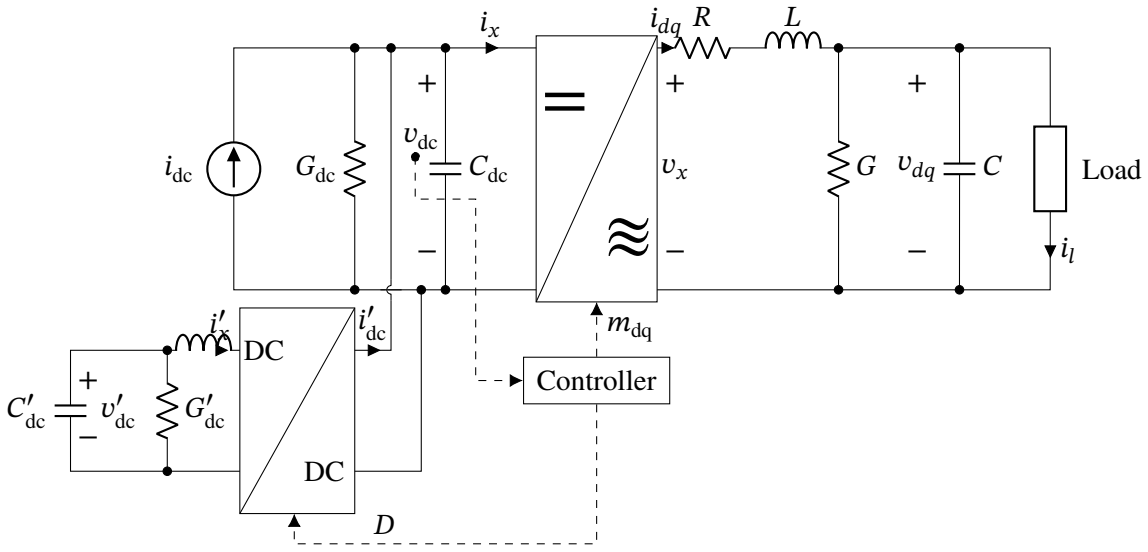

Figure. 2.5.: C_{dc} is replaced with a hybrid capacitor.

Table. 2.1.: ENTSO-e's requirement on RoCoF [50].

RoCoF (Hz/s)	window (ms)
±2	500
±1.5	1000
±1.25	2000

converter with an appropriate conversion ratio so that

$$\frac{\Delta v_{dc}}{\Delta v'_{dc}} = \frac{v_{dc} - v_{dc_{nominal}}}{v'_{dc} - v'_{dc_{nominal}}} = k, \tag{2.25}$$

where k is the scale of voltage amplification, and $v_{dc_{nominal}}$ and $v'_{dc_{nominal}}$ are the voltage level of DC capacitors in normal operational condition. For a small deviation of DC voltage Δv_{dc} at the DC-link capacitor,

$$v'_{dc} = k\,\Delta v_{dc} + v'_{dc_{nominal}}. \tag{2.26}$$

The voltage deviation of DC-link capacitor v_{dc} is the virtual rotational speed linked to the frequency deviation under the matching control. According to TSOs requirements on the

system's frequency deviation in Table 1.1, $-0.06\ p.u. \leq \Delta v_{\mathrm{dc}} \leq 0.04\ p.u.$, the value for the scale of voltage amplification k can be set to 10, and the $v'_{\mathrm{dc}_{\mathrm{nominal}}}$ to 0.6 *p.u.* The variation of v'_{dc} is between 0.0 *p.u.* and 1.0 *p.u.*

The external electricity storage system sits in tandem with the controlled-current source representing capturing and converting renewable energy into electricity. The external power source provides additional electric power for emulating virtual inertia response. The topology design enlarges the effective size of DC-link capacitor. In summary, the overall dynamic can be written as

$$\begin{aligned} i_x &= \frac{1}{2} m_{dq}^{\top} i_{dq} \\ v_x &= \frac{1}{2} m_{dq} v_{\mathrm{dc}}, \\ C_{\mathrm{dc}} \dot{v}_{\mathrm{dc}} &= -G_{\mathrm{dc}} v_{\mathrm{dc}} + i_{\mathrm{dc}} + i'_{\mathrm{dc}} - i_x \\ L \dot{i}_{dq} &= -R i_{dq} - \eta v_{\mathrm{dc}} L \mathbf{J} i_{dq} - v_{dq} + v_x \\ C \dot{v}_{dq} &= -G v_{dq} - \eta v_{\mathrm{dc}} C \mathbf{J} v_{dq} + i_{dq} - i_l \end{aligned} \tag{2.27a}$$

$$\begin{aligned} v'_x - v'_{\mathrm{dc}_{\mathrm{nominal}}} &= k\left(v_{\mathrm{dc}} - v_{\mathrm{dc}_{\mathrm{nominal}}}\right) \\ v'_x i'_x &= v_{\mathrm{dc}} i'_{\mathrm{dc}} \\ C'_{\mathrm{dc}} \dot{v}'_{\mathrm{dc}} &= -G'_{\mathrm{dc}} v'_{\mathrm{dc}} - i'_x \\ L'_{\mathrm{dc}} \dot{i}'_x &= v'_{\mathrm{dc}} - v'_x \end{aligned} \tag{2.27b}$$

To appropriately size the external storage system, it requires that the external electric power output should be as large as the rotational mass of a synchronous generator may support. The size of the power output required of the external electricity storage system can be estimated from the RoCoF in extreme.

The requirements on RoCoF $\dot{f}$ by ENTSO-e are shown in Table 2.1. Assume a large system fault resulting a large system frequency variation and RoCoF, $\max_{t \geq 0} \dot{f}(t) = \pm 2$. In this case, the power output from the rotational mass of a synchronous generator is

$$p_{\mathrm{mass}} = \frac{\mathrm{d}E_{\mathrm{mechanical}}}{\mathrm{d}t} = M \omega \dot{\omega}, \tag{2.28}$$

Table. 2.2.: Specification and cost of Different Energy Storage Devices [51].

Parameter	**Li Ion**	**Lead Acid**	**NaS**	**Super-capacitor**
Power (W/kg)	250−340	75−300	80−150	≈100k
Energy (W·h/kg)	75−350	30−50	10−50	0.05−5
Power capital cost ($/kW)	1.2k	300−600	1k−3k	100−300
Energy capital cost ($/kW·h)	0.6k−2.5k	200−400	300−500	0.3k−2k
Discharge time	mins−hrs	secs − hrs	secs − hrs	secs − mins
Self-discharge rate per day	0.001−0.004	0.0003−0.001	0.1−0.2	0.2−0.4
Efficiency (%)	70−90	80−95	68−90	75−83
Lifetime (yrs)	5− 15	5− 20	10− 20	5− 15

which should equal to

$$p_{\text{mass}} = P_{\text{VI}} = \frac{\mathrm{d}E_{\text{VI}}}{\mathrm{d}t} = C v_{\text{dc}} \dot{v}_{\text{dc}}.$$

It can be computed that, for emulating a second of virtual inertia in *per-unit*, the required power can be computed:

$$p_{\text{mass}} = \frac{S_{\text{base}}}{\omega^2_{\text{nominal}}} 2\pi f \dot{f} \tag{2.29}$$

$$\approx \frac{100\ \text{M}}{(2\pi \times 50)^2}(2\pi \times 50) \times (2\pi \times 2) \approx 2\ \text{MW}. \tag{2.30}$$

According to the "power capital" items in Table. 2.2, the capital investment per second of emulated virtual inertia can be computed as follows for a 100 MW CIG.

For Li-Ion:	$1.2\ \text{k} \times 2\ \text{k} = 2.4\ \text{M\$}/s$
For Lead Acid:	$600 \times 2\ \text{k} = 1.2\ \text{M\$}/s$
For super-capacitor:	$300 \times 2\ \text{k} = 600\ \text{k\$}/s.$

It can be seen that the super-capacitor is the most cost-effective form of electricity storage

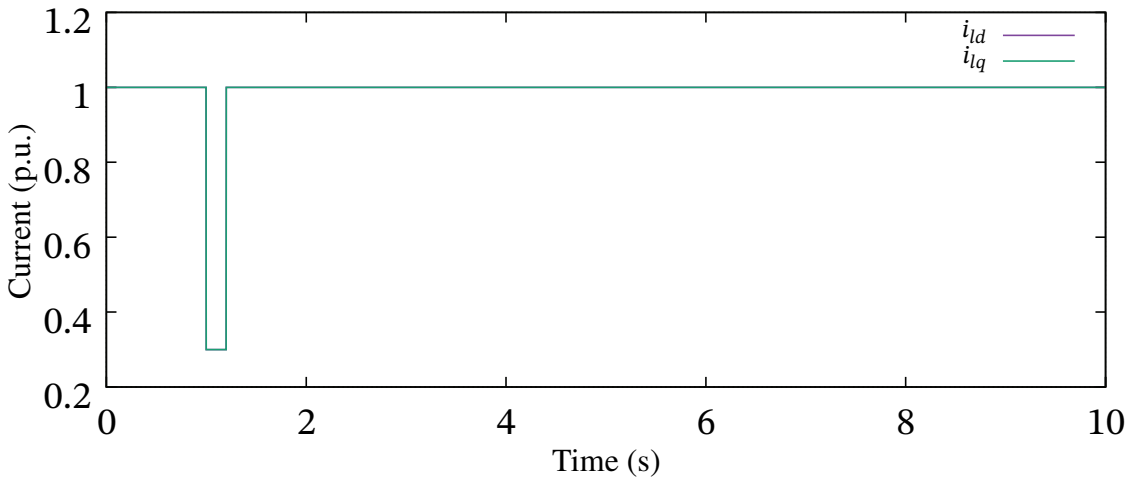

Figure. 2.6.: The disturbance in loading current i_l.

media.

The above investment estimation is based on the power requirement of emulated virtual inertia response. The design of external electricity storage should also consider the energy density. The energy density of super-capacitor is very low, which is only 180–18000 W/s. That is to say, in the worst-case scenario, around 17.68 kg of super-capacitor installation is required to support the response of a second of virtual inertia at RoCoF of ± 2 Hz/s for 2 seconds. Though a new generation of ultra-capacitors' energy density is ten times higher than the existing ultra-capacitor, this new type of ultra-capacitor is still not available in large size.

Finally, a simple simulation of the implementation (2.27a) and (2.27b) is made to demonstrate its effectiveness. This study of simulation neglects its switching and PWM signal generation. Assume a system disturbance resulting in a sudden drop in the loading current i_l as shown in Figure. 2.6. The simulated frequency responses to the assumed disturbance are plotted in Figure. 2.7, which demonstrates the performances of the virtual inertia implementation with and without the external electricity storage C'_{dc}.

The DC capacitor C'_{dc} can be seen as energy buffer in the hybrid implementation Figure. 2.2 that helps boost the effective capacitance C_{dc} in (2.12). Therefore, other energy storage devices, like BESSs, can take the C'_{dc}'s place as long as they can be quickly discharged to fulfil the deficiency in DC power input or be quickly charged consume the excess of the DC power generation. In such a case, additional controller units are required to control the power

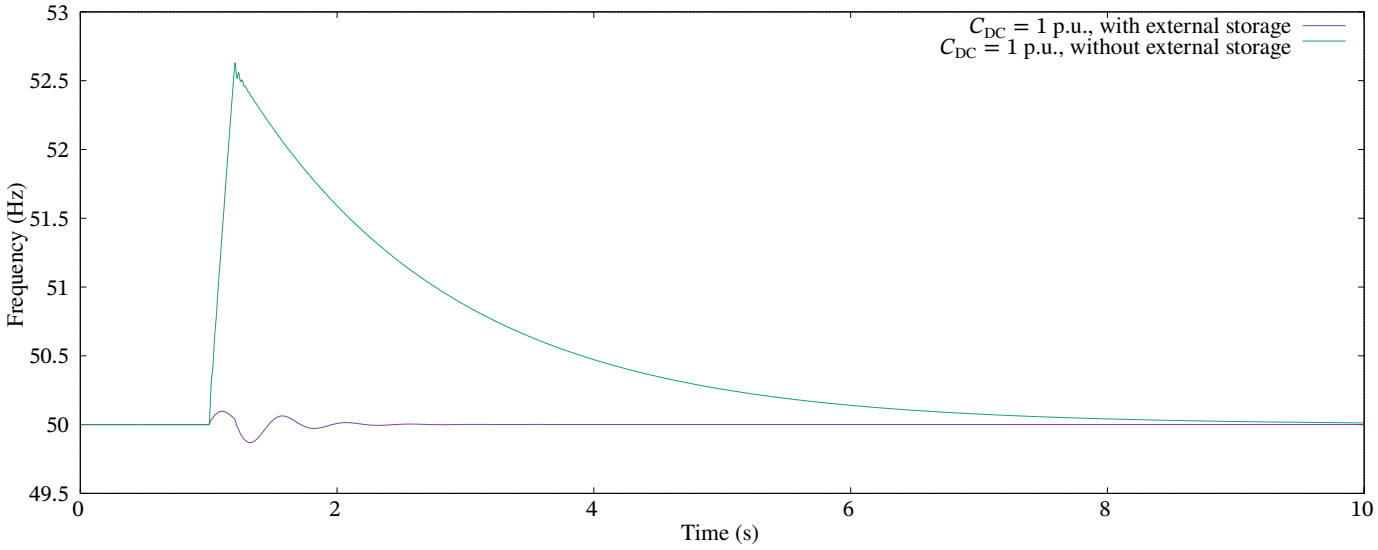

Figure. 2.7.: Frequency response with and without the external electricity storage.

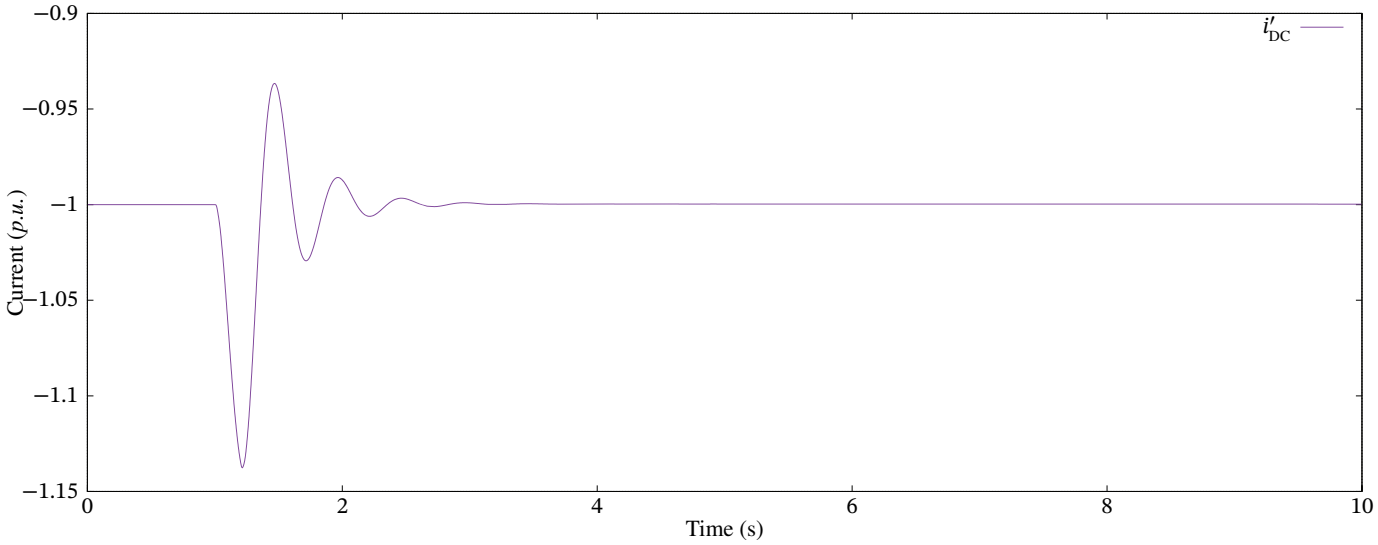

Figure. 2.8.: Current injection of the hybrid DC capacitors.

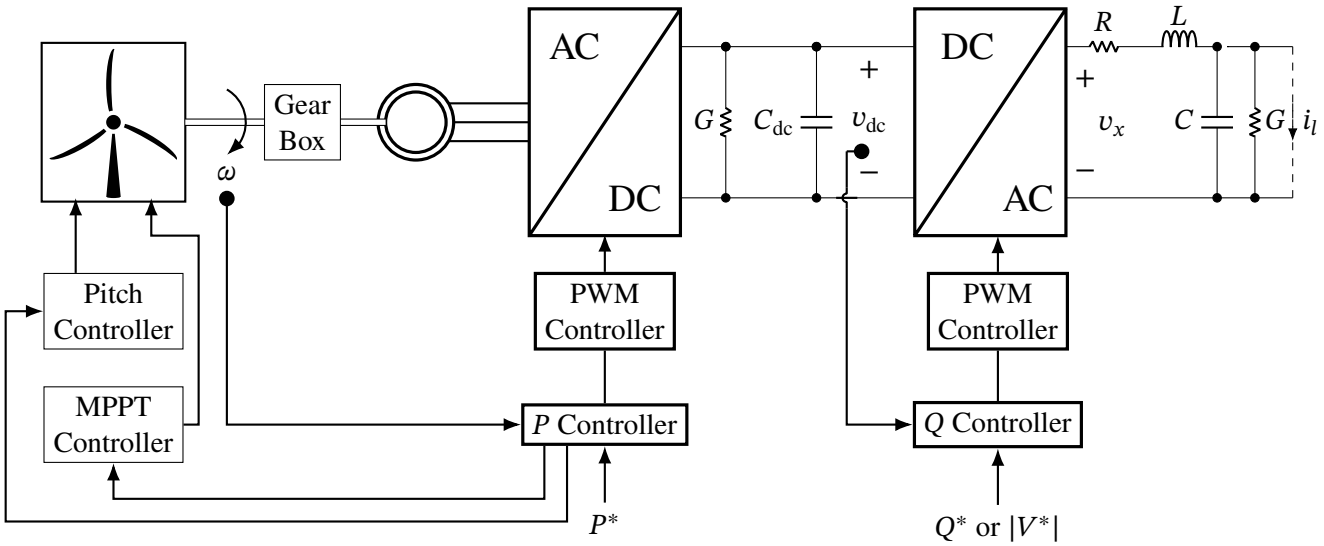

aod

Figure. 2.9.: Separated active and reactive power control for wind turbine.

in and out of the energy storage device.

2.2. A Supplementary Controller for Voltage Stabilization

As mentioned in Section 1.4.1, the CIG's active and reactive power generations are regulated independently for the modern types of wind turbines and solar panels under the traditional control scheme. The machine side converter regulates its active power generation and participates in *Maximum Power Point Tracking* (MPPT) control; whereas, the grid side converter regulates its reactive power generation and maintains a voltage across its DC-link capacitor in Figure. 2.9 .

2.2.1. Coupled Active and Reactive Power Control

While in steady-state, the independence of active and reactive power regulation remains valid for a CIG unit under the matching control. However, while in a system transient, the matching control may alter CIG's virtual rotational speed, which is the voltage of DC-link capacitor v_{dc}. The variations on v_{dc} can influence both the active and reactive power generation and, therefore, couple the active and reactive power generation.

The proper inertia response in a synchronous generator is an integral part of active power regulation. The rotational speed would not significantly change its terminal voltage and reactive power output. It is expected that the emulated virtual inertia response of matching control can only influence its active power and kept constant its reactive power output.

Denote v_x the CIG unit's "inner" AC voltage in Figure. 2.9. Then, the active and reactive power generation can be expressed as

$$q_{\text{inner}} = v_{xq} i_d - v_{xd} i_q \tag{2.31a}$$

$$p_{\text{inner}} = v_{xd} i_d + v_{xq} i_q \tag{2.31b}$$

where the v_{xd} and v_{xq} is defined in (2.13b). The active and reactive power outputs are

$$q_{\text{inner}} = v_{xq} i_q = \frac{1}{\mu} v_{\text{dc}} i_d \tag{2.32a}$$

$$p_{\text{inner}} = v_{xq} i_d = \frac{1}{\mu} v_{\text{dc}} i_q. \tag{2.32b}$$

The time derivative of q_{inner} is

$$\begin{aligned}
\dot{q}_{\text{inner}} &= \frac{1}{\mu} \dot{v}_{\text{dc}} i_d + \frac{1}{\mu} v_{\text{dc}} \dot{i}_d \\
&= \frac{1}{\mu} \left(-\frac{G_{\text{dc}}}{C_{\text{dc}}} v_{\text{dc}} + \frac{1}{C_{\text{dc}}} i_{\text{dc}} - \frac{1}{\mu C_{\text{dc}}} i_q \right) i_d \\
&\quad + \frac{1}{\mu} v_{\text{dc}} \left(-\frac{R}{L} i_d + \eta v_{\text{dc}} i_q - \frac{1}{L} v_d \right) \\
&= -\left(\frac{G_{\text{dc}}}{C_{\text{dc}}} + \frac{R}{L} \right) q_{\text{inner}} + \eta v_{\text{dc}} p_{\text{inner}} - \frac{1}{L} v_q v_d + \frac{1}{\mu C_{\text{dc}}} i_d i_{\text{dc}} - \frac{1}{\mu C_{\text{dc}}} i_d i_x \\
&= -\left(\frac{G_{\text{dc}}}{C_{\text{dc}}} + \frac{R}{L} \right) q_{\text{inner}} + \eta v_{\text{dc}} p_{\text{inner}} - \frac{1}{L} v_q v_d + \frac{1}{\mu} \dot{v}_{\text{dc}} i_d.
\end{aligned} \tag{2.33}$$

In steady-state, it is verified both sides of the above equation equal zeros. However, in a system transient, the variation of "inner" reactive power generation depends on DC capacitor's voltage v_{dc} as well as the "inner" active and reactive power production (2.32b) and (2.32a).

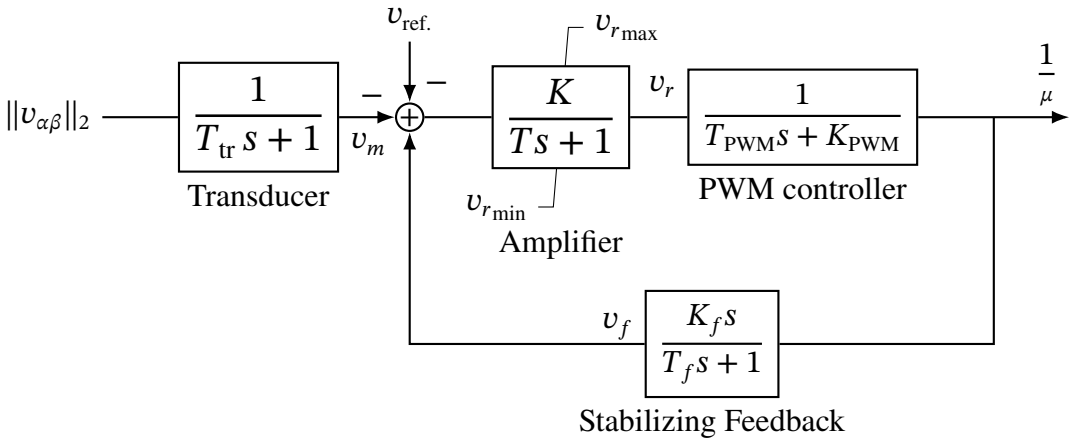

Figure. 2.10.: A schematic diagram of Matching Control's reactive power supplement controller.

Moreover, if the CIG implements additionally the drooping control (2.18),

$$\dot{x} = \frac{1}{r}(v_{dc} - v_{dc_0}) - x$$
$$i_{dc} = x + i_{dc0},$$

it will arrive at a new steady-state operation conditions in that $i_{\text{dc}_{\text{new}}} \neq i_{\text{dc}_0}$, $x_{\text{new}} \neq x_0 := x(0)$, and $v_{\text{dc}} \neq v_{\text{dc}_0}$. From the formula for "inner" active and reactive power generation (2.32b) and (2.32a), it is known that the "inner" active and reactive power generation will arrive at new states that is decided by the post-fault DC voltage v_{dc}.

Therefore, the active and reactive power generations are no longer independent under matching control. Consequently, a supplementary controller is required to compensate for the reactive power variation.

2.2.2. Supplementary Reactive Power Controller

The Type IV wind generation and DFIG are all capable of generating reactive power and seen from the grid size as a voltage source. Therefore, a simple supplementary control can be designed to stabilize a CIG unit's reactive power output. In this subsection, a design of the supplementary controller is proposed that models after a synchronous generator's Automatic Voltage Regulation (AVR) in Figure. 2.10.

This design is similar to a synchronous generator' IEEE type-DC1 AVR. It takes voltage measurement as input and outputs a signal $\frac{1}{\mu}$ for the magnitude of PWM. The time constant T_{Tr} is the time constant of the voltage transducer modelled as a first-order low-pass filter. The voltage measurement is taken at the CIG unit's terminal on the stationary $\alpha\beta$-frame. Notice that $\|v_{dq}\| = \|v_{\alpha\beta}\|$. The controller design is composed of an amplifier of time constant T with an anti-windup limiter. The "*PWM controller*" translates the amplifier output into the magnitude of modulation signal $\frac{1}{\mu}$ and is modeled as a block of low-pass filter of time constant T_{PWM}. The feedback loop is a high-pass filter for improving the supplementary controller's dynamic characteristics. The dynamic can be equivalently expressed in the following O.D.E.s:

$$\dot{v}_r = \frac{1}{T}\left(K\left(v_{\text{ref.}} - v_{\text{m}}\right) - v_f - \frac{K_f}{T_f}\frac{1}{\mu}\right) \tag{2.34a}$$

$$\dot{v}_f = -\frac{1}{T_f}\left(\frac{K_f}{T_f}\frac{1}{\mu} + v_f\right) \tag{2.34b}$$

$$\frac{\mathrm{d}}{\mathrm{d}\,t}\left(\frac{1}{\mu}\right) = -\frac{1}{T_{\text{PWM}}}\left(\frac{1}{\mu}K_{\text{PWM}} - v_r\right), \tag{2.34c}$$

where the dynamics of voltage transducer is omitted. The controller can be installed with several additional lead-lag filters before the amplifier. In the design, the CIG's terminal voltage is regulated at a constant value. The reactive power control can also be controlled by similarly modeling the output voltage phasor's magnitude and orientation.

In order to demonstrate the effectiveness of the proposed supplementary controller, the controller is implemented with the PST package on MATLAB platform and tested on a single CIG unit on the Southeast Australian power system with and without this controller. Figure 2.11 shows the response of a CIG's terminal voltage when subject to a large system disturbance. The CIG's power source, i.e., the controlled current source i_{dc} in Figure. 2.2, is disconnected at time $t = 1$ s. The simulation shows that CIG unit's terminal voltage variation is within a more limited range and settles at the same pre-fault voltage value if equipped with the supplementary controller. Otherwise, the voltage settles at a lower voltage. In contrast, The CIG unit's voltage responses are similar with and without the supplementary controller.

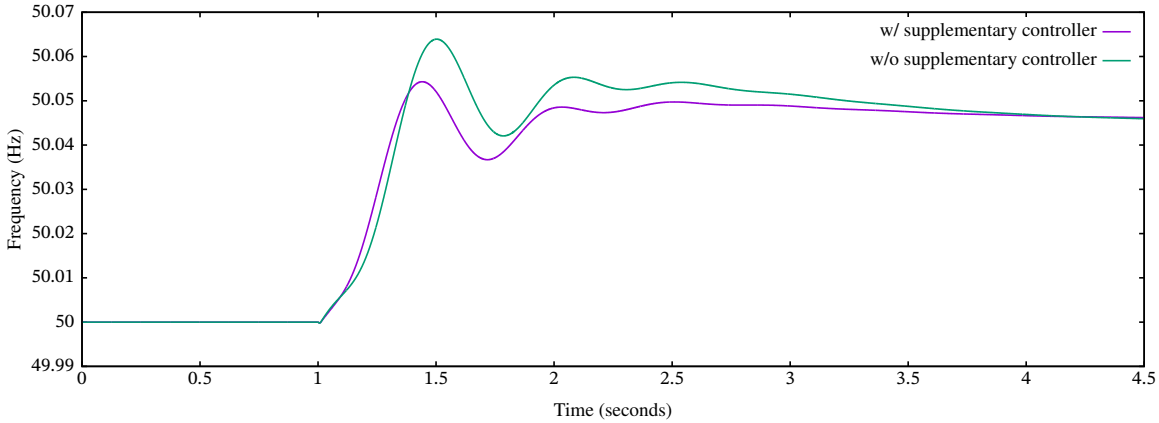

Figure. 2.11.: The CIG's terminal voltage response with and without the supplement voltage controller.

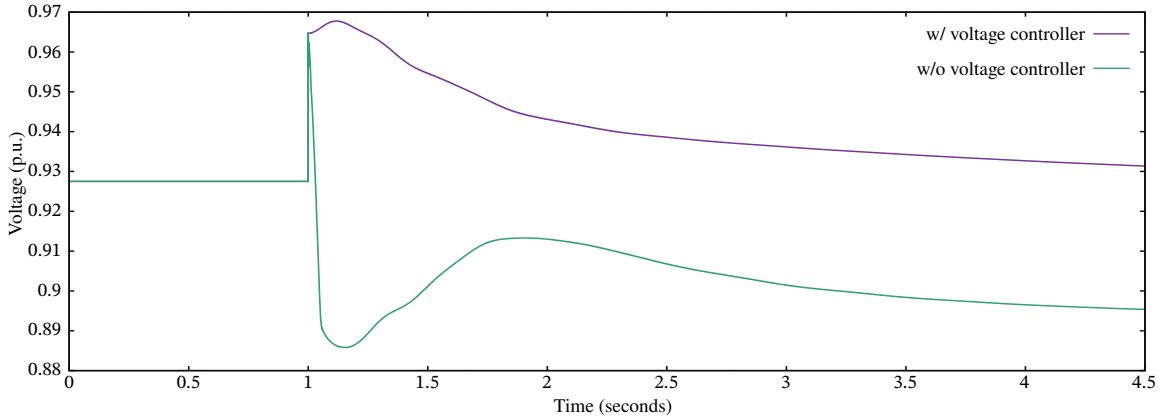

Figure. 2.12.: The CIG's terminal voltage response with and without the supplement voltage controller.

Chapter 3

Singular Perturbation and Inertia Response

Traditionally, the system's frequency nadir, frequency overshoot, and RoCoF, defined in Sub-section 1.3.1, have been used as indices to characterize the qualities of frequency response. The grid code's requirements on the frequency response are also formulated on these indices. These indices are also used conveniently to size the reserve for the primary frequency control, setting appropriate drooping coefficient, and coordinating settings for the power system's protection relays [44], [52].

However, these indices, seen as a mathematical function, belong to $\mathcal{L}_\infty$ and are difficult to compute. The linearization technique can be used to simplify the non-linear power system and find an analytic mathematical expression for these indices [12]. Even so, the resulting formulae are too complex to be used to form a constraint in formulating an optimization problem.

Furthermore, as a subtle aspect of drawback, unilaterally improving one of the frequency indices may deteriorate other indices. For example, large synchronous coefficient, i.e., the coefficient d in (2.10b), can reduce the frequency nadir but also increase RoCoF $\dot{f}$ because of the complexity of a power system. Therefore, a new metric definition is required in place of these indices to plan investment in virtual inertia installation in the power system.

An $\mathcal{L}_2$ or, equivalently, $\mathcal{H}_2$ metric is proposed in [19] is proposed. This metric had been widely used in studying the synchronization of network-connected oscillators and commonly used in the $\mathcal{H}_2$ optimal control [53], [54].

The newly proposed metric is also based on $\mathcal{L}_2$ norm. Instead of measuring the degree of synchronization of these network-connected oscillators, this metric measures how the

internal response or virtual inertia response influences the system's frequency response with the help of singular perturbation technique.

The singular perturbation technique helps to separate the frequency response to two constituting dynamics of lower order. One captures the component of fast transient, whereas the other slowing moving component. It shows the fast transitory component is inertia-sensitive, and the slow component is not. Therefore, the new metric is defined on the fast transitory component. The slow transitory component is shown equivalent to the classical dynamics of network-connected Kuramoto oscillators and decides the stability of the power system.

3.1. Singular Perturbation Techniques

3.1.1. Regular Perturbation

Before delving into the singular perturbation technique, the *regular perturbation technique* is worthy of an examination. Both the regular and singular perturbation techniques are proposed to obtain an asymptotic approximation of a solution to an ordinary or partial differential equations $\frac{\mathrm{d}}{\mathrm{d}t}x = f(x,t,\epsilon)$, or $\frac{\partial}{\partial x}f(x,t,\epsilon) \wedge \frac{\partial}{\partial t}f(x,t,\epsilon)$ in a formal power series,

$$x(t) = x_0(t) + \epsilon x_1(t) + \epsilon^2 x_2(t) + ... + \epsilon^n x_n(t) + \mathcal{O}(\epsilon^{n+1}) \tag{3.1}$$

where the ϵ is the dimensionless perturbation term and is sufficiently small. The $x_0(t)$ is the solution to the O.D.E. $\frac{\mathrm{d}}{\mathrm{d}t}x = f(x,t,0)$ or P.D.E. system $\frac{\partial}{\partial x}f(x,t,0) \wedge \frac{\partial}{\partial t}f(x,t,\epsilon)$. The functions $x_1, x_2, \ldots, x_n$, etc. can be solved mechanistically by collecting and equaling terms of the same order in ϵ at the initial conditions.

The thermokinetic system can be used to describe the regular perturbation technique. A thermokinetic system is formulated as

$$\dot{u} = 1 - u\, e^{\epsilon(q-1)} \tag{3.2a}$$

$$\dot{q} = u\, e^{\epsilon(q-1)} - q, \tag{3.2b}$$

with initial condition $u(0) = q(0) = 0$. In general, not all O.D.E. or P.D.E. systems admit an asymptotic solution estimate. Nevertheless, assume the solution $\big(u(t), q(t)\big)$ can be approximated by a formal series of form (3.1). The zero-order estimate $x_0(t)$ can be easily found with the initial conditions by setting $\epsilon \to 0$:

$$x_0(t) = \begin{bmatrix} 1 - e^{-t} & 1 - te^{-t} - e^{-t} \end{bmatrix}^\top.$$

With the expression the $x_0(t)$, the expression for $x_1(t)$ can be found easily by collecting those ϵ terms

$$x_1(t) = \left[\frac{1}{2}\left(t^2 + 2t - 4\right)e^{-t} + (2+t)e^{-2t} \quad \frac{1}{6}\left(t^3 - 18t + 30\right)e^{-t} - (2t+5)e^{-2t} \right]^\top.$$

The zero-order and first-order estimates, $x_0(t) = [u_0(t)\ q_0(t)]^\top$ and $x_0(t) + \epsilon x_1(t) = [u_0(t) + \epsilon u_1(t)\ q_0(t) + \epsilon q_1(t)]^\top$, respectively, are plotted in Figure. 3.1(a) and Figure. 3.1(b) along with the system's numeric solutions $[\hat{u}(t)\ \hat{q}(t)]^\top$.

The results show that the first-order solution estimate $x_0(t) + \epsilon x_1(t)$ can satisfactorily approximate the "true" response of numerical solution. It also demonstrates that the n-order asymptotic series (3.1) given by the successful regular perturbation technique approximates the true solution uniformly in $t \geq t_0$ with approximation error of $o(\epsilon^n)$ if the system is stable or in the time domain of interest if the dynamics are unstable. Otherwise, if the resulting asymptotic series cannot uniformly approximate the true solution, the dynamics under study do not admit approximation in asymptotic terms.

In summary, the regular perturbation technique starts with identifying a small dimensionless perturbation term ϵ in O.D.E.s $\frac{\mathrm{d}}{\mathrm{d}t} f(x, t, \epsilon)$ or P.D.E. $\frac{\partial}{\partial x} f(x, t, \epsilon) \wedge \frac{\partial}{\partial t} f(x, t, \epsilon)$. Setting $\epsilon \to 0$ gives the zero-order term x_0 in (3.1). The first-order terms, second-order terms, etc.,i.e, ϵx_1, $\epsilon^2 x_2$ etc., can be derived sequentially.

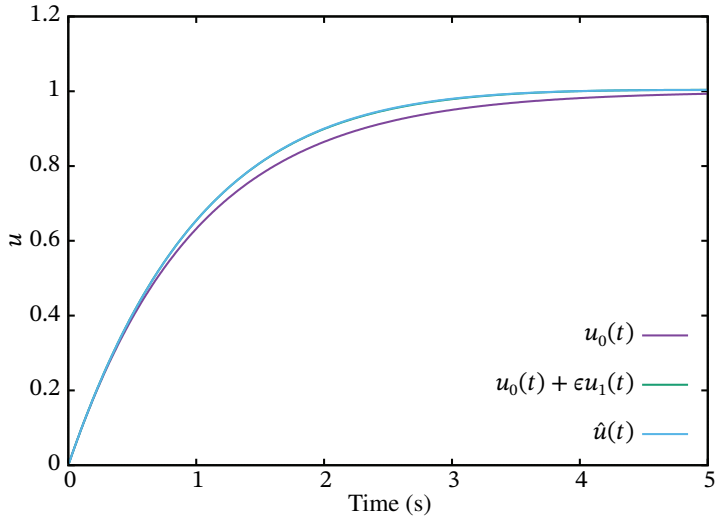

(a)

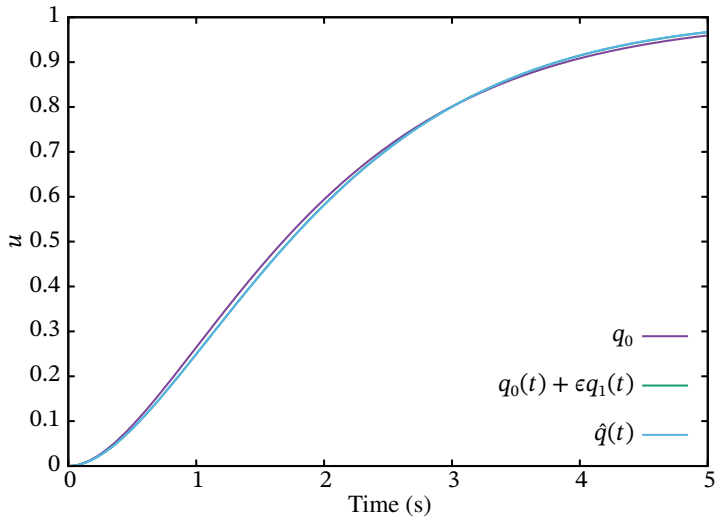

(b)

Figure. 3.1.: Comparison of the numeric and estimated solution to the thermokinetic system.

3.1.2. Singular Perturbation

Singular Perturbation Problem

The regular perturbation method cannot always find a uniform solution to all O.D.E. or O.D.E. systems. As an example, consider the following *Initial Value Problem* (I.V.P.),

$$\dot{x} = y \tag{3.3a}$$

$$\epsilon\dot{y} = -y - k\,x \tag{3.3b}$$

with $x(0) = a$ and $\dot{x}(0) = y(0) = b$, modelled after the swing equations of a synchronous generator:

$$\dot{\theta} = \omega \tag{3.4a}$$

$$\dot{\omega} = p - d\theta - \sum_{j=1}^{n} \kappa_j \sin(\theta - \theta_j). \tag{3.4b}$$

The meanings of various parameters is deferred to Section 3.2 when applying the singular perturbation technique on the synchronous generators' swing equations. The system (3.3) can be written compactly as

$$\epsilon\ddot{x} + \dot{x} + k\,x = 0.$$

A substitution of a formal series (3.1) for $x(t)$ in O.D.E. (3.3) results in

$$\epsilon\,(\ddot{x}_0 + \epsilon\ddot{x}_1 + ...) + (\dot{x}_0 + \epsilon\dot{x}_1 + ...) + k\,(x_0 + \epsilon x_1 + ...) = 0.$$

By setting $\epsilon \to 0$, (3.3) reduces to an unperturbed system

$$\dot{x}_0(t) + kx_0(t) = 0. \tag{3.5}$$

At $t = 0$, the initial conditions give

$$b + ka = 0.$$

Therefore, we must assume $b = -ka$. Otherwise, the regular perturbation cannot give a solution. For example, when $x(0) = a = 1.5$, $k = 2$ and $\dot{x}(0) = y(0) = b = -3$, (3.5) gives

$$x_0(t) = 1.5\, e^{-2t}, \tag{3.6}$$

whereas the real result can be obtained by Laplace transformation as, with $\epsilon = 0.1$

$$\begin{aligned} x(t) &= \mathcal{L}^{-1}\left\{\frac{\epsilon a\, s}{\epsilon\, s^2 + s + k} + \frac{a + \epsilon b}{\epsilon\, s^2 + s + k}\right\} \\ &= \frac{e^{-\frac{t\left(\sqrt{1-4k\epsilon}+1\right)}{2\epsilon}}\left(a\left(\left(\sqrt{1-4k\epsilon}+1\right)e^{\frac{t\sqrt{1-4k\epsilon}}{\epsilon}} + \sqrt{1-4k\epsilon} - 1\right) + 2b\epsilon\left(e^{\frac{t\sqrt{1-4k\epsilon}}{\epsilon}} - 1\right)\right)}{2\sqrt{1-4k\epsilon}} \\ &= \begin{cases} 1.75623e^{-2.76393t} - 0.256231e^{-7.23607t} & \text{when } b = -3 \\ 1.97984e^{-2.76393t} - 0.479837e^{-7.23607t} & \text{when } b = -2 \end{cases} \end{aligned} \tag{3.7}$$

and

$$y(t) = \dot{x}(t) = \begin{cases} 1.8541e^{-7.23607t} - 4.8541e^{-2.76393t} & \text{when } b = -3 \\ 3.47214e^{-7.23607t} - 5.47214e^{-2.76393t} & \text{when } b = -2. \end{cases} \tag{3.8}$$

Figure. 3.2(a) and Figure. 3.3(a) show the plots of the real solution $x(t)$ and the $O(1)$ solution estimate $x_0(t)$ as well as the solution $y(t)$ and the $O(1)$-order solution estimate $y_0(t)$. It can be visually identified that $x_0(t)$ and $y_0(t)$ are good uniform estimates of the corresponding real solutions $x(t)$ and $y(t)$.

However, if $b \neq -ka$, we have to relax one of the initial conditions, often the the higher order state, i.e., $\dot{x}(0)$ is not assumed equal to b. Otherwise, the solution estimate of the form

$$x_0(t) = x_0(0)\, e^{-kt}$$

cannot satisfy, for example, the initial condition $y(0) = \dot{x}(0) = -2$ and $x(0) = 1.5$ at the same time. The best that one can do is to expect the corresponding estimate $\big(x_0(t), y_0(t)\big)$, $\big(x_0(t) + \epsilon x_1(t), y_0(t) + \epsilon y_1(t)\big)$, etc. can satisfactorily estimate the true system response at later time $t \geq t^*$.

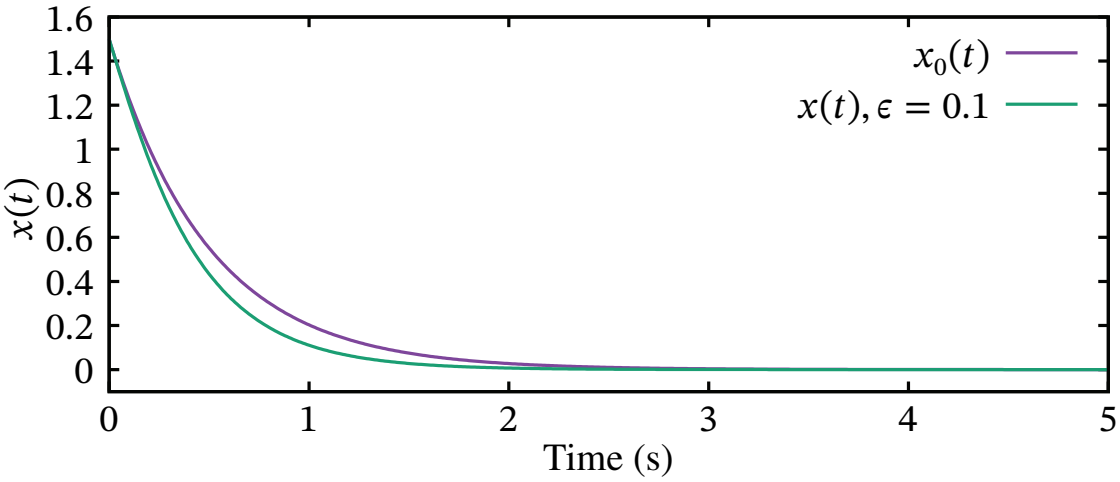

(a) when $x(0) = a = 1.5$ and $y(0) = b = -3.0$

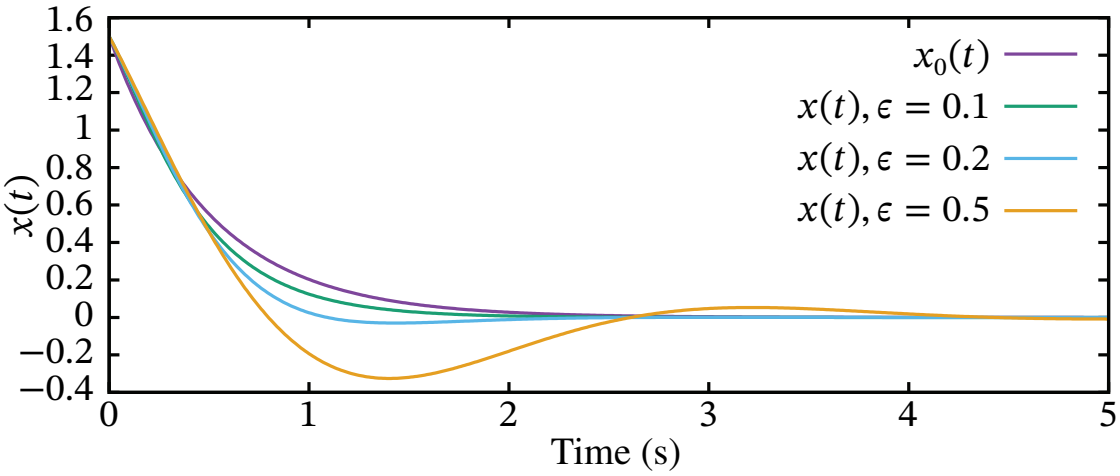

(b) when $x(0) = a = 1.5$ and $y(0) = b = -2.0$

Figure. 3.2.: Plots of the estimated and real solution ($x_0(t)$ and $x(t)$) to the example O.D.E. system for illustrating singular perturbation method.

It is indeed the case, Figure. 3.2b and Figure. 3.3b show a plot of the corresponding x- and y-estimate, i.e., $x_0(t)$ and $y_0(t)$, and the true response $x(t)$ and $y(t)$. The results show that $y_0(t)$ can uniformly estimate the true dynamic response for time $t \geq t^*$. The $t^* = t^*(\epsilon)$ depends on ϵ. But, for $t \in [0, t^*(\epsilon)]$ the $y_0(t)$ cannot estimate the real solution uniformly. It is evident that there is an additional order of dynamic comes into play in the perturbed dynamic system; and the large the perturbation ϵ is, the larger the t^* is, and so the $x_0(t)$ and

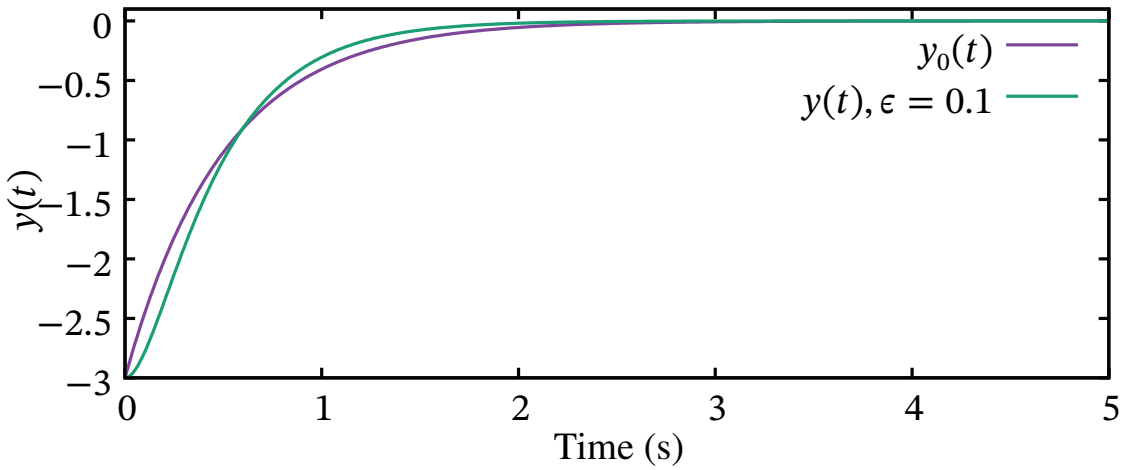

(a) when $x(0) = a = 1.5$ and $y(0) = b = -3.0$

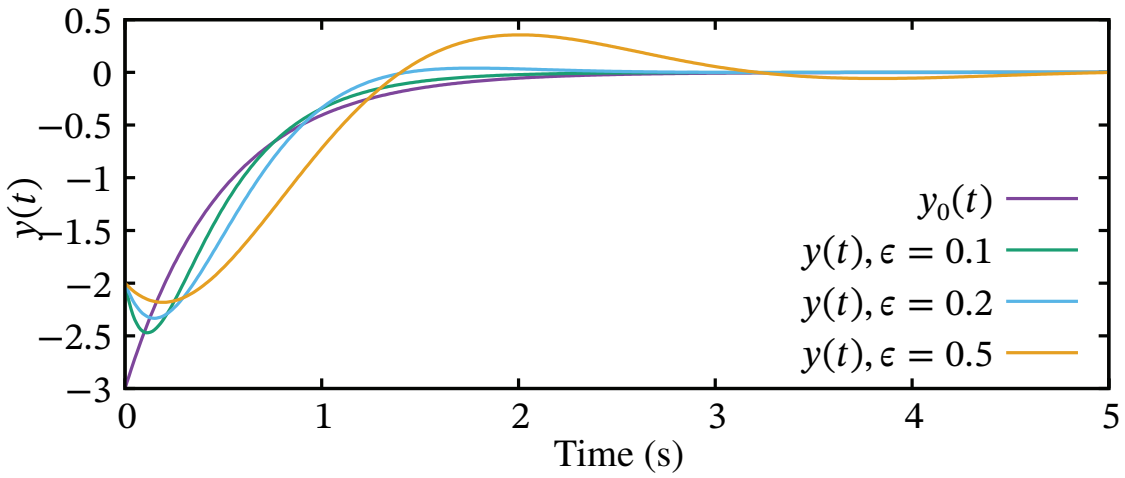

(b) when $x(0) = a = 1.5$ and $y(0) = b = -2.0$

Figure. 3.3.: Plots of the estimated and real solution ($y_0(t)$ and $y(t)$) to the example O.D.E. system for illustrating singular perturbation method.

$y_0(t)$ are less satisfactory as shown in Figure. 3.2(b) and Figure. 3.3(b). In all cases, the regular perturbation method cannot give a uniform estimation of the true solution over the whole time domain.

The O.D.E. problem (3.3) represents a general class of problems that can be written in the

following form,

$$\dot{x}_1 = f_1(t, x_1, x_2, \epsilon) \tag{3.9a}$$

$$\epsilon\dot{x}_2 = f_2(t, x_1, x_2, \epsilon). \tag{3.9b}$$

It can be shown that regular perturbation method cannot produce a uniform estimate solution in $t \in [t_0, \infty[$ for this class of functions, but the *singular perturbation method* can. The principle of singular perturbation method is to find another dynamic trajectory $(X_2)_0 : [0, \infty[\to \mathbb{R}^n$ to be superimposed into the $O(1)$-order estimate $(x_2)_0 : [0, \infty[\to \mathbb{R}^n$ obtained via the regular perturbation method. The $O(1)$-order estimate $(x_2)_0$ is called *outer approximation* characterizing the slow response dynamic, whereas the estimate $(X_2)_0$ is referred at as *inner approximation* characterizing the fast dynamic.

Slow and Fast Dynamics

In the following, an algorithm is introduced that separates the disturbed O.D.E. system (3.9) into two parts: *1*) *boundary layer dynamics* (also called *inner layer dynamics*) and *2*) *outer layer dynamics*. The outer layer dynamics is formulated in the same time scale of t and captures only the slow response component, so the outer layer dynamics is also called *slow dynamics*. The inner layer dynamics, however, is in the time scale of $\frac{t}{\epsilon}$ capturing the fast transitory component; hence, the inner layer dynamics is referred to as *fast dynamics*. The solution to the original system (3.9) can then be approximated by superimposing the solution to the fast dynamic system on the solution slow dynamic solution with the *matching technique* [55]

It is generally difficult to obtain a separation of general dynamics into a slow and fast part in general because the process depends on the unique characteristic of dynamics under consideration. However, the basic principles of each step can be explained with an example of the simplified swing equations (3.3).

Step 1) As shown previously, the outer approximation is obtained by substituting the formal series (3.1) into the original O.D.E., and then set $\epsilon \to 0$ to get the out layer dynamics.

For the swing dynamics (3.3), the out layer dynamic is

$$\dot{x} = y \tag{3.10a}$$

$$0 = -y - k\,x, \tag{3.10b}$$

subject to only one initial condition on $x(0)$. It is obvious that the order of out layer dynamics is one less than the original O.D.E.. Moreover, y is no longer a state variable but as an algebraic function of the state variables,

$$y = h(x). \tag{3.11}$$

A topological space $\{(y, x) \in \mathbb{R}^n \,||y = h(x)\}$ can then be defined with regards to the out layer dynamic (3.10). This topological space is called *slow manifold* of the original singular perturbed system.

Step 2) Then, a coordinate transformation, named *time dilution*, is applied on the time t

$$\bar{t} = \frac{t}{\epsilon^\alpha}. \tag{3.12}$$

Under the diluted time coordinate, the time derivative becomes

$$\frac{\mathrm{d}}{\mathrm{d}\bar{t}} = \epsilon^\alpha \frac{\mathrm{d}}{\mathrm{d}t}.$$

Denote $X(\bar{t}) := x(\epsilon^\alpha t)$ and $Y(\bar{t}) := x(\epsilon^\alpha t)$, the swing equations (3.3) become

$$\epsilon^{-\alpha} \frac{\mathrm{d}X}{\mathrm{d}\bar{t}} = Y \tag{3.13a}$$

$$\epsilon^{1-\alpha} \frac{\mathrm{d}Y}{\mathrm{d}\bar{t}} = -Y - kX. \tag{3.13b}$$

On this O.D.E. system, the regular perturbation technique can be reapplied by substituting the formal series expansion for X:

$$X = X_0 + \zeta X_1 + ...$$

$$Y = \epsilon^{-\alpha} \frac{\mathrm{d}X_0}{\mathrm{d}\bar{t}} + \zeta \epsilon^{-\alpha} \frac{\mathrm{d}X_1}{\mathrm{d}\bar{t}} + ...$$

for some small ζ, $0 < \zeta << 1$. Without lose of generality, the ζ is set to be $\zeta = \epsilon^\beta$, the

expansions become

$$X = X_0 + \epsilon^{\beta} X_1 + \dots \tag{3.14a}$$

$$Y = \epsilon^{-\alpha} \frac{\mathrm{d}X_0}{\mathrm{d}\bar{t}} + \epsilon^{\beta-\alpha} \frac{\mathrm{d}X_1}{\mathrm{d}\bar{t}} + \dots . \tag{3.14b}$$

As $\beta \to \infty$, that is $\zeta \to 0$, (3.13b) becomes

$$\epsilon^{1-2\alpha} \frac{\mathrm{d}^2 X_0}{\mathrm{d}\bar{t}^2} = -\epsilon^{-\alpha} \frac{\mathrm{d}X_0}{\mathrm{d}\bar{t}} - kX_0. \tag{3.15}$$

Depending on the choice of value for α, there may have the following arguments

a) Assuming $\alpha = 0$, as $\epsilon \to 0$ (3.15) becomes $0 = \frac{\mathrm{d}X_0}{\mathrm{d}\bar{t}} - kX_0$ and correspondingly $\bar{t} = \frac{t}{\epsilon^0} = t$, which is the same as for the slow dynamics (3.10).

b) Assuming $\alpha = 1$, as $\epsilon \to 0$ (3.15) becomes $\epsilon^{-1} \frac{\mathrm{d}^2 X_0}{\mathrm{d}\bar{t}^2} = \epsilon^{-1} \frac{\mathrm{d}X_0}{\mathrm{d}t} - o(\epsilon^{-1})$. Accordingly, $\bar{t} = \frac{t}{\epsilon}$. Multiplying ϵ on the both sides of the equation,

$$\frac{\mathrm{d}^2 X_0}{\mathrm{d}\bar{t}^2} = -\frac{\mathrm{d}X_0}{\mathrm{d}\bar{t}}. \tag{3.16}$$

Notice $\epsilon o(\epsilon^{-1}) = 0$ as $\epsilon \to 0$. The solution to (3.16) is

$$X_0\left(\frac{t}{\epsilon}\right) = c_1 e^{-\frac{t}{\epsilon}} + c_2$$

whose time derivative is

$$\dot{X}_0\left(\frac{t}{\epsilon}\right) = \frac{1}{\epsilon} X_0'\left(\frac{t}{\epsilon}\right) = -\frac{1}{\epsilon} c_1 e^{-\frac{t}{\epsilon}}. \tag{3.17}$$

(3.17) The (3.16) along with the initial conditions constitutes the *boundary layer dynamics*. Regarding the initial conditions, it is a bit tricky and deferred to the *Step 3*).

c) The other possible choice for α is $\alpha = \frac{1}{2}$. In such case,

$$\frac{\mathrm{d}^2 X_0}{\mathrm{d}\bar{t}^2} = -\epsilon^{-\frac{1}{2}} \frac{\mathrm{d}X_0}{\mathrm{d}\bar{t}} - kX_0.$$

As $\epsilon \to 0$, it becomes $0 = \frac{\mathrm{d}X_0}{\mathrm{d}\bar{t}}$. It means that the choice of $\alpha = \frac{1}{2}$ gives a degenerate

solution.

d) Other choices for α cannot make (3.15) hold. Therefore, $\alpha = 1$ and (3.16) is the only possible choice for the boundary layer dynamics.

Step 3) Finally, the coefficient matching technique is used to get a proper value of c_2 and construct a solution estimate uniformly approximating the true solution over the whole time domain.

The coefficient matching technique starts with the following coordinate transform,

$$t_\eta = \frac{t}{\eta(\epsilon)}, \tag{3.18}$$

where $\eta(\epsilon)$ satisfies the following inequity

$$\epsilon < \eta(\epsilon) < 1$$

and other conditions (Kaplun extension theorem [56]). So the new state x_η is also diluted in the time space but not to the extent of $\bar{t} = \frac{t}{\epsilon^1}$. For this example. (3.15), the $\eta(\epsilon)$ can be set as

$$\eta(\epsilon) = \epsilon^\gamma,$$

where $0 < \gamma < 1$. Let $x_{\text{inner}}(t) := X_0(t\,\epsilon^\gamma)$ and $x_{\text{outer}} := x_0\left(\frac{t}{\epsilon^\gamma}\right)$, and $y_{\text{inner}}(t) = \dot{x}_{\text{inner}}(t)$ and $y_{\text{outer}}(t) = \dot{x}_{\text{outer}}(t)$. In the diluted time-scale,

$$x_{\text{outer}}(t_\eta) = x_0\left(\frac{t_\eta}{\epsilon^{-\gamma}}\right) = 1.5\, e^{-2\frac{t_\eta}{\epsilon^{-\gamma}}} \tag{3.19a}$$

$$x_{\text{inner}}(t_\eta) = X_0\left(\frac{t_\eta}{\epsilon^{1-\gamma}}\right) = c_1\, e^{-\frac{t_\eta}{\epsilon^{1-\gamma}}} + c_2 \tag{3.19b}$$

Their series expansions with regards to ϵ are

$$x_{\text{outer}}(t_\eta) = 1.5\left(1 - 2\,t_\eta\epsilon^\gamma + ...\right) \tag{3.20a}$$

$$x_{\text{inner}}(t_\eta) = c_2 + c_1\left(1 - t_\eta\epsilon^{\gamma-1} + \frac{1}{2}t_\eta^2\epsilon^{2\gamma-2} + ...\right). \tag{3.20b}$$

The matching technique requires that the coefficient for the $O(1)$ terms in the series expansion

of x_{outer} and x_{inner}, (3.20a) and (3.20b), respectively. Therefore,

$$c_2 + c_1 = 1.5. \tag{3.21}$$

Moreover, the $\dot{x}_{\text{outer}}$ and $\dot{x}_{\text{inner}}$ are

$$\dot{x}_{\text{outer}}(t_\eta) = \frac{1}{\epsilon^\gamma}\frac{\mathrm{d}}{\mathrm{d}t_\eta}x_{\text{outer}}(t_\eta) = -3 + ... \tag{3.22a}$$

$$\dot{x}_{\text{inner}}(t_\eta) = \frac{1}{\epsilon^\gamma}\frac{\mathrm{d}}{\mathrm{d}t_\eta}x'_{\text{inner}}(t_\eta) = -c_1\epsilon^{-1} + ... \tag{3.22b}$$

The matching control method asks that

$$\dot{x}_{\text{outer}}(0) + \dot{x}_{\text{inner}}(0) = -\frac{c_1}{\epsilon} - 3 = y(0) = \dot{x}(0). \tag{3.23}$$

Conditions (3.21) and (3.23) are due to different causes. Condition (3.21) states that, in the time scale of t_η, it is diluted by the scale of ϵ^γ, the $O(1)$ order estimates given by inner and outer approximations should be identical. Instead, Condition (3.23) requires satisfaction of other initial conditions on $\dot{x}(0)$.

Note, on the other hand, that the ϵ^{-1} term in (3.23) is due to the perturbation term in the original O.E.D. (3.15) other than the time dilution.

The inner approximation (3.19b) is obtained by solving conditions (3.21) and (3.23). For the case $y(0) = -2$,

$$-\frac{c_1}{\epsilon} - 3 = y(0) = -2 \quad \Rightarrow \quad c_1 = -0.1 \quad \text{and} \quad c_1 + c_2 = 1.5 \quad \Rightarrow \quad c_2 = 1.6;$$

similarly, when $y(0) = -3$,

$$-\frac{c_1}{\epsilon} - 3 = y(0) = -3 \quad \Rightarrow \quad c_1 = 0 \quad \text{and} \quad c_1 + c_2 = 1.5 \quad \Rightarrow \quad c_2 = 1.5.$$

Eventually, the uniform estimate for the O.D.E. of the swing equations (3.3) is given by summing up the $x_0(t)$ and $X_0\left(\frac{t}{\epsilon}\right)$ and deducting the common $O(1)$-term from the summation, which is a constant of value 1.5 in this example. The singular perturbation method gives the

a solution estimate:

$$\begin{aligned}\hat{x}_0(t) &= x_0(t) + X_0\left(\frac{t}{\epsilon}\right) - 1.5 \\ &= \begin{cases} 1.5\,e^{-2t} + 1.5 - 1.5 = 1.5\,e^{-2t} & \text{when } y(0) = -3 \\ 1.5\,e^{-2t} - 0.1e^{-10t} + 1.6 - 1.5 = 1.5\,e^{-2t} - 0.1e^{-10t} + 0.1 & \text{when } y(0) = -2, \end{cases}\end{aligned} \tag{3.24}$$

and

$$\begin{aligned}\hat{y}_0(t) &= x_0'(t) + \frac{1}{\epsilon}X_0'\left(\frac{t}{\epsilon}\right) \\ &= \begin{cases} -3\,e^{-2t} & \text{when } y(0) = -3 \\ -3\,e^{-2t} + e^{-10t} & \text{when } y(0) = -2 \end{cases}\end{aligned} \tag{3.25}$$

It can be verified $\hat{y}_0(0) = -2$, so the initial condition on $y(0)$ is indeed satisfied. The singular perturbation method gives the following solution estimate:

$$\begin{aligned}\hat{x}_0(t) &= a\,e^{-kt} - \epsilon\,e^{-\frac{1}{\epsilon}t} + \epsilon \\ \hat{y}_0(t) &= -ka\,e^{-kt} + (b + ka)\,e^{-\frac{1}{\epsilon}t}\end{aligned} \qquad \text{where } x(0) = a \text{ and } y(0) = b. \tag{3.26}$$

Figure. 3.4 shows the numerical solution to (3.3) for $\epsilon = 0.1, 0.2$, and 0.5, as well as the corresponding $O(1)$-order estimation produced using the singular perturbation method.

Comments

Firstly, it can be seen in Figure. 3.4 that the singular perturbation method can give a more accurate estimation in the whole time domain, thanks to the fast dynamic component added to the slow dynamic response.

Secondly, the singular perturbation technique is suitable for cases where ϵ is sufficiently small. For a more significant value of ϵ, e.g, $\epsilon = 0.5$, for the swing dynamic (3.4). Because this example happens to be linear, the decaying factors (the poles) can be accurately computed by solving for the roots of the denominators of (3.7). When $\epsilon > \frac{1}{4k}$, the decaying factor will be no real, and thus the solution will have oscillation modes that the singular perturbation technique cannot capture.

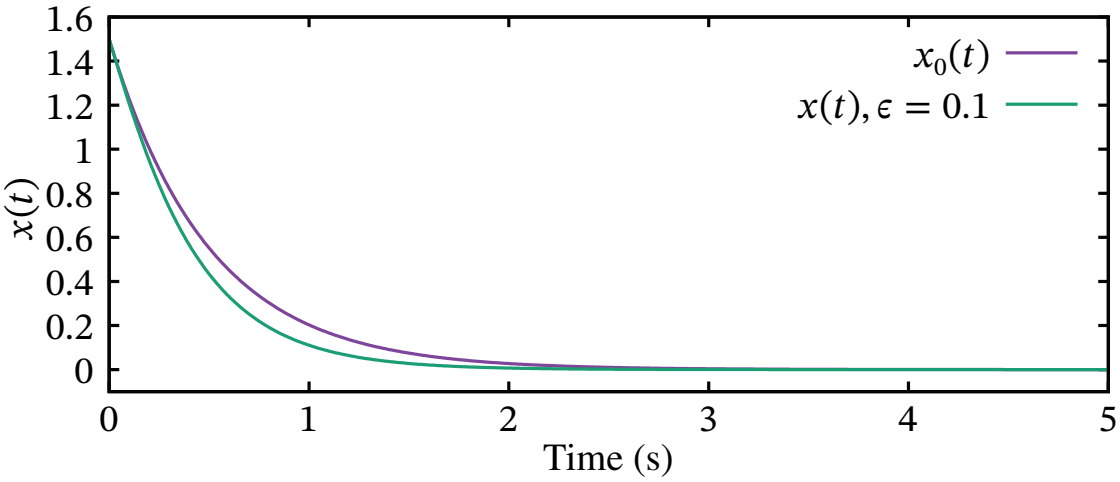

(a) when $x(0) = a = 1.5$ and $y(0) = b = -3.0$

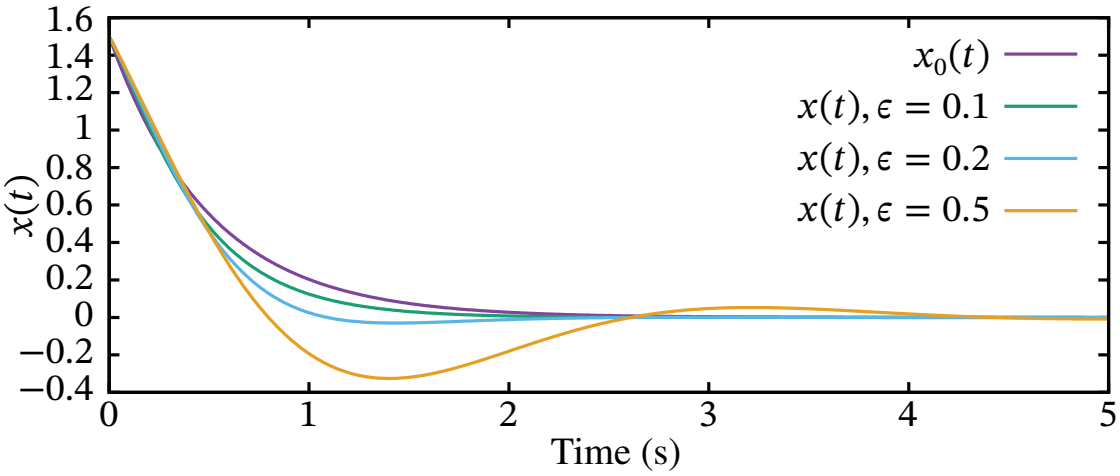

(b) when $x(0) = a = 1.5$ and $y(0) = b = -2.0$

Figure. 3.4.: Plots of the estimated and real solution ($x_0(t)$ and $x(t)$) to the example O.D.E. system for illustrating singular perturbation method.

In general, the singular perturbation method is not a mechanical process, where every step can be programmed. Still, it requires some basic insights into the mechanism and a bit of ingenuity in reformulating the original O.D.E. into a form that the perturbation term ϵ can be sufficiently small.

3.1.3. Tikhonov's Theorem

Tikhonov's theorem on dynamic systems characterizes the stability of the composite solution given by the singular perturbation theory and the error of approximation. The theorem shows that, for a disturbance ϵ sufficiently small, the singular perturbation method can indeed give a plausible approximation of the dynamic's solution under some stability and continuity conditions.

Consider a generic singular perturbation problem (3.9). The slow dynamic and outer approximation is given by setting $\epsilon \to 0$.

$$\dot{x}_1 = f_1(t, x_1, x_2, 0) \tag{3.27a}$$

$$0 = f_2(t, x_1, x_2, 0). \tag{3.27b}$$

Assume that the outer dynamic gives an *isolate* solution for $x_2(t)$

$$x_2(t) = h\big(t, x_1(t)\big), \tag{3.28}$$

Therefore, we can define an invariant manifold with

$$x_1(t) = h(t, x_2) \tag{3.29}$$

for all x_1 and x_2 in the spatial domain and $t \geq 0$ and a convex state domain $x_1 \in D_{x_1}$.

The difference between the real solution $x_2(t, \epsilon)$ for a nonzero ϵ and outer approximation $h(x_1)$ for $\epsilon = 0$ is approximated by the fast dynamics up to an error of $O(\epsilon)$ as long as f_1, f_2, and h satisfy some stability conditions given by *Tikhonov's theorem* [57]–[59].

Tikhonov's theorem *Consider the perturbation problem of form* (3.9) *and let* $x_2 = h(t, x_1)$ *be an isolated root of* (3.27). *For all*

$$\big(t, x_1, x_2 - h(t, x), \epsilon\big) \in [0, t_1] \times D_{x_1} \times D_{x_2} \times [0, \epsilon_0],$$

where $D_{x_1} \subset \mathbb{R}^n$ *is convex and* $D_{x_2} \subset \mathbb{R}^m$ *contains the origin* $x_2 = 0$, *assume the following conditions are met*:

1) *The first-order partial derivatives of* f_1 *w.r.t.* (x, z, ϵ) *are continuous. The first-order partial derivative of* f_2 *w.r.t. time* t *is continuous. First partial derivative of* h *w.r.t.* t *and* x *are also continuous.*

2) *The Jacobian* $\frac{\partial f_2(t,x_1,x_2,0)}{\partial x_2}$ *have continuous first partial derivative w.r.t.* t, x_1, *and* x_2.

3) *Initial conditions* $x_1(0) = \xi(\epsilon)$ *and* $x_2(0) = \eta(\epsilon)$ *are smooth function of* ϵ.

4) *The slow dynamics* (3.27) *has a unique solution* $\bar{x}_1(t) \in S$ *for* $t \in [t_0, t_1]$. *The* $S \subset D_{x_1}$ *is a compact subset.*

5) *The origin* $x_2 = 0$ *is an uniformly exponentially stable equilibrium point of*

$$\frac{\mathrm{d}y}{\mathrm{d}\tau} = f_2\big(t, x_1, y + h(t, x), 0\big),$$

uniformly on (t, x_1).

Let $\mathcal{R}_y \subset D_y$ *be the region of attraction of the following dynamics*

$$\frac{\mathrm{d}y(\tau)}{\mathrm{d}\tau} = f_2\left(t_0, x_1(0), y(\tau) + h\big(t_0, x(t_0)\big), 0\right) \quad y(0) = x_2(0) - h\big(0, x_1(0)\big),$$

and Ω_y *be a compact subset of* $\mathcal{R}_y$.

Then, there exists a positive constant ϵ^* *such that for all* $x_2(0) - x_1(1) = y(0) \in \Omega_y$ *and* $0 < \epsilon < \epsilon^*$, *the singular perturbation problem* (3.9) *has a unique solution* $x_1(t, \epsilon)$ *and* $x_2(t, \epsilon)$ *on* $[0, t_1]$, *and*

$$\begin{aligned} x_1(t, \epsilon) - \bar{x}_1(t) &= O(\epsilon) \\ x_2(t, \epsilon) - h\big(t, \bar{x}(t)\big) - \hat{x}_2(t) &= O(\epsilon), \end{aligned}$$

where $\hat{x}_1$ *is the solution approximation given with the singular perturbation method.* □

3.2. Inertia Response Estimate

The singular perturbation method is applied to the network-connected synchronous generators to separate the frequency response to fast and slow dynamic components. The *inertia dynamics* is defined to be the fast dynamic component because the physical or emulated system inertia

has more influence on the component of fast dynamic response than the slow dynamic component. Finally, a new metric is defined on the inertia dynamics for optimally planning the virtual inertia installation.

3.2.1. System Modelling

Modelling of electricity network

The large-scale power system can be viewed as composed of synchronous generators, transformers, and loads, linked together via intermediate devices/equipment, e.g., transmission lines, transformers.

The transformers and transmissions are often modelled one and represented by an equivalent admittance. The loads are modelled either as constant active and reactive power sink or as constant impedance. The result is a graph consisting of power sources or loads as the vertices and transformer or transmission lines as the edges. As an example, Figure. 5.1 shows a simplified Southeast Australian network consisting of 58 buses and a 14 synchronous generators. Kron reduction [39] (effectively a generalization of Y-Δ transformation formulated in matrix theory) can be applied to prune all buses where there is no generators or loads. The resulting power system network is referred to as *reduced network*.

Therefore, a large scale power system can be modelled mathematically as a weighted undirected graph $G = G(\mathcal{V}, \mathcal{E}, A)$. The vertex (node) set $\mathcal{V} = \{1, \dots, n\}$ models all the buses in the network. A vertex (or a node*) in $\mathcal{V}$ is either a synchronous generator, a converter-interfaced generator under *matching control* (c.f. Chapter 2), or a negative load impedance. The set of nodes of electricity generation is denoted $\mathcal{G} \subset \mathcal{V}$. Every edge in the edge set $\mathcal{E} = \{(i, j) \mid (i \times j \in \mathcal{V}^2) \wedge (Y_{ij} \neq 0)\}$ models either a transmission line or transformer, and each edge is associated with a edge weight equal to the admittance Y_{ij} between vertex i and j. Because the graph is undirectional, $(i, j) \in \mathcal{E} \Rightarrow (j, i) \in \mathcal{E}$. We denote A the graph's *adjacency matrix*, whose element at the cross of the i-th row and j-th column, $i \neq j$, is the (i, j)-edge's weight corresponding to the *effective conductance*

*The term *bus* is used more often in the context of power system; *node* is more used in electricity circuit, and *vertex* is predominately used in graph theory related study. With a slight misuse of terminology, a vertex or a node may also refer to the device behind the corresponding bus.

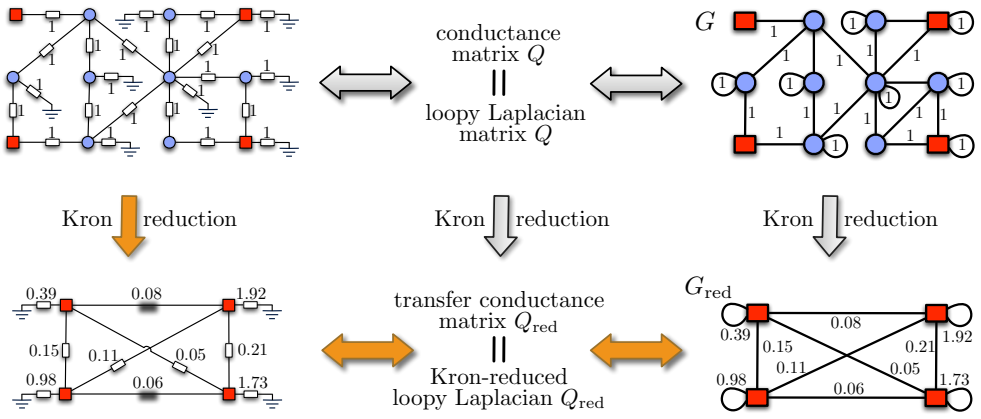

Figure. 3.5.: Illustration of electrical network reduction. The vertices (buses) are represented by either square ■ or ●. The four boundary vertices ■ are kept after Kron reduction; all other vertices ● are internal nodes and eliminated after Kron reduction [39].

between vertex i and j of the reduced network, obtained from the original system with Kron's reduction method. The diagonal elements of A are the self-loop weight at vertex i and model the internal impedance of a synchronous generator between its terminal and its internal voltage $E'_{q\,i}$ or the equivalent load impedance. The adjacency matrix A is symmetric for an un-directional graph and irreducible if the graph is connected, i.e., there is no islanding. The whole process of network modelling is summarized in Figure. 3.5.

On the reduced network, the *Laplacian matrix* L is defined as $L := \text{diag}\left(\left\{\sum_{j=1}^{n} A_{ij}\right\}_i\right) - A$. The *loopy Laplacian matrix* is defined as $Y := L + \text{diag}\left(\{A_{ii}\}_i\right)$. The loopy Laplacian matrix is also called *admittance matrix* in circuit theory. The element at the cross of the i-th row and j-th column models the *effective impedance* between vertex i and j.

Network-connected synchronous generators

After modelling the system loads as constant impedance and the network connection as a mathematical graph, the modelling of synchronous generators and CIGs units needs to be studied.

For the synchronous generator, only the swing equations, a.k.a., the first three equations

of (2.10), are considered for simplicity. The fielding flux ϕ_{fd} is assumed constant, so the transient internal q-axis potential $E'_{\text{q}} = \frac{L_{\text{ad}}}{L_{\text{ffd}}}\psi_{\text{fd}}$. All CIG units are assumed under the matching control and represented by the swing equation-like O.D.E. (2.12).

In non-islanding operation, the synchronous generators and CIG units are connected with each other via the reduced power network, and we can write the dynamics of CIG units and synchronous generators collectively in the following form:

$$M_i\ddot{\theta}_i + D_i\dot{\theta}_i = \Omega_i - \sum_{j=1}^{n} a_{ij}\sin(\theta_i - \theta_j - \phi_{ij}), \tag{3.30}$$

where the $\theta_i \in \mathbb{T}$ is the *angular position* relative to a reference frame rotating at synchronous speed $2\pi f_{\text{nominal}}$. If the i-th node is a CIG unit under grid-forming control, the *relative virtual angular position* is defined as

$$\theta_i(t) = \int_{t_0}^{t} \frac{v_{\text{dc}}(\tau) - v_{\text{dc}_{\text{nominal}}}}{v_{\text{dc}_{\text{nominal}}}} 2\pi\, f_{\text{nominal}}\, \mathrm{d}\tau, \tag{3.31}$$

where $\theta(t_0) = \left[\theta_1(t)\ \ldots\ \theta_N(t)\right]^\top$ is decided from the power flow computation at steady-state. The *phase shift* $\phi_{ij} := -\arctan\left(\frac{\mathfrak{Re}(Y_{ij})}{\mathfrak{Im}(Y_{ij})}\right)$ represents energy loss due to the effective conductance between node i and j. The $a_{ij} := E'_i E'_j |Y_{ij}|$ is the theoretic maximum active power transfer capability between node i and node j allowed by the power network. The $\Omega := P_{m_i} - E'^2_i\, \mathfrak{Re}(Y_{ii})$ is the real power injection of a generation unit at node i. In analogue to conventions related to studying network-connected oscillators [60], the term Ω_i is also referred *natural frequency*. The $M_i$and D_i are generator's inertia and damping factor respectively.

The system (3.31) is constructed upon the reduced system network and, therefore, gives no details on the network connection. Therefore, (3.31) is called *network-reduced power system models* [61] and is an example of *second order Kuramoto oscillators* [60]. The second-order Kuramoto oscillators have been studied in many contexts out of power system like in chemistry, neuroscience to Earth science [47], [62], which is an extension to the

classic *nonuniform Kuramoto Oscillators*:

$$D_i\dot{\theta}_i = \Omega_i - \sum_{j=1}^{n} a_{ij}\sin(\theta_i - \theta_j). \tag{3.32}$$

The similarity between the nonuniform (first-order) Kuramoto Oscillators and network reduced power system models have long been identified in the power system community and been used for stability assessment [63] and was used to define potential energy $U(\theta)$:

$$U(\theta) = -\sum_{i=i}^{n}\left(\Omega_i\theta_i + \sum_{\substack{i=i\\ j<i}}^{n} a_{ij}\big(1-\cos(\theta_i-\theta_j)\big)\right), \tag{3.33}$$

which is very helpful in using Lyapunov's method to assess the stability of the power system. Neglecting the transmission losses, the network-reduced power system model is the gradient flow of $U(\theta)$ [61], [63],

$$\dot{\theta} = -\nabla U(\theta)^{\top}. \tag{3.34}$$

The renowned PEBS [64] uses the separatrices of (3.32) of (3.33), calculated as the stable manifold of an unstable fixed point of (3.32), and some transversality conditions to assess the stability at a certain system state. Because of the topological similarity between (3.32) and (3.30), many conclusions made for nonuniform Kuramoto system (3.32) can be extended for the original dynamics (3.30).

Finally, without giving rigorous proof, we would like to make some remarks regarding the nonuniform Kuramoto system (3.32) and network reduced power system modelling (3.30):

1) For a small phase shift term, the stability of nonuniform Kuramoto model (3.32) implies the stability of the network reduced power system (3.30). That is to say, the size of system inertia *does not* alter the system's stability. The stability refers to the system's capability of returning to a stable equilibrium after a disturbance without considering how the system behaves in the transient from the old to the new states.

2) However, increasing system inertia may improve the system's dynamics in terms of more smooth transient into a new steady-state. As discussed and demonstrated in

Chapter 3 and Figure. 3.4 for the simplified swing equations, an exceedingly large rotational inertia may reduce the damping ratio, increase settling time. But, at the same time, increasing system inertia can reduce the frequency nadir and RoCoF. Therefore, from the mathematical point of view, there is no rigorous standard to compare how the dynamic is better.

It will be shown that slow dynamic given by the separation of the singular perturbation method equals to the model of nonuniform Kuramoto Oscillator(3.32).

3.2.2. The Inertia Response

The singular perturbation technique on the network-reduced power system (3.30) gives a separation of fast and slow dynamic components. Figure. 1.1 shows the frequency response exhibits different characteristics in the time-scale separation, where system inertia has a direct influence on the fastest dynamic response. Based on this observation, the *inertia response* is defined to be the fastest response component of the frequency response. This subsection applies the singular perturbation technique to the network-reduced power system and defines the inertia response mathematically.

Assumption of strong over-dampness

The difficulty of singular perturbation technique lies in finding a suitable perturbation term ϵ and formulating the system in a standard perturbation form (3.9). The choice of ϵ was given in [61], which is based on the assumption of *strong over-dampness*.

Though synchronous generators' damping coefficient D_i is small, which is commonly less than 3 s, the inclusion of other mechanisms like the power system stabilizer and the automatic voltage regulator greatly increases the effective value of D_i. The value of D reaches around $10-35$ s [65]. The same assumption has been adopted in many classical studies of power system stability [63], [64].

Singular perturbation analysis

The analysis was first given by Prof. Döfler in [61]. The main steps is summarized in following paragraphs.

Consider a power system $G(\mathcal{V}, \mathcal{E}, A)$, and assume that all system loads are modelled as constant impedance. Kron reduction technique helps prune all intermediate buses to obtain a network-reduced power system as represented by a graph $\tilde{G}(\mathcal{V}, \mathcal{E}, A)$. The vertex set $\mathcal{V} = \{1, \dots, n\}$ is a representation of synchronous generators and CIG units.

Because the states of the network-reduced power system model (3.30) are in n-dimensional torus $\theta = \left[\theta_1, \dots, \theta_n\right]^\top \in \mathbb{T}^n$ rather than Euclidean space. A smooth map, named *ground map* and denoted as grnd, is defined to map the states in torus to Euclidean space so that the singular perturbation technique can be applied. The grnd is defined as follows.

$$\begin{aligned} \text{grnd} : \Delta(\gamma) \to \Delta_{\text{grnd}}(\gamma) := \left\{ \theta_i - \theta_n \in \mathbb{R}^{n-1} : \max_{i,j} |\theta_i - \theta_n| < \gamma, \quad i, j \in \{1, \dots, n-1\} \right\} \\ \theta_i \mapsto \theta_i - \theta_n, \end{aligned} \tag{3.35}$$

where $\Delta(\gamma) := \left\{ [\theta_1, \dots, \theta_n]^\top : \max_{i,j \in \{1,\dots,n\}} |\theta_i - \theta_j| < \gamma \right\}$. In fact, the ground map `grnd` is nothing more than a mathematical expression of the common engineering practice of selecting a reference generator.

Applying the ground map on the network-reduced power system (3.30) reformulates it into the *grounded network-reduced power system*

$$\begin{aligned} M_i \ddot{\delta}_i + D_i \dot{\delta}_i = \Omega_i - \Omega_n - \sum_{\substack{j \in \mathcal{E}[i] \\ j \neq n}} \frac{a_{ij}}{D_i} \sin(\delta_i - \delta_j - \phi_{ij}) + \frac{a_{nj}}{D_n} \sin(\delta_n + \phi_{jn}) \\ - \frac{a_{ij}}{D_i} \sin(\delta_i - \phi_{in}) - \frac{a_{in}}{D_n} \sin(\delta_i + \phi_{in}), \end{aligned} \tag{3.36}$$

and its initial conditions become $\delta(0) = \text{grnd}\big(\theta(0)\big)$.

The ground map translate the nonuniform Kuramoto Oscillators (3.32) into a *grounded*

nonuniform Kuramoto Oscillators

$$\begin{aligned}\dot{\delta}_i = \frac{\Omega_i}{D_i} - \frac{\Omega_n}{D_n} - \sum_{\substack{j \in \mathcal{E}[i] \\ j \neq n}} \frac{a_{ij}}{D_i}\sin(\delta_i - \delta_j - \phi_{ij}) + \frac{a_{nj}}{D_n}\sin(\delta_n + \phi_{jn}) \\ - \frac{a_{ij}}{D_i}\sin(\delta_i - \phi_{in}) - \frac{a_{in}}{D_n}\sin(\delta_i + \phi_{in}) \qquad i = 1, \dots, n-1,\end{aligned} \tag{3.37}$$

with its initial conditions $\delta(0) = \mathrm{grnd}\big(\theta(0)\big)$.

Under the *phase cohesiveness* assumption [61, Lemma 3.1], it can be proved that, if $\theta(t)$ is a solution to network-reduced power system (3.30) or non-uniform Kuramoto oscillator system (3.32), the $\delta(t) = \mathrm{grnd}\big(\theta(t)\big)$ is also a solution to the grounded network-reduced power system (3.37) or the grounded non-uniform Kuramato oscillator systems, respectively.

Finally, rewrite the grounded network-reduced power system (3.36) in form of vector fields,

$$\dot{\delta}_i = f_i(\dot{\theta}) := \dot{\theta}_i - \dot{\theta}_n \qquad i = 1, \dots, n-1 \tag{3.38a}$$

$$\ddot{\theta}_i = g_i(\delta, \dot{\theta}) := -\frac{D_i}{M_i}\dot{\theta}_i + \frac{1}{M_i}\left(\Omega_i - \sum_{j \in \mathcal{E}[i]} a_{ij}\sin(\delta_i - \delta_j - \phi_{ij})\right) \qquad 1 = 1, \dots, n. \tag{3.38b}$$

Define the perturbations term as

$$\epsilon := \frac{\max_i M_i}{\min_i D_i}. \tag{3.39}$$

Because of the assumption of strong over-dampness, the size of the perturbation term ϵ is shown to be sufficiently small so that the singular perturbation technique can be safely applied. With this choice of ϵ (3.39), the grounded the network-reduced power system (3.38) can be expressed in the standard perturbation form (3.9):

$$\dot{\delta}_i = f_i(\dot{\theta}) := \dot{\theta}_i - \dot{\theta}_n \qquad i = 1, \dots, n-1 \tag{3.40a}$$

$$\epsilon\ddot{\theta}_i = \epsilon g_i(\delta, \dot{\theta}) = -F_i\dot{\theta}_i + \frac{F_i}{D_i}\left(\Omega_i - \sum_{j \in \mathcal{E}[i]} \sin(\delta_i - \delta_j - \phi_{ij})\right) \qquad 1 = 1, \dots, n, \tag{3.40b}$$

where $F_i = \frac{D_i}{D_{\min}} \frac{M_{\max}}{M_i}$ is a $O(1)$ term.

The singular perturbation technique can then be applied to (3.40) in a way similar to that for the simplified swing equations (3.3). By setting perturbation term to zero, $\epsilon = 0$, the slow dynamics is obtained as:

$$\dot{\delta}_i = \dot{\theta}_i - \dot{\theta}_n \qquad i = 1, \dots, n-1 \tag{3.41a}$$

$$D_i \dot{\theta}_i = \Omega_i - \sum_{j \in \mathcal{E}[i]} a_{ij} \sin(\delta_i - \delta_j - \phi_{ij}) \qquad 1 = 1, \dots, n, \tag{3.41b}$$

which turns out to be exactly the nonuniform Kuramoto system (3.33). Denote $\bar{\delta}_i(t)$ its solution and solve for $\dot{\theta}_i$ in terms of $\bar{\delta}_i$,

$$\dot{\theta}_i(t) = h\big(\bar{\delta}(t)\big). \tag{3.42}$$

Because (3.41) is autonomous, function h here is independent of time t. Finally, Tikhonov theorem can immediately give the following conclusion [61, Theorem 3.2].

Theorem (singular perturbation approximation) *Assume the nonuniform Kuramoto system is uniformly exponentially stable with an equilibrium* $(\delta_\infty, 0)$*, and the initial condition* $\delta(0)$ *is in a compact subset* Ω_δ *of region of attraction of the dynamic system* (3.41)*. Denote the solution to* (3.36) *as* $\big(\delta(t,\epsilon), \dot{\theta}(t,\epsilon)\big)$.

1) $\exists \epsilon_* > 0$ *such that* $\forall \epsilon < \epsilon_*$*, the grounded network reduced system* (3.36) *has a unique solution* $\big(\delta(t,\epsilon), \dot{\theta}(t,\epsilon)\big)$ *for all* $t \geq 0$*. Furthermore,*

$$\delta_i(t,\epsilon) - \bar{\delta}_i(t) = O(\epsilon), \qquad \dot{\theta}_i(t) - h\big(\bar{\delta(t)}\big) - y_i\left(\frac{t}{\epsilon}\right) = O(\epsilon), \tag{3.43}$$

where $y\left(\frac{t}{\epsilon}\right)$ *is the solution of fast approximation* (*c.f., page* 68).

2) $\forall t_b > 0$*,* $\exists \epsilon^* < \epsilon_*$ *such that for all* $t > t_b$ *and whenever* $\epsilon < \epsilon^*$*, it holds uniformly that*

$$\dot{\theta}(t,\epsilon) - h\big(\bar{\delta}(t)\big) = O(\epsilon). \tag{3.44}$$

3) *Furthermore, if* ϵ *and* $\max_{(i,j)\in\mathcal{E}} \phi_{ij}$ *are sufficiently small, then all error terms* (3.43) *and* (3.44) *converges exponentially to zeros as* $t \to \infty$. □

Definition of inertia response

Now, the singular perturbation technique helped separate the grounded network-reduced power system into slow and fast dynamic components. The system inertia M does not present on the O.D.E.s of the slow dynamics (3.41), from which it can be deduced that the system inertia has much sway over the fast dynamic component rather than the slow dynamic. The influence of system inertia on the slow dynamic is negligible up to a scale of $\epsilon = \frac{\max_i M_i}{\min_i D_i}$.

Therefore, it is safe to defined the *inertia response* to be the fast dynamic $y_i\left(\frac{t}{\epsilon}\right)$. The derivation of the fast dynamic is similar to the three step process on Page 68 to Page 73, except that the term of $k X_0$ in the simplified swing dynamics (3.15) is replaced with a more complicated sinusoidal summation $\frac{F_i}{D_i} \sum_{j\in\mathcal{E}[i]} a_{ij} \sin(\delta_i - \delta_j - \phi_{ij})$:

$$\epsilon^{1-2\alpha} \frac{\mathrm{d}^2\hat{\theta}}{\mathrm{d}\bar{t}^2} = -\epsilon^{-\alpha} F_i \frac{\mathrm{d}\hat{\theta}}{\mathrm{d}\bar{t}} - \frac{F_i}{D_i} \sum_{j\in\mathcal{E}[i]} a_{ij} \sin\big(\hat{\delta}_i - \hat{\delta}_j - \phi_{ij}\big). \tag{3.45}$$

As discussed previously, $\alpha = -1$ is the only sensible choice. The balancing equality (3.45) becomes

$$\begin{aligned} \epsilon^{-1} \frac{\mathrm{d}^2\hat{\theta}}{\mathrm{d}\bar{t}^2} &= -\epsilon^{-1} F_i \frac{\mathrm{d}\hat{\delta}}{\mathrm{d}\bar{t}} - \frac{F_i}{D_i} \sum_{j\in\mathcal{E}[i]} a_{ij} \sin\big(\hat{\delta}_i - \hat{\delta}_j - \phi_{ij}\big). \\ \Rightarrow \qquad \frac{\mathrm{d}^2\hat{\theta}}{\mathrm{d}\bar{t}^2} &= -F_i \frac{\mathrm{d}\hat{\delta}}{\mathrm{d}\bar{t}} - \epsilon \frac{F_i}{D_i} \sum_{j\in\mathcal{E}[i]} a_{ij} \sin\big(\hat{\delta}_i - \hat{\delta}_j - \phi_{ij}\big), \end{aligned} \tag{3.46}$$

where $\hat{\delta}(\bar{t}) = \hat{\delta}(\epsilon^\alpha t)$.

Further simplification on (3.46) can be achieved by observing that coefficient for the sinusoidal term $\epsilon\frac{F_i}{D_i}$, where $F_i = \frac{D_i}{D_{\min}} \frac{M_{\max}}{M_i}$ is a $O(1)$ term, and $D_i \gg F_i$. Therefore, the sinusoidal term is an $o(1)$ term. Note $\frac{\mathrm{d}\hat{\theta}}{\mathrm{d}\bar{t}} = \frac{\mathrm{d}\hat{\delta}}{\mathrm{d}\bar{t}}$, the fast dynamics can be conveniently estimated from (3.46) on the $O(1)$ level:

$$\frac{\mathrm{d}^2}{\mathrm{d}\bar{t}^2} \hat{\delta}_i(\bar{t}) = -F_i \frac{\mathrm{d}}{\mathrm{d}\bar{t}} \hat{\delta}_i(\bar{t}) \tag{3.47}$$

with initial condition $\frac{\mathrm{d}}{\mathrm{d}\bar{t}}\hat{\delta}(0) = \epsilon^{-1}\Big(\dot{\theta}(t) - h_i\big(\bar{\theta}(0)\big)\Big)$. Then, the resulting system (3.47) is defined as the the inertia response estimation. It is obvious that (3.47) is a linear system.

Therefore, the solution to (3.47) is,

$$\frac{\mathrm{d}}{\mathrm{d}\bar{t}}\hat{\delta}_i(\bar{t}) = \epsilon^{-1}\left(\dot{\theta}(0) - h_i\big(\bar{\theta}(0)\big)\right)e^{-F_i\bar{t}}, \tag{3.48}$$

which is formulated on the diluted time scale. On the real time scale, i.e., $\bar{t} = \epsilon^{-1}t$, it becomes

$$\dot{\delta}(t) = \left(\dot{\theta}_i(0_+) - h_i\big(\theta(0)\big)\right)e^{-\frac{F_i}{\epsilon}t}, \tag{3.49}$$

where h_i is the solution to the associated nonuniform Kuramoto system (3.37).

3.2.3. Measuring Inertia Response

Like all dynamics system, the estimated inertia response is determined by both the vector field (3.47) and initial conditions $\dot{\theta}_i(0) - h_i\big(\delta(0)\big)$. Parameters F_i and ϵ are deterministic and are associated with the given power system on a given operating condition immediately after fault occurrence. That is say the initial conditions for the dynamic of inertia response are fault-specific. Therefore, fault modelling will be the first topic to be discussed in this subsection. It will be shown that simulation-based method is used to model a system fault and give an initial condition for the inertia response (3.47).

A proper fault model and simulation-based program routine give a value for $\dot{\theta}(0_+)$ for a specific fault.

On the other side, the flow[†] h of the nonuniform Kuramoto model is hard to obtain. Fortunately, we need only $h(t)$ evaluated at $t = 0_+$ to obtain the inertia response. It turns out that $h(0)$ can also be solved on the basis of power flow computation and the initialization step of dynamics simulation.

Finally, a new metric is proposed based on the inertia response estimate. Compared with the synchronization measurement [19] based on the classical observability measurement for the nonuniform Kuramoto oscillators, the proposed metric is defined on the fast dynamic of inertia response, and therefore, it is a better metric of quantifying the influence of system inertia on the frequency response. Due to its simplicity, it can be efficiently incorporated

[†]*flow* is a collection of solutions to a O.E.D. problem with all initial states $x_0 \in D_X$

into the optimization problem formulation.

Fault Models

Consider a power system operating in a steady condition prior to $t = 0$ s when a system fault occurs. The fault may change the system current and triggers relay actuation, resulting in changes of the O.D.E.s of the vector field and effectively altering the system states.

The physical principles dictate that all physical states cannot be altered in a snap. However, the grounded network-reduced power system, arising from the swing equation, is not a complete physical description of the physics. The electromagnetic dynamics are neglected. Therefore, the system faults are modelled as Dirac impulses of limited energy in [17]. The effect of Dirac impulses on the dynamic system is equivalent to a jump at the system states, i.e., $x(0_+) \neq x(0_-)$. Alternatively, system fault is modelled as a step impulses.

Classic fault modelling In [17], the model of system fault is an additional term Δp_{in_o} in

$$\dot{\delta}_i = \dot{\theta}_i - \dot{\theta}_n \tag{3.50a}$$

$$M_i \ddot{\delta}_i = -D_i \dot{\theta} + \left(\Omega_i - \sum_{j \in \mathcal{E}[i]} \frac{a_{ij}}{D_i} \sin(\delta_i - \delta_j - \phi_{ij}) \right) + \Delta p_{\text{in}_i}. \tag{3.50b}$$

The Δp_{in_i} models the amount of active power imbalance seen at the terminal of generation units:

$$\begin{aligned} \Delta p_{\text{in}} = \left[\Delta p_{\text{in}_1}, \dots, \Delta p_{\text{in}_n}\right]^\top &= \text{diag}\left(\left[v_{i1}^{\frac{1}{2}}, \dots, v_{in}^{\frac{1}{2}} \right]^\top \right) \left[\eta_1, \dots, \eta_n\right]^\top \\ &= V^{\frac{1}{2}} \eta, \end{aligned} \tag{3.51}$$

where v_{ij} models both the occurrence probability of the j-th system fault and the size of the impact of the j-th fault on the i-th synchronous generator or CIG unit under matching control. The value for v_{ij} is obtained from records of historical faults or simulations. The η_i's are either a unit Dirac function or unit step function.

This kind of fault modelling method has long been used in many power system stability-

related studies [17], [19], [44]. However, a system fault might not only result in changes of active power balance at the terminals of generation units but also changes in system settings, e.g., grid connections, loading levels. The changes of system settings alter the grid topology $G(\mathcal{V}, \mathcal{E}, A)$ and consequently the effective admittance between generator i and j. Therefore, this method cannot be applied on a wide range of fault scenarios.

Simulation based fault modelling Instead, another scheme of fault modelling is proposed based on the dynamic simulation. A set of initial conditions for system states, $x(0_+)$ is then derived in the context of updated system settings (system admittance, grid connections, etc.). The scheme is based on the following assumptions at $t = 0$:

1) Electromagnetic states and parameters of the grid network can be changed instantaneously. But the the generator's fielding flux are assumed remaining constant.

2) Relay switches' status can also be changed instantaneously (neglecting the time for relays to actuate and for the electricity breaker to be engaged/disengaged).

3) Mechanical parameters and states cannot be changed instantaneously, except for the state of RoCoF $\dot{\omega} = \ddot{\delta}$.

The first assumption arises from the negligence of electromagnetic dynamic. The constant fielding flux is inherent from classic dynamic modelling of synchronous generator; higher orders of flux dynamics are neglected in the following analysis but as well considered in the time-domain simulation of the case studies in Chapter 5.

The second assumption is based on the rapid speed of the power system's protection system. The switch-induced transient current and voltage of the grid network are also neglected.

The third assumption is due to the physical limitation. The exception for state of RoCoF $\ddot{\theta}(0_-) \neq \ddot{\theta}(0_+)$ is attributed to the change on the balance of the electrical-mechanical torque brought by a system fault. In contrast, the Dirac function in (3.50) in classical modelling of system faults implies a jump in the $\dot{\delta}(t)$ at $t = 0$, which is not reasonable.

Under these assumptions, the impact of faults on the system states and status can be computed with the following steps:

1) Compute power flow on the pre-fault conditions and get initial states for the synchronous generators. Register the active power output of generators $P_{e_i}(0_-) \leftarrow P_{\mathrm{e}_i}$. Initialize and

register synchronous generators' dynamic states and parameters, especially generators' transient emf E'_{q_i} and generators' mechanical inputs $P_{\mathrm{m}_i}(0_-)$.

2) If the considered fault alters power grid topology, the admittance matrix Y is recomputed with the new value grid topology.

3) Solve for the the reduced power system network using Kron's reduction method (see page 78 and [39]), and compute the reduced network's impedance matrix Y_{red}.

4) Compute each generator's electric power injection, $P_{\mathrm{e}_i}(0_-) \leftarrow \mathfrak{Re}\{VV^*Y^*\}$.

In the process, generators' mechanical power inputs and electrical power outputs are registered, which will be used later for initializing $h(\delta(0_+))$.

Initialization of Inertia Dynamics

Prior to a fault occurrence, it assumed that the power system is running at steady-state $\dot{x} = f_-(x) = 0$, at which the active power generation and consumption are balanced. The fault occurrence, along with the ensuing relay operation and electromagnetic dynamic transient, alters the vector field:

$$\dot{x} = f(x) = \begin{cases} f_-(x) & \text{for } t < 0 \\ f_+(x) & \text{for } t \geq 0. \end{cases}$$

The interest of frequency stability study focuses on $t \geq 0$, and the initialization process therefore includes:

1) deciding the new vector field $f_+(x)$,

2) determining the initial system states $x(0)$ at a $t = 0$, and

3) finding the solution $h\big(x(t)\big)$ to the slow dynamic at $t = 0$.

The computation for the vector field has been covered above in the simulation-based fault modulation. The remaining part is the initialization of the solution $h\big(x(t)\big)$ of slow dynamic (3.41). Unlike the network-reduced power system, the slow dynamic lacks the second order term $M\ddot{\theta}$. Therefore, the rotational speed $\omega(t)$ is allowed to jump at $t = 0$.

The process is similar to that for computing the changes in the system states and parameters caused by a system fault, except

1) Angular velocity $\dot{\theta}$ is allowed to assume a different value at $t = 0_+$.
2) The Kuramoto oscillators are also assumed having the same fielding flux, i.e., the fictitious transient EMF E'_q.
3) All (physical and fictitious) Kuramoto oscillators' parameters are set the same value as for synchronous generators before and immediately after the fault ($t = 0_+$).
4) Finally, $\dot{\theta}(0_+)$ is obtained by solving

$$\begin{aligned} D_i\dot{\theta}_i(0_+) &= \Delta P_{\mathrm{m}i} - \Delta P_{\mathrm{e}i} \\ &= \big(P_{\mathrm{m}i}(0_-) - P_{\mathrm{m}i}(0_+)\big) - \big(P_{\mathrm{e}i}(0_-) - P_{\mathrm{e}i}(0_+)\big) \end{aligned}$$

in per-unit with the post-fault mechanical power $P_{\mathrm{m}i}(0_+)$ and electrical power $P_{\mathrm{e}i}(0_+)$ obtained from power flow computation.

Metric of System Inertia Response

After the initialization steps of the network-reduced power system (3.38) and the slow dynamic, the fast dynamic of inertia dynamic (3.47) is also naturally initialized with initial conditions:

$$\hat{\delta}_i(0) = \dot{\theta}_i(0_+) - h_i\big(\theta(0_+)\big).$$

To quantitatively measure and compare inertia responses, a metric m_i is defined based on

the $\mathcal{L}_2[0,\infty[$ integral of the inertia dynamic response:

$$\begin{aligned} m_i &:= \left(\int_0^\infty \dot{\hat{\delta}}(t)^2 \, \mathrm{d}t \right)^{\frac{1}{2}} \\ &= \left(\int_0^\infty \left| \left(\dot{\theta}_i(0_+) - h_i\big(\theta(0_+)\big) \right) e^{-\frac{F_i}{\epsilon} t} \right|^2 \, \mathrm{d}t \right)^{\frac{1}{2}}, \end{aligned} \tag{3.52}$$

where $\hat{\delta}(t)$ is the flow of the inertia dynamics (3.47). If the considered power system regains stability after the considered fault, the inertia response will be asymptotically stable at $\hat{\delta} = 0$, and the metric is well defined.

Usually, a large power system consists of several coherent groups. The electric components are more closely connected within each group than between different coherent groups. The generators of the same subsystem usually exhibit similar responses in a system transient. The COI quantities are often used to characterize the collective behaviour of a coherent group. In study of the frequency response, the COI frequency is used to characterize the common behaviour of generators' rotational speeds in a coherent group:

$$\dot{\theta}_{\mathrm{COI}} = \frac{1}{\sum_{i=1}^n m_i} \sum_{i=1}^n m_i \, \dot{\theta}_i. \tag{3.53}$$

Furthermore, the COI frequency $\dot{\theta}_{\mathrm{COI}}$ is better than a single generator's rotational speed in measuring the power frequency quality, because the frequency measurement at a location is decided by the rotational speed of nearby generators and the electricity distances from these generators [66].

The metric of inertia response can be extended to a whole coherent area. Assume the coherent area is represented as a sub-graph $\mathcal{A}_i(\mathcal{V}_i, \mathcal{E}_i, A_i)$ of the reduced power network $\tilde{G}(\mathcal{V}, \mathcal{E}, A)$. The vertex set $\mathcal{V}_i$ is composed of synchronous generators in a coherent group, e.g., Area I–IV in Figure. 5.1. The set $\mathcal{A}_i(\mathcal{V}_i, \mathcal{E}_i, A_i)$ is the spanning sub-graph of $\tilde{G}(\mathcal{V}, \mathcal{E}, A)$ induced by the node subset $\mathcal{V}_i \subset \mathcal{V}$. The COI version of inertia response measurement $f_{m_{\mathcal{A}_i}}$

is defined analogously on the COI frequency (3.53),

$$
\begin{aligned}
f_{m_{\mathcal{A}_i}} &:= \left(\int_0^\infty \hat{\dot{\delta}}^2_{\mathrm{COI}}(t)\,\mathrm{d}t \right)^{\frac{1}{2}} = \left(\int_0^\infty \left(\frac{1}{\sum_{k\in\mathcal{A}_i} m_k} \sum_{k\in\mathcal{A}_i} m_k \hat{\dot{\delta}}_k(t) \right)^2 \mathrm{d}t \right)^{\frac{1}{2}} \\
&= \langle \mathbb{1}, m_{\mathcal{A}_i} \rangle^{-1} \left(\int_0^\infty \left(\left[m_{k_1} \hat{\dot{\delta}}_{k_1}(t), \dots, m_{k_{\mathrm{m}}} \hat{\dot{\delta}}_{k_{\mathrm{m}}}(t) \right] \mathbb{1}^\top \mathbb{1} \begin{bmatrix} m_{k_1} \hat{\dot{\delta}}_{k_1}(t) \\ \vdots \\ m_{k_{\mathrm{m}}} \hat{\dot{\delta}}_{k_{\mathrm{m}}}(t) \end{bmatrix} \right) \mathrm{d}t \right)^{\frac{1}{2}} \\
&= \langle \mathbb{1}, m_{\mathcal{A}_i} \rangle^{-1} \left(\left[\left| \dot{\delta}_{k_1}(0_+) - h_{k_1}\big(\delta_{k_1}(0_+)\big) \right|_{F_{k_1}}^{\epsilon}, \dots, \left| \dot{\delta}_{k_{\mathrm{m}}}(0_+) - h\big(\delta_{k_{\mathrm{m}}}(0_+)\big) \right|_{F_{k_{\mathrm{m}}}}^{\epsilon} \right] \mathbb{1}\mathbb{1}^\top \right. \\
&\qquad \left. \begin{bmatrix} \left| \dot{\delta}_{k_1}(0_+) - h\big(\delta_{k_1}(0_+)\big) \right|_{F_{k_1}}^{\epsilon} \\ \vdots \\ \left| \dot{\delta}_{k_{\mathrm{m}}}(0_+) - h\big(\delta_{k_{\mathrm{m}}}(0_+)\big) \right|_{F_{k_{\mathrm{m}}}}^{\epsilon} \end{bmatrix} \right)^{\frac{1}{2}},
\end{aligned}
\tag{3.54}
$$

where $m_{\mathcal{A}_i}$ is a vector of physical or virtual rotational masses of the generators in subarea $\mathcal{A}_i$, and $\hat{\dot{\delta}}_{\mathcal{A}_i}$ is a vector of generator's fast dynamic states.

Finally, the whole process from fault-based state initialization to metric evaluation can be summarized in Algorithm 3.1.

Algorithm 3.1.: Formulating the metric $f_{\text{a}i}$.

Given the system fault, the Algorithm aims to obtain $y(t_{0_+})$ base on the specified fault and the current power system configuration.

procedure GETMETRIC(Fault$_i$) ▷ Fault$_i$ is a data structure consisting of fault type, the fault size, etc.

Power flow computation on original system
Register active power generation $P_{e_i}(t_{0\_}) \leftarrow P_{e_i}$
for $i \in \mathcal{G}$ **do** ▷ $\mathcal{G}$ denotes all synchronous generators and CIG units with matching controls.

Register mechanical power $P_{m_i}(t_{0\_}) \leftarrow P_{m_i}$
end for
if Fault$_i$ changes network topology **then**
Recompute Y_{ij}
end if
Adjust the PQ and PV nodes according to the fault
Recompute *Power Flow*
Register generators' active power injection as $P_{e_i}(t_{0_+})$
if Fault$_i$ involves generator fault **then**
Set new mechanical power $P_{m_i}(t_{0_+})$
end if
Compute $y_i(0) \leftarrow \frac{1}{D_i}\left(P_{m_i}(t_{0_+}) - P_{m_i}(t_{0\_}) - P_{e_i}(0_+) + P_{e_i}(0\_)\right)$
Compute f_i according to (3.52) and $f_{m_{\mathcal{A}_i}}$ according to (3.54) ▷ $y_i(0)$ equals $\dot{\theta}(0_+) - h(\delta(0_+))$
return f_i and $f_{m_{\mathcal{A}_i}}$
end procedure

Chapter 4

The Problem of Planning Virtual Inertia Installation

In the previous chapter, we have discussed fault modelling techniques and developed a metric for measuring how rotational inertia may influence the frequency response. Chapter 2 shows that matching control helps emulate the inertia response on a CIG unit. The maximum amount of emulated inertia that can be emulated at a CIG unit is related to the size of the DC coupling capacitor and/or the external energy storage. More virtual inertia in the power system means more significant investment in the energy storage system, sensors, controllers, and other expenses like the construction expenses related to substation expansion. But optimally planning virtual inertia installation at some key locations, the amount of investment is reduced while achieving the same or better level of frequency response.

By taking advantage of the newly proposed metric of inertia response, this chapter formulates the search for an optimal virtual inertia investment in a mathematical optimization problem. This optimization problem is of mixed-integer, non-convex, and non-linear type. Two solution techniques are proposed to effectively find a solution to the problem. One method is based on dynamic programming, and the other method takes advantage of the MM (Majorize-Minimization or Minorize-Maximization) technique [67], [68].

Since the proposed metric of inertia response depends on a specific fault and working condition, every possible combination of working conditions and fault scenarios shall be considered when forming the optimization problem. The *stability scanning framework* [41] ensures that all combinations of working conditions and fault scenarios are traversed.

Finally, a cloud-based computation framework is proposed. The data-level parallelism is used to tackle the immense computation of the time-domain simulation in the stability scanning framework and the solving of the optimization problem. The cloud-based computation framework leverages the great computational resources in the Microsoft Azure platform to enable large-scale parallelism. The solver of the optimization problem is developed in C++ language to gain the fastest solution speed, and the solver is packaged as a python module for greater integration with the cloud computation framework.

4.1. The Optimization Model

4.1.1. Assumptions

Before delving into the mathematical formulation, the following are assumed:

1) The matching control or other grid-forming type methods are used to emulate virtual inertia at CIG units.

2) Damping coefficients D_i in (3.36) are sized prior to determining the system inertia. The choice of D_i considers both the required amount of Primary Frequency Control Reserve and the "synchronization strength" to ensure stability of system's frequency response.

3) The TSO is assumed responsible for investing in or subsidizing the virtual inertia installation.

For the first assumption, as discussed in Chapter 2, the grid-forming type of inertia emulation techniques does not depend on the external mechanisms for synchronization, e.g., PLL, and, therefore, is capable of providing true virtual inertia emulation. The grid-following type of virtual inertia emulation, on the other hand, requires a strong power frequency reference. Hence, it cannot be used in a weak power system with a high penetration level of renewable generation. For this reason, only the matching control and other grid-forming types of virtual inertia emulation are invested.

The second assumption is made to simplify the inertia planning problem. The power system's frequency dynamics are predominately influenced by two factors D_i and M_i. The

damping coefficient D_i participates in both the fast dynamic of inertia response (3.47) and the slower dynamic of primary frequency control. But, the inertia term M only participates in the fast dynamic (inertia response). An appropriate selection of the damping coefficients D_i makes the system stable * [61], [64], whereas appropriate virtual and physical inertia distribution in the power network makes a smoother response of system frequency. Hence, the second assumption is justified.

Finally, the TSO is assumed responsible for the virtual inertia installation by either directly providing or subsidizing the cost of investment in the last assumption. More complicated scenarios, e.g., a smart grid disconnected from the main power grid, are not considered.

4.1.2. The Mathematical Model

Given a power system with a high level of renewable installation, the problem considered here is to find an optimal plan of virtual inertia installation (including the locations and the size of virtual inertia installations) in the power system to achieve a satisfactory level of performance of system frequency response. In this subsection, this objective is translated into a mathematical problem.

The investment cost is taken as the optimization objective. The constraints of the optimization problem consider the physical limits of virtual inertia installation modelled as box constraints, and the requirement on the performance improvement of frequency response is formulated as constraints with the proposed metric of inertia response.

Scenario Generations

As discussed above, the metric of inertia response is fault and operating condition-specified. Therefore, a framework is required to scan all possible combinations of operating and fault conditions; the performance improvement constraints of frequency response are formulated on those *boundary cases* where the worst frequency responses can occur. Furthermore, the constraints are area-wise, in that the metric of inertia response is formulated for each coherent area. The operating conditions are decided by the system loading and the amount of renewable generation being dispatched. The relations of the fault and operating conditions

*This stability refers to the asymptotic stability in Liapunov's sense.

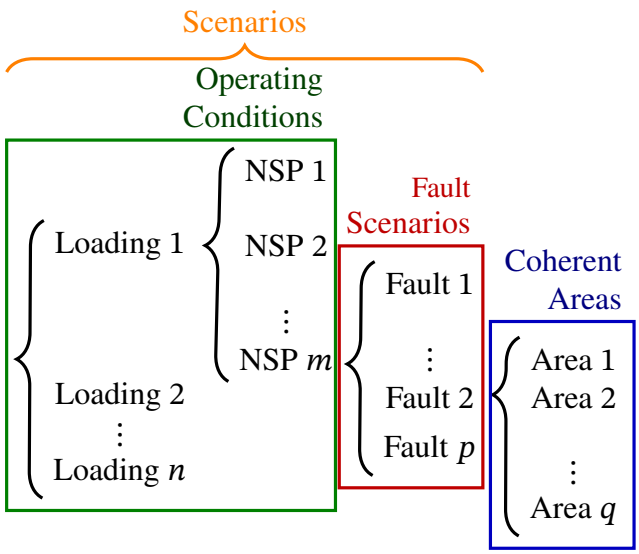

Figure. 4.1.: Scenario-based schemes for optimal virtual inertia planning. The "NSP" in the figure stands for "Non-Synchronous generation Penetration."

and the requirements on the performance improvement of frequency response are illustrated in Figure 4.1.

The screening framework proposed in [8], [41] is used to find out the boundary cases. The framework is a two-stage process based on the market and dynamic simulation.

In the first stage (line 3 in Algorithm. 4.1), a market simulation is conducted for each half-hour in a year with the foretasted system loading and renewable generation profiles. The market simulation generates references for each generation unit's active and reactive power output, and the dynamic states are initialized from the active and reactive power outputs.

Then, in the second stage (line 4–21), dynamic simulation is conducted against a list of possible faults on each operating condition obtained by the market simulation at each half-hour. A three-second simulated system response is needed to obtain the RoCoF and largest frequency excursion. If the results (maximum RoCoF and maximum frequency excursion) of a dynamic simulation does not conform to the frequency requirement, the corresponding operating condition and faults are registered as *critical scenarios*:

$$\mathcal{C} := \{(1, \mathcal{F}_1), \dots, (i, \mathcal{F}_i), \dots, (N, \mathcal{F}_N)\}, \tag{4.1}$$

where $(i, \mathcal{F}_i)$ for $i = 1, \dots, N$ indicates the set of critical faults $\mathcal{F}_i$ on the i-th working condition. The requirement on the system inertia response for the improvement of frequency response is formulated on these critical scenarios.

In the stability screening framework [8], [41], the system faults are selected to be the trip of a generator in the power system that has the largest active power output,

$$\arg\max_i P_i \qquad \forall\, i \in \mathcal{G}, \tag{4.2}$$

where P_i is the active power output of the i-th generator in the power system, and $\mathcal{G} \subset \mathcal{G}$ is the set of all generators. In practice, other types of system faults, e.g., the $N-1$ contingency screening, can be applied as long as the time and computation power allows.

The above screening framework is summarized in Algorithm. 4.1.

Constraints

Box constraints The virtual inertia installation h_i at a candidate location, Bus i, is subject to physical limits,

$$h_i \leq \overline{h}_i \tag{4.3a}$$

$$h_i \geq \underline{h}_i, \tag{4.3b}$$

where $\overline{h}_i$ is upper limit, and $\underline{h}_i$ is the lower limit.

The upper limit $\overline{h}_i$ is due to the availability of installation space and the maximum capacity of the energy storage system or other forms of fast-responsive energy reserve that are practically available.

The under limit $\underline{h}_i$ is set to be zero to exclude negative inertia installation for the buses where there is no installation of synchronous generator. For the buses of synchronous generators, the under limit $\underline{h}_i$ is set to the total physical inertia of all synchronous generators connected at Bus i.

Algorithm 4.1.: Scenario generations.

Input: Given 1) the network graph and all generation units and loads; 2) the loading conditions at each half-hour P_{Load}; 3) the amounts of dispatchable renewable generation $\overline{P}_{\text{renewable}}$ at each half-hour; 3) the critical frequency deviation $\Delta f_{\text{critical}}$; and 4) the critical RoCoF $\Delta \dot{f}_{\text{critical}}$.

Output: critical scenarios C.

procedure GETSCENARIOS($P_{\text{load}}, \overline{P}_{\text{renewable}}$)
  for $k = 1 \ldots 8760$ **do**
    MarketDispatch$\big(P_{\text{renewable}}(i), \overline{P}_{\text{load}}(i)\big)$ with prioritization in dispatching renewable units
    Initialize $\mathcal{C} \leftarrow \emptyset$ and $j \leftarrow 0$
    for $\alpha = 1 \ldots N_A$ **do**
      for $i \in \mathcal{G}_{\mathcal{A}_\alpha}$ **do**
        Initialize dynamics models
        Trip one generation unit at generation node i
        Conduct a time-domain simulation of 3 seconds
        Obtain $\max_t |\Delta f(t)|$ and $\max_t |\dot{f}(t)|$
        if $\max_t |\Delta f(t)| > f_{\text{critical}}$ or $\max_t |\dot{f}(t)| > \dot{f}_{\text{critical}}$ **then**
          Update $i \leftarrow i + 1$
          Set $\mathcal{F}_\alpha \leftarrow \{i\} \cup \mathcal{F}_\alpha$
        end if
      end for
      Update $\mathcal{C} \leftarrow (\alpha, \mathcal{F}_\alpha) \cup \mathcal{C}$
    end for
  end for
end procedure

▷ $P_{\text{load}}(i)$ is the system's loading condition at time i. Similarly, $\overline{P}_{\text{renewable}}(i)$ is maximum dispatchable generation for the renewables at time i.

▷ $\mathcal{G}_{\mathcal{A}_\alpha}$ is the set of generation unit in coherent area $\mathcal{A}_\alpha$.

▷ α indicates the working condition at the α-th hour, and $\mathcal{F}_\alpha$ is a set of critical faults on the α-indexed working condition.

Constraints on the inertia response

In the mathematical optimization problem setup, the grid code requirements on system frequency are translated into surrogate constraints on the amount of inertia response for the power system formulated using the newly proposed metric of inertia response.

In a power system, the frequency measurement at one location might be different from another during a transient event [66], although the frequency measurements at different

locations will converge to a uniform value when reaching a new steady state.

The studies, e.g., [69], show that the rotational speeds of synchronous generators and the virtual rotational speeds have a transitory clustering pattern in response to a system fault. A power system can be divided into multiple coherent areas based on clustering behaviour. Different frequency measurements at one coherent area at the same time instance have similar value; different frequency measurements across different coherent areas at the same time instant are also different.

To take into account the spatial difference in frequency measurements during the system transient, the required improvement on the system's frequency response is thus formulated with the surrogate constraints using the newly proposed metric of inertia response:

$$\tilde{f}_{m_{\mathcal{A}_i}} \geq \underline{f}_{m_{\mathcal{A}_i}} \qquad \text{for each area } i, \tag{4.4}$$

where $\tilde{f}_{m_{\mathcal{A}_i}}$ is the lowest measurement of the inertia response for the i-th coherent area:

$$\tilde{f}_{m_{\mathcal{A}_i}} = \min_{c_j \in \mathcal{C}} f^{(j)}_{m_{\mathcal{A}_i}}, \tag{4.5}$$

where $f^{(j)}_{m_{\mathcal{A}_i}}$ is the metric of coherent area inertia response defined in (3.54) for the j-th critical scenario, and the set $\mathcal{C}$ is set of critical scenarios defined in (4.1). The limit $\underline{f}_{m_{\mathcal{A}_i}}$ specifies the amount of minimum inertia response that a coherent system should have in need to satisfy the grid code regulation on system frequency. The value for $\underline{f}_{m_{\mathcal{A}_i}}$ may be decided using the trial-and-error method.

Number of virtual inertia installation Finally, another constraint should be put to limit the maximum number of virtual inertia installation. Denote $\mathcal{J}$ the set of virtual inertia installation locations:

$$\mathcal{J} := \{j_1, j_2, \dots, j_n\}, \tag{4.6}$$

where the j_i indicates the bus for virtual inertia installation. Then, the constraints on the number of virtual inertia installation can be written as

$$\text{card}\,(\mathcal{J}) \leq N, \tag{4.7}$$

where "card" is the cardinality (size) of the set $\mathcal{J}$, and N is the maximum number of virtual inertia installations required set by the TSO.

Objective Functions

The main topic of this thesis work is to find the most cost-effective plan of investment in the virtual inertia installation under the above-discussed physical and stability constraints. Therefore, the objective function f_c is the total investment cost to be minimized in the mathematical optimization problem.

The cost objective f_c can have many different types of formulation. For now, a simple linear function design is considered:

$$f_c(\mathcal{J}, h) = \sum_{j \in \mathcal{J}} \alpha_j h_j + c_j, \tag{4.8}$$

where α_j is the required investment cost for installing a second[†] of virtual inertia at Bus j, and c_j is the fixed-term investment. The virtual inertia installation locations $\mathcal{J} = \{j_1, \dots, j_n\}$ and the size of those virtual inertia installations $h = \left[h_{j_1}, \dots, h_{j_n}\right]$, are the decision variable. The cost function $f_c(\mathcal{J}, h)$ is a set function, and the optimization problem is of mixed-integer type.

The value for the affine terms α_i depends on the different implementations of virtual inertia emulation and different types of external energy storage used for the energy demand of virtual inertia emulation. The fixed-term c_i, on the other hand, is related to the cost of land procurement, purchase and installation of power converters, controllers, etc. The per-second cost α_i in the per-unit system of 100 MW has been examined on page 52 of Chapter 2.

The value for the fixed-term c_i varies a lot depending on the different locations of virtual

[†] in the per-unit system of power system, the unit of system inertia is second.

Table. 4.1.: Parameters for f_c with linear design.

α_i	c_i
0.6 m−2.03 m	5.0−30

inertia installation. For example, if the virtual inertia is installed at a bus where there are highly-rated power converters, e.g., buses of STATCOM, Static var Compensator, the fixed-term of investment c_i is much lower than installing at a load bus. The range for the affine term α_i and fixed term c_i are listed in Table. 4.1.

The Mathematical Formulation

Finally, the mathematical optimization problem can be formulated as follows.

$$\underset{\mathcal{J},h}{\text{minimize}}\, f_c(\mathcal{J}, h) \tag{4.9}$$

subject to

$$\mathcal{J} \subset \mathcal{J}_{\text{candidate}} \subset \mathcal{V} \tag{4.10a}$$
$$h_j \leq \overline{h}_j, \qquad \forall j \in \mathcal{J} \tag{4.10b}$$
$$h_j \geq \underline{h}_j, \qquad \forall j \in \mathcal{J} \tag{4.10c}$$
$$\text{Card}(\mathcal{J}) \leq N \tag{4.10d}$$
$$\tilde{f}_{m_{\mathcal{A}_i}} \geq \underline{f}_{m_{\mathcal{A}_i}} \qquad \forall\, i \in \{1, \ldots, N_{\mathcal{A}}\}, \tag{4.10e}$$

where the function f_c is the objective function defined by (4.8)

$$f_c(\mathcal{J}, h) = \sum_{j, c_j \in \mathcal{J}} \alpha_j h_j + c_j,$$

and $\tilde{f}_{m_{\mathcal{A}_i}}$ defined by (4.5) is the metric of the i-th coherent area inertia response defined in (3.54) for the j-th critical scenario,

$$\tilde{f}_{m_{\mathcal{A}_i}} = \min_{c_j \in \mathcal{C}} f^{(j)}_{m_{\mathcal{A}_i}}. \tag{4.11}$$

where $f_{m_{\mathcal{A}_i}}$ is defined by

$$\begin{aligned}
\tilde{f}^{(j)}_{m_{\mathcal{A}_i}} &:= \left(\int_0^\infty \dot{\hat{\delta}}^2_{\mathrm{COI}}(t)\, \mathrm{d}t \right)^{\frac{1}{2}} = \left(\int_0^\infty \left(\frac{1}{\sum_{k \in \mathcal{A}_i} m_k} \sum_{k \in \mathcal{A}_i} m_k \dot{\hat{\delta}}_k(t) \right)^2 \mathrm{d}t \right)^{\frac{1}{2}} \\
&= \langle \mathbb{1}, m_{\mathcal{A}_i} \rangle^{-1} \left(\left[\left| \dot{\hat{\delta}}_{k_1}(0_+) - h_{k_1}\big(\hat{\delta}_{k_1}(0_+)\big) \right| \frac{\epsilon}{F_{k_1}}, \dots, \left| \dot{\hat{\delta}}_{k_{\mathrm{m}}}(0_+) - h\big(\hat{\delta}_{k_{\mathrm{m}}}(0_+)\big) \right| \frac{\epsilon}{F_{k_{\mathrm{m}}}} \right] \mathbb{1}\mathbb{1}^\top \right. \\
&\qquad \left. \begin{bmatrix} \left| \dot{\hat{\delta}}_{k_1}(0_+) - h\big(\hat{\delta}_{k_1}(0_+)\big) \right| \frac{\epsilon}{F_{k_1}} \\ \vdots \\ \left| \dot{\hat{\delta}}_{k_{\mathrm{m}}}(0_+) - h\big(\hat{\delta}_{k_{\mathrm{m}}}(0_+)\big) \right| \frac{\epsilon}{F_{k_{\mathrm{m}}}} \end{bmatrix} \right)^{\frac{1}{2}},
\end{aligned}$$

where $\delta_{\mathrm{COI}}(0_+)$, $\dot{\delta}_{\mathrm{COI}}(0_+)$, and $\delta_k(0_+)$ corresponds to the k-th fault on the i-th working condition. The $m_{\mathcal{A}_i}$ is a vector of compensated system inertia at each generation units in a coherent area:

$$m_{\mathcal{A}_i} = \left[m_{g_1} + h_{g_1}, m_{g_2} + h_{g_2}, \dots, m_{g_n} + h_{g_n} \right]^\top \quad \text{for all generation buses } g_i \in \mathcal{G}_{\mathcal{A}_i},$$

where h_{g_i} is the amount of emulated virtual inertia to be installed at generation bus g_i. Considering the definition (4.11) for $\tilde{f}_{m_{\mathcal{A}_i}}$, the constraint (4.10e) is equivalent to

$$f^{(j)}_{m_{\mathcal{A}_i}} \geq \underline{f}_{m_{\mathcal{A}_i}} \qquad \text{for } j : c_j \in \mathcal{C}.$$

The set $\mathcal{J}$ is composed of the buses of virtual inertia installations. The vector h is composed

of the amount of virtual inertia installation at the indexed buses of the set $\mathcal{J}$

$$h = \left[h_{j_1}, \dots, h_{j_i}, \dots, h_{j_n}\right]^\top \qquad \forall\, j_i \in \mathcal{J}.$$

The objective function (4.9) and constraints (4.10) are explained in other parts of this sub-section. $N_{\mathcal{A}}$ is the number of coherent areas in the power system.

The mathematical optimization problem (4.9) to (4.10) is of mixed-integer type because of the limits on the number of virtual inertia installation (4.10d):

$$\text{Card}(\mathcal{J}) \leq N,$$

which is a constraint formulated on the domain of natural numbers. Furthermore, the decision variable also presents in the denominators in constraint (4.10e); hence, the optimization problem is not convex. In general, solving the optimization problem of mixed-integer and non-convex types is challenging. This thesis project explored two solution techniques, which will be discussed in the next section.

The Flowchart

To conclude this section, the steps of obtaining an optimal plan of virtual inertia installation is summarized in Figure. 4.2 of a flowchart.

The flowchart starts from the *scenario generation* adopted from the stability scanning framework [8], [41]. The scenario generation process begins with the inputs of *network topology*, *predicted CIG generation* and *load demand profile*, where the predicted CIG generation and system load profiles span a year with prediction points at each half-hour. Hence, there are in total $365 \times 24 \times 2 = 17520$ prediction points. For the amount of renewable generation available to be dispatched and system load at each half-hour, the market and time-domain simulation are conducted to generate a set of critical scenarios $\mathcal{C}$, where excessive levels of frequency excursion and RoCoF are observed.

The scenario generation process is followed by evaluating the metric of inertia response for each coherent area under every critical scenario. Each coherent area $\mathcal{A}_i$ is related with one of the critical scenarios $c^*_{\mathcal{A}_i}$, under which the evaluation of $f_{m_{\mathcal{A}_i}}$ is the lowest. The

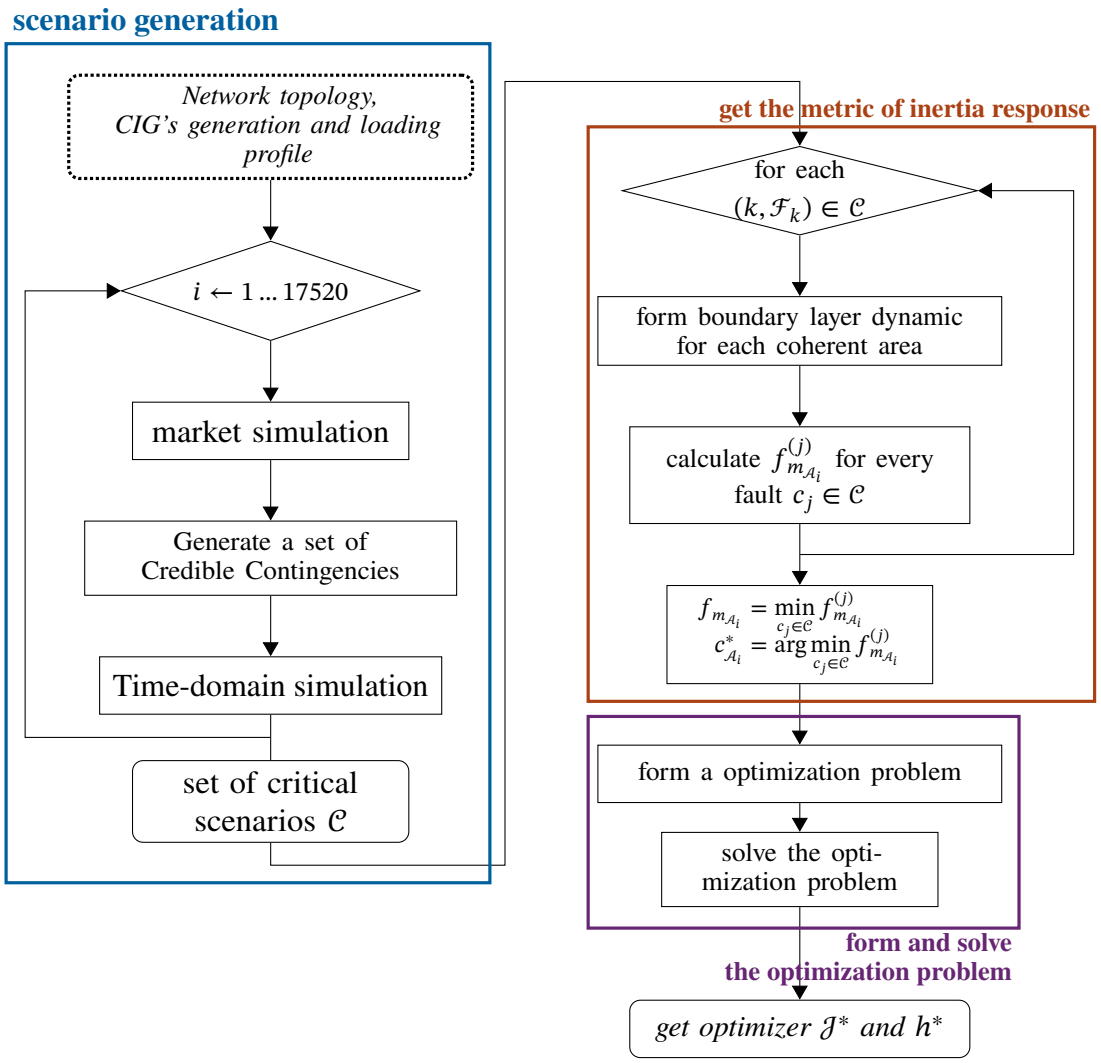

Figure. 4.2.: The diagram of the whole solution framework.

correspondences between coherent area $\mathcal{A}_i$ and the critical fault scenario $c^*_{\mathcal{A}_i}$ are then used to form constraints on the inertia response.

In the next process, a mathematical optimization problem is formulated with the above defined formula for the inertia response. Afterwards, the resulting mathematical optimization problem is solved to produce the optimal locations $\mathcal{J}^*$ and sizes h^* of the virtual inertia installation. The solution techniques are introduced in the following section.

4.2. Solution Techniques

As previously mentioned and indicated by the natures of optimizer $\mathcal{J}$ and h in (4.9), the problem is of mixed-integer type. Therefore, a special care should be given to find a way to efficiently solve the optimization problem of mixed-integer type ("form and solve optimization problem" in Figure. 4.2). Two methods are considered to tackle the mixed-integer property; they are *1*) dynamic programming-based method and *2*) Majorize-Minimization or Minorize-Maximization (MM)-based techniques.

4.2.1. Dynamic Programming Method

Overview

The *Dynamic Programming* is a traditional method to solve a particular kind of decision making problems in that the optimization problem is broken down into a number of sub-optimization problems in a recursive manner.

Dynamic programming The principle of dynamic programming can be explained with a discrete dynamic system:

$$x_{k+1} = f_k(x_k, u_k, w_k), \quad k = 0, 1, \dots, N-1, \tag{4.12}$$

where $x_k \in S_k$ is system state at stage k, $u_k \in U_k(x_k)$ is a control input at stage k, and $w_k \in D_k$ encapsulates the stochastic influence $w_k \sim P_k(\cdot \mid x_k, u_k)$. For deterministic dynamic programming, the dimension of w_k is zero and the state evolution dynamic is effectively

$$x_{k+1} = f_k(x_k, u_k).$$

The decisions at each stage are given as

$$\pi = \{\mu_0, \dots, \mu_N\} \quad \text{for stage } 1, \dots, N-1, \tag{4.13}$$

where the decision is a feedback rule mapping the system states x_k at stage k to a control input $\pi_k(x_k)$:

$$\begin{aligned} \mu_k(\cdot) : & S_k \to U_k \\ & x_k \mapsto \mu_k(x_k) = u_k. \end{aligned} \tag{4.14}$$

The aim of dynamic programming is to find a set of decisions $\pi = \{\mu_1, \dots, \mu_N\}$ prior to the start $k = 0$ of the discrete dynamic system. Under the optimal feedback rule, the cost function J_π is to be minimized. The cost function J_π has the following form:

$$J_\pi = \mathop{\mathbb{E}}_{w}\left[g_N(x_N) + \sum_{k=1}^{N-1} g_k\big(x_k, \mu_k(x_k), \omega_k\big) \right], \tag{4.15}$$

where the expectation is taken over the stochastic variables $w = (w_1, \dots, w_{N-1})$, $w \sim P_k(\cdot \mid x_k, u_k)$. The *terminal cost* $g_N = g_N(x_N)$ is incurred at the end of the process, whereas $g_k = g_k\big(x_k, \mu_k(x_k), \omega_k\big)$ is the accumulative cost incurred at stage k. For a deterministic problem, the cost at every stage is

$$g_k = g_k\big(x_k, \mu_k(x_k)\big).$$

Solving Dynamic Programming Problem

The *label correcting method* is a class of well-established techniques of dynamic programming. It can be understood as a general form of branch-and-bound algorithm widely used to solve mix-integer and combinatorial optimization. For deterministic problems, an improved version of label correcting algorithms—A^* *algorithm* is a more efficient approach. The problem of virtual inertia planning can be formulated and solved as DP problem. However, special care should also be given. In the following texts, the general label correcting method and A^* algorithm are first introduced; then, special considerations are given to the virtual inertia planning problem in Sub-section 4.2.2.

Basic label correcting method To begin with, more mathematical notations are introduced for ease of discussion. For a DP defined in (4.12), assume the optimal cost $J^*_{\pi^*}$ is attained

with the optimal feedback rule $\pi^* = (\mu_1^*, \dots, \mu_N^*)$:

$$J_{\pi^*}^* := J_{\pi^*} = \mathop{\mathbb{E}}_{w}\left[g_N(x_N^*) + \sum_{k=1}^{N-1} g_k\left(x_k^*, \mu_k^*\left(x_k^*\right), w_k\right)\right],$$

where $\left(x_1^*, \dots, x_N^*\right)$ is the system's state transition under the optimal control $\pi^* = \left(\mu_1^*, \dots, \mu_N^*\right)$ under a realization of stochastic variables $w_k \sim P\left(\cdot \middle| x_k^*, \mu_k^*\left(x_k^*\right)\right)$:

$$x_{k+1}^* = f_k\left(x_k^*, \mu_k^*(x_k^*)\right).$$

For a deterministic dynamic programming problem and a feedback rule π, the cost-to-go function $\tilde{J}_\pi(k)$ can be defined:

$$\tilde{J}_\pi(x_N) = g_N(x_N) \tag{4.16a}$$

$$\tilde{J}_\pi(x_k) = \mathop{\mathbb{E}}_{w_k}\left[g_k(x_k, w_k) + \tilde{J}_\pi(x_{k+1})\right] \qquad \text{for } k = 1, \dots, N-1, \tag{4.16b}$$

where $\tilde{J}_\pi(x_k)$ is the cost-to-go with the decision π (actually only the tail of π, $\pi_k, \dots, \pi_{N-1}$) and at the k-th stage. The optimal cost-to-go $\tilde{J}_{k+1}^* = \tilde{J}_{k+1}^*(x_{k+1})$ at state x_{k+1} is found by solving the following optimization problem:

$$\tilde{J}_\pi^*(x_{k+1}) = \min_{\mu_{k+1}, \dots, \mu_{N-1}} \mathop{\mathbb{E}}_{w_{k+1}, \dots, w_{N-1}}\left[g_N\left(x_N\right) + \sum_{i=k+1}^{N-1} g_i\left(x_i, \mu_i(x_i), w_i\right)\right]. \tag{4.17}$$

Assuming the optimal feedback rules $(\mu_{k+1}^*, \dots, \mu_{N-1}^*)$ for the state $k+1$ to $N-1$ are known. The best control decision at stage k for the state x_k is given by

$$\mu_k^*(x_k) = \arg\min_{\mu_k} \mathop{\mathbb{E}}_{w_k, \dots, w_{N-1}}\left[g_k\left(x_k, \mu_k(x_k), w_k\right) + J_{k+1}^*(x_{k+1})\right]. \tag{4.18}$$

By finding $\mu_k^*(x_k)$ for all system state x_k at Stage k, the optimal feedback rules $(\mu_{k+1}^*, \dots, \mu_{N-1}^*)$ is extended to Stage k: $(\mu_k^*, \mu_{k+1}^*, \dots, \mu_{N-1}^*)$. It can be proved that the optimal feedback rule $(\mu_k^*, \mu_{k+1}^*, \dots, \mu_{N-1}^*)$ obtained above is equivalent to solving the following optimization problem:

$$\arg\min_{\mu_k, \dots, \mu_{N-1}} \tilde{J}_\pi(x_k).$$

Based on this observation, an algorithm is designed as following:

Step 1) Compute

$$\tilde{J}^*_\pi(x_N) = g_N(x_N)$$

for all possible terminal states x_N.

Step 2) Compute the optimal control decision backward from final stage to stage 1,

$$\mu^*_k(x_k) = \arg\min_{\mu_k} \mathop{\mathbb{E}}_{w_k}\Big[g_k\big(x_k, \mu_k(x_k), w_k\big) + \tilde{J}^*(x_{k+1})\Big]$$
$$\tilde{J}^*(x_k) = \mathop{\mathbb{E}}_{w_k}\Big[g_k\big(x_k, \mu^*_k(x_k), w_k\big) + \tilde{J}^*(x_{k+1})\Big].$$

Repeating *Step 2* for stage $k = N-1, \dots, 1$, we obtain the optimal control decisions

$$\pi^* = \big(\mu^*_1, \dots, \mu^*_{N-1}\big), \tag{4.19}$$

and the problem's optimal cost is the optimal cost-to-go at stage one, i.e., $k = 1$,

$$J_{\pi^*}(x_1) = \tilde{J}^*_\pi(x_1). \tag{4.20}$$

The above steps constitute the (backward) DP algorithm.

For a deterministic discrete system (4.12), we can define a reverse problem by conversing discrete time horizon (or the order of stages):

$$\left.\begin{array}{l} x_{N-i} \mapsto x_i \\ \pi := (\mu_1, \dots, \mu_{N-1}) \to \rho := (\nu_2, \dots, \nu_N) \qquad \mu_i \mapsto \nu_{N+1-i} \\ f_i \mapsto f'_{N+1-i} \end{array}\right\} \quad \forall\, i \in 1, \dots, N, \tag{4.21}$$

where $\rho = (\nu_2, \dots, \nu_N)$, $\nu_i : x_i \mapsto u_{i-1}$, is the control decisions for the reverse DP problem, and the f'_k is the (backward) difference equations for the converse DP problem.

The discrete dynamics of the converse DP problem f'_{k+1} is defined from f_k as follows. Firstly, define a helper function

$$\tilde{f}_{u_i}(\cdot) := f_i(\cdot, u_i) := x_i \mapsto x_{i+1} \qquad \forall\, (x_i, \mu_i) \text{ so that } f_i(x_i, \mu_i) \text{ is defined.}$$

Then, the reverse function of $\tilde{f}_{k+1}$ is

$$\tilde{f}_{u_i}^{-1} : x_{i+1} \mapsto x_i.$$

Another helper function $\tilde{f}'_{i+1}$ is defined as

$$\tilde{f}'_{i+1}(x_{i+1}, u_i) := \tilde{f}_{u_i}^{-1}(x_{i+1}).$$

Finally, $u_i = \mu_i(x_i)$ is the application of the decision rule μ_i on x_i. But, we expect u_i is formulated on x_{i+1} instead of x_i. Therefore, another set of control decisions should be defined for the reverse problem, such that a relation between the control inputs u_i and x_{i+1} for $i = 1, \dots, N-1$.

To do so, yet another helper function needs to be defined

$$\hat{f}_{x_i}(\cdot) = f_i(x_i, \cdot) : u_i \mapsto x_{i+1}, \tag{4.22}$$

whose inverse

$$\hat{f}_{x_i}^{-1} : x_{i+1} \mapsto u_i \tag{4.23}$$

is well defined. Therefore, there is a function defined on x_{i+1} for the control input u_i that has an one-to-one correspondence with x_i. This function ν_i is defined to be decision rule for the reverse problem. The decision rules for stage $N, \dots, 1$ is collectively denoted as $\rho = (\nu_2, \dots, \nu_N)$. The relations between (forward) DP problem and the converse DP problem are shown in Figure. 4.3. Finally, the dynamics of the converse DP problem is

$$x_i = f'_{i+1}\big(x_{i+1}, \nu_{i+1}(x_{i+1})\big) \qquad \text{for } i = 1, \dots, N. \tag{4.24}$$

It should be noted that the converse DP problem progresses backwards from $i = N$ to $i = 1$.

For a stochastic DP problem, however, it is not possible to be conversed, because x_{i+1} of the original system depends on a realization of w_i, and $w_i \sim P(\cdot \mid x_i, u_i)$ is contingent on x_i and u_i. Therefore, no stochastic causal system can be a converse of a stochastic DP problem $x_{i+1} = f_i\big(x_i, \mu_i(x_i), w_i\big)$.

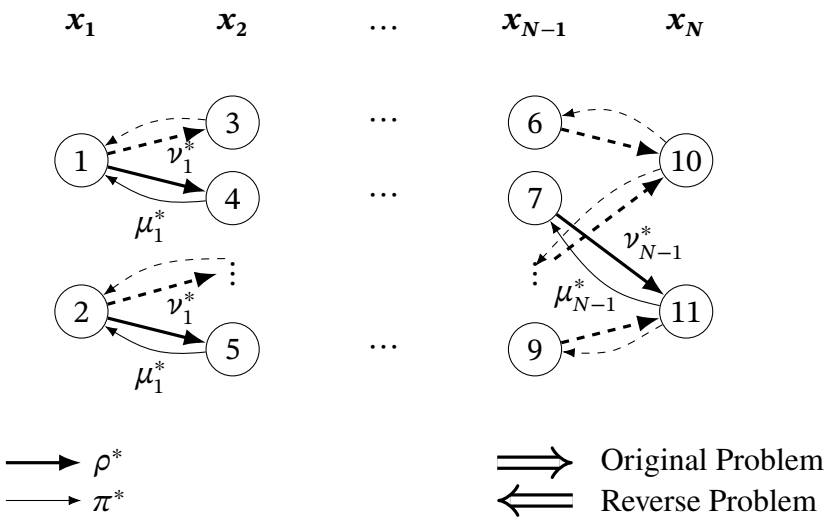

Figure. 4.3.: The dynamic programming problem and its converse problem.

Finally, assume a deterministic DP problem P of finite stage, we can define a reverse problem P' with (4.21). The backward DP algorithm gives an optimal solution $\pi^* = (\mu_1^*, \dots, \mu_{N-1}^*)$ for the original problem P. The backward DP also produces an optimal control decisions $\rho^* = (\nu_2^*, \dots, \nu_N^*)$ for the backward deterministic DP problem P'. Denote $(x_1^*, \dots, x_N^*)$ the state transition under the optimal feedback rule, i.e.,

$$x_{i+1}^* = f_i\big(x_i^*, \mu_i^*(x_i^*)\big),$$

and $(x_1'^*, \dots, x_N'^*)$ are the states of the converse DP dynamic

$$x_i'^* = f'_{k+1}\big(x_{k+1}'^*, \nu_{k+1}^*(x_{i+1}^*)\big).$$

It is not hard to prove that, if $x_i^* = x_i'^*$ at Stage i, then

$$x_k^* = x_k'^* \qquad \forall\, i = 1, \dots, N.$$

Moreover,

$$u_i^* = \mu^*(x_i^*) = \upsilon_{k+1}^*(x_{k+1}^*).$$

The relation is graphically illustrated also in Figure. 4.3. Hence, instead of applying DP

algorithm backwards on the original DP problem from $i = 1$ to $i = N$, the same optimal control decisions can be obtained by applying the DP algorithm on the converse DP problem from $i = 1$ to $i = N$, which is equivalent to forwardly solving the deterministic problem starting from the initial condition x_1. However, this method is still of high computational complexity in time and space. One way to accelerate the solution speed is to prune off "branches" (that are (x_i, x_{i+1}) pairs and the associated control decisions "linking" x_i and x_{i+1}) that are known not optimal at early stages of the algorithm iterations. The resulting algorithms is *label correcting algorithm*.

The label correcting and A^* algorithm The way to accelerate DP algorithm is setting up a label to track the preference of the complete/incomplete solutions so far searched along the forward DP algorithm. Suppose an incomplete solution has already been shown needing more cost to arrive at a state of an intermediate stage than other incomplete solutions arriving at the same state or the total cost of a complete solution. In that case, there is no need to continue pursuing to complete this inferior incomplete solution.

The label correction method makes the following assumptions: *1)* The concerned DP problem is deterministic. Therefore, it can be solved with the forward DP algorithm. *2)* The problem has finite time horizon (stages). *3)* There may be multiple starting and terminal nodes $\mathrm{Card}(x_1) \geq 1$ and $\mathrm{Card}(x_N) \geq 1$. In the labelling correction method, a label d_i is defined for each state to track the lowest accumulated cost known so far to arrive at x_i,

$$d_i(x_i) := \min_{\substack{\mu_1,\dots,\mu_i \\ x_1}} \sum_{k=1}^{k=i} g_k\big(x_k, \mu_k(x_k)\big) \qquad \text{for all } x_1 \text{ and } \mu_1, \dots, \mu_{i-1} \text{ considered so far, where } i = 2, \dots, N-1.$$

$$d_1(x_1) := 0,$$

and another label `UPPER` defined to be the optimal total cost found so far to arrive at the final stage:

$$\texttt{UPPER} := \min_{\substack{\mu_1,\dots,\mu_{N-1} \\ x_1}} \sum_{k=1}^{N} g_i\big(x_i, \mu_i(x_i)\big) + g_N(x_N) \qquad \text{for all } x_1 \text{ and } \mu_1, \dots, \mu_{N-1} \text{ searched so far,}$$

where $x_{i+1} = f_i\big(x_i, \mu_i(x_i)\big)$. To every x_i, an optimal "state route" $p_i(x_i)$ from stage 1 to the

state x_i at Stage i and the corresponding controls $q_i(x_i)$ are defined by

$$p_i(x_i) = (\hat{x}_1, \dots, \hat{x}_{i-1}, x_i)$$
$$q_i(x_i) = (\hat{\mu}_1, \dots, \hat{\mu}_i),$$

in that

$$\hat{x}_{k+1} = f_k\big(\hat{x}_k, \hat{\mu}_k(\hat{x}_k)\big) \qquad \text{for all } k = 1, \dots, i-1$$
$$\hat{x}_i = x_i.$$

With these three labels defined above, the *label correction algorithm* [70] is summarized by the following steps:

Step 1) Initiate a set `BIN`

$$\texttt{BIN} \leftarrow S_1, \tag{4.25}$$

initialize labels as

$$\begin{aligned} d_1(x_1) &\leftarrow 0 \\ d_i(x_i) &\leftarrow \infty \qquad \text{for all } i = 2, \dots, N, \end{aligned} \tag{4.26}$$

and stage counter $i \leftarrow 1$.

Step 2) Remove a node x_i from `BIN` and register the children x_{i+1} of node x_i in a set `CHILDREN`.

$$\texttt{CHILDREN}(x_i) := \Big\{ x_{i+1} \mid x_{i+1} = f_i(x_i, u_i)\ \forall u_i \in U_i(x_i) \Big\}.$$

Step 3) Remove a x_{i+1} from $\texttt{CHILDREN}(x_i)$. If $i \neq N-1$, compute

$$\tilde{d}_{i+1}(x_{i+1}) \leftarrow d_i(x_i) + g_i\big(x_i,\, \mu_i(x_i)\big),$$

where the μ_i is defined such that $x_{i+1} = f_i\big(x_i, \mu_i(x_i)\big)$. If $i = N-1$,

$$\tilde{d}(x_N) \leftarrow d_{N-1} + g_{N-1}\big(x_{N-1},\, \mu_{N-1}(x_{N-1})\big) + g_N(x_N),$$

where $x_N = f_{N-1}\big(x_{N-1}, \mu_{N-1}(x_{N-1})\big)$. Furthermore, register the best "route" arriving at node x_{i+1}

$$p_{i+1}(x_{i+1}) = \big(\hat{x}_1, \dots, \hat{x}_{i-1}, x_i, x_{i+1}\big)$$

and the corresponding control decisions

$$q_{i+1}(x_{i+1}) = \big(\hat{\mu}_1, \dots, \hat{\mu}_{i-1}, \hat{\mu}_i\big).$$

Accordingly, the label is updated

$$d_{i+1}(x_{i+1}) = \sum_{k=1}^{i-1} g_k\big(\hat{x}_k, \hat{\mu}_k(\hat{x}_k)\big) + g_i\big(x_i, \hat{\mu}_i(x_i)\big) \qquad \text{if } i \neq N-1$$

and

$$d_N(x_N) = \sum_{k=1}^{N-2} g_k\big(\hat{x}_k, \hat{\mu}_k(\hat{x}_k)\big) + g_{N-1}\big(x_{N-1}, \hat{\mu}_{N-1}(x_{N-1})\big) + g_N(x_N) \qquad \text{if } i = N-1,$$

where $x_{i+1} = f_i\big(x_i, \hat{\mu}_i(x_i)\big)$ and $x_N = f_{N-1}\big(x_{N-1}, \hat{\mu}_{N-1}(x_{N-1})\big)$.

Step 4) If $i \neq N-1$, and $\tilde{d}_{i+1}(x_{i+1}) < d_{i+1}(x_{i+1})$ and $\tilde{d}_i(x_i) < \texttt{UPEER}$, insert child x_{i+1} into the set `BIN`

$$\texttt{BIN} = \texttt{BIN} \bigcup \{x_j\},$$

and update the value for $d_{i+1}(x_{i+1})$

$$d_{i+1}(x_{i+1}) \leftarrow \tilde{d}_{i+1}(x_{i+1}).$$

If $i = N-1$ and $\tilde{d}_N(x_N) < d_N(x_N)$, update $d_N(x_N)$

$$d_N(x_N) \leftarrow \tilde{d}_N(x_N).$$

Step 5) Repeat *Step 3*) and *Step 4*) to deplete all $\texttt{CHILDREN}(x_i)$.

Step 6) Repeat *Step 2*) to *Step 4*) to deplete all elements in set `BIN`. Finally, the optimal

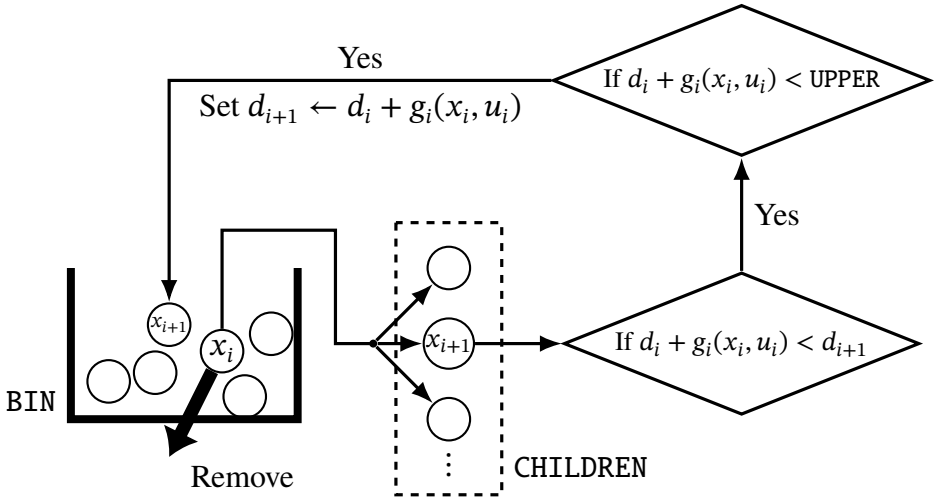

Figure. 4.4.: The schematic plot of label correction algorithm.

value is UPPER,

$$\texttt{UPPER} = d_N(x_N^*) = \min_{x_N} d_N(x_N)$$
$$x_N^* = \arg\min_{x_N} d_N(x_N),$$

and the optimal controls π^* is the chain of best control decisions $q_N(x_N^*)$ arriving at x_N^*,

$$\pi^* = q_N(x_N^*) = (\mu_1^*, \dots, \mu_N^*)$$

with the initial state x_1^* being the Stage 1 state of the optimal route reaching x_N^*, $p(x_1^*) = (x_1^*, \dots, x_N^*)$.

***A** algorithm** Compared with the basic label correcting method, the A^* method benefits from additional improvements with stronger inequality tests than

$$\tilde{d}_i(x_i) < d_i(x_i) \tag{4.27a}$$
$$\tilde{d}_i(x_i) < \texttt{UPPER} \tag{4.27b}$$

and a better initialization scheme for $d_i(x_i)$, $\forall\, i = 1, \dots, N$.

The label correcting method is illustrated represented as Figure. 4.4. Instead of initializing

$d_1(x_1) = 0$ and $d_i(x_i) = \infty, i = 2, \dots, N$ as in classical label correcting method, A^* algorithm requires a feasible solution $(x_1, \dots, x_N)$ known beforehand through, for example, heuristic approaches. With the feasible solution, Labels d_i are initialised to be the accumulated functions along the known feasible solution $(x_1, \dots, x_N)$ and corresponding control sequence $\pi = \{\mu_1, \dots, \mu_{N-1}\}$,

$$d_i \leftarrow \tilde{J}_\pi(x_i). \tag{4.28}$$

Therefore, the d_i and `UPPER` are no longer 0 or ∞ at the initial state, and the inequality tests (4.27) becomes stricter. Hence, less promising routes can be pruned off at earlier stage, and the computational speed gets accelerated.

Moreover, a term h_i is the *positive underestimate* of the cost-to-go from the "node" x_i to any terminal "node," i.e., x_N,

$$h_i(x_i) \leq \min_{u_{i+1}, \dots, u_{N-1}} \sum_{k=i+1}^{N-1} g(x_k, u_k) + g(x_N), \tag{4.29}$$

which also helps to make a stricter test. The inequality test (4.27a) and (4.27b) are substituted by the stricter constraints

$$\tilde{d}_i(x_i) + h_i(x_i) < d_i(x_i) \tag{4.30a}$$

$$\tilde{d}_i(x_i) + h_i(x_i) < \texttt{UPPER}, \tag{4.30b}$$

respectively. In this way, even fewer nodes will enter the set `BIN` and therefore the computational speed gets an extra bit of acceleration. An example of of $h_i(x_i)$ choice can be

$$h_i(x_i) = \min_{x_N} g_N(x_N) + \sum_{k=i+1}^{N-1} \min_{x_i, u_i} g(x_k, u_k), \tag{4.31}$$

where it is assumed that (4.31) is easier to compute than the Right-Hand-Side of (4.29).

The A^* algorithm's has a time and space complexity of $O(b^s)$ in the worst scenario, where b is the average size of u_i at each stage, i.e., $\mathbb{E}_{x_i} \operatorname{card}\big(U(x_i)\big)$, and s is the number of stages that a problem has.

4.2.2. Obtain Virtual Inertia Installation in Dynamic Programming (DP) Framework

The DP algorithm, label correction, or the improved version of label correction—A^* algorithm can be applied to obtain an optimal plan of virtual inertia installation. However, special considerations should be taken into account because of

1) the complicated formulation of inertia response metric in the frequency stability constraint

$$f_{m_{\mathcal{A}_i}} \geq \underline{f}^{(k)}_{m_{\mathcal{A}_i}} \qquad \forall\, i \in \{1, \dots, N_{\mathcal{A}}\} \tag{4.32}$$

where $f_{m_{\mathcal{A}_i}}$ is defined as

$$f_{m_{\mathcal{A}_i}}(h) = \langle \mathbb{1}, m^{(k)}_{\mathcal{A}_i} \rangle^{-1} \left(\left[\left| \dot{\delta}_{k_1}(0_+) - h_{k_1}\big(\delta_{k_1}(0_+)\big) \right| \frac{\epsilon^{(k)}_{\mathcal{A}_1}}{F_{k_1}} \;\; \dots \;\; \left| \dot{\delta}_{k_n}(0_+) - h_{k_n}\big(\delta_{k_n}(0_+)\big) \right| \frac{\epsilon^{(k)}_{\mathcal{A}_n}}{F_{k_n}} \right] \mathbb{1}\mathbb{1}^\top \right.$$
$$\left. \begin{bmatrix} \left| \dot{\delta}_{k_1}(0_+) - h_{k_1}\big(\delta_{k_1}(0_+)\big) \right| \frac{\epsilon^{(k)}_{\mathcal{A}_1}}{F_{k_1}} \\ \vdots \\ \left| \dot{\delta}_{k_n}(0_+) - h_{k_n}\big(\delta_{k_n}(0_+)\big) \right| \frac{\epsilon^{(k)}_{\mathcal{A}_n}}{F_{k_n}} \end{bmatrix} \right), \tag{4.33}$$

and $N_{\mathcal{A}}$ is the number of coherent areas in the system.

2) the simple bounds on the size of virtual inertia installation

$$\underline{h}_i < h_i \leq \overline{h}_i.$$

The simple bounds in *2*) can be handled easily by translating the limits into a limit on the control signal:

$$U_i(x_i) = \left\{ \{k\} \times \left[\underline{h}_k, \overline{h}_k \right] \;\middle|\; \forall\, k \in \mathcal{V}_G \setminus \{k_1, \dots, k_i\} \right\}. \tag{4.34}$$

But, the complexity of first constraint (4.32) demands more special considerations. Therefore, a modified version of A^* algorithm is designed.

For virtual inertia installation at no more than N locations $\left(\text{card}(\mathcal{J}) \leq N\right)$ in a N_A area system, the modified A^* algorithm divides the stages into N_A segments. One segment corresponds to a coherent area, and a sub-optimization problem is defined for each segment. Each sub-optimization problem is a dynamic programming problem of an indefinite number of stages N_i,

$$\sum_{i=1}^{N_{\mathcal{A}}} \leq N,$$

whose optimal solution should satisfy the frequency constraint for the corresponding coherent area

$$f_{m_{\mathcal{A}_i}} \geq \underline{f}_{m_{\mathcal{A}_i}}.$$

In the end, the optimal solutions to those sub-optimization problems are combined to get a final solution.

Therefore, the solution scheme of a bi-level structure shall be used to find the optimal plan of virtual inertia installation. On the first level, the label correcting method can be used to solve the sub-optimization problems with a list of tentative choices for the number of stages $N_{\mathcal{A}_i} = 1, 2, ...$, as shown in Table. 4.2. On the second level, another optimization problem is designed to make the best combination of solutions to different sub-optimization problems of each segment.

Bi-level solution scheme Before introducing the bi-level solution scheme, the following variables are introduced to facilitate the definition of the first-level sub-optimization problem:

Vectors of virtual inertia installation $h_{\mathcal{A}_k}$ for the area $h_{\mathcal{A}_k}$: The j-th element of $h_{\mathcal{A}_k}$ is defined as

$$\left[h_{\mathcal{A}_k}\right]_j := \begin{cases} \text{the size of virtual inertia installation at bus } j & \text{if } k \in \mathcal{A}_k \cap \texttt{VIBUS} \\ 0 & \text{if } k \notin \mathcal{A}_k \setminus \texttt{VIBUS}, \end{cases}$$

Vectors of updated virtual inertia installation $m'_{\mathcal{A}_k}$:

$$m'_{\mathcal{A}_k}\left(h_{\mathcal{A}_k}\right) := m_{\mathcal{A}_k} + h_{\mathcal{A}_k},$$

where $m_{\mathcal{A}_i}$ is a vector of existing rotational inertia at buses of the i-th coherent area.

Metric of Frequency Performance $f_{m'_{\mathcal{A}_k}}$ *with Updated Vector of Inertia* $m'_{\mathcal{A}_k}$ A frequency performance metric can be defined with updated virtual inertia installation $m'_{\mathcal{A}_k}$

$$f_{m'_{\mathcal{A}_k}}\left(h_{\mathcal{A}_k}\right) = \langle \mathbb{1}, m'_{\mathcal{A}_k}\rangle^{-1}\left(\left[\left|\dot{\delta}_{k_1}(0_+) - h_{k_1}(\delta_{k_1}(0_+))\right|\frac{\epsilon_{\mathcal{A}_1}\left(h_{\mathcal{A}_k}\right)}{F_{k_1}\left(h_{\mathcal{A}_k}\right)} \;\cdots\; \left|\dot{\delta}_{k_n}(0_+) - h_{k_n}(\delta_{k_n}(0_+))\right|\frac{\epsilon_{\mathcal{A}_n}\left(h_{\mathcal{A}_k}\right)}{F_{k_n}\left(h_{\mathcal{A}_k}\right)}\right]\mathbb{1}\mathbb{1}^\top \left[\begin{array}{c}\left|\dot{\delta}_{k_1}(0_+) - h_{k_1}(\delta_{k_1}(0_+))\right|\frac{\epsilon_{\mathcal{A}_1}\left(h_{\mathcal{A}_k}\right)}{F_{k_1}\left(h_{\mathcal{A}_k}\right)}\\ \vdots \\ \left|\dot{\delta}_{k_n}(0_+) - h_{k_n}(\delta_{k_n}(0_+))\right|\frac{\epsilon_{\mathcal{A}_n}\left(h_{\mathcal{A}_k}\right)}{F_{k_n}\left(h_{\mathcal{A}_k}\right)}\end{array}\right]\right). \tag{4.35}$$

where $\epsilon_{\mathcal{A}_i}\left(h_{\mathcal{A}_i}\right) := \frac{\max_{k\in\mathcal{A}_i} m'_k(h_{\mathcal{A}_i})}{\min_{k\in\mathcal{A}_i} D_k}$ and $F_k := \frac{m'_k}{D_k}$.

Coefficient vectors of $\alpha^{(i)}_{\mathcal{A}_k}$ *and* $c^{(i)}_{\mathcal{A}_k}$ *in cost function* :

$$\alpha_{\mathcal{A}_k} = \begin{cases} \alpha_k & \text{if } k \in \mathcal{A}_k \cap \texttt{VIBUS}^{(i)} \\ 0 & \text{if } k \notin \mathcal{A}_k \setminus \texttt{VIBUS}^{(i)}, \end{cases} \tag{4.36}$$

and

$$c^{(i)}_{\mathcal{A}_k} = \begin{cases} c_k & \text{if } k \in \mathcal{A}_k \cap \texttt{VIBUS}^{(i)} \\ 0 & \text{if } k \notin \mathcal{A}_k \setminus \texttt{VIBUS}^{(i)}. \end{cases} \tag{4.37}$$

For the i-th coherent area $\mathcal{A}_i$, the sub-optimization problem is described by the following problem:

$$\underset{\mathcal{J}_i, h^{(i)}_{\mathcal{A}_k}}{\text{minimize}}\; f^{(i)}_{c_{\mathcal{A}_k}} := \left\langle \alpha^{(i)}_{\mathcal{A}_k},\, h^{(i)}_{\mathcal{A}_k}\right\rangle + \left\langle \mathbb{1},\, c^{(i)}_{\mathcal{A}_k}\right\rangle. \tag{4.38}$$

subject to a limit on a sufficient level of system inertia

$$f^{(i)}_{m'_{\mathcal{A}_k}}\left(h^{(i)}_{\mathcal{A}_k}\right) \geq \underline{f}_{m_{\mathcal{A}_k}} \tag{4.39a}$$

and the box limit on the size of virtual inertia installation

$$\underline{h}^{i}_{\mathcal{A}_k} \preceq h^{i}_{\mathcal{A}_k} \preceq \overline{h}^{i}_{\mathcal{A}_k}, \tag{4.39b}$$

and finally the constraints on the total number of virtual inertia installation

$$\dim\left(h^{(i)}_{\mathcal{A}_k}\right) \leq N_k. \tag{4.39c}$$

Solving the sub-optimization problem The following steps are proposed based on the label correcting algorithm for the sub-optimization problems of area $\mathcal{A}_i$:

Step 1) Initialize an ordered set $\texttt{BIN}$ to consist of all candidate buses $\mathcal{V}_{\text{candidate}}$ in $\mathcal{A}_i$ for virtual inertia installation,

$$\texttt{BIN} \leftarrow \mathcal{V}_{\text{candidate}} \cap \mathcal{A}_i,$$

and set the stage counter

$$i \leftarrow 1.$$

Prepare a set $\texttt{VIBUS}^{(i)}$ to register all the buses selected for virtual inertia installation so far. Since no buses have been selected at the beginning, the set $\texttt{VIBUS}^{(i)}$ is initialized to null set:

$$\texttt{VIBUS}^{(i)} \leftarrow \varnothing \qquad \forall\, i.$$

Finally, prepare an ordered set $\texttt{SOL}^{(i)}$ consisting of all feasible solutions obtained at stage i:

$$\texttt{SOL}^{(i)} \leftarrow \varnothing \qquad \forall\, i.$$

Step 2) For $i \neq 1$, pop (select from the top and remove) a solution $\texttt{sol}^{(i-1)}$ from previous

stage, $\texttt{SOL}^{(i-1)}$, and register its installation buses in set $\texttt{bus}^{(i-1)}$:

$$\begin{aligned}
&\texttt{sol}^{(i-1)} \leftarrow \text{pop}\left(\texttt{SOL}^{(i-1)}\right) \\
&\texttt{bus}^{(i-1)} \leftarrow \{k_1, \dots, k_{i-1}\} \qquad \text{where } k_1, \dots, k_{i-1} \text{ are from } \texttt{sol}^{(i-1)};
\end{aligned}$$

otherwise,

$$\texttt{bus}^{(i-1)} \leftarrow \varnothing.$$

Then, remove a candidate bus, bus k_i, from $\texttt{BIN} \setminus \texttt{bus}^{(i-1)}$, and set

$$\texttt{bus} \leftarrow \texttt{bus}^{(i-1)} \bigcup \{k_i\}.$$

If $\texttt{bus} \in \texttt{VIBUS}^{(i)}$, then repeat this step; otherwise, insert this selection of bus into $\texttt{VIBUS}^{(i)}$

$$\texttt{VIBUS}^{(i)} \leftarrow \texttt{VIBUS}^{(i)} \cup \texttt{bus}.$$

Step 3) Pop a set of bus selection for virtual inertia installation

$$\texttt{bus} \leftarrow \text{pop}\left(\texttt{VIBUS}^{(i)}\right).$$

Define and solve the following *continuous* variable optimization problem,

$$\underset{\substack{h_{k_1,\dots,h_{k_i}}, \\ k_1,\dots,k_i \in \texttt{bus}}}{\text{minimize}} f^{(i)}_{c_{\mathcal{A}_k}}\left(h_{k_1}, \dots, h_{k_i}\right) = \left\langle \alpha^{(i)}_{\mathcal{A}_k},\, h^{(i)}_{\mathcal{A}_k} \right\rangle + \left\langle \mathbb{1},\, c^{(i)}_{\mathcal{A}_k} \right\rangle \tag{4.40}$$

subject to

$$f_{m'_{\mathcal{A}_i}}\left(h_{k_1}, \cdots, h_{k_i}\right) \geq \underline{f}_{m_{\mathcal{A}_i}} \tag{4.41a}$$

$$\underline{h}_k \leq h_k \leq \overline{h}_k. \qquad \forall\, i \in \{k_1, \dots, k_i\} \tag{4.41b}$$

The continuous optimization problem can be efficiently solved with existing methods, e.g., sequential quadratic programming and or augmented Lagrangian [71]. Denote the solution as $h^*_{k_1}, \dots, h^*_{k_i}$ if there are feasible solutions.

Step 4) Repeat *Step 2*) and *Step 3*) until set BIN is depleted. Rank and register all *acceptable*

Table. 4.2.: The best solutions for the sub-optimization problem for area $\mathcal{A}_k$.

$\mathtt{sol}_i^k$	$f^*_{c_{\mathcal{A}_k}}$	$\mathtt{bus}_k^*$	$h^*_{\mathcal{A}_k}$
1.	$*$	k_1	$h^*_{k_1}$
2.	$*$	k_1, k_2	$h^*_{k_1}, h^*_{k_2}$
$\vdots$	$\vdots$	$\vdots \cdots \ddots$	$\vdots \cdots \ddots$

solutions $\mathtt{sol}_1, \ldots, \mathtt{sol}_n$ ordered by required investment,

$$\mathtt{SOL}^{(i)} \leftarrow \{\mathtt{sol}_1, \ldots, \mathtt{sol}_n\}$$

where $\mathtt{sol}_j$ is the j-th best one among n feasible solutions. $\mathtt{sol}_j = \left(f^*_c,\ (k_1, h^*_{k_1}),\ \ldots,\ (k_i, h^*_{k_i})\right)$ where f^*_c is j-th best result given by installing $h^*_{k_1}$, ..., $h^*_{k_i}$ at bus k_1, ..., k_i.

Step 5) Increment the stage counter

$$i \leftarrow i + 1,$$

and repeat *Step 2*) to *Step 4*) until a preset number $\overline{N}_k$ is reached:

$$i = \overline{N}_k.$$

Step 6) Finally, a list of optimal solutions of different "length" is output in Table 4.2.

System-wide optimization After solving the sub-optimization problem of each coherent area, the final solution can be obtained by solving a second-level optimization problem. The second-level optimization problem aims at finding the best combination of solutions to the sub-optimization problem of each coherent area that satisfies all constraints discussed above under Subsection 4.1.2, including the limit on the total number of virtual inertia installations (4.10d).

In mathematical language, the system-wide second-level optimization problem is

$$\underset{\substack{\mathtt{sol}_i^k \\ k=1,\ldots,n}}{\text{minimize}} \sum_k f_{c_{\mathcal{A}_k}}\left(\mathtt{sol}_i^k\right), \tag{4.42}$$

subject to

$$\sum_i \text{length}\left(\texttt{sol}_i^k\right) \leq N. \tag{4.43}$$

In the above equations, $\texttt{sol}_i^k$ denotes the i-th optimal solution to the sub-optimization problem of the k-th coherent area $\mathcal{A}_k$, i.e., the first column of Table. 4.2, $f_{c_{\mathcal{A}_k}}(\texttt{sol}_i^k)$ is the corresponding investment cost of virtual inertia installation in area $\mathcal{A}_i$ of solution $\texttt{sol}_i^k$, i.e., the second column of Table. 4.2, labelled $f^*_{c_{\mathcal{A}_k}}$, and length($\texttt{sol}_i^k$) is the number of virtual inertia installations of the i-the solution to the sub-optimization problem of the k-th coherent area.

The second-level problem is a discrete dynamic programming problem, which can be solved with the standard algorithm, e.g., (forward) DP or label correcting algorithms.

4.2.3. Sparsity Promotion and MM Method

Apart from the above solution technique based on the classical dynamic programming method, the mixed-integer optimization can be solved efficiently by relaxing it into a continuous optimization problem. In this thesis work, a relaxation technique is proposed based on *majorize-minimization* or *minorize-maximization (MM)* method [68], [72]. The MM method is a class of techniques proposed originally to solve likelihood maximizing and least square estimation problems in statistic studies. The principle of this method is to convert the problem of minimizing a discrete objective function into a series of surrogate optimization problems minimizing a quadratic approximation of the original objective function. Since the objective functions are quadratic, the problem can be solved efficiently via, e.g., the conjugate gradient method.

The MM methods are used for other applications, like in variable selection [73], sparsity promotion problems [67], [74], and sparsity promotion control [75]. In the context of power system, the MM algorithm has been used in designing a minimum number of wide-area PSSs at best locations to damp the inter-area oscillation [74].

In the following, the basic principles of MM and sparsity promotion are introduced. The MM method is then exploited to solve the mixed-integer optimization problem (4.9)– (4.10).

Principles of MM method

As the name "majorize-Minimization" and "minorize-Maximization" suggest, the MM method involves two major steps: *1)* designing a surrogate function majorizing or minorizing the original objective function, and *2)* minimizing or maximizing, respectively, the surrogate function.

The variable selection or sparsity promotion problem involves solving the following optimization problem:

$$\underset{\theta}{\text{minimize}} \|\theta\|_{\ell_0} \tag{4.44}$$

where $\|\cdot\|_{\ell_0}$ is the ℓ_0 "norm" that measures the number of non-zeros elements of a vector. With the definition of $0^0 = 0$,

$$\|\theta\|_{\ell_0} = \sum_k \theta_k^0.$$

This optimization problem is a standard example of problems of combinatorial optimization.

The MM method converters the optimization problem on ℓ_0 norm into the following form

$$\underset{\theta}{\text{minimize}}\, f_c(\theta) = \sum_{k=1}^{n} p_k(\theta_k), \tag{4.45}$$

where $\theta = (\theta_1, \ldots, \theta_n)$. The penalty function $p_1, \ldots, p_n$ should simultaneously satisfy the following conditions [76]

1) $p_k(\theta)$ should be a concave function over $\theta \in]0, +\infty[$, and

2) $\frac{\mathrm{d}\, p_k}{\mathrm{d}\theta}(0_+) \geq 0$ but $p_k(x)$ is singular at $x = 0$.

With an appropriate choice for p_i, the minimizer of (4.45) can also minimize the combinatorial optimization problem (4.44) on ℓ_0 norm. Examples of the penalty function can be of $\mathcal{L}_0$ measurable,

$$p_k(x) = \frac{1}{2} I(x \neq 0) \tag{4.46}$$

where $I(\cdot)$ is an indicator function. With a slight abuse of mathematical notation, the indicator

function is defined by

$$I(x \neq x_0) = \begin{cases} 1 & x \neq x_0 \\ 0 & x = x_0. \end{cases}$$

This penalty definition is commonly referred to as *entropy penalty*. Another example is the absolute value metric

$$p_k(x) = \gamma \left| x_k \right|, \tag{4.47}$$

which is used frequently in statistical analysis. As the final example, the logarithm penalty

$$p_k(x) = \log\big(|x_k|\big), \tag{4.48}$$

is of particular interests and plays a significant role in relaxing the optimization problem of the virtual inertia planning.

The MM method is an iterative optimization method. At each iteration, instead of the original penalty function $p_k(x_k)$ that is concave in $x_k \in \left]0, \infty\right[$, a convex surrogate function defined at the i-th iterate $x_{k_0}^{(i)}$ is to be minimized. The commonly used surrogate functions are a linear function:

$$q_k^{(i)}(x_k) = p_k\Big(\big|x_{k_0}^{(i)}\big|\Big) + \frac{\mathrm{d}\, p_k}{\mathrm{d}x_k}\Big(\big|x_{k_0}^{(i)}\big|\Big) \cdot \big(|x_k| - |x_{k_0}^{(i)}|\big), \tag{4.49}$$

where the superscript (i) indicates i-th iterate. Another example of surrogate functions is of quadratic form,

$$q_k^{(i)}(x_k) = p_k\Big(\big|x_{k_0}^{(i)}\big|\Big) + \frac{\left(x_k^2 - \left(x_{k_0}^{(i)}\right)^2\right) \cdot \dfrac{\mathrm{d}\, p_k}{\mathrm{d}x_k}\Big(\big|x_{k_0}^{(i)}\big|\Big)}{2\left|x_{k_0}^{(i)}\right|}. \tag{4.50}$$

It is evident that

$$q_k^{(i)}\big(x_{k_0}^{(i)}\big) = p_k\big(x_{k_0}^{(i)}\big). \tag{4.51a}$$

Furthermore, since $q_k^{(i)}$ is convex and p_k is concave,

$$q_k^{(i)}\left(x_{k_0}^{(i)}\right) \geq p_k\left(x_{k_0}^{(i)}\right). \tag{4.51b}$$

Any surrogate functions $q_k^{(i)}$ satisfying (4.51a) and (4.51b), including (4.49) and (4.50), are referred to as *majorizing function*.

The surrogate functions $q_k^{(i)}$ are then to be minimized at each iteration with the optimizer denoted $x_{k_0}^{(i+1)}$:

$$x_{k_0}^{(i+1)} = \arg\min_{x_k} \sum_k q_k(x_k), \tag{4.52}$$

where $x_{k_0}^{(i)}$ is associated with the optimizer $x_{k0}^{(i)}$ of the previous iteration.

Then, update the iteration counter,

$$i \leftarrow i + 1,$$

and formulate a new surrogate function at the new iterate $x_{k_0}^{(i+1)}$. Repeat the process until the changes in $\Delta x_{k_0}^{(i)} = x_{k_0}^{(i+1)} - x_{k_0}^{(i)}$ is sufficiently small. It can be proved [72] that

$$p_k\left(x_{k_0}^{(i+1)}\right) \geq p_k\left(x_{k_0}^{(i)}\right). \tag{4.53}$$

Since $\left(x_{k_0}^{(0)}, \ldots, x_{k_0}^{(i)}, \ldots\right)$ is Cauchy sequence, $x_{k_0}^{(i)}$ converges to the minimizer as $i \to +\infty$.

However, one of the caveats is that at $x_{k_0}^{(i)} = 0$, the surrogate function may not be well defined. In the linear surrogate function (4.49), the derivative term $\frac{\mathrm{d}\, p_k}{\mathrm{d} x_k}$ might become singular. As an example, for $p_k = \log(|x_k|)$,

$$\frac{\mathrm{d}\, p_k}{\mathrm{d} x_k} = \pm\frac{1}{x_k},$$

which becomes singular at $x_k = 0$. Hence, the linear majoring function (4.49) is not well defined at $x_{k_0}^{(i)} = 0$. In the quadratic form function (4.50), $\left|x_k^{(i)}\right|$ is at denominator; therefore, (4.50) is also not defined at $x_{k_0}^{(i)} = 0$. To address the difficulty, a modification to surrogate function $q_{k_0}^{(i)}$ is proposed. Instead of minimizing the majorizing functions (4.49) and (4.50),

the following functions are to be minimized, respectively,

$$q_k^{(i)}(x_k) = p_k\left(\left|x_{k_0}^{(i)}\right|\right) + \left(\frac{\mathrm{d}\, p_k}{\mathrm{d}x_k}\left(|x_{k_0}^{(i)}|\right) + \epsilon\right) \cdot \left(|x_k| - |x_{k_0}^{(i)}|\right) \tag{4.54}$$

and

$$q_k^{(i)}(x_k) = p_k\left(\left|x_{k_0}^{(i)}\right|\right) + \frac{\left(x_k^2 - \left(x_{k_0}^2\right)^2\right) \cdot p_k'\left(x_{k_0}^{(i)}\right)}{2\left(|x_{k_0}^{(i)}| + \epsilon\right)}, \tag{4.55}$$

where $\epsilon > 0$ is a perturbation parameter sufficiently small so that the decent property (4.53) still holds.

Planning virtual inertia installation with MM method The principle of MM method can be used to handle the constraint on the number of virtual inertia (4.10d) because of its similarity with the variable selection and sparsity promotion promotion problems.

Rewrite the limit on the number of virtual inertia installation:

$$\|h\|_{\ell_0} \leq N. \tag{4.56}$$

If the surrogate function p_i is chosen to be $\log(|x_k|)$, it is equivalent to

$$\sum_i w_i \, \log\left(h_i\right) \leq N. \tag{4.57}$$

Denote $b = \left(b_1, \ldots, b_n\right)$ a list of buses of virtual inertia installation and $h = \left(h_{b_1}, \ldots, h_{b_n}\right)$ the corresponding amounts of virtual inertia installation at the buses. Denote $(b^*, h^*) = \left((b_1^*, \ldots, b_M^*),\ (h_{b_1}^*, \ldots, h_{b_M}^*)\right)$ an optimal plan of virtual inertia installation. If the weighting factors are defined as

$$w_k := \frac{c_k}{\log\left(|h_k^*| + \epsilon\right)} \quad \text{for } k = b_1, \ldots, b_n, \tag{4.58}$$

for ϵ sufficiently small, the relax limit on the number of virtual inertia installation (4.57)

equals that of the original limit (4.56), i.e.,

$$\|h^*\|_{\ell_0} = \sum_i w_i \log\left(h_i^*\right) + O(\epsilon).$$

However, we have no *a priori* knowledge about the optimal plan (b^*, h^*). Therefore, the following procedure is proposed inspired by MM algorithm.

Step 1) *Initialization of weighting coefficients*: Initialize the perturbation term ϵ to a small positive value.

The weighting factors w_i can be either initialized with a fixed term investment cost c_i or a reasonable guess $\hat{h}_k$ from the optimal sizes and locations of virtual inertia installations, i.e.,

$$w_k^{(1)} \leftarrow 1$$

or

$$w_k^{(1)} \leftarrow \frac{1}{\log\left(\hat{h}_k + \epsilon\right)},$$

where $\hat{h}_k^{(i)}$ is the initial guess of virtual inertia installation at Bus k. If the virtual inertia is discouraged to be installed at Bus k, $\hat{h}_k^{(i)}$ is set to zeros.

Set the iteration counter

$$i \leftarrow 1.$$

Step 2) *Relaxation of the penalty functions*: A surrogate majorizing objective function is defined by replacing the p_i with q_i defined in (4.54),

$$\begin{aligned} s^{(i)}(h) &:= \sum_k \alpha_k \hat{h}_k + \sum_k q_k^{(i)}(\hat{h}_k) \\ &= \sum_k \alpha_k \hat{h}_k + \sum_k c_k w_k^{(i)} \left(\log(\hat{h}_k^{(i)} + \epsilon) + \frac{1}{\left|\hat{h}_k^{(i)} + \epsilon\right|}(h - \hat{h}_k^{(i)}) \right). \end{aligned} \tag{4.59}$$

Solve the following optimization problem:

$$\underset{h}{\text{minimize}}\, s^{(i)}(h_i) \tag{4.60}$$

subject to

$$h_k \leq \overline{h}_k \qquad \forall\, k \text{ and } h_k > 0 \tag{4.61a}$$

$$h_k \geq \underline{h}_k \qquad \forall\, k \text{ and } h_k > 0 \tag{4.61b}$$

$$f_{m_{\mathcal{A}_i}} \geq \underline{f}_{m_{\mathcal{A}_i}} \tag{4.61c}$$

$$\sum_i w_k \log(h_i) \leq N. \tag{4.61d}$$

Denote $h^{*(i)}$ the optimal optimizer. The majorizing surrogate function's optimal value $s^{*(i)}$ is defined to be

$$s^{*(i)} := s^{(i)}\left(h^{*(i)}\right),$$

and set

$$\hat{h}_k^{(i+1)} \leftarrow h^{*(i)}.$$

Step 3) *Update weighting factors w_i and construct a new surrogate function*: Update the weighting coefficients,

$$w_k^{(i+1)} \leftarrow \frac{1}{\log\left(\hat{h}_k^{(i+1)} + \epsilon\right)}. \tag{4.62}$$

Update the function $f^{(i)}$ with the new $w_k^{(i)}$

$$f^{(i+1)}(h) = \sum_k \alpha_k \hat{h}_k + \sum_k c_k w_k^{(i+1)} \log\left(|\hat{h}_k| + \epsilon\right) \tag{4.63a}$$

and its surrogate majorizing objective

$$\begin{aligned} s^{(i+1)}(h) &= \sum_k \alpha_k \hat{h}_k + \sum_k q_k^{(i+1)}(h_k) \\ &= \sum_k \alpha_k \hat{h}_k + \sum_k c_k w_k^{(i+1)} \left(\log\left(\hat{h}^{(i+1)} + \epsilon\right) + \frac{1}{\left|\hat{h}_k^{(i+1)} + \epsilon\right|}\left(h - \hat{h}^{(i+1)}\right) \right). \end{aligned} \tag{4.63b}$$

Step 4) *Repetition*: Update the iteration counter

$$i \leftarrow i + 1,$$

and repeat *Step 2*) to *Step 3*) until the surrogate's optimal value changes are smaller than a threshold ζ

$$\Delta s^{*(i)} = \left| s^{*(i+1)} - s^{*(i)} \right| < \zeta,$$

Then, the optimal solution $\hat{h}^*$ is

$$\hat{h}^* \leftarrow h^{*(i)}, \tag{4.64}$$

$$\hat{s}^* \leftarrow s^{*(i)} \tag{4.65}$$

and the optimal value $\hat{f}^*$ is

$$\hat{f}_c^* \leftarrow f_c(\hat{h}^*), \tag{4.66}$$

4.3. Implementation of the Proposed Optimization Algorithms in Cloud Computation

There many computations involved in forming and solving the optimization problems. It is evident from Figure. 4.2 that three main computational processes are involved: *1*) market simulation to obtain a list of working conditions and identification of faults likely to happen in the power system, *2*) time-domain simulation for all possible faults on the working conditions identified in the previous step and identification of the critical scenarios (working

condition / fault pairs) where excessive frequency excursions or RoCoF may occur, and *3*) formation of an optimization problem with the critical scenarios identified from the previous steps and find an optimal solution.

Data-level parallelism The first two computation tasks of market and time-domain simulation need to scan a total of 17520 cases, which is a daunting amount of computation tasks. To facilitate computational speed, a data-level parallelism technique can be used to run multiple market and time-domain simulation processes simultaneously for different combinations of generation and fault profiles.

The data-level parallelism can be visualized as multiple independent pipelines. Each pipeline is an independent executor and fed with a distinct set of data. The pipeline then processes the feed-in data, which is market and time-domain simulation in this case, and output maximum frequency excursion $\max_t|\Delta f_{COI}(t)|$ and maximum RoCoF $\max_t|\dot{f}|$ as computation results. Since each pipeline is independent and fed wth different input data, multiple pipelines are created to run concurrently; thus, the overall computation speed can be improved. The number of "pipelines" one can create depends on the computational power and memory size of the computation hardware.

Thread-level parallelism Suppose the dynamic programming-based method is chosen to find the most economical plan of virtual inertia installation. The multi-threading technique can be used in solving the optimization problem of the sub-optimization level, in that each thread takes a $\text{sol}^{(i-1)}$ from the set $\texttt{SOL}^{(i-1)}$, form and solve an optimization problem (4.40)–(4.41). Unlike the data-level parallelism, each computation threads share resources of single or multiple cores and can access and write a shared process memory space, e.g., set `BIN` and set $\texttt{SOL}^{(i)}$.

Though computational parallelization increases the computational time efficiency, the improvement on the computation speed comes to a limit set by the hardware. In order to facilitate parallelism of a larger scale, the cloud computation could be used [77].

Cloud platforms Cloud computing is defined as "a model for enabling ubiquitous, convenient and on-demand network access to a shared pool of configurable computing resources

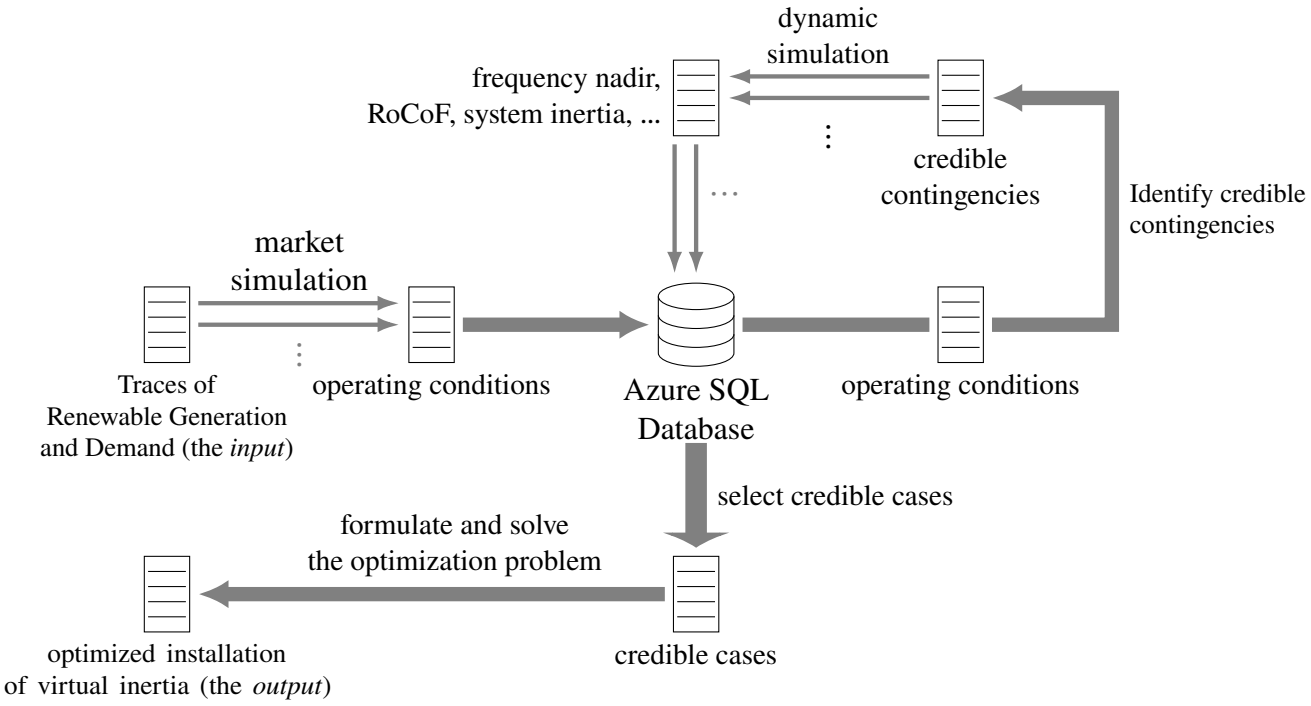

Figure. 4.5.: The implementation of solution platform.

that can be rapidly provisioned and released with minimal management effort from the user side and minimal services provider interaction" [78]. The basic technologies involved in cloud computing have been existing for decades and are not fundamentally new. Cloud computing provides on-demand computing capacities in terms of computing time, computational speed to the users. It is considered the most cost-efficient way of realizing large-scale parallelism.

The AEMO, the TSO of the Australian power system, provides system loading and renewable generation forecast for each hour of a year [6]. Therefore, the market simulation and time-domain simulation shall be studied on $365 \times 24 \times 2 = 17520$ working conditions against a large number of system faults. From these simulation results, a list of critical cases is to be identified as shown in Figure. 4.2. The amount of computation involved in this process is significant. Were a single PC used to handle the amount of computation, it would need weeks of computational time. By spawning large-scale paralleling processes and threads, a cloud computing framework can easily increase the computation speed by five-fold.

The design of the cloud computational framework of this thesis work is plotted in Figure. 4.5

in a functional representation, where each "node" represents an entry of data input/output. The computations applied to these data entries are represented as an operation and labelled beside the thick arrows that symbolize information transformation. The parallel arrows indicate the computation steps which can be parallelized at data-level, i.e., the market and time-domain simulation.

In order to spawn as many parallelized computations as possible, the platform is run in a computation cloud (`Microsoft Azure`). The cloud platform has the computational capacity to support as many parallelized computations as the budget allows.

`Docker` technology Since its debut in 2013, the avant-garde technology of `Docker` container quickly rose as an efficient and elastic way to achieve data-level parallelism. The `docker` technology evolves from the OS-level virtualization that encapsulates all required binary codes, compilers, libraries, configuration files, etc. for the computation process to execute. Therefore, a `docker` container is seen as an independent unit, which can be placed at any compatible computational platform regardless of their underlying hardware and operating systems.

Compared to the full-scale virtualization, `docker`'s virtualization is a partial one, which provides an extent of virtualization just enough to isolate a running process. The underling system calls are handled directly by the host operating system. For this reason, `docker` technology is more lightweight and can exploit the host's full computational power.

The programs of market and time-domain simulation, their dependencies, and their working environment are all scripted into a `docker` imagine that can be easily cloned and version controlled. From the `docker` imagines, a number of docker containers can be created and run on any compatible hardware, e.g., PC, workstation, HPC, and cloud platform, where the `docker` system is installed.

Chapter 5

Case Study

Finally, the above-mentioned computational scheme was tested on a simplified model of Southeast Australia interconnections [6], which had been widely used in many stability studies related to virtual inertia compensation [8], [16]. The result was compared with other schemes of virtual inertia placement (e.g., Poolla's scheme [17]) to show that the proposed method can indeed produce a more economical plan of virtual inertia installations while ensuring satisfactory improvement on the system's frequency response.

5.1. The Test System

The benchmark system In this case, the simplified 14 machine system of Southeast Australia interconnections was taken as the test system by simplifying the lower-level connections (e.g., distribution networks) as either constant loads or synchronous generators. Figure 5.1 is a single line diagram representation of the simplified test system. The system is composed of four coherent areas that roughly correspond to Australian geographic administrative divisions. They are New South Wales (NSW), Victoria (VIC), Queensland (QLD), and South Australia (SA). The four coherent areas are numbered in Roman numerals from Area I to Area IV, respectively. Renewable generations of the CIG type are fitted at 14 locations in the power system according to the AEMO's forecast and development plans [6] to reflect the penetration level of wind and solar generations forecast for the decades to come. These converter-interfaced renewable generations are marked with "$\overset{\sim}{=}$" and highlighted in Figure. 5.1.

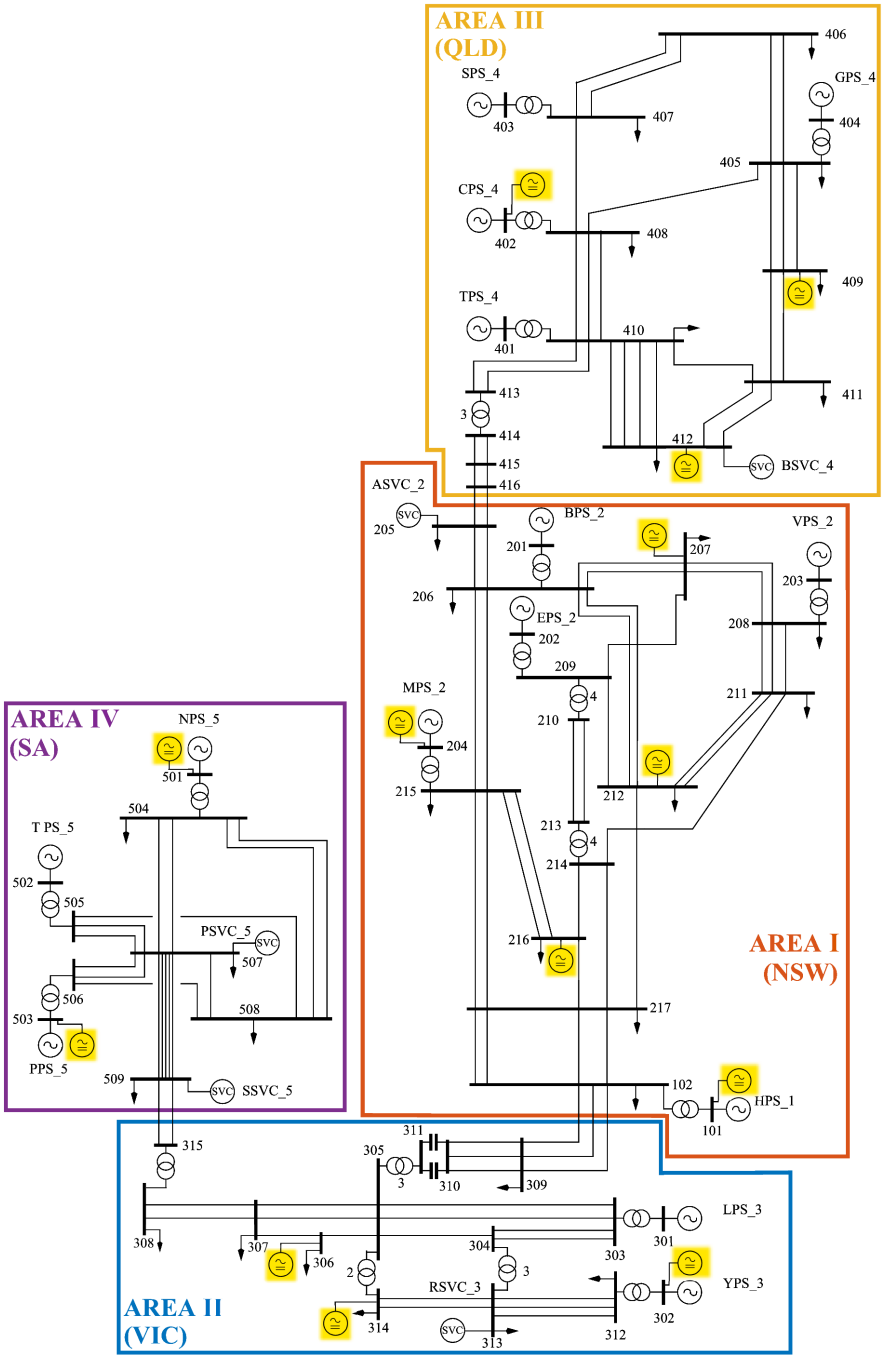

Figure. 5.1.: 4 area, 59 bus simplified Southeast Australian Power System modified with inclusion of 13 candidate renewable generations, highlighted and indicated with ⏦ symbols.

Table. 5.1.: Ratings of synchronous generations.

Area	Bus	Rating (MW)	Percentage of regional demand
Area I	101	333.3×12	53.32%
	201	555.6×6	53.32%
	202	666.7×6	53.32%
	203	555.6×5	37.04%
	204	666.7×6	53.32%
Area II	301	666.7×8	108.89%
	302	444.4 × 4	36.30%
Area III	401	444.4×4	39.31%
	402	333.3×3	22.11%
	403	444.4×4	39.39%
	404	333.3×6	44.22%
Area IV	501	333.3×2	38.45%
	502	250×4	57.68%
	503	166.7×6	57.69%

Setups of market and time-domain simulation Each synchronous and renewable generator in the test system consists of multiple generation units in the mathematical models of market and time-domain simulations, rather than a single lumped representation as in many studies of time-domain simulation. Table 5.1 shows the number of the parallel-connected generation units at each generation bus.

This setup benefits from two aspects. On the one hand, a single bus in the Southeast Australia interconnections, Figure 5.1, is a representation of a bus bar within a physical power plant, e.g., generation stations and substations. The bus bar is the coupling point of multiple power generation units. Not all synchronous generators are switched on at all times. The on/off status of generators may affect the system's total inertia level, as shown with the orange line in Figure. 5.2. Were only one lumped representation model used, the level of rotational inertia at the bus would be overestimated, as shown with the flat blue line. Therefore, the on/off status behind the generation bus should be modelled explicitly in the market simulation.

On the other hand, differentiation of different generation units behind a bus helps separate different identities of the running cost, turn-on, turn-off cost etc. for each of the generation units and can better approximate the real electricity market.

Table. 5.2.: Ratings of renewable generations.

Area	Bus	Rating (MW)	Percentage of regional demand
Area I	101	600×2	16%
	204	440×3	17.51%
	207	660×2	16%
	212	333.3×2	8.89%
	216	333.3×2	8.89%
Area II	302	600 × 1	12.25%
	306	550 × 2	22.45%
	314	333.3×2	13.61%
Area III	402	333.3×2	14.73%
	409	450×1	9.95%
	412	600×3	39.79%
Area IV	501	333.3×2	38.45%
	508	333.3×2	38.45%

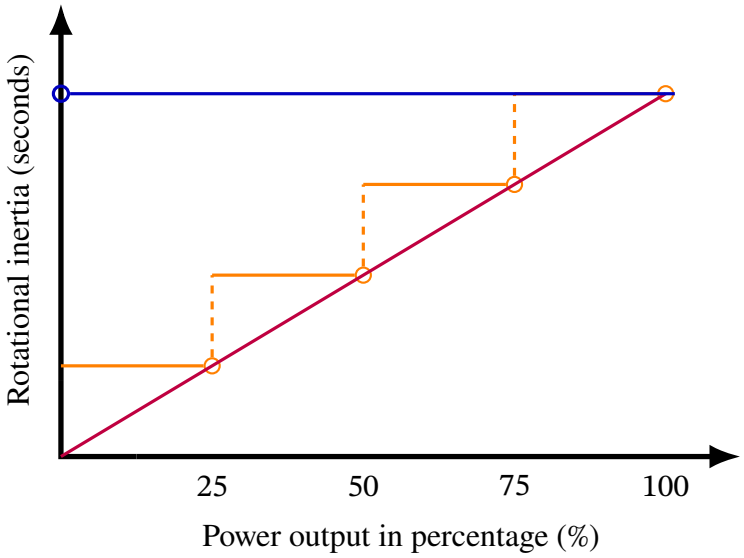

Figure. 5.2.: Rotational inertia versus percentage of committed power generation.

In the time domain simulation, The SG units were modelled in standard five-order dynamic model [79], [80]. Each generator was assumed equipped with a governor and a PSS. In the market simulation, all SG generation units were assumed associated with identical quadratic operational costs and startup & shutdown costs for simplicity. In addition, the power generation units at a bus were required to provide an extra 10% over the dispatched

amount of active power output as a spanning reserve for the primary frequency control.

Renewable generations except for the hydro-power are assumed to be of converter-interfaced type. As discussed above, a parallel connection of multiple CIGs units is used to model the arrays of solar panels or clusters of wind turbines in a wind park. Unlike the case for SG, the number of generation units in parallel connection does not reflect the real system configuration but is chosen to be sufficiently large to approximate the real electricity market. In this case, the running cost, start-up, and turn-off costs for the renewable are set to be zero to encourage producing power generation profiles with the highest possible level of renewable penetration. Table 5.2 lists the number of CIG generation units at a generation bus.

In the time-domain simulation, virtual inertia emulation on a CIG unit is assumed of grid-forming type. In this case study, the matching control introduced in Chapter 2 is used. External energy storage, e.g., battery storage, provides the energy reserve for the virtual inertia emulation. The MPPT control provides a constant reference of active power output for these CIG units. For the sake of simplicity, the Low Voltage Ride Through (LVRT) capacity is neglected, and the switching dynamics of the power converter are omitted in the averaging switching model.

The loads are converted to constant impedance in the time-domain simulation.

Load and renewable generation profile AEMO, the operator of the Southeast Australian interconnection, provided load and generation forecast at every generation bus and major load feeder [6]. The load and generation forecasts are plotted in the in Figure. 5.3 and 5.4 at each half-hour in a year for each coherent area and the whole power system respectively.

Figure. 5.5 and Figure. 5.6 are renewable generation available to dispatch in each coherent area and the whole power system at each half-hour in a year.

5.2. Market and Time-Domain Simulation

As the first step of our solution framework (Figure. 4.2) for planning the optimal virtual inertia installation, the market simulation was conducted to generate a list of steady-state

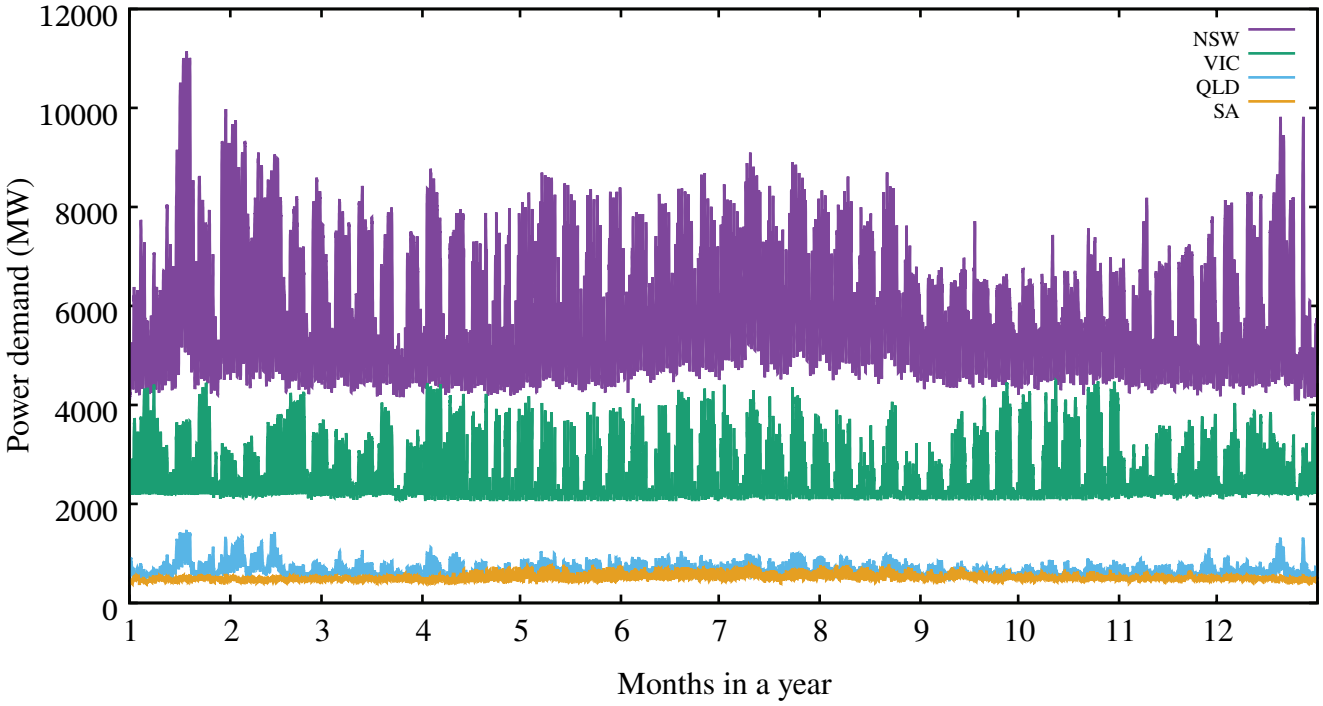

Figure. 5.3.: Traces of load demand in each area.

operating points. All standard constraints of market simulation were be observed.

A piece of software, `MATPOWER`, was used for the market simulation. `MATPOWER` is a high-quality `MATLAB`-based package for static power flow analysis and optimal generation dispatch. Based on the system loading forecast and the maximum amount of active power output available to dispatch at the CIG units, market simulation gave both the on/off status of each generation unit and their power output being dispatched.

From the status of generation unit commitment, the amount of physical and virtual inertia can then be computed. The physical inertia, without the compensation of virtual inertia, can reach as low as 119.6329 s in a 100 MW based per-unit system, as shown in Figure. 5.7. In comparison, were SG the only type of active power generation in the test system, the physical inertia would be at least 209.9695 s in the worst case. The results also demonstrated significant variations of system inertia in a day. The inclusion of renewable generation units nearly doubles the daily system inertia variation.

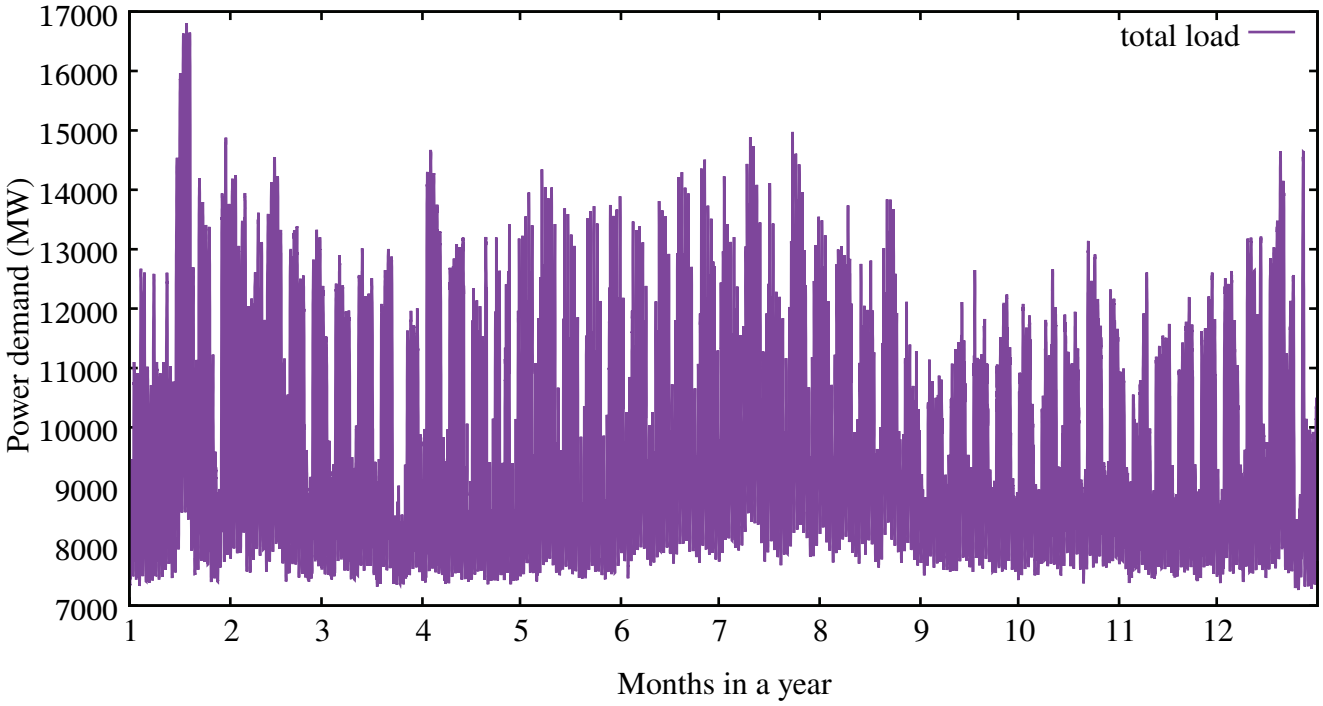

Figure. 5.4.: Traces of total load demand.

Then, in the next step, time-domain simulations were conducted on these working conditions given by the market simulation against different fault scenarios. In this study, the system faults were selected to be the trip of a single generation unit or a transmission tie line. A three-second post-fault response was simulated to reveal the maximum frequency excursion $\max_t|\Delta f|$ and RoCoF $\max_t|\dot{f}(t)|$ for each combination of working and fault scenarios. Meanwhile, $y_i(0)$ in the `GetMetric` of Algorithm 3.1 was computed with the dynamic states immediately before and after the fault occurrence and registered for the evaluation of inertia response metric $f_{m_{\mathcal{A}_i}}$ in later steps to solve the optimization problem (4.9)–(4.10). Finally, critical scenarios were identified as those where an excessive level of frequency deviation and RoCoF can be found. The critical scenarios were marked with red vertical lines in Figure. 5.7. The details of 10 most critical scenarios are listed in Table. 5.3.

The market simulation and, especially, time-domain simulation are a computationally intensive step. There are a total of 17520 ($2 \times 24 \times 365$) instances of market simulation at each half-hour of a year. For the time-domain simulation, there are as many as 420480

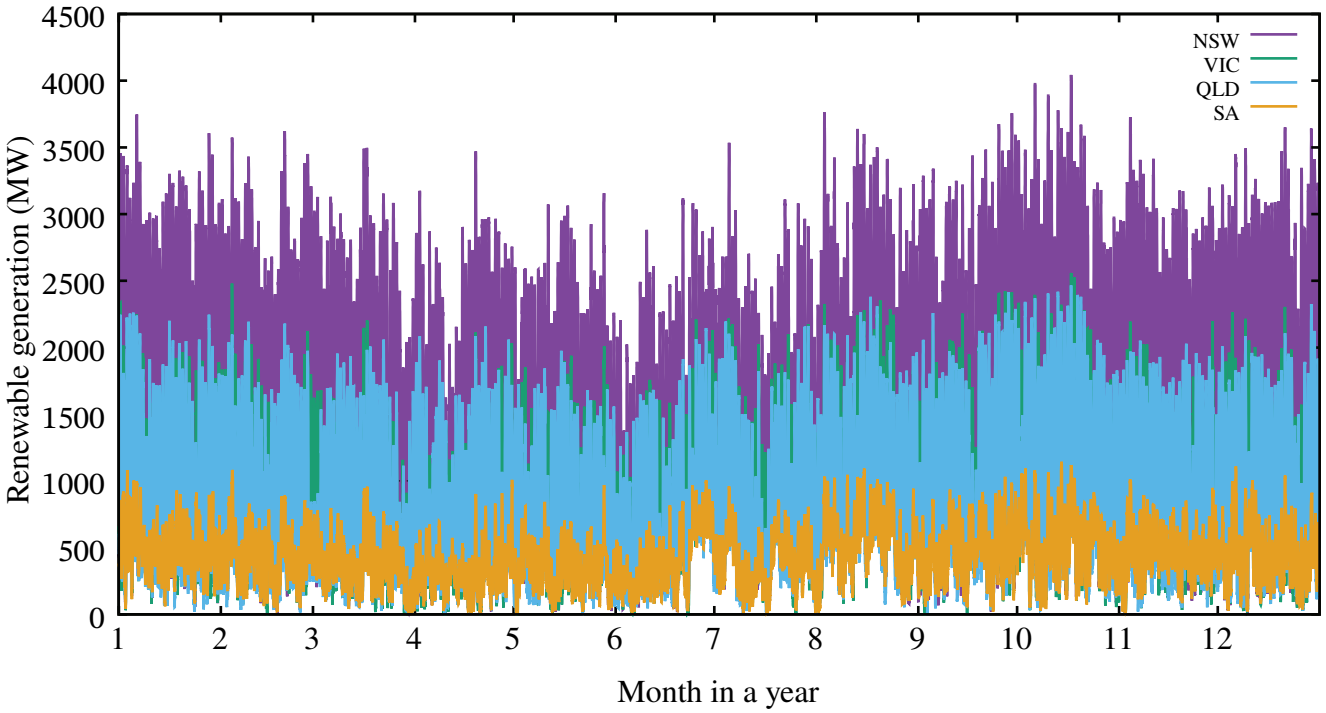

Figure. 5.5.: Traces of renewable generation in each subsystem area.

Table. 5.3.: Selection of critical cases.

Date-Time (MM-DD HH:MM)	$\|\Delta f\|$	**Inertia (w/ renewable)**	**Inertia (w/o renewable)**
10-13 12:00	0.558 Hz	119.81 s	206.72 s
09-04 15:30	1.188 Hz	116.03 s	196.72 s
09-04 15:00	1.800 Hz	146.03 s	196.72 s
04-07 12:00	0.490 Hz	142.92 s	213.84 s
12-09 10:30	1.392 Hz	119.81 s	196.72 s
09-30 11:30	0.552 Hz	119.81 s	196.72 s
09-29 07:30	2.257 Hz	119.81 s	196.72 s
04-07 13:30	1.781 Hz	142.92 s	213.84 s
09-04 12:30	1.598 Hz	140.25 s	204.50 s
11-04 07:00	0.586 Hz	118.58 s	196.72 s

$(2 \times 24 \times 365 \times 24)$ considering every possible combinations of working conditions and fault scenarios.

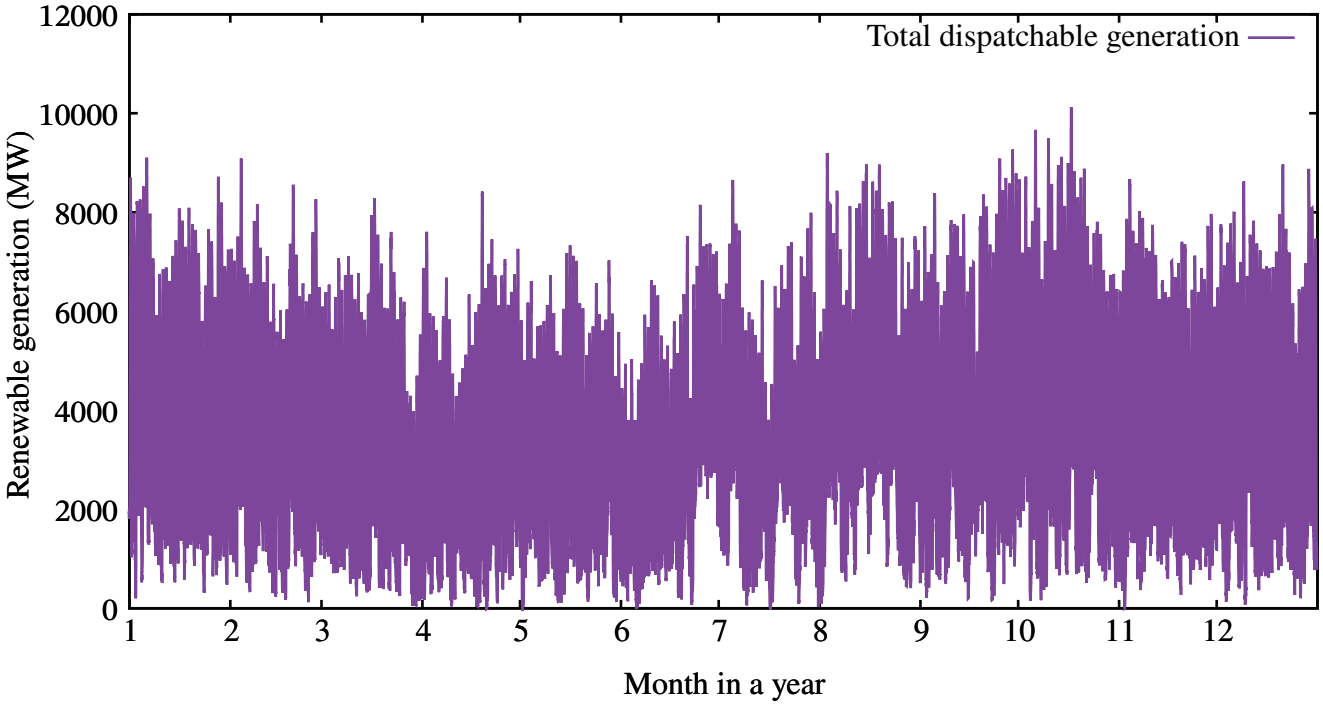

Figure. 5.6.: Traces of total renewable generation.

In order to facilitate the computational speed, the data-level parallel computation structure, discussed in Section 4.3 and shown in Figure. 4.5, is implemented on the `Microsoft Azure` cloud computation platform. 17520 working conditions were split into six parts, and six independent computational "workers" were spawned on the cloud computing platform to process the simulations on the six disjoint input sets concurrently. Thanks to the parallelism, all the market and time-domain simulations were finished within a week. Otherwise, the whole computation may take around a month to complete.

In the end, the market and time-domain simulation steps identified in total 60 working conditions where significant frequency deviation and RoCoF can occur.

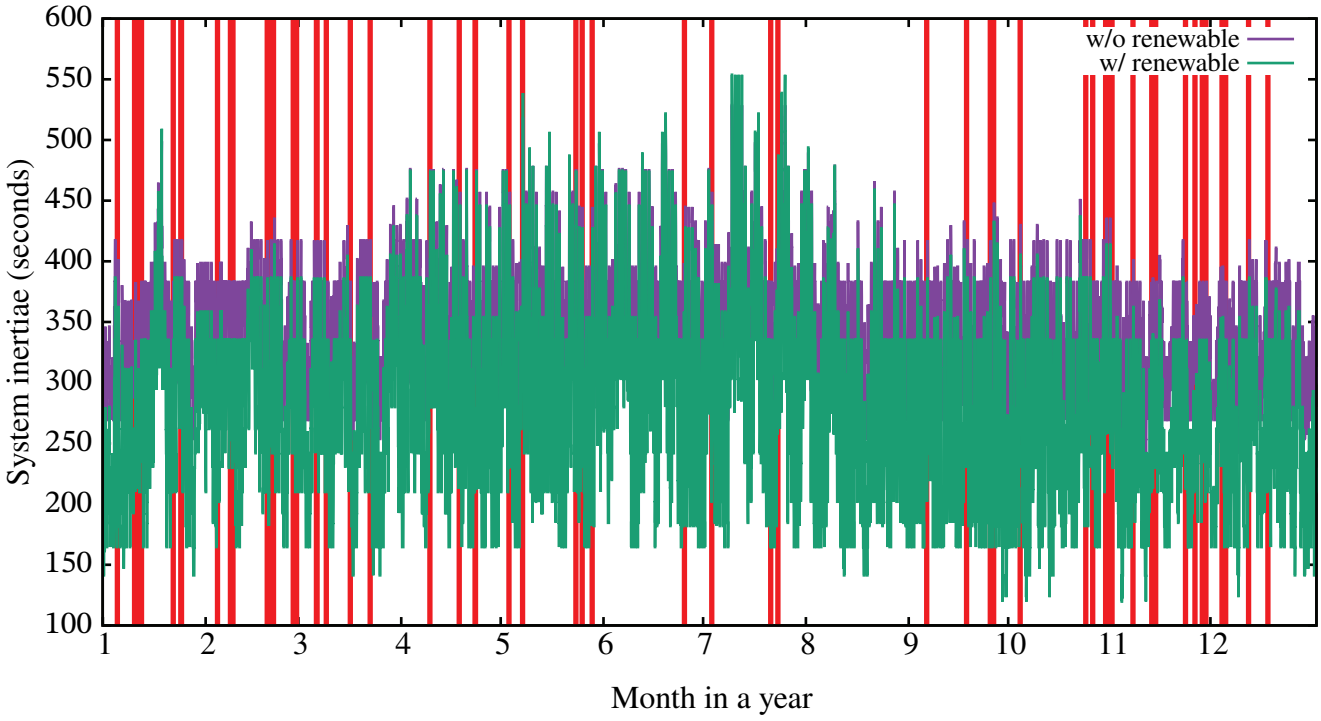

Figure. 5.7.: Changes of system's inertia in a year with granule sizes of 30 minutes. The red vertical lines indicate the critical scenarios. The vertical lines refer to critical scenarios. These scenarios are later used to evaluate $f_{m_{\mathcal{A}_i}}$ in the frequency constraints (see also (4.9)–(4.10)).

5.3. Results and Performance Comparisons

Finally, a mathematical problem (4.9) to (4.10) was formulated with the above identified critical cases to plan the optimal virtual inertia installation. The `GetMetric` procedure of Algorithm 3.1 helped compute the proposed metric of inertia response of a coherent area on these critical cases. The expected frequency response improvement was translated as a constraint in terms of the newly proposed metric.

The cost function $f_{c_{\mathcal{A}_k}}$ was selected to be of affine type as in (4.8):

$$f_c(\mathcal{J}, h) = \sum_{j \in \mathcal{J}} \alpha_j h_j + c_j,$$

where the per-second α_j and fixed term of investment c_j are listed in Table. **??**. These values

Table. 5.4.: Optimization parameters for the candidate Buses of virtual inertia installation.

Area	**No.**	**Bus**	α_i	c_i	**Area**	**No.**	**Bus**	α_i	c_i
Area I	1	101	1.0	10.0	Area III	9	402	1.0	10.0
	2	204	1.0	10.0		10	409	1.0	20.0
	3	207	1.0	20.0		11	412	1.0	10.0
	4	212	1.0	10.0	Area IV	12	501	1.0	10.0
	5	216	1.0	10.0		13	503	1.0	10.0
Area II	6	302	1.0	10.0	———				
	7	306	1.0	24.0					
	8	314	1.0	20.0					

were selected based on the estimates in Section 2.1.2. The candidate locations for the virtual inertia installation include the renewable generation buses with power converters in place, which may help to reduce the fixed-term investment c_j, and also some selected load buses.

The under limits $\underline{f}_{m_i}$ of constraints (4.10e) on the system's inertia response were tuned manually via trial-and-error method, so that COI frequency variations of all coherent areas are within a limited range (Table 1.1). In this study case, the maximum amount of virtual inertia that can be install at a candidate location, i.e., $\overline{h}$ in (4.10b), was set to be 30 s (in a 100 MW based per-unit system), and the maximum number of virtual inertia installations, i.e., N in (4.10d), was set to 6. This mixed-integer optimization problem was solved using the sparsity promotion method (Sub-Section 4.2.3). The results are listed in the second column of Table. 5.5 named h^*.

Two other methods of planning the virtual inertia installation were also studied compared to the proposed one. The first one is Poolla's method [19]. Unlike the proposed method, Poolla's method does not consider the limits on the number of virtual inertia installations. Instead of optimizing the total investment cost, the sole target of Poolla's method is to achieve the best system-wise COI frequency response. The resulting plan of virtual inertia installation is subject to a limit on the total amount of virtual inertia that can be installed in the system and a set of boxed constraints on the maximum amount of virtual inertia that is physically possible.

Table. 5.5.: Optimal plans of virtual inertia installations.

Bus	$\boldsymbol{h}^*$	$\boldsymbol{h}^*$ **(equal)**	$\boldsymbol{h}^*$ **(Poolla)**
101	0.00 s	13.2 s	4.18 s
204	30.0 s	13.2 s	30.00 s
207	0.0 s	13.2 s	12.60 s
212	30.0 s	13.2 s	24.10 s
216	30.0 s	13.2 s	20.96 s
302	0.0 s	13.2 s	10.15 s
306	21.6 s	13.2 s	29.24 s
314	30.0 s	13.2 s	23.12 s
402	0.0 s	13.2 s	0.66 s
409	0.0 s	13.2 s	0.06 s
412	0.0 s	13.2 s	1.06 s
501	30.0 s	13.2 s	12.48 s
508	0.0 s	13.2 s	2.60 s
cost (m$)	255.6	345.6	345.21

Poolla's method consists in solving the following problem:

$$\underset{h_i}{\text{minimize}} \sum_i \frac{v_i}{m_{0_i} + h_i} \tag{5.1}$$

subject to

$$\sum_i h_i \leq \overline{h}_{\text{total}} \tag{5.2a}$$

$$h_i \leq \overline{h}_i \qquad \forall\, i \in \{1, \ldots, n\} \tag{5.2b}$$

$$h_i \geq \underline{h}_i \qquad \forall\, i \in \{1, \ldots, n\}, \tag{5.2c}$$

where v_i models the "strength of disturbance" at bus i due to a system fault. In practice, the value of v_i is set considering the possibility and severity of all possible faults that may take place in the power system.

Denote $\Delta P_i[j,k]$ the change of active power demand from the i-th generation bus due to the k-th critical fault against the j-th working condition. In the comparative study of Poolla's

method, v_i was chosen as

$$v_i = \underset{j,k}{\text{minimize}} \left(\Delta P_i^{(j)} \right)^2.$$

The changes in the active power demand $\Delta P_i^{(j)}$ at the i-th generation unit under the j-th critical scenario were computed with the pre-fault active power output $P_e(t_{0_+})$ and after-fault output $P_e(t_{0_-})$ from Algorithm 3.1. The j-th critical scenario, denoted as c_j in (4.1), is a combination of critical working condition and fault scenario.

The solution to Poolla's optimization problem (5.1) to (5.2) is shown in the last column of Table 5.5, named "h^* (Poolla)." The virtual inertia installation plan given by Poolla's method assigns installation at all candidate buses. The investment costs required by the optimal solutions of both the proposed and Poolla's method are listed in the bottom row of Table 5.5. The installation plan of Poolla's method requires more cost than that of our proposed method, \$345.21 m versus \$255.6 m. A closer comparison shows that the same generation buses (Bus 204, Bus 212, etc.) were chosen to allocate the most significant virtual inertia installation in both plans.

As the second comparative plan of virtual inertia installation, the same total amount of virtual inertia installation as that required by the proposed method can be equally installed at all candidate buses as listed in the column of Table. 5.5 under the name "h^* (average)." The investment cost of this method is the highest among the three plans.

In order to demonstrate the effectiveness of the proposed method of virtual inertia installation in comparison with other methods, multiple cases of the time-domain simulation were conducted on some of the critical combinations of working conditions and system faults identified in the time-domain simulation Table. 5.3, where the critical operating conditions are identified with "date-time" stamps in the first column. The second column shows the maximum frequency deviation observed at a generation unit when no virtual inertia installations were installed; the third and fourth columns show the amount of system inertia with and without virtual inertia installations.

Table. 5.6.: Reduction of COI frequency deviation in response to an outage of a single generation unit with different plans of virtual inertia installation

No.	Date-time (MM-DD HH:MM)	Fault Gen.	$\|\Delta f\|$ (uncompensated)	$\|\Delta f\|$ (proposed)	$\|\Delta f\|$ (equal)	$\|\Delta f\|$ (Poolla's)	Area
1.	11-04 07:00	508	0.3314 Hz	0.0551 Hz	0.0505 Hz	0.0402 Hz	I
2.	09-30 11:30	508	0.2088 Hz	0.0648 Hz	0.0528 Hz	0.0418 Hz	II
3.	12-09 10:30	412	0.2276 Hz	0.0778 Hz	0.0642 Hz	0.0534 Hz	II
4.	10-13 12:00	412	0.1282 Hz	0.0618 Hz	0.0306 Hz	0.0350 Hz	III
5.	09-29 07:30	101	0.1378 Hz	0.0184 Hz	0.0248 Hz	0.0274 Hz	IV
6.	04-07 13:30	301	0.3224 Hz	0.1812 Hz	0.2102 Hz	0.1676 Hz	II
7.	04-07 13:00	302	0.1430 Hz	0.0632 Hz	0.0686 Hz	0.0602 Hz	II
8.	09-04 15:30	202	0.1810 Hz	0.0800 Hz	0.0944 Hz	0.0706 Hz	I
9.	09-04 15:00	301	0.4472 Hz	0.1636 Hz	0.1920 Hz	0.1846 Hz	II
10.	09-04 12:30	401	0.1270 Hz	0.0322 Hz	0.0220 Hz	0.0248 Hz	IV

5.3.1. Fault I: Trip of a Single Generator

Two types of faults were considered in the time-domain simulation. The first type of fault was the outage of a single generation unit, which disrupted the balance of active power generation and consumption in the power system. The simulation results are listed in Table. 5.6, where the critical combinations of working conditions and fault scenarios are listed in the "Data-time" and "Fault Gen." columns.

The "$|\Delta f|$ (uncompensated)" column in Table 5.6 shows the most significant amount of COI frequency deviations of four coherent areas in the original power system without any virtual inertia installation. The corresponding coherent areas where the COI frequency deviation was found to be the largest are listed in the "Area" column in Table. 5.6.

The virtual inertia generation effectively reduces the frequency deviation. The maximum COI frequency deviations of the test system are listed in columns, "$|\Delta f|$ (proposed)," "$|\Delta f|$ (equal)," and "$|\Delta f|$ (Poolla's)" under the optimal plan of virtual inertia installations given by the proposed method, installing virtual inertia equally at all candidate buses, and Poolla's method, respectively. The results show that virtual inertia installations can significantly reduce COI frequency. The virtual inertia installation of the proposed method limited COI frequency variations within $\pm$0.1 Hz in all selected cases, except for a few exceptions. The overall performance of the optimal plan of virtual inertia installation given by the newly

proposed method is similar to Poolla's method, but it requires the lowest amount of investment cost among the three.

Furthermore, the simulated response of COI frequency of four coherent areas are plotted in Figure. 5.8 to Figure. 5.11 for the 5-th case in Table 5.6. On this working condition, the system has a total system loading of 7382.7 MW of which 64.73% are provided by renewable generations. The system fault was selected to be a trip of a 600 MW generation unit at Bus 101 at time $t = 1$ s. The test system remained synchronous and settled at a new frequency value in a new steady-state even without any virtual inertia compensation. However, as shown in Figure. 5.8 to Figure. 5.11, an excessive level of frequency deviation and RoCoF were observed during the transitory period.

As shown in the plot of CIG frequency of Area I (Figure 5.8), the three schemes of virtual inertia installation all can limit the maximum frequency deviation within a range of ± 0.03 Hz in all coherent areas. The virtual inertia installation plans of the proposed method gave a smooth frequency transient comparable to that of Poolla's method.

For Area II (Figure. 5.9), the COI frequencies of inertia compensated systems were all within the tolerance band of ± 0.02 HZ. In comparison, the COI frequency deviation of the uncompensated system can be as high as 0.042 Hz. The virtual inertia installation given by the Poolla's method gave the best result. It was followed by the optimal installation plan given by the proposed method.

Figure 5.10 shows the plots of COI frequencies of Area III. For Area III, even the uncompensated system exhibited a satisfactory response of COI frequency. Therefore, both the proposed and Poolla's methods did not assign much virtual inertia installation in Area III, as shown in Table. 5.5. The best performance was given by installing virtual inertia installation equally at all candidate buses.

The COI frequency transients of Area IV are plotted in Figure. 5.11. In this case, the best performance was achieved with the optimal plan of virtual inertia installation given by the proposed method and by installing an equal amount of virtual inertia installation at all candidate buses. Nevertheless, all three methods could effectively reduce the frequency to ± 0.05 Hz from ± 0.14 Hz if no virtual inertia is installed.

In summary, the power system can significantly improve its frequency dynamics with any plan of virtual inertia installation. However, the virtual inertia installation plan of the

proposed method demonstrated a performance no worse than that of Poolla's method but required less investment (Table. 5.5).

Moreover, these observations corroborate the statement made in Chapter 3 when deriving the inertia response dynamic: the amount of physical or virtual rotational inertia in the power system does not change the system's frequency stability, but it can improve the transitory process.

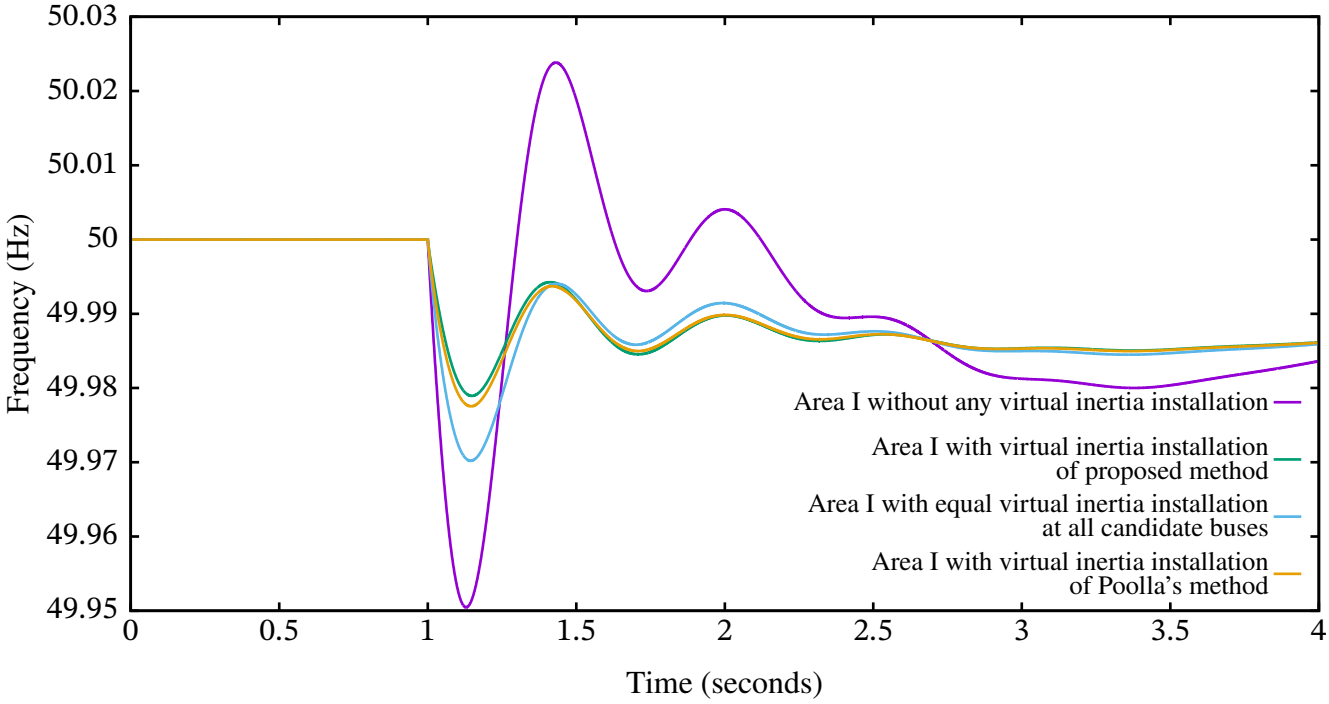

Figure. 5.8.: The COI frequency response of Area I for a selected fault scenario.

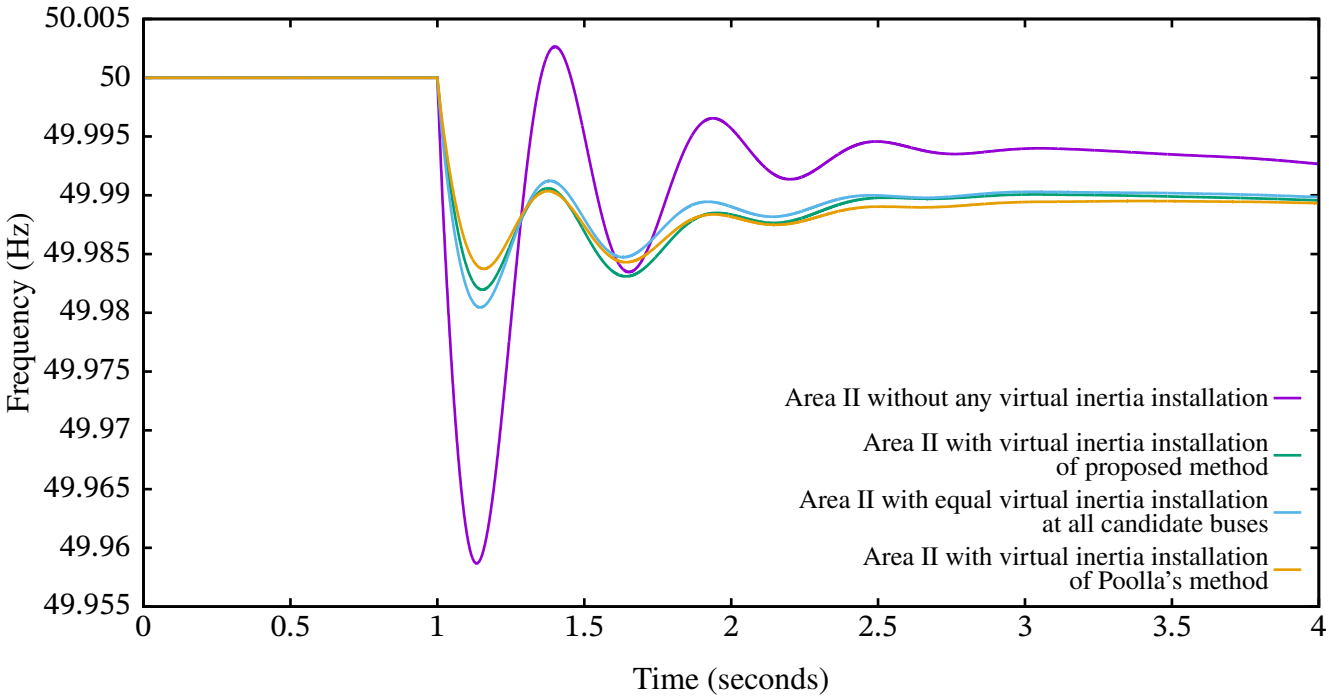

Figure. 5.9.: The COI frequency response of Area II for a selected fault scenario.

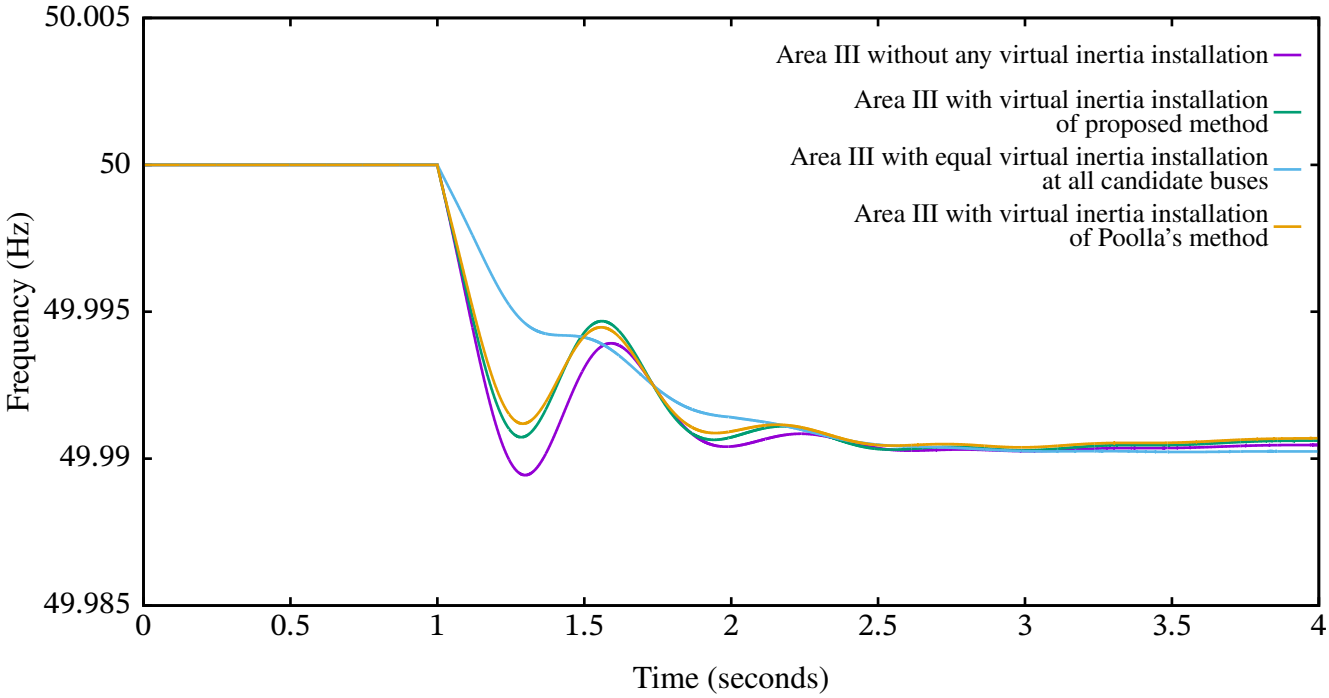

Figure. 5.10.: The COI frequency response of Area III for a selected fault scenario.

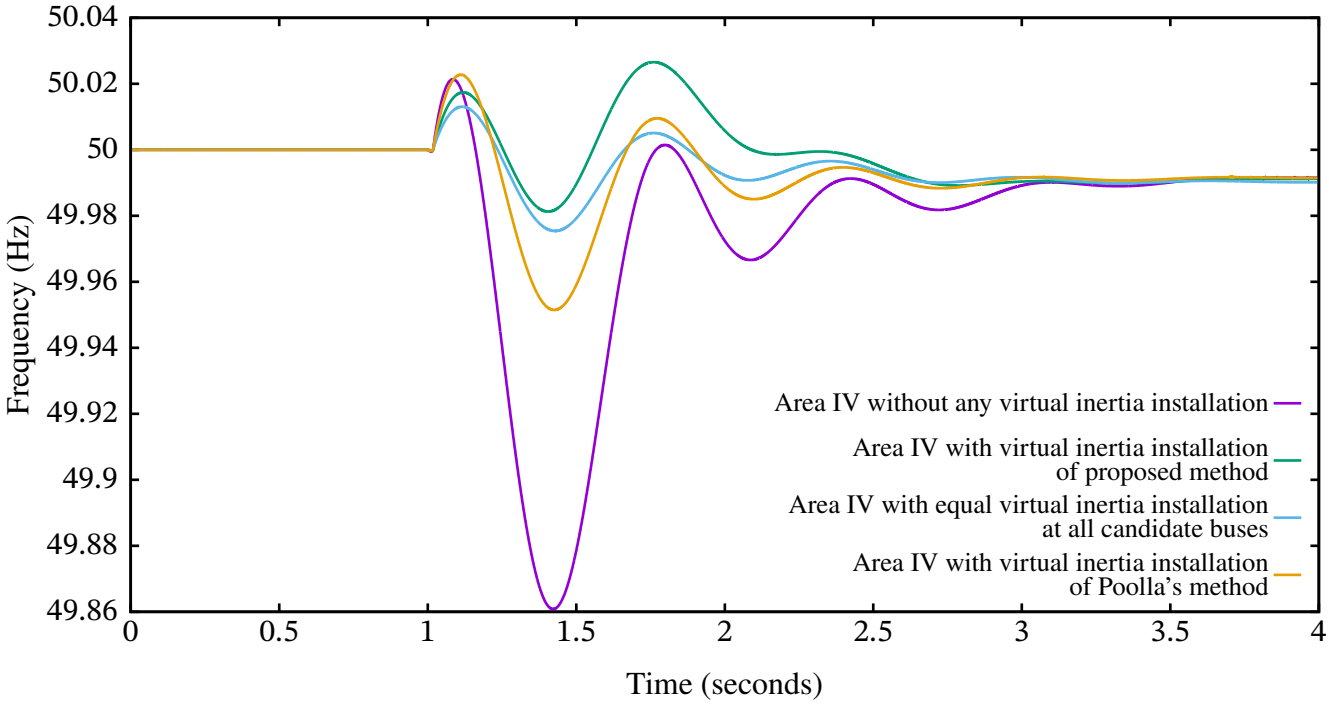

Figure. 5.11.: The COI frequency response of Area IV for a selected fault scenario.

5.3.2. Fault II: Trip of a Single Transmission Line

Time-domain simulations were also conducted for the second type of fault. In this case, the faults were selected to be trips of the most loaded transmission line in the power system. The most loaded transmission lines are identified by their buses at both ends and listed in "from bus" and "to bus" columns in Table. 5.7 for some of the critical working conditions. Compared with the first type of fault, which put active power generation and consumption off balance, the line trip fault may only lead to power transmission through different routes, provided the power transfer capability is assumed sufficiently high at these transmission lines. Therefore, the second type of faults is not as severe as the first type.

As with the previous sub-section, the time-domain simulations were done on the same working conditions in the simplified southeast Australian power system. The line-trip faults were set to occur at $t = 1$ s, and tripped lines would not be re-connected. The time-domain simulation would continue for another 3 s. The line transfer capability was not considered in the simulations. The simulation results of the largest COI frequency deviation $|\Delta f|$ in response to the second type of faults are shown in Table. 5.8 in "Δf (uncompensated)" column for the case with no virtual inertia compensation and in the columns named "$|\Delta f|$ (proposed)," "$|\Delta f|$ (equal)," and "$|\Delta f|$ (Poolla's)" for systems under the optimal plans of virtual inertia installation given by the proposed method, equal virtual inertia installations at all candidate buses, and Poolla's method, respectively. The same virtual inertia installation plans in Table. 5.5 used in time-domain simulation against the first type of fault were used against the second type of fault.

The results show that the system without any virtual inertia installations already exhibited a satisfactory level of COI frequency response. The virtual inertia installation plans of the three methods helped reduced the COI frequency deviation even further. Though the selected fault is in Area II, the most significant COI frequency deviations were found in Area IV. Therefore, Table. 5.8 lists the maximum COI frequency deviations of Area II and Area IV.

Furthermore, the simulated COI frequency response of the four coherent areas are plotted in Figure. 5.14 to Figure. 5.17 for the working condition identified by date-time `09-04 15:30` in Table. 5.8. On this working condition, the heaviest loaded line is a double circuit transmission line connecting Bus 303 and Bus 305. One of the circuits was tripped at time $t = 1$ s, and the tripped line would not be re-closed thenceforth. Since the power transfer

Table. 5.7.: Selection of line trip faults in simulation study

	Data-Time	**Fault line**			
No.	**(MM-DD HH:MM)**	**From Bus**	**To Bus**	**Throughput**	**Inertia (p.u.)**
1.	09-04 15:30	303	305	669.70 MW	166.03 s
2.	09-04 15:00	303	305	677.60 MW	146.03 s
3.	04-07 12:00	303	305	643.91 MW	142.92 s
4.	09-30 11:30	306	307	502.56 MW	119.81 s
5.	09-29 07:30	306	307	500.94 MW	119.81 s
6.	04-07 13:30	303	305	672.03 MW	142.92 s
7.	11-04 07:00	306	307	500.85 MW	118.58 s

Table. 5.8.: Reduction of COI frequency deviation in response to an outage of a single transmission line with different plans of virtual inertia installation

No.	**Date-time (MM-DD HH:MM)**	$\|\Delta f\|$ **(uncompensated)**	$\|\Delta f\|$ **(proposed)**	$\|\Delta f\|$ **(equal)**	$\|\Delta f\|$ **(Poolla's)**	**Area**
1.	09-04 15:30	0.1445 Hz	0.0560 Hz	0.0317 Hz	0.0489 Hz	IV
		0.0782 Hz	0.0292 Hz	0.0350 Hz	0.0257 Hz	II
2.	09-04 15:00	0.1428 Hz	0.0546 Hz	0.0307 Hz	0.0476 Hz	IV
		0.1083 Hz	0.0319 Hz	0.0394 Hz	0.0273 Hz	II
3.	04-07 12:00	0.1442 Hz	0.0562 Hz	0.0317 Hz	0.0491 Hz	IV
		0.1029 Hz	0.0372 Hz	0.0451 Hz	0.0327 Hz	II
4.	09-30 11:30	0.1286 Hz	0.0482 Hz	0.0277 Hz	0.0422 Hz	IV
		0.0093 Hz	0.0028 Hz	0.0023 Hz	0.0027 Hz	II
5.	09-29 07:30	0.1285 Hz	0.0489 Hz	0.0286 Hz	0.0429 Hz	IV
		0.0100 Hz	0.0026 Hz	0.0028 Hz	0.0027 Hz	II
6.	04-07 13:30	0.1431 Hz	0.0565 Hz	0.0319 Hz	0.0494 Hz	IV
		0.0988 Hz	0.0355 Hz	0.0424 Hz	0.0309 Hz	II
7.	11-04 07:00	0.1263 Hz	0.0481 Hz	0.0282 Hz	0.0423 Hz	IV
		0.0097 Hz	0.0026 Hz	0.0028 Hz	0.0025 Hz	II

capacity was not considered in the time-domain simulation, the lost active power transfer via the tripped transmission circuit was shown rerouted into other lines, as shown in Figure. 5.12. The impact of the line trip fault was not only limited to Area II, where the tripped line was

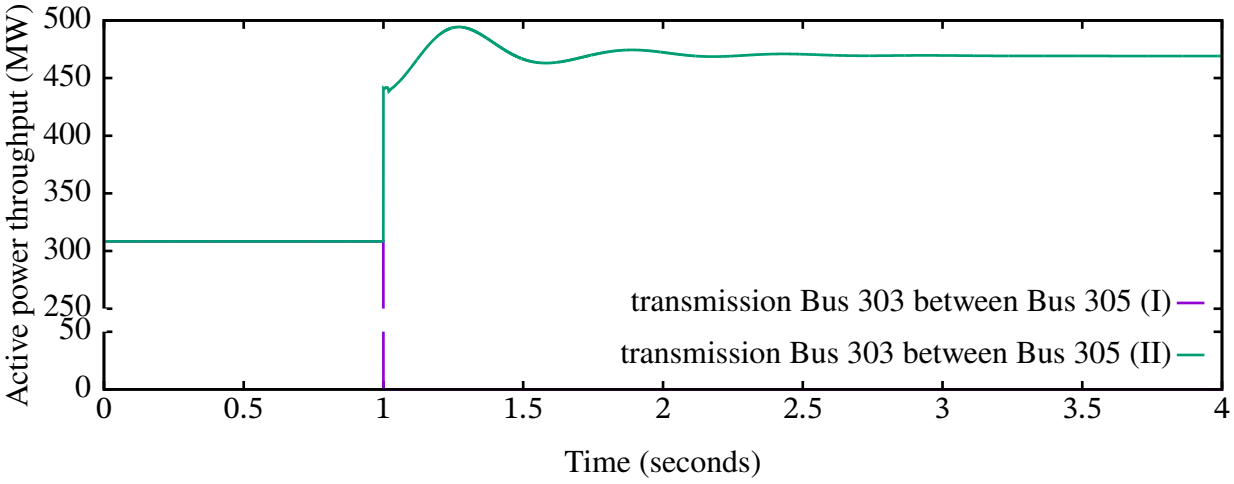

Figure. 5.12.: The active power throughput of the tripped transmission line between Bus 303 and Bus 305 for the selected study case.

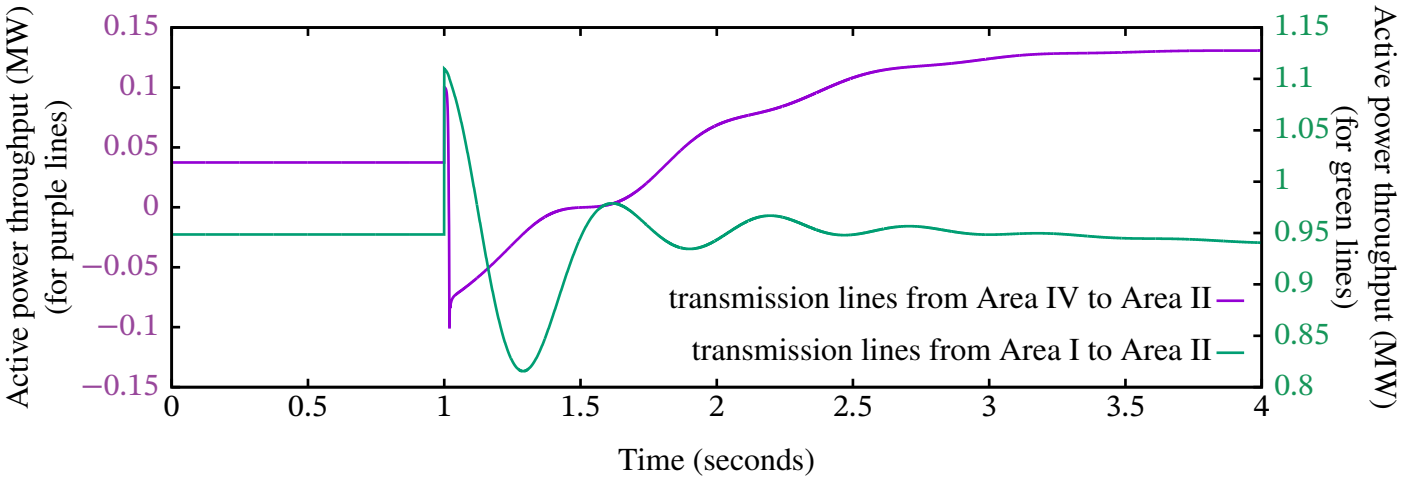

Figure. 5.13.: The active power throughput of the boundary transmission lines from Area IV to Area II for the selected study case.

located, but also had an effect on the adjacent areas as well, as shown in Figure. 5.13. The direction of active power flowing across the boundary between Area I and Area IV was reversed during the transient.

The simulated COI frequency responses are plotted in Figure. 5.14 to Figure. 5.17 for the coherent areas Area I to Area IV. Unlike the outage of a single generation unit considered in the previous study, the trip of a single transmission line did not alter the balance of power

generation and consumption. Therefore, the COI frequencies settled at the same frequency prior to the onset of this system fault in all coherent areas.

The largest COI frequency deviation was observed in Area IV and Area II, and the COI frequency deviation of Area I and Area III were much lower due to the larger electric distance of the two coherent areas away from the tripped line.

Even though the system already had a satisfactory level of frequency response in all coherent areas, the virtual inertia installation further improved the frequency response.

In Area I, the results show that the virtual inertia installation plans given by the proposed and Poolla's methods produced a similar performance that was slightly better than installing virtual inertia equally at all candidate buses.

In Area II, a larger frequency deviation was observed in response to the selected fault. The deviation of the uncompensated COI frequency response reached 0.0782 Hz. All three plans virtual inertia installation reduced the maximum deviation of COI frequency to within $\pm$0.032 Hz. The best result was given by the Poolla's method, which was followed by the proposed method and the equal virtual inertia installation at all candidate buses.

Area III is farthest coherent area away from the tripped transmission line. The disturbances on the frequency response were negligible for the cases without virtual inertia installations. The three plans of virtual inertia installation further improved the response with the equal virtual inertia installation at all candidate buses achieving the best performance.

Finally, the largest COI frequency variations were observed in Area IV. The COI frequency deviation of the uncompensated system was 0.1445 Hz for the case without any virtual inertia installations. The three plans of virtual inertia installations helped reduce the deviation of COI frequency to within $\pm$0.06 Hz. The installation plan given by the proposed method performed slightly worse than the other two plans. The largest COI frequency deviation of Area IV was reduced to 0.056 Hz with the proposed virtual inertia installation. In contrast, the virtual inertia installation plan of Poolla's method and equal installation at all candidate buses limited the maximum deviation of COI frequency to 0.0489 Hz and 0.0317 Hz, respectively.

In conclusion, the second type of faults did not excite as much frequency variation as the first type of faults considered in the previous sub-section. A properly planned virtual

inertia installation was proved to be effective in mitigating frequency disturbance. The plan of virtual inertia installations produced performance similar to Poolla's method but at much less investment (in Table. 5.5).

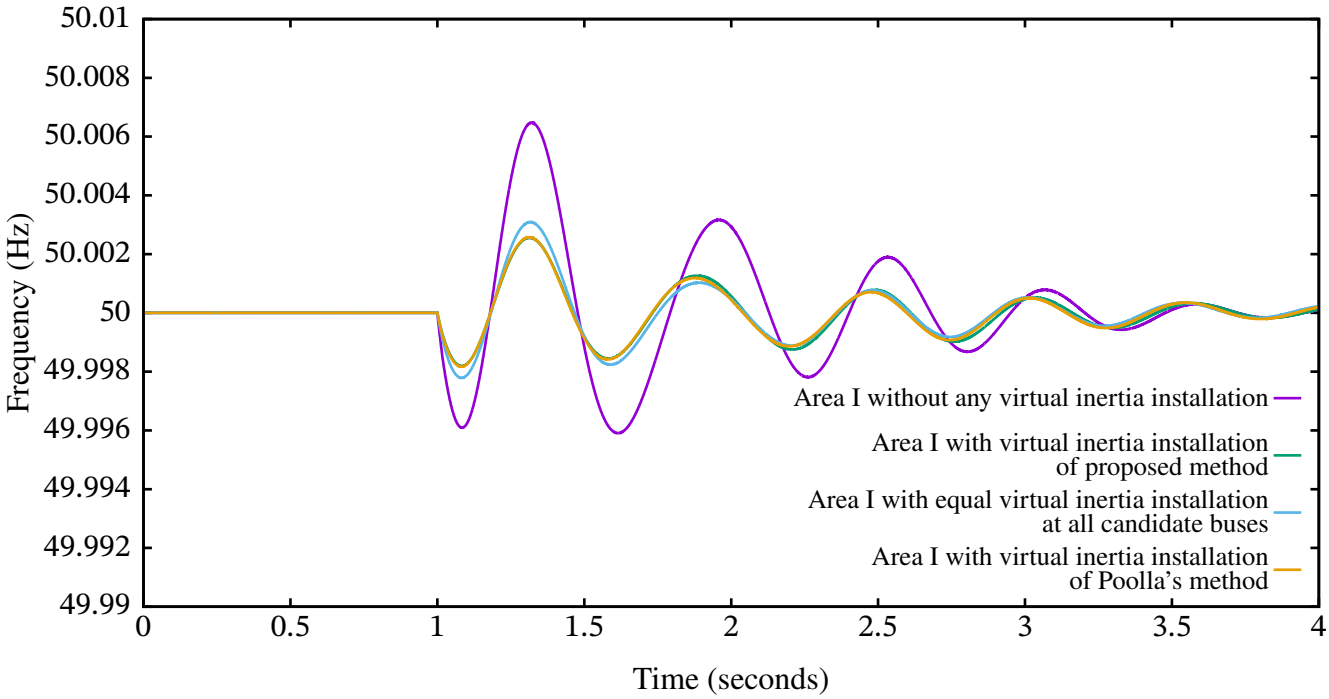

Figure. 5.14.: The COI frequency response of Area I for the selected fault scenario at `09-04 15:30`.

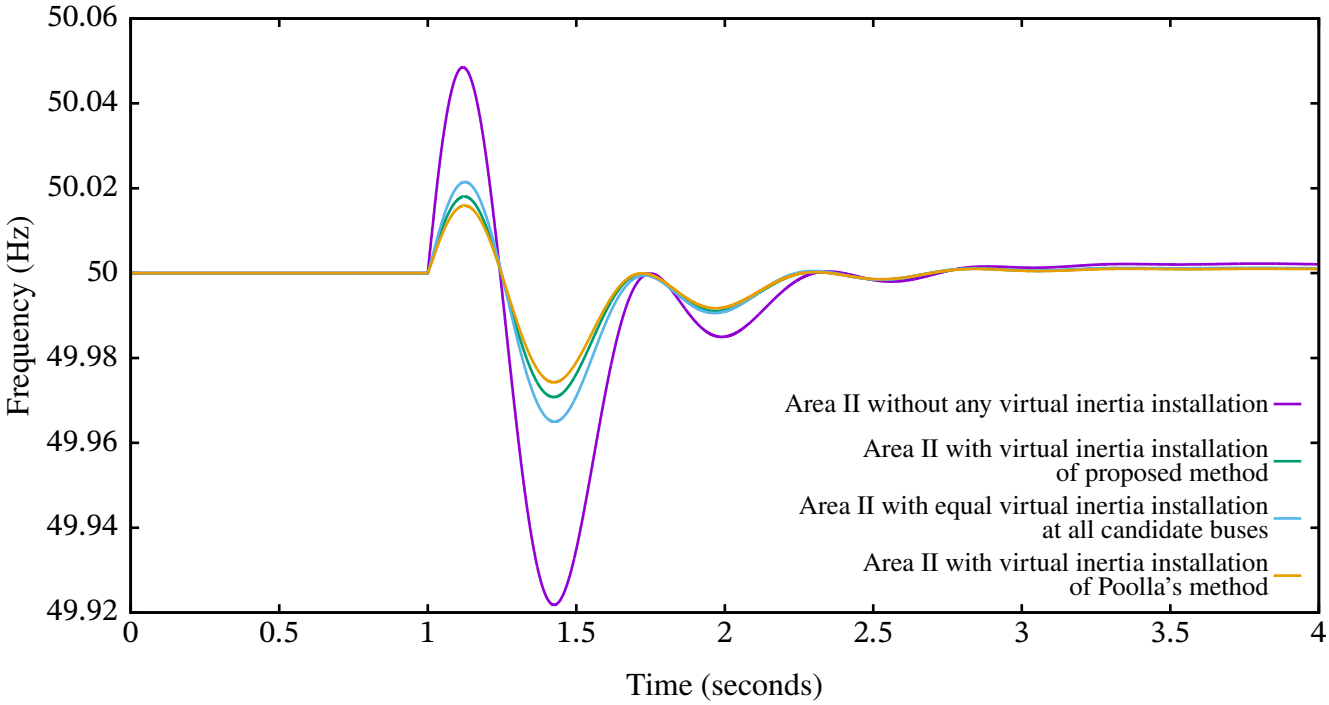

Figure. 5.15.: The COI frequency response of Area II for the selected fault and operating scenario at `09-04 15:30`.

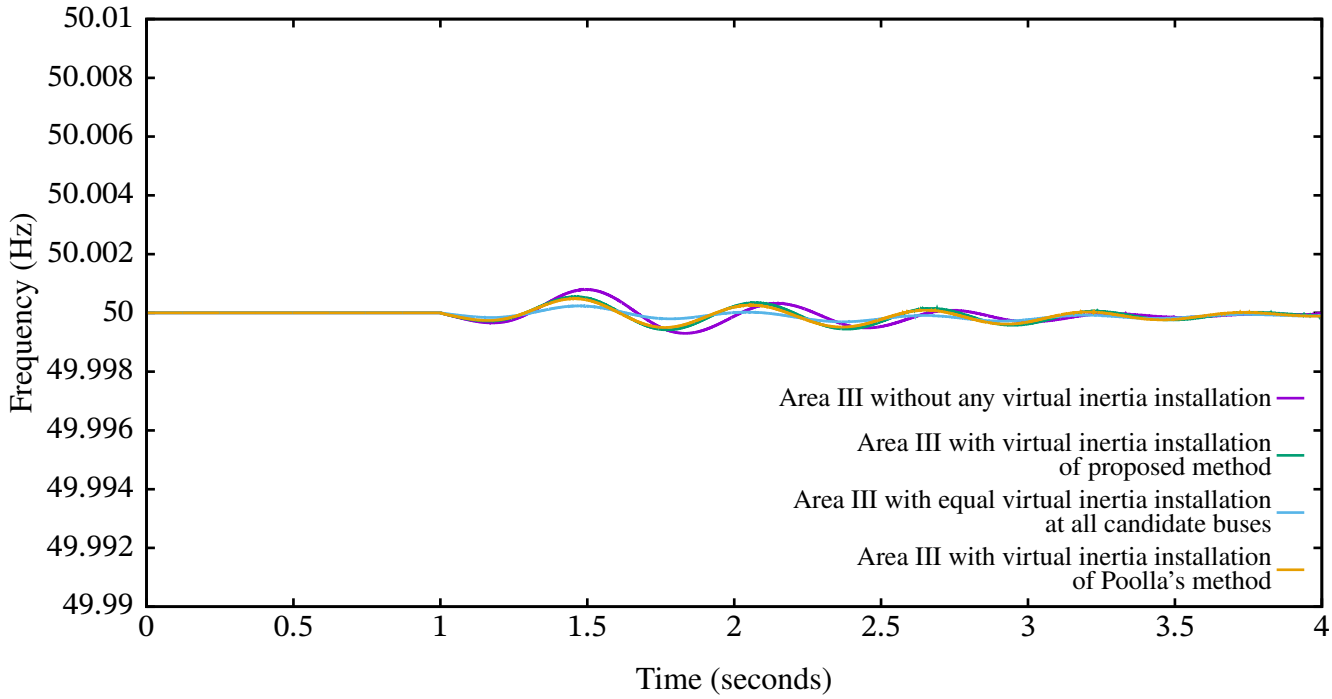

Figure. 5.16.: The COI frequency response of Area III for the selected fault and operating scenario at `09-04 15:30`.

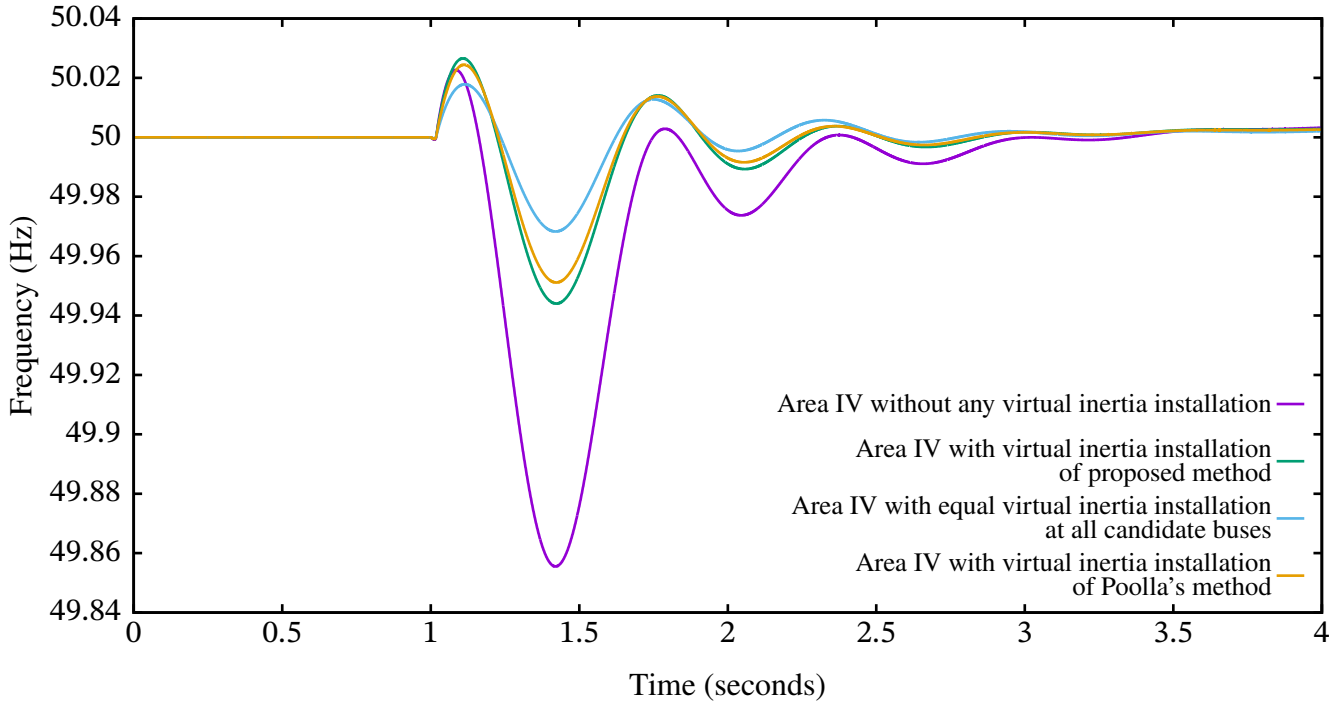

Figure. 5.17.: The COI frequency response of Area IV for the selected fault and operating scenario at `09-04 15:30`.

Chapter 6

Conclusion and Suggestions for Future Works

6.1. Conclusion

With an increasing level of renewable penetration in a modern power system, the system's frequency dynamics deteriorate in terms of higher frequency deviation, larger RoCoF, etc. The degradation in frequency response is often related to reducing system inertia caused by the high level of renewable generation that displaces existing synchronous generators in the power system. Because most renewable generation units are converter-interfaced and stationary, they cannot contribute additional inertia on their own. At the same time, decommissioning synchronous generators takes existing physical rotational inertia out of service. Under the two factors combined, the system inertia decreases.

The inertia response helps mitigate the impact of power disturbance on the frequency response and maintain the balance of active power generation and consumption. Large system inertia implies a higher level of inertia response in the power system; a strong inertia response means a more limited range of frequency deviation when subject to the same power disturbance. Lacking sufficient system inertia, the power systems are more likely to experience large frequency deviations and abrupt changes of frequency, which poses challenges to the operation of the future power system with a high penetration of renewable generation.

The virtual inertia emulation techniques [28], [43] can be applied at CIG units or converter-interfaced units of electric energy storage to compensate for the deficiency of system inertia. The controls of virtual inertia emulation are often classified into grid-forming and grid-following types. Depending not on external frequency measurement, the grid-forming type

of virtual inertia can be used in a weak AC power system with a high CIG penetration, where the grid-following type of virtual inertia emulation cannot be used. The matching control [20] is an example of the grid-forming type of virtual inertia emulation and is studied specifically in this thesis work. On top of the basic design of virtual inertia emulation, this thesis work adds a control mechanism for regulating reactive power generation. An improved control topology is proposed to incorporate external electricity storage units in the virtual inertia emulation.

However, virtual inertia emulation requires considerable investment in energy storage, advanced controller, etc., which brings a significant financial burden on the TSO. The locations selected to implement the virtual inertia and the amount of virtual inertia to be emulated at the selected locations could significantly affect the performance of virtual inertia emulation and the investment cost. That is to say that an optimal plan of virtual inertia installation helps integrate more renewable generation while ensuring a satisfactory level of frequency response.

The thesis proposed a new method to find such an optimal plan of virtual inertia installation based on the new metric definition measuring the strength of the system's inertia response. The requirements on the system's frequency can then be translated into surrogate constraints in terms of the newly proposed metric. Compared with the classical indices of frequency response, e.g., frequency deviation or RoCoF, the surrogate constraints are mathematically easier to handle. In comparison with the $\mathcal{L}_2$ metric used by Poolla's method in measuring the degree of synchronization of the generation units, the proposed metric characterizes the direct influence of system inertia on the frequency response. On the contrary, the $\mathcal{L}_2$ synchronization measurement depends on many factors other than the system inertia. In the end, the search for an optimal virtual inertia installation was formulated as solving a mathematical optimization problem of mixed-integer type.

The optimization problem can be solved with two methods. The first method is based on classic dynamic programming, and the other method is a newly proposed one that uses the MM-based relaxation technique to convert the mixed-integer optimization problem into a normal one. Furthermore, this research adopted parallelization and cloud computing technologies to facilitate computing speed.

The summaries of every chapter are found below:

Chapter 1 discusses the shift in the energy landscape. An increasing number of renewable generations have displaced synchronous generators in the mix of electric power generation units. Consequently, the system inertia is decreasing. As shown in the postmortem investigation after some significant power outage incidents, the diminished level of system inertia was identified as the key contributing factor to these events. Low system inertia can lead to significant frequency variations, which may trigger unexpected relay actions, eventually leading to a power outage. In response to large frequency variations in the power system, some system operators limit the amount of renewable generation connected to the power system while seeking to install virtual inertia to compensate for the lost system inertia.

Chapter 2 focuses on a specific kind of method of virtual inertia emulation—the matching control. The matching control is a grid-forming type of virtual inertia emulation, which does not rely on an external synchronization mechanism. The basic principles of matching control are discussed in this chapter, and a control topology is proposed that incorporates external electricity storage into the matching control to reduce the investment cost. Moreover, a supplementary voltage control is proposed on top of the basic form of matching control.

Chapter 3 proposes a new metric of the system's inertia response as the $\mathcal{L}_2$ measure of the fast component of the frequency response. The fast dynamic component is obtained with the singular perturbation technique, which helps separate the frequency response into fast and slow components. The fast component is closely related to the system inertia, whereas the slow response is insensitive to the system inertia.

In Chapter 4, the search for the optimal plan of virtual inertia installation is formulated as a mathematical optimization problem with the help of the newly proposed metric in the previous chapter. The mathematical optimization problem considers all possible combinations of working conditions and system faults in its formulation, and the optimal virtual inertia installation plan is obtained as the solution to the mathematical optimization problem. Two methods are proposed to solve the problem. One is based on dynamic programming, and the other method takes advantage of MM techniques. Moreover, cloud computation techniques are applied to facilitate the parallelization and the solution speed.

Finally, in Chapter 5, the proposed method was tested on a modified version of the simplified south Australia power system in comparison with two other planning methods of virtual inertia installation. The instantaneous renewable penetration in the test system is

as high as 50%. The simulation results showed that the performance of the optimal plan of virtual inertia installations produced by the proposed method was comparable to the classical Poolla's method in the test system. But the virtual inertia installation plan given by the proposed method requires less number of virtual inertia installations and needs less investment.

6.2. Suggestions for Future Work

Inertia emulation in micro-grids The thesis work assumes TSO is responsible for planning the virtual inertia installation and the investment. Therefore, the centralized virtual inertia installations at prime locations of the main electricity grid are considered. However, with the proliferation of micro-grids in the modern power system, virtual inertia installation can be installed at micro-grids.

The benefits of installing virtual inertia inside micro-grids are twofold. Firstly, it accommodates the dual operational mode of micro-grid. The micro-grid can operate either in connection with the main transmission system or independently as a local islanded grid. Implementing virtual inertia installation within micro-grids can make the emulated virtual inertia available to the whole power network connection and its own when the micro-grid is not connected to the main power grid. Secondly, there is a considerable amount of electricity storage inside micro-grids. The electricity storage within micro-grids can be effectively utilized as the reserve of inertia emulation. However, it also makes the planning of virtual inertia installation more complicated. How to optimally coordinate existing electricity storage inside micro-grids and tackle the dual operational modes of micro-grids will be the topic of future researches.

Ancillary market With the development of the electricity market, many types of system resources of stability control can be traded in ancillary markets. For example, an ancillary market has been created for trading the spinning reserve of primary frequency control. A similar ancillary market can also be created for trading the system inertia. Unlike planning the virtual inertia installation, this design of the ancillary market focuses on the aspect of system operation. Via the ancillary market, it is expected that a sufficient amount of system inertia is secured at all times at the most economical cost while ensuring the profitability of

electricity storage providers, owners of renewable electricity generators, etc.

Appendix A

Network Data of the Original Southeast Australian Power System

Table. A.1.: Parameters of system buses.

From bus	To bus	R	X	B	Tap Changer tap_{min}	Tap Changer tap_{max}	Multiplicity
101	102	0.000	0.01200	0.000	0.9	1.1	
201	206	0.000	0.00480	0.000	0.9	1.1	
202	209	0.000	0.00720	0.000	0.9	1.1	
203	208	0.000	0.01530	0.000	0.9	1.1	
204	215	0.000	0.00600	0.000	0.9	1.1	
209	210	0.000	0.02720	0.000	0.9	1.1	×4
213	214	0.000	0.02720	0.000	0.9	1.1	×4
301	303	0.000	0.00300	0.000	0.9	1.1	
302	312	0.000	0.01127	0.000	0.9	1.1	
304	313	0.000	0.03200	0.000	0.9	1.1	×2
305	311	0.000	0.03600	0.000	0.9	1.1	×3
305	314	0.000	0.02400	0.000	0.9	1.1	×2
308	315	0.000	0.02700	0.000	0.9	1.1	×2
401	410	0.000	0.00845	0.000	0.9	1.1	
402	408	0.000	0.01700	0.000	0.9	1.1	
403	407	0.000	0.00845	0.000	0.9	1.1	
404	405	0.000	0.01020	0.000	0.9	1.1	

413	414	0.000	0.00800	0.000	0.9	1.1	×3
501	504	0.000	0.02550	0.000	0.9	1.1	
502	505	0.000	0.01600	0.000	0.9	1.1	
503	506	0.000	0.05000	0.000	0.9	1.1	
102	217	0.0084	0.0667	0.817	1.0	1.0	×2
102	217	0.0078	0.0620	0.760	1.0	1.0	×2
102	309	0.0045	0.0356	0.437	1.0	1.0	×2
102	309	0.0109	0.0868	0.760	1.0	1.0	
205	206	0.0096	0.0760	0.931	1.0	1.0	×2
205	416	0.0037	0.0460	0.730	1.0	1.0	×2
206	207	0.004500	0.035600	0.437	1.0	1.0×2	
206	212	0.006600	0.052700	0.646	1.0	1.0×2	
206	215	0.006600	0.052700	0.646	1.0	1.0×2	
207	208	0.001800	0.014000	0.171	1.0	1.0×2	
207	209	0.000800	0.006200	0.076	1.0	1.0	
208	211	0.003100	0.024800	0.304	1.0	1.0×3	
209	212	0.004500	0.035600	0.437	1.0	1.0	
210	213	0.001000	0.014500	1.540	1.0	1.0×2	
211	212	0.001400	0.010800	0.133	1.0	1.0×2	
211	214	0.001900	0.015500	0.190	1.0	1.0	
212	217	0.007000	0.055800	0.684	1.0	1.0	
214	216	0.001000	0.007700	0.095	1.0	1.0	
214	217	0.004900	0.038800	0.475	1.0	1.0	
215	216	0.005100	0.040300	0.494	1.0	1.0×2	
215	217	0.007200	0.057400	0.703	1.0	1.0×2	
216	217	0.005100	0.040300	0.494	1.0	1.0	
303	304	0.002000	0.028000	0.740	1.0	1.0×2	
303	305	0.001100	0.016000	1.700	1.0	1.0×2	
304	305	0.000300	0.004000	0.424	1.0	1.0	
305	306	0.000200	0.003000	0.320	1.0	1.0	
307	308	0.002300	0.032500	3.445	1.0	1.0×2	
309	310	0.013500	0.106950	0.5826	1.0	1.0×3	

310	311	0.000000	−0.033700*	0.000	1.0	1.0 × 2
312	313	0.006000	0.045000	0.300	1.0	1.0 × 3
313	314	0.001000	0.010000	0.260	1.0	1.0 × 2
315	509	0.007000	0.050000	0.190	1.0	1.0 × 2
405	406	0.003900	0.047500	0.381	1.0	1.0 × 2
405	408	0.005400	0.050000	0.189	1.0	1.0
405	409	0.018000	0.122000	0.790	1.0	1.0 × 3
406	407	0.000600	0.007600	0.062	1.0	1.0 × 2
407	408	0.004200	0.051300	0.412	1.0	1.0
408	410	0.016500	0.192000	0.673	1.0	1.0 × 3
409	411	0.010300	0.070900	0.460	1.0	1.0 × 2
410	411	0.004300	0.053200	0.427	1.0	1.0
410	412	0.004300	0.053200	0.427	1.0	1.0 × 4
410	413	0.004000	0.049400	0.400	1.0	1.0 × 2
411	412	0.001200	0.015200	0.122	1.0	1.0 × 2
414	415	0.002000	0.025000	0.390	1.0	1.0 × 2
415	416	0.003700	0.046000	0.730	1.0	1.0 × 2
504	507	0.023000	0.150000	0.560	1.0	1.0 × 2
504	508	0.026000	0.019000	0.870	1.0	1.0 × 2
505	507	0.001600	0.017000	0.030	1.0	1.0 × 2
505	508	0.002500	0.028000	0.170	1.0	1.0
506	507	0.001600	0.017000	0.030	1.0	1.0 × 2
506	508	0.003000	0.028000	0.140	1.0	1.0
507	508	0.002000	0.019000	0.090	1.0	1.0
507	509	0.090000	0.660000	0.300	1.0	1.0 × 6

Table. A.2.: Parameters of synchronous generators.

Bus	MBASE	X_l	R_a	X_d	X'_d	X''_d	T'_{do}	T''_{do}	X_q	X'_q	X''_q	T'_{q0}	T''_{qo}	H	d_0	d_1
101	999.90	0.14	0.00	1.10	0.25	0.20	8.50	0.050	0.65	0.25	0.20	1.00	0.20	1.80	0.00	0.00
201	3333.50	0.20	0.00	1.80	0.30	0.21	8.50	0.040	1.75	0.70	0.21	0.30	0.08	1.60	0.00	0.00

*As shown in Figure. 5.1 and the original source [6], these links together with links between bus `309` and `310` likely models the static synchronous series compensator (SCCC)-compensated transmission lines.

202	2222.40	0.17	0.00	2.20	0.30	0.20	4.50	0.040	2.10	0.50	0.20	1.50	0.06	1.40	0.00	0.00
203	1111.20	0.20	0.00	2.30	0.30	0.25	5.00	0.030	1.70	0.40	0.25	2.00	0.25	1.30	0.00	0.00
204	2666.80	0.20	0.00	1.80	0.30	0.21	8.50	0.040	1.75	0.70	0.21	0.30	0.08	1.60	0.00	0.00
301	5333.60	0.20	0.00	2.70	0.30	0.25	7.50	0.040	1.50	0.85	0.25	0.85	0.12	2.80	0.00	0.00
302	1333.20	0.15	0.00	2.00	0.25	0.20	7.50	0.040	1.80	0.25	0.20	1.25	0.25	3.50	0.00	0.00
401	1777.60	0.20	0.00	2.30	0.30	0.25	5.00	0.030	1.70	0.40	0.25	2.00	0.25	2.60	0.00	0.00
402	999.90	0.20	0.00	1.90	0.30	0.26	6.50	0.035	1.80	0.55	0.26	1.40	0.04	3.00	0.00	0.00
403	1777.60	0.20	0.00	2.30	0.30	0.25	5.00	0.030	1.70	0.40	0.25	2.00	0.25	2.60	0.00	0.00
404	1666.50	0.18	0.00	2.20	0.32	0.24	9.00	0.040	1.40	0.75	0.24	1.40	0.75	0.24	0.00	0.00
501	666.60	0.15	0.00	2.20	0.30	0.24	7.50	0.025	1.70	0.80	0.24	1.50	0.10	3.50	0.00	0.00
502	1000.00	0.20	0.00	2.00	0.30	0.22	7.50	0.040	1.50	0.80	0.22	3.00	0.20	4.00	0.00	0.00
503	333.40	0.25	0.00	2.30	0.25	0.17	5.00	0.0220	2.00	0.35	0.17	1.00	0.035	7.50	0.00	0.00

Bibliography

[1] United Nations, "Paris agreement," *Conference of the Parties*, 2015.

[2] M. Foley and J. Aston, "All-island generation capacity statement 2019–2028," EriGrid and SONI, Tech. Rep., 2019. [Online]. Available: http://www.eirgridgroup.com/site-files/library/EirGrid/EirGrid-Group-All-Island-Generation-Capacity-Statement-2019-2028.pdf.

[3] AEMO, "2021 national transmission network developoment plan," Tech. Rep., 2021. [Online]. Available: https://www.aemo.com.au/energy-systems/electricity/national-electricity-market-nem/nem-forecasting-and-planning/forecasting-and-planning-data/generation-information.

[4] N. R. Canada, "About renewable energy," Tech. Rep., 2018. [Online]. Available: https://www.nrcan.gc.ca/our-natural-resources/energy-sources-distribution/renewable-energy/about-renewable-energy/7295.

[5] UCTE, "Final report—system disturbance on 4 november 2006," Tech. Rep., 2006. [Online]. Available: http://ecolo.org/documents/documents_in_english/blackout-nov-06-UCTE-report.pdf.

[6] AEMO, "Update report—black system event in south australia on 28 september 2016," Tech. Rep., 2016. [Online]. Available: https://www.aemo.com.au/Media-Centre/-/media/BE174B1732CB4B3ABB74BD507664B270.ashx.

[7] F. Milano, D. Florian, Z. Eth, D. J. Hill, and G. Verbič, "Foundations and Challenges of Low-Inertia Systems," *2018 Power Systems Computation Conference (PSCC)*, p. 26,

[8] A. S. Ahmadyar, S. Riaz, G. Verbic, A. Chapman, and D. J. Hill, "A Framework for Assessing Renewable Integration Limits with Respect to Frequency Performance," *IEEE Transactions on Power Systems*, vol. 33, no. 4, pp. 4444–4453, 2018, ISSN: 08858950. DOI: 10.1109/TPWRS.2017.2773091.

[9] N. Miller, M. Shao, S. Pajic, and R. D'Aquila, "Western wind and solar integration study phase 3 – frequency response and transient stability," Tech. Rep., 2014. [Online]. Available: https://www.nrel.gov/docs/fy15osti/62906.pdf.

[10] M. C. Chandorkar, D. M. Divan, and R. Adapa, "Control of parallel connected inverters in standalone ac supply systems," *IEEE transactions on industry applications*, vol. 29, no. 1, pp. 136–143, 1993.

[11] T. V. Van, K. Visscher, J. Diaz, V. Karapanos, A. Woyte, M. Albu, J. Bozelie, T. Loix, and D. Federenciuc, "Virtual synchronous generator: An element of future grids," in *2010 IEEE PES Innovative Smart Grid Technologies Conference Europe (ISGT Europe)*, IEEE, 2010, pp. 1–7.

[12] D. Groß, S. Bolognani, B. K. Poolla, and F. Dörfler, "Increasing the resilience of low-inertia power systems by virtual inertia and damping," in *Proceedings of IREP'2017 Symposium*, International Institute of Research and Education in Power System Dynamics . . ., 2017, p. 64.

[13] J. Khazaei, Z. Tu, and W. Liu, "Small-signal modeling and analysis of virtual inertia-based pv systems," *IEEE Transactions on Energy Conversion*, vol. 35, no. 2, pp. 1129–1138, 2020. DOI: 10.1109/TEC.2020.2973102.

[14] U. Markovic, Z. Chu, P. Aristidou, and G. Hug, "LQR-based adaptive virtual synchronous machine for power systems with high inverter penetration," *IEEE Transactions on Sustainable Energy*, vol. 10, no. 3, pp. 1501–1512, 2019. DOI: 10.1109/TSTE.2018.2887147.

[15] E. Ela, V. Gevorgian, A. Tuohy, B. Kirby, M. Milligan, and M. O'Malley, "Market Designs for the Primary Frequency Response Ancillary Service—Part I: Motivation and Design," *IEEE Transactions on Power Systems*, vol. 29, no. 1, pp. 421–431, Jan. 2014, ISSN: 0885-8950. DOI: 10.1109/TPWRS.2013.2264942. [Online]. Available: http://ieeexplore.ieee.org/document/6544662/.

[16] B. K. Poolla, S. Bolognani, and F. Dorfler, "Optimal Placement of Virtual Inertia in Power Grids," vol. 62, no. 12, pp. 6209–6220, 2015, ISSN: 0018-9286. DOI: 10.1109/TAC.2017.2703302. arXiv: 1510.01497. [Online]. Available: http://arxiv.org/abs/1510.01497%7B%5C%%7D0Ahttp://dx.doi.org/10.1109/TAC.2017.2703302.

[17] B. K. Poolla, D. Gross, and F. Dörfler, "Placement and implementation of grid-forming and grid-following virtual inertia and fast frequency response," *IEEE Transactions on Power Systems*, 2019.

[18] E. Lovisari and S. Zampieri, "Performance metrics in the average consensus problem: A tutorial," *Annual Reviews in Control*, vol. 36, no. 1, pp. 26–41, Apr. 2012, ISSN: 13675788. DOI: 10.1016/j.arcontrol.2012.03.003. [Online]. Available: http://dx.doi.org/10.1016/j.arcontrol.2012.03.003%20https://linkinghub.elsevier.com/retrieve/pii/S1367578812000041.

[19] B. K. Poolla, S. Bolognani, and F. Dorfler, "Optimal Placement of Virtual Inertia in Power Grids," *IEEE Transactions on Automatic Control*, vol. 62, no. 12, pp. 6209–6220, Dec. 2017, ISSN: 0018-9286. DOI: 10.1109/TAC.2017.2703302. arXiv: 1510.01497. [Online]. Available: http://ieeexplore.ieee.org/document/7924418/.

[20] C. Arghir, T. Jouini, and F. Dörfler, "Grid-forming control for power converters based on matching of synchronous machines," *Automatica*, vol. 95, pp. 273–282, 2018, ISSN: 00051098. DOI: 10.1016/j.automatica.2018.05.037. arXiv: 1706.09495. [Online]. Available: https://doi.org/10.1016/j.automatica.2018.05.037.

[21] N. Pogaku, M. Prodanovic, and T. C. Green, "Modeling, analysis and testing of autonomous operation of an inverter-based microgrid," *IEEE Transactions on Power Electronics*, vol. 22, no. 2, pp. 613–625, 2007. DOI: 10.1109/TPEL.2006.890003.

[22] U. Tamrakar, D. Shrestha, M. Maharjan, B. P. Bhattarai, T. M. Hansen, and R. Tonkoski, "Virtual inertia: Current trends and future directions," *Applied Sciences*, vol. 7, no. 7, 2017, ISSN: 2076-3417. DOI: 10.3390/app7070654. [Online]. Available: https://www.mdpi.com/2076-3417/7/7/654.

[23] Q.-C. Zhong, "Virtual synchronous machines: A unified interface for grid integration," *IEEE Power Electronics Magazine*, vol. 3, no. 4, pp. 18–27, Dec. 2016, ISSN: 2329-9215. DOI: 10.1109/MPEL.2016.2614906.

[24] J. Alipoor, Y. Miura, and T. Ise, "Power system stabilization using virtual synchronous generator with alternating moment of inertia," *IEEE Journal of Emerging and Selected Topics in Power Electronics*, vol. 3, no. 2, pp. 451–458, Jun. 2015, ISSN: 2168-6785. DOI: 10.1109/JESTPE.2014.2362530.

[25] V. Natarajan and G. Weiss, "Synchronverters with better stability due to virtual inductors, virtual capacitors, and anti-windup," *IEEE Transactions on Industrial Electronics*, vol. 64, no. 7, pp. 5994–6004, Jul. 2017, ISSN: 1557-9948. DOI: 10.1109/TIE.2017.2674611.

[26] M. van Wesenbeeck, S. de Haan, P. Varela, and K. Visscher, "Grid tied converter with virtual kinetic storage," in *2009 IEEE Bucharest PowerTech*, Jun. 2009, pp. 1–7. DOI: 10.1109/PTC.2009.5282048.

[27] J. Fang, Y. Tang, H. Li, and X. Li, "A battery/ultracapacitor hybrid energy storage system for implementing the power management of virtual synchronous generators," *IEEE Transactions on Power Electronics*, vol. 33, no. 4, pp. 2820–2824, Apr. 2018, ISSN: 1941-0107. DOI: 10.1109/TPEL.2017.2759256.

[28] G. Delille, B. François, and G. Malarange, "Dynamic frequency control support: A virtual inertia provided by distributed energy storage to isolated power systems," in *2010 IEEE PES Innovative Smart Grid Technologies Conference Europe (ISGT Europe)*, Oct. 2010, pp. 1–8. DOI: 10.1109/ISGTEUROPE.2010.5638887.

[29] L. Zeni, A. J. Rudolph, J. Münster-Swendsen, I. Margaris, A. D. Hansen, and P. Sørensen, "Virtual inertia for variable speed wind turbines," *Wind energy*, vol. 16, no. 8, pp. 1225–1239, 2013.

[30] M. F. M. Arani and E. F. El-Saadany, "Implementing virtual inertia in dfig-based wind power generation," *IEEE Transactions on Power Systems*, vol. 28, no. 2, pp. 1373–1384, May 2013, ISSN: 1558-0679. DOI: 10.1109/TPWRS.2012.2207972.

[31] Q. Ren, H. Liu, Q. Li, J. He, B. Xu, and X. Yuan, "A novel inertia control strategy for dfig wind turbines based on slip feedback," in *2017 IEEE 7th Annual International Conference on CYBER Technology in Automation, Control, and Intelligent Systems (CYBER)*, Jul. 2017, pp. 668–672. DOI: 10.1109/CYBER.2017.8446334.

[32] *Active Aerodynamic Load Control of Wind Turbine Blades*, vol. Volume 2: Fora, Parts A and B, Fluids Engineering Division Summer Meeting, Jul. 2007, pp. 1119–1127. DOI: 10.1115/FEDSM2007-37604. eprint: https://asmedigitalcollection.asme.org/FEDSM/proceedings-pdf/FEDSM2007/42894/1119/2670598/1119_1.pdf. [Online]. Available: https://doi.org/10.1115/FEDSM2007-37604.

[33] E. Muljadi and C. Butterfield, "Pitch-controlled variable-speed wind turbine generation," *IEEE Transactions on Industry Applications*, vol. 37, no. 1, pp. 240–246, Jan. 2001, ISSN: 1939-9367. DOI: 10.1109/28.903156.

[34] F. Zhou and J. Liu, "Pitch controller design of wind turbine based on nonlinear pi/pd control," *Shock and Vibration*, vol. 2018, p. 7 859 510, Oct. 2018, ISSN: 1070-9622. DOI: 10.1155/2018/7859510. [Online]. Available: https://doi.org/10.1155/2018/7859510.

[35] M. Rasul, *Clean energy for sustainable development: comparisons and contrasts of new approaches*. Academic Press, 2016.

[36] J. Lee, E. Muljadi, P. Srensen, and Y. C. Kang, "Releasable kinetic energy-based inertial control of a dfig wind power plant," *IEEE Transactions on Sustainable Energy*, vol. 7, no. 1, pp. 279–288, Jan. 2016, ISSN: 1949-3037. DOI: 10.1109/TSTE.2015.2493165.

[37] D. Yang, Z. Jin, T. Zheng, and E. Jin, "An adaptive droop control strategy with smooth rotor speed recovery capability for type iii wind turbine generators," *International Journal of Electrical Power & Energy Systems*, vol. 135, p. 107 532, 2022, ISSN: 0142-0615. DOI: https://doi.org/10.1016/j.ijepes.2021.107532. [Online]. Available: https://www.sciencedirect.com/science/article/pii/S0142061521007699.

[38] F. Milano, "Rotor speed-free estimation of the frequency of the center of inertia," *IEEE Transactions on Power Systems*, vol. 33, no. 1, pp. 1153–1155, 2018, ISSN: 08858950. DOI: 10.1109/TPWRS.2017.2750423.

[39] F. Dörfler and F. Bullo, "Kron reduction of graphs with applications to electrical networks," *IEEE Transactions on Circuits and Systems I: Regular Papers*, vol. 60, no. 1, pp. 150–163, 2013. DOI: 10.1109/TCSI.2012.2215780.

[40] L. Perko, *Differential Equations and Dynamical Systems*. New York: Springer, 1991.

[41] R. Liu, G. Verbič, J. Ma, and D. J. Hill, "Fast stability scanning for future grid scenario analysis," *IEEE Transactions on Power Systems*, vol. 33, no. 1, pp. 514–524, Jan. 2018. DOI: 10.1109/TPWRS.2017.2694048.

[42] B. K. Poolla, S. Bolognani, N. Li, and F. Dörfler, "A market mechanism for virtual inertia," *IEEE Transactions on Smart Grid*, vol. 11, no. 4, pp. 3570–3579, 2020. DOI: 10.1109/TSG.2020.2969518.

[43] L. Ruttledge and D. Flynn, "Emulated inertial response from wind turbines: Gain scheduling and resource coordination," *IEEE Transactions on Power Systems*, vol. 31, no. 5, pp. 3747–3755, 2016, ISSN: 08858950. DOI: 10.1109/TPWRS.2015.2493058.

[44] P. Kundur, N. J. Balu, and M. G. Lauby, *Power system stability and control*. McGraw-hill New York, 1994, vol. 7.

[45] P. W. Sauer and M. A. Pai, *Power system dynamics and stability*. Wiley Online Library, 1998, vol. 101.

[46] P. M. Anderson and A. A. Fouad, *Power system control and stability*. John Wiley & Sons, 2008.

[47] T. Van Cutsem and C. Vournas, *Voltage stability of electric power systems*. Springer Science & Business Media, 1998, vol. 441.

[48] Z. Li, S. Gadipelli, H. Li, C. A. Howard, D. J. L. Brett, P. R. Shearing, Z. Guo, I. P. Parkin, and F. Li, "Tuning the interlayer spacing of graphene laminate films for efficient pore utilization towards compact capacitive energy storage," *Nature Energy*, vol. 5, no. 2, pp. 160–168, Feb. 2020, ISSN: 2058-7546. DOI: 10.1038/s41560-020-0560-6. [Online]. Available: https://doi.org/10.1038/s41560-020-0560-6.

[49] T. A. Faunce, J. Prest, D. Su, S. J. Hearne, and F. Iacopi, "On-grid batteries for large-scale energy storage: Challenges and opportunities for policy and technology," *MRS Energy & Sustainability*, vol. 5, E11, 2018. DOI: 10.1557/mre.2018.11.

[50] ENTSO-E, "Frequency measurement requirements and usage," 2018.

[51] A. Mamen and U. Supatti, "A survey of hybrid energy storage systems applied for intermittent renewable energy systems," in *2017 14th International Conference on Electrical Engineering/Electronics, Computer, Telecommunications and Information Technology (ECTI-CON)*, 2017, pp. 729–732. DOI: 10.1109/ECTICon.2017.8096342.

[52] V. Knap, S. K. Chaudhary, D.-I. Stroe, M. Swierczynski, B.-I. Craciun, and R. Teodorescu, "Sizing of an energy storage system for grid inertial response and primary frequency reserve," *IEEE Transactions on Power Systems*, vol. 31, no. 5, pp. 3447–3456, 2015.

[53] K. Zhou, J. C. Doyle, K. Glover, *et al.*, *Robust and optimal control*. Prentice hall New Jersey, 1996, vol. 40.

[54] J. Medanic, H. S. Tharp, and W. R. Perkins, "Pole placement by performance criterion modification," *IEEE Transactions on Automatic Control*, vol. 33, no. 5, pp. 469–472, 1988. DOI: 10.1109/9.1229.

[55] M. H. Holmes, *Introduction to perturbation methods*. Springer Science & Business Media, 2012, vol. 20.

[56] P. A. Lagerstrom, *Matched asymptotic expansions: ideas and techniques*. Springer Science & Business Media, 2013, vol. 76.

[57] H. K. Khalil, *Nonlinear systems*. Upper Saddle River, 2002.

[58] F. Verhulst, "Singular perturbation methods for slow–fast dynamics," *Nonlinear Dynamics*, vol. 50, no. 4, pp. 747–753, 2007.

[59] A. N. Tikhonov, "Systems of differential equations containing small parameters in the derivatives," *Matematicheskii sbornik*, vol. 73, no. 3, pp. 575–586, 1952.

[60] J. M. V. Grzybowski, E. E. N. Macau, and T. Yoneyama, "On synchronization in power-grids modelled as networks of second-order kuramoto oscillators," *Chaos: An Interdisciplinary Journal of Nonlinear Science*, vol. 26, no. 11, p. 113 113, 2016. DOI: 10.1063/1.4967850. eprint: https://doi.org/10.1063/1.4967850. [Online]. Available: https://doi.org/10.1063/1.4967850.

[61] F. Dörfler and F. Bullo, "Synchronization and transient stability in power networks and nonuniform kuramoto oscillators," *SIAM Journal on Control and Optimization*, vol. 50, no. 3, pp. 1616–1642, 2012. DOI: 10.1137/110851584. eprint: https://doi.org/10.1137/110851584. [Online]. Available: https://doi.org/10.1137/110851584.

[62] S. Olmi, A. Navas, S. Boccaletti, and A. Torcini, "Hysteretic transitions in the kuramoto model with inertia," *Phys. Rev. E*, vol. 90, p. 042 905, 4 Oct. 2014. DOI: 10.1103/PhysRevE.90.042905. [Online]. Available: https://link.aps.org/doi/10.1103/PhysRevE.90.042905.

[63] H. D. Chiang and C. C. Chu, "Theoretical Foundation of the BCU Method for Direct Stability Analysis of Network-Reduction Power System Models with Small Transfer Conductances," *IEEE Transactions on Circuits and Systems I: Fundamental Theory and Applications*, vol. 42, no. 5, pp. 252–265, 1995, ISSN: 10577122. DOI: 10.1109/81.386159.

[64] H. D. Chiang, F. F. Wu, and P. P. Varaiya, "Foundations of the potential energy boundary surface method for power system transient stability analysis," *IEEE Transactions on Circuits and Systems*, vol. 35, no. 6, pp. 712–728, 1988. DOI: 10.1109/31.1808.

[65] F. Dörfler and F. Bullo, "Synchronization and Transient Stability in Power Networks and Nonuniform Kuramoto Oscillators," *SIAM Journal on Control and Optimization*, vol. 50, no. 3, pp. 1616–1642, Jan. 2012, ISSN: 0363-0129. DOI: 10.1137/110851584. [Online]. Available: http://epubs.siam.org/doi/10.1137/110851584.

[66] F. Milano and Á. Ortega, "Frequency Divider," *IEEE Transactions on Power Systems*, vol. 32, no. 2, pp. 1493–1501, 2017, ISSN: 08858950. DOI: 10.1109/TPWRS.2016.2569563.

[67] E. J. Candès, M. B. Wakin, and S. P. Boyd, "Enhancing Sparsity by Reweighted ℓ_1 Minimization," *Journal of Fourier Analysis and Applications*, vol. 14, no. 5-6, pp. 877–905, Dec. 2008, ISSN: 1069-5869. DOI: 10.1007/s00041-008-9045-x. arXiv: 0711.1612. [Online]. Available: http://link.springer.com/10.1007/s00041-008-9045-x.

[68] K. Lange, *MM Optimization Algorithms*. Philadelphia, PA: Society for Industrial and Applied Mathematics, 2016. DOI: 10.1137/1.9781611974409. eprint: https://epubs.siam.org/doi/pdf/10.1137/1.9781611974409. [Online]. Available: https://epubs.siam.org/doi/abs/10.1137/1.9781611974409.

[69] J. H. Chow, *Power system coherency and model reduction*. Springer, 2013, vol. 84.

[70] D. P. Bertsekas *et al.*, *Dynamic programming and optimal control: Vol. 1*. Athena scientific Belmont, 2000.

[71] J. Nocedal and S. Wright, *Numerical optimization*. Springer Science & Business Media, 2006.

[72] D. R. Hunter and K. Lange, "A tutorial on mm algorithms," *The American Statistician*, vol. 58, no. 1, pp. 30–37, 2004. DOI: 10.1198/0003130042836. eprint: https://doi.org/10.1198/0003130042836. [Online]. Available: https://doi.org/10.1198/0003130042836.

[73] D. R. Hunter and R. Li, "Variable selection using MM algorithms," *The Annals of Statistics*, vol. 33, no. 4, Aug. 2005. DOI: 10.1214/009053605000000200. [Online]. Available: https://doi.org/10.1214/009053605000000200.

[74] F. Dörfler, M. R. Jovanović, M. Chertkov, and F. Bullo, "Sparsity-promoting optimal wide-area control of power networks," *IEEE Transactions on Power Systems*, vol. 29, no. 5, pp. 2281–2291, Sep. 2014, ISSN: 1558-0679. DOI: 10.1109/TPWRS.2014.2304465.

[75] F. Lin, M. Fardad, and M. R. Jovanović, "Design of optimal sparse feedback gains via the alternating direction method of multipliers," *IEEE Transactions on Automatic Control*, vol. 58, no. 9, pp. 2426–2431, 2013. DOI: 10.1109/TAC.2013.2257618.

[76] D. R. Hunter and R. Li, "A connection between variable selection and em-type algorithms," *Pennsylvania State University statistics department technical report*, vol. 201, 2002.

[77] R. Diao, S. Jin, F. Howell, Z. Huang, L. Wang, D. Wu, and Y. Chen, "On parallelizing single dynamic simulation using hpc techniques and apis of commercial software," *IEEE Transactions on Power Systems*, vol. 32, no. 3, pp. 2225–2233, May 2017, ISSN: 1558-0679. DOI: 10.1109/TPWRS.2016.2601024.

[78] A. M. Gamaleldin, "An introduction to cloud computing concepts," *Software Engineering Competence Center*, p. 2, 2013.

[79] J. Machowski, J. Bialek, J. R. Bumby, and J. Bumby, *Power system dynamics and stability*. John Wiley & Sons, 1997.

[80] F. Milano, *Power System Modelling and Scripting*, ser. Power Systems. Berlin, Heidelberg: Springer Berlin Heidelberg, 2010, ISBN: 978-3-642-13668-9. DOI: 10.1007/978-3-642-13669-6. [Online]. Available: http://link.springer.com/10.1007/978-3-642-13669-6.